

Spin-orbit Coupled Bose Gases

by

Boris Shteynas

B.Sc., Moscow Institute of Physics and Technology (2010)

Submitted to the Department of Physics
in partial fulfillment of the requirements for the degree of

Doctor of Philosophy in Physics

at the

MASSACHUSETTS INSTITUTE OF TECHNOLOGY

September 2019

© Massachusetts Institute of Technology 2019. All rights reserved.

Author
Department of Physics
August 30, 2019

Certified by.....
Wolfgang Ketterle
John D. MacArthur Professor of Physics
Thesis Supervisor

Accepted by
Nergis Mavalvala
Associate Department Head for Physics

Spin-orbit Coupled Bose Gases

by

Boris Shteynas

Submitted to the Department of Physics
on August 30, 2019, in partial fulfillment of the
requirements for the degree of
Doctor of Philosophy in Physics

Abstract

Quantum simulation is a very active and growing field. Various quantum systems can be used to emulate existing materials in an accurate and controllable way, as well as to generate new states of matter that have not been found in the real world but the existence of which does not contradict the fundamental laws of physics. Ultracold atoms form a perfect system to realize idealized models and study physical mechanisms that stand out clearly in them.

Recent efforts have been made to simulate artificial gauge fields with ultracold atoms, including spin-dependent gauge fields, such as spin-orbit coupling. Motivated by this goal our lab explored several approaches to generate a one-dimensional spin-orbit coupling interaction, which has a rich phase diagram and plays an important role for topological insulators, the quantum spin Hall effect and spintronics. The first method we developed allowed us to detect a stripe phase by dressing Bose-Einstein condensates with an optical superlattice and Raman beams. The observed density modulation in the ground state meets the definition of the long-awaited supersolid state of matter.

The second approach we took was to generate spin-orbit coupling without use of lasers. The method is based on the idea of periodic driving of the quantum system and dressing its evolution with fast micromotion, often referred to as Floquet engineering. Our experiment provided an insightful pedagogical example of what Floquet engineering is capable of. In the experiment we endowed a low energy radio-frequency photon with tunable momentum. When dressed with recoil momentum, the interaction of a radio-frequency photon with an atom occurred in a Doppler-sensitive way. We also demonstrated how to tune the momentum and flip its direction.

In this thesis, I first describe the experiments done in the optical superlattice. Then I discuss the behavior of periodically driven classical and quantum systems and provide detailed analysis of how a radio-frequency photon can be magnetically dressed with tunable momentum.

The experiments we carried out demonstrated novel methods of generation for spin-dependent gauge fields and showed pedagogical examples and interpretations of evolution of periodically driven systems. The scheme of periodically driven atoms

inspired a theoretical study of heating in Floquet systems.

Thesis Supervisor: Wolfgang Ketterle

Title: John D. MacArthur Professor of Physics

*Dedicated to my parents
and to the memory of
my grandparents.*

Acknowledgments

It is hard to find the right words to fully express how grateful I am to the people who were around me during my PhD and how important the experience of graduate school is for me. It has been a time of enormous challenges and hard work, but at the same time it has been an incredibly rewarding period of life. MIT not only pushed me to my intellectual and physical limits, but also formed my personality. After all, graduate school at MIT made me realize who I am and to what circle of people I belong.

Absolutely the highest honor of my life was to learn from Professor Wolfgang Ketterle. The years spent in his group have definitely been, and most likely will remain, the highlight of my life. Observing his striking analytical mind, the way he views physics, his incredible intuition for sorting out experimental questions – all of that is the school of physics of which one can only dream. I'm also very grateful to Wolfgang for being very kind to me (perhaps, more than I deserved). Without his timely encouragements I would not be able to make it to the end of graduate school.

During all 7 years at MIT I was happy to be surrounded by brilliant wonderful people. I will not be able to mention all of them here, but I would like to say that the intellectual environment at MIT itself is a unique medium which stimulates and inspires personal growth. It has been a great honor to be a part of the MIT Physics Department and the Center for Ultracold Atoms.

I'd like to thank the other professors at the CUA. Professor Vladan Vuletic was my academic advisor. I always knew I could rely on his advice in physics and on the choice of academic path. Professor Martin Zwierlein's genuine excitement about physics inspires not only his students, but also those who happen to come across him in the corridor or those like me, who have their office just next door. I will also remember insightful discussions with Professor Ike Chuang, whose expertise in various fields of physics and technology is absolutely overwhelming.

I'd like to thank former members of BEC2 lab Ed Su and Wujie Huang, who built the machine I eventually used. Wujie, your guidance helped me make the first

semi-independent steps in the lab. I also enjoy remembering our road trips including the last one when Junru and I gave you a ride from Boston towards your new place and new life.

I'd like to thank Junru Li who started MIT the same year with me. Junru has always been an example to me of what a successful graduate student should be like. I always admired his dedication to lab work and his talent for physics. We share a lot of memories inside and outside of the lab.

I was happy to work with two great postdocs Alan Jamison and Jeongwon (Chris) Lee. Chris and I worked particularly closely on the experiment on which this thesis focuses. Our styles in the lab were quite different, but we both were determined to make this project work, and, I think, we not only both enjoyed working together but also benefited from this collaboration. I learnt a lot from Chris, and there were several moments when I had no strength to push the experiment, but Chris was ready to continue the effort. So, I can unhesitatingly say that without Chris this work would not be completed. Alan has been in the group during most of my PhD, and I asked him so many physics questions I was confused about. Every time the answer was prompt, accurate and comprehensive. It is really important that such people as Alan keep going the “thorny” path of academia, and I was genuinely happy to hear the news that Alan got appointed to a well-deserved professorship and very soon will start his own cold atoms lab. Good luck at the new place, Alan, and thank you for your help during those many years!

I would like to acknowledge all the members of the Ketterle group, past and present. Sometimes the boundaries between our labs vanish and the ideas (along with equipment) flow from one team to another. For example, every electronics project in our group starts with a “pilgrimage” to Will Lunden. I am very grateful to him for all the very valuable suggestions and ideas which helped to implement our experiment.

I have not worked together with Timur Rvachov from the BEC3 lab, but from the very first days in the group he helped me a lot. Even now, many years later, I remember his transparent explanations of fundamental concepts, not to mention the many technical skills in optics and other areas I picked up directly from him.

Timur was always ready to help even at 5 am when he was busy with running his own experiment. Our conversations on life issues (happening around 5 am, as well) are also something I will always remember. Thank you, Timur!

I would like to thank Jesse Amato-Grill from the BEC5 lab. Even before we became groupmates I remember seeing him for the first time in the atomic physics class. I thought this guy must be from Harvard: well-dressed and with very good manners... I was happy to get to know Jesse closer after I joined the group. It turned out that from the inside he was no less refined a person. After almost seven years spent side by side I can conclude that Jesse is one of the smartest and most knowledgeable people I've known. I've been happy to have him as a colleague and a friend.

Other members of the BEC5 lab, Niklas Jepsen and Ivana Dimitrova, have also been around throughout my entire PhD. Niki, your presence in the group made a lot of difference to me. So many times you saved my day from frustration. Just chatting with you about the lab problems or life helped me to pull through the difficulties of the PhD. I am also thankful to Ivana. I've always been impressed by her sharp mind and critical thinking.

At the end of my PhD I was happy to overlap with Yair Margalit. He made a very good impression on me when he visited MIT for the interview in our group. It was immediately clear that Yair is very a smart physicist and a very easy-going friendly person. I was very glad when he joined our lab and, in my opinion, he is an excellent team member. I really enjoyed working together with him and it is a pity this collaboration was not very long.

Sean Burchesky spent his undergraduate years in our lab and I've been absolutely amazed by his skills and talent for experimental physics. Sean revealed all the good stereotypes about MIT students. He enjoys making things work, and things actually work. Thank you, Sean, for being part of our team! Furkan Top is next in line for graduation in BEC2 lab. I have always been impressed by his diligence and accuracy in solving problems. I have no doubts Furkan will have new results from BEC2 soon and will bring our machine to the new stage of experiments with fermions.

The most closely connected lab to ours in all aspects is BEC3. Not only do they work with the same atoms but also we are located right next door from each other. We borrowed your equipment without asking, and you borrowed ours – and nevertheless we are still friends. Hyungmok, I have always been impressed by how hard-working you are. Julie, it's been such a pleasure to have you as a groupmate. We have had quite a few conversations on different aspects of physics and those discussions made me a better physicist. I know how smart and strong you are. With your dedication to work, Lithium and Sodium will have no choice but to surrender and be at your service. I wish you good luck and look forward to hearing from you about the advances in cold molecules.

Pierre Barral has been a relatively recent addition to the group. He is definitely not hesitant to ask questions, and this is great. Thanks to his curiosity in physics, I have learned so much myself. I would have learned even more if Pierre spoke a little slower though... Keep having a lot of fun in physics, Pierre! Good luck to Li and Michael with Dysprosium and Pierre. Your lab is really cool, even after it has been on fire. Li, we had a great time at the last DAMOP conference. I was happy to get to know you better. Now I agree with you: academia is great (or at least nothing is better than it). So, "Vivat academia!"

I'd also like to thank BEC4 team: Woo Chang, Julius and Jinggang. You, guys, put our group on the new level of understanding optics. I still remember Jinggang's talk on microscope design at our group seminar: that was so eye-opening. Good luck to you, guys!

I would like to thank my physicist friends, and first of all Janos Perczel. We met at the first gathering of the incoming grad students at MIT, and I am still convinced that it was one of the most valuable connections I made at MIT. We went through classes and exams together; we accompanied each other in our struggles with research, though Janos struggled a little less since he is a theorist. Enough for the foundation of a life-long friendship!

Grisha Tarnopolsky has been my friend forever (since undergrad). Our life paths keep intertwining, and I can't be happier to have you as a friend and colleague. Max

Metlitsky is a brilliant person and an incredible friend. It is a joy to know that such Renaissance people still exist, and I am particularly happy to meet one of the very few (if not unique, who knows...)

I am also grateful to many people here at the CUA working in other groups. Parth, Matt, Ian, Sergio, Biswaroop and many others. I will have many warm recollections about our hallway and those who inhabit it. Parth Patel has been a great friend and a roommate during the last couple of years at MIT. I always knew I could rely on you, Parth. I am sure, wherever life disperses us we will always be in touch.

I would also like to thank Cathy Modica, Sydney Miller, Joanna Welch and Paula Sack for arranging the research and education to be smooth and thus letting me focus on physics. At the time I started the graduate program at MIT I was practically a 23 year-old child. Cathy took good care of me and kept an eye on my growth from the very first days and up to graduation. Thank you, Cathy!

At the end, I would like to thank my parents, for whom this degree probably means more than for anyone else in the world including myself. I always had your support. Thank you for everything you did for me.

Contents

1	Introduction	15
1.1	Quantum simulations	15
1.2	Ultracold atoms as a quantum simulator	17
1.3	Thesis Outline	18
1.4	^{23}Na Bose-Einstein Condensate Production	19
1.5	Overview of the Experimental Machine	20
1.6	Laser systems	21
2	Introduction to spin-orbit coupling	23
2.1	Synthetic spin-orbit coupling in cold atoms	24
2.2	1D spin-orbit coupling. Λ -scheme.	25
3	Spin-Orbit Coupling in a Superlattice	29
3.1	States in a superlattice	32
3.2	Spin-orbit-coupling Hamiltonian	39
3.3	Antiferromagnetic spin texture	40
3.4	Phase of the Superlattice	41
3.5	Green light generation	42
3.5.1	Generation of double-frequency wave	43
3.5.2	Plane wave passing through the crystal	44
3.5.3	Phase-matching	46
3.5.4	Gaussian beam analysis	48
3.5.5	Operation of SHG	49

3.5.6	Buyer's catalog	51
3.6	Experimental Results	52
3.7	Stripe phase detection	57
4	Introduction to periodically driven systems	61
4.1	Classical systems	62
4.1.1	Kapitsa pendulum	63
4.1.2	Paul trap	64
4.2	Quantum systems	66
4.3	Effective Hamiltonian	68
4.4	Extended Hilbert space	69
5	Floquet Engineering of Recoil-dressed Photons	71
5.1	Magnetic shaking experiment	71
5.2	Our scheme	72
5.2.1	Bloch sphere representaion	75
5.2.2	Floquet treatment	77
5.2.3	Evolution of the system	80
5.2.4	Canonical vs mechanical momenta	82
5.3	Experimental realization	83
5.3.1	High current	87
5.3.2	Stability of magnetic field and gradient	89
5.3.3	Symmetry of the modulated magnetic field gradient	92
5.3.4	Minimize modulation of magnetic bias field	94
5.3.5	Timing of the RF pulses with respect to the magnetic modulation	95
5.3.6	Induced shaking	95
5.4	Heating due to collisions between the spin states	100
6	Conclusions and Outlook	103

List of Figures

1-1	A schematic plot of the BEC2 two-species apparatus	21
2-1	1D spin-orbit coupling in Λ -scheme	26
3-1	Pseudo-spin states in an asymmetric double-well potential.	31
3-2	Superlattice band structure.	34
3-3	Superlattice and Raman beams.	35
3-4	Phase of the superlattice.	42
3-5	Phase-vectors diagram for the second harmonic generation.	47
3-6	Efficiency of the second harmonic generation as a function of a beam's geometry.	49
3-7	Green light power measurement.	50
3-8	TOF images for $q = 0$ and $q = \pi/d$ states in the superlattice.	53
3-9	TOF image for equal populations of atoms prepared in the ground and first excited bands.	53
3-10	TOF images of atoms loaded in the ground and first excited bands with and without Raman potential.	54
3-11	Mapped out spin-orbit coupling resonances	55
3-12	Calibration of the offset Δ between the wells.	56
3-13	A schematic plot of a stationary density modulation.	57
3-14	Angle resolved Bragg signal.	58
5-1	Illustration of the scheme for creating a tunable atomic recoil momentum.	73
5-2	Phase accumulation between the spins.	74

5-3	Bloch sphere representation of magnetic shaking and RF pulses. . . .	76
5-4	Energy-momentum dispersion relations for spin-orbit coupled spin 1/2 states	83
5-5	Ramsey fringe overlapped with the thermal cloud distribution. . . .	84
5-6	Experimental data for spin-flipped atoms.	86
5-7	Doppler shift mapped for different velocity groups of atoms.	88
5-8	Scheme of the coils circuit.	89
5-9	Hall probe measurement of the current.	90
5-10	Schematic plot of the atomic cloud in the field of a quadrupole. . . .	92
5-11	An H-bridge with built-in asymmetry.	93
5-12	A position of the cloud when it is more sensitive to inhomogeneous Zeeman shift.	94
5-13	Slicing of the momentum distribution at an angle.	96
5-14	An effect of eddy currents.	97
5-15	Steering of polarized spin due to induced field.	98

Chapter 1

Introduction

1.1 Quantum simulations

The goal of science and physics, in particular, is to understand nature, its fundamental laws, and take it under control. Physicists during the last two centuries achieved tremendous technological progress while looking at complex systems and phenomena and decomposing them into simple building blocks. It is striking how few exactly solvable problems there are in physics. The job of a physicist is to take very complicated problems, decompose and simplify them, and eventually reduce them to basic concepts and models. If we make the complicated problem look trivial, it means we did our job well and we really understand what is happening. Even though the number of exactly solvable quantum problems is so small, and the number of methods we can apply to them is very limited, the beauty of physics is that it can always surprise us. My journey to atomic physics was like a stroll in a forest: a forest which basically consists of three trees: a two-level system, a hydrogen-like atom and a harmonic oscillator. And still one can easily go astray in a forest of three trees. It is really beautiful how simple complexity can be, and how complex is simplicity.

The study of the universe starts from an attempt to understand of a two-body problem – how Earth travels around the Sun. The study of matter that surrounds us led to the discovery of atoms, nuclei and elementary particles. Understanding the properties of light required us to look at it at a single-photon level. The interest in

understanding the laws of nature made us look at it on a single-particle level, and when we got there we started to move in the opposite direction. We now want to construct matter atom-by-atom, or photon-by-photon. From single-particle physics, we move to two-body systems, three-body systems, and eventually we want to build controllable many-body systems.

Understanding physics on the single-particle level mainly confirms the existing theories. Building new states of matter paves the way to the area of science, where theoretical and computational methods are limited.

The difficulty of quantum problems is that their complexity grows exponentially with their size. A proposed solution to such problems was envisioned by Richard Feynman [1]. We can simulate quantum phenomena with quantum objects: atoms, ions, artificial atoms and other quantum systems. One has to think up how to reformulate the problem in terms of the chosen quantum system and then ask nature to provide us with the answer. In other words we want to ask nature to do the hard part: to simulate, to perform the “calculation”, whereas on our side we still need to initialize the problem and do the measurements. Both things can be difficult enough by themselves.

The idea of a quantum simulator can be generally formulated as 1) mapping the initial state of the system $|\psi(0)\rangle$ to the initial state of the simulator $|\phi(0)\rangle$; 2) initializing the state $|\phi(0)\rangle$; 3) engineering the Hamiltonian \hat{H} and evolving the state of the simulator with the unitary operator $U = e^{-i\hat{H}t/\hbar}$; 4) measuring the state $|\phi(t)\rangle = U|\phi(0)\rangle$; 5) mapping the obtained final state of the simulator $|\phi(t)\rangle$ on the state of the system. Thus, the major questions we pose before setting up the experiment are how to map the Hamiltonian and the state of the system onto the Hamiltonian and state of the simulator.

In the present work I would like to show two examples how this mapping can be done in the case of the spin-orbit coupling Hamiltonian, a fundamental interaction that combines both internal and motional degrees of freedom of a particle. Two different approaches to simulating spin-orbit coupling were developed in our lab, both having their own advantages and shortcomings. The scheme I want to focus on in

this thesis is based on utilizing a method of engineering Hamiltonians in periodically driven quantum systems, known as Floquet engineering. Our experiment provides a lucid example of how powerful Floquet engineering is and what it is capable of.

1.2 Ultracold atoms as a quantum simulator

The field of quantum simulations has been growing rapidly over the past decade. The demand in analysis of complicated many-body problems in condensed matter physics and chemistry stimulates advances in the development of coherent control of various platforms for quantum simulations. Different systems, such as ultracold atoms, trapped ions, quantum dots, superconducting circuits, and nuclear spins provide tools for the simulation of a broad range of problems. Each of these quantum simulators has its own strengths and can tackle special problems, which are particularly suitable for them.

Ultracold atoms have already proved to be a great platform for quantum simulations. Neutral atoms in optical lattices mimic the behavior of electrons in crystals. However, unlike real crystal structures, optical lattices are easily tunable and different geometries can be explored (such as triangular [2] and honeycomb [3] lattices). By controlling the depth of the optical lattice potential it has become possible to observe the Mott insulator to superfluid quantum phase transition [4]. In general, optical lattices are natural systems to explore both Bose- and Fermi-Hubbard models [5].

In our experiments atoms are not only cold, but also very dilute. Interactions between the atoms are determined by a single parameter — the scattering length, which in turn can be controlled by the magnetic field through Feshbach resonances. By tuning the interaction between two fermionic spin states, one can make a smooth transition from BEC molecules to BCS pairs and investigate the formation of fermionic superfluid [6].

Recent addition to the advantageous qualities of ultracold atoms, such controllability and accuracy, was the development of single-site resolution microscopes [7, 8]. It is now possible to study the dynamics of atoms in an optical lattice and perform new

measurements, which are not accessible in other fields (for example, measurement of entanglement entropy [9]).

An important direction of research in the field of ultracold atoms is the simulation of artificial gauge fields. Neutral atoms emulate the motion of an electron in a magnetic field, when its wave function acquires a phase while moving in space. This approach allowed to simulate incredibly high magnetic fields (equivalent to 10000 T in real life) [10, 11]. Our recent work in the BEC2 lab belongs to the same theme of developing new methods for engineering exotic gauge fields. We have realized a spin-dependent gauge field by two very different methods. One of them led to the observation of the new state of matter - a supersolid, while the other method created a new physical concept — a recoil-dressed photon. Both projects explored fundamental aspects of quantum mechanics and resulted in the creation of new man-made systems, which are not forbidden by the laws of nature, but have not been realized in the real world.

1.3 Thesis Outline

This thesis will present the results of the experimental realization of a spin-orbit coupling Hamiltonian in an optical superlattice and with periodically driven atoms. The superlattice model allowed us to explore the spin-orbit coupled Bose-Einstein Condensate (BEC) in new regimes, and led to the subsequent detection of density modulation in the ground state, the so-called stripe phase, which serves as an example of supersolid state matter. The approach of engineering spin-orbit coupling as an effect of periodic drive realized an alternative laser-free scheme. It allowed us to demonstrate an exotic phenomenon of recoil-dressed radio-frequency (RF) photon. The thesis is organized as follows:

- **Chapter 1** overviews BEC2 lab experimental apparatus.
- **Chapter 2** explains what spin-orbit coupling interaction is. This chapter discusses spin-orbit coupling in the context of solid state physics and earlier real-

izations with ultracold atoms.

- **Chapter 3** discusses physics in an optical superlattice. It starts with the description of the states in the superlattice, followed by the physical implementation of the optical superlattice and experimental data on the realization of the spin-orbit coupling Hamiltonian and stripe phase detection.
- **Chapter 4** reviews the principles of the description of periodically driven classical and quantum systems.
- **Chapter 5** presents the idea of Floquet-engineered recoil-dressed radio-frequency photon, its connection to spin-orbit coupling and its experimental realization with oscillating magnetic force and the synchronized sequence of RF pulses.
- **Chapter 6** provides the conclusion and an outlook.

1.4 ^{23}Na Bose-Einstein Condensate Production

In 2013 when I walked into the BEC2 lab for the first time, I was absolutely shocked by the complexity of the apparatus built by the previous generation of graduate students. Hundreds of cables from the floor to the ceiling, forests of mirrors, lenses and other elements on the optical tables. It takes a lot of effort and expertise to maintain the apparatus and run experiments with cold atoms. However, it took even more effort to build this machine and conduct the first experiments: produce the first BEC, set-up lattices and carry out the test experiments. These difficult steps were done by the graduate students before I joined the group. My goal was to keep performance of the machine on the same level and possibly modify, improve if needed, and adjust it for the upcoming scientific agenda of our lab. Due to the increase of the laser power needs in our lab, our laser system experienced significant changes. We have also had two vacuum failures in the course of the last 6 years. Brining the machine back to work required us to go through the basic steps of laser cooling in order to produce BEC again. In this chapter I would like to overview the existing BEC machine. For

the more detailed description of the apparatus I recommend early theses from our lab [12, 13, 14].

1.5 Overview of the Experimental Machine

Our BEC2 apparatus is a general-purpose machine for experiments with ultracold ^{23}Na and ^6Li . Fig.1-1 shows a schematic plot of the whole apparatus. On the right is the two-species oven which is the source of ^{23}Na and ^7Li . The oven is connected to a small intermediate chamber through the differential pumping tube. The VAT gate valves before and after the intermediate chamber allow the isolation of different segments of the apparatus in order to protect the vacuum. The intermediate chamber is connected to the Zeeman slower another differential pumping tube. Atoms which travel through the Zeeman slower arrive to the main chamber, where they are trapped and cooled to quantum degeneracy. Each of the chambers are pumped by their own ion pump and the pressure is monitored by ion gauges or by the RGA (Residual Gas Analyzer) in the main chamber.

The magnetic coils are mounted in the top and bottom buckets of the main chamber. A detailed description of the coils and winding procedure can be found in [12]. Here I just want to mention that the coils are water cooled and can carry high current up to 500A. Being connected in a circuit with mechanical H-bridge, they can work in both Helmholtz and anti-Helmholtz configurations. When running current through all the segments of the coils, one can achieve magnetic bias fields up to 1 kGs and magnetic gradient up to 1 kGs/cm. The ability to handle high currents and produce high magnetic gradient was a critically important point for the experiment we did on magnetically generated spin-orbit coupling described in Chapter 6. The strong gradient is also important to do efficient evaporative cooling, since we want to compress atoms to high densities by loading them into a tight magnetic trap. For the future experiment with ^6Li , high bias magnetic field is needed to reach s-wave Feshbach resonance around 830 Gs, which is the way to control the interactions between the atoms.

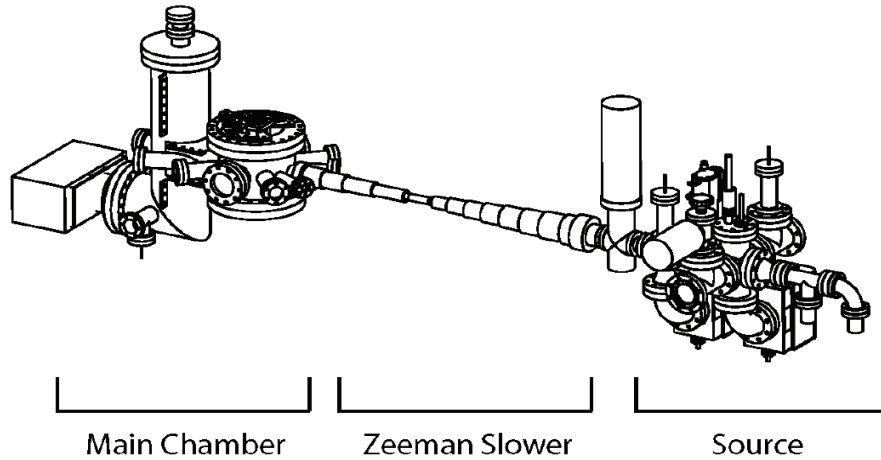


Figure 1-1: A schematic plot of the two-species apparatus. The cups on the right contain sodium and lithium. They are heated to produce atomic flux. The atoms undergo the first cooling stage while traveling through the Zeeman slower. Once they arrive to the main chamber, atoms are trapped and cooled further. The custom-made stainless steel chamber provides optical access through many viewports. High-current coils are mounted in the top/bottom buckets to provide strong magnetic fields. The figure is adapted from [12]

1.6 Laser systems

Resonant light for sodium ^{23}Na is provided by a laser from MPB Photonics. 1178 nm light from Topitca DL Pro diode laser is seeded to a Raman amplifier, which gives around 6W of power. Then the light is frequency-doubled to produce 1.4W of 589 nm yellow light. Over the years, Toptica diode degraded and currently our lab is using a temporary replacement laser diode and our home-built delivery system which shapes the beam and provides the minimal required power (18-20mW) to the next stage - Raman Amplifier. Back-up diode from the company Innolume were ordered to be shared between BEC2 and BEC3 labs for the future replacement in order to solve this problem permanently.

Green 532 nm light is needed for several purposes in the lab. First, it is required to plug the low field region in the magnetic trap [15]. Second, it was needed for the experiment with optical superlattice. While the second application required single-

mode light phase-locked with the 1064 light source, the plug beam application is rather simple - a multimode laser can be used. However, due to the failure of our old Millennia from Spectra-Physics lasers, we had to use the same light source (described in details in the Chapter 4) as we used for the superlattice as a plug laser. Eventually, a new 10W Sprout was purchased and installed specifically to serve only as a plug laser.

High power 1064 infra-red (IR) light is needed to trap atoms in optical dipole traps and to generate optical lattices. Usually, several Watts of IR is needed for each of the beams used for these application. Our home-made 532nm frequency-doubling setup required around 30W of IR. Our lab is equipped with two NUFERN amplifiers, each of them can safely produce 40W of power. In addition to them we have an old IPG fiber laser giving around 15W. As seed source for NUFERN amplifiers, we used a 2W Mephisto laser from Coherent.

Over the course of several years we have tried different parameters of sample preparation. The typical path to BEC is the following: we load 10^9 atoms from MOT to the magnetic quadrupole trap with a gradient of 50 Gs/cm. Then the trap is ramped up to 500 Gs/cm for further evaporation either by driving microwave ($|F = 1, m_F = -1\rangle \rightarrow |F = 2, m_F = -2\rangle$) or radio-frequency ($|F = 1, m_F = -1\rangle \rightarrow |F = 1, m_F = 0\rangle$) transitions. After evaporation, about $1 - 10 \cdot 10^6$ condensed atoms can be loaded into the optical dipole trap.

Chapter 2

Introduction to spin-orbit coupling

One of the major motivations for the research in our lab has been the study of spin-orbit coupling. Why is it important to simulate spin-orbit coupling for neutral atoms? Implementation of the interaction which includes both internal degree of freedom (spin) and motional (orbital) degrees of freedom is interesting by itself, and the $\hat{p} \cdot \hat{s}$ term is the simplest combination of the two operators. It naturally appears from the Hamiltonian of a particle in spin-dependent gauge field $(\hat{p} - A\hat{s})^2$. The goal of quantum simulations is to implement various hamiltonians and this is one of the most generic ones.

In addition to being important as a fundamental concept spin-orbit coupling (SOC) also plays an important in many phenomena. It first appears as an interaction between electrons spin and the field of nucleus in an atom, leading to a fine structure of the energy levels. In the field of ultracold atoms we find motivation for our experiment in phenomena inspired by solid state physics. SOC also plays a fundamental role there.

A paradigmatic example is the velocity-dependent energy splitting in heterostructures [16]. An electric field intrinsically appears due to the charge redistribution at the interface of a bilayer system. In the frame moving with electrons at velocity \vec{v} the electric field is transformed into magnetic field, which depends on \vec{v} through the Lorentz transform.

$$B_{SO} = \frac{E_0 \hbar}{mc^2} (k_x e_y - k_y e_x)$$

This magnetic field in the frame of electrons leads to a momentum dependent Zeeman effect. The interaction of the form $k_x e_y - k_y e_x$ is known as Rashba SOC. One can say that the asymmetry of the structure in the growth direction leads to Rashba SOC. Another type of the spin-orbit interaction, which has a form of $k_x e_x - k_y e_y$, is referred to as Dresselhaus interaction, and it originates from lack of inversion asymmetry in the bulk of semiconductors.

Solid-state devices which rely on electron charge are ubiquitous parts of our everyday life. Another boost for the modern electronics, memory storage and computations, could be the use of the spin degree of freedom of electrons. Devices based on spin transfer are studied in the field of spintronics [17]. One of the advantages of using spin transistors is that in order to change the spin-state one does not need to provide electrical current as for the commonly used field transistors. The smaller size, reduced consumption of power and better sensitivity would enable a significant improvement of current electronics technology. The spin degree of freedom can also be used as non-volatile storage of memory. Spin-orbit interaction is essential for spintronics devices. It allows electrical control of the spin by perturbing the motional degree of freedom.

SOC also plays an important role in physics of topological insulators [18]. The spin degree of freedom enriches the band structure of electrons in solids. Due to the coupling between the spin and momentum a spin texture appears in momentum space. Winding of the spin in momentum space when the quasimomentum is swept over the Brillouin zone can give nonzero winding numbers and topological bands.

2.1 Synthetic spin-orbit coupling in cold atoms

For neutral atoms coupling between motional degree of freedom and atom's spin does not happen naturally like for charged particles. However, the effective spin-orbit coupling can be mimicked with the help of external fields. Simulation of 2D spin-orbit coupling is particularly interesting [19], since it is equivalent to generation of non-Abelian gauge fields (proposals [20, 21]) and will give rise to study topologically nontrivial phenomena. For instance, realization of Rashba-type spin-orbit coupling

is very exciting because, because it would emulate a solid states system in a controllable way. But cold atoms experiments aim not only to serve solid state physics by untangling its problems and reproducing analogous systems, but can also create the states of matter which do not naturally occur in life. In this sense, simulating a one-dimensional spin-orbit coupling, which is equivalent to Abelian gauge, is interesting by itself and not only as a stepping stone towards 2D spin-orbit coupling. In some sense engineering the systems which do not have an existing material counterpart may be even more exciting than trying to mimic nature.

1D spin-orbit coupling was proposed to be seen in Λ -type schemes [22]. It was shown that the ground states of the Λ -scheme coupled via two-photon transition gives rise to the interaction with equal combination of Rashba and Dresselhaus terms, which in the convenient basis can be written as $k_z \hat{\sigma}_z$.

Gauge potentials can be simulated by affecting atom's dynamics with external forces (for instance, by rotating the condensate [23]) or fields through atom-light interaction [24]. The idea of generating Abelian and non-Abelian gauge fields goes back to the work of Wilczek and Zee [25].

2.2 1D spin-orbit coupling. Λ -scheme.

Apparently, the simplest form of spin-orbit coupling can be realized and very simple Λ -type scheme. It was shown that 1D spin-orbit coupling $k_z \hat{\sigma}_z$, which is a sum of Rashba and Dresselhaus terms, arises as a synthetic gauge field in three-level system dressed with two Raman laser beams [26]. This gauge field is spin-dependent, but Abelian, unlike 2D spin-orbit coupling.

The Λ -type configuration can be realized with the hyperfine states of alkali atoms. In the work of Ian Spielman's group ^{87}Rb atoms were used [27]. The Hamiltonian corresponding to the dressed level structure on the Fig.2-1 is

$$H = \hbar\Delta - (\hbar\Omega_1 \sin |g_1\rangle \langle e| + \hbar\Omega_2 |g_1\rangle \langle e| + h.c.) \quad (2.1)$$

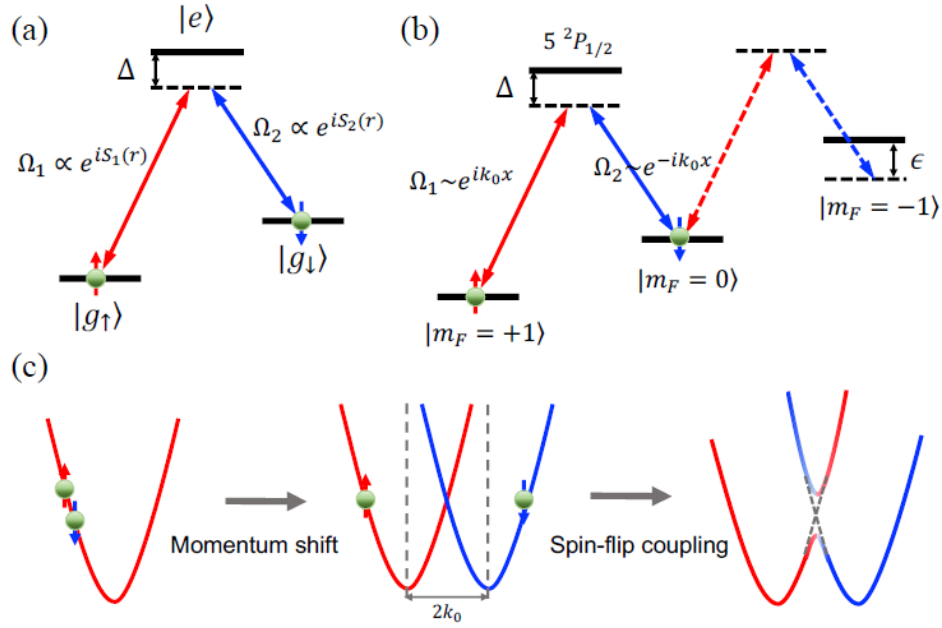


Figure 2-1: 1D spin-orbit coupling in Λ -scheme. (a) A three-level system dressed with two Raman laser beams. (b) Level structure for ^{87}Rb used in the of the Spielman group. (c) Raman beams provide momentum transfer which accompanies spinflip which shifts the parabolic dispersions and opens the gap at the level crossing. The image is adopted from [22]

, where the strengths of the coupling between the ground states and the excited state manifold $\Omega_\uparrow = \Omega \sin \theta e^{i\phi_1}$ and $\Omega_\downarrow = \Omega \cos \theta e^{i\phi_2}$ are determined by the two-photon Rabi frequencies of the Raman beams Ω , their alignment captured by angle θ and the phases of the laser beams.

In the case of large detuning $\Delta \gg |\Omega|$, the single-photon transition from the ground states to the excited state $|e\rangle$ is suppressed, and the excited state then can be adiabatically eliminated. So, the Λ scheme is reduced to effective two-level system, coupled by a two-photon process. After adiabatic elimination the eigen states of the 2-by-2 Hamiltonian are:

$$|\chi_1(\mathbf{r})\rangle = \cos \theta e^{iS_2(\mathbf{r})} |g_\uparrow\rangle - \sin \theta e^{iS_1(\mathbf{r})} |g_\downarrow\rangle \quad (2.2)$$

$$|\chi_2(\mathbf{r})\rangle = \sin\theta e^{iS_2(\mathbf{r})} |g_\uparrow\rangle + \sin\theta e^{iS_1(\mathbf{r})} |g_\downarrow\rangle \quad (2.3)$$

In the simplest case when the Raman beams are propagating along \hat{z} , i.e. the Rabi frequencies are $\Omega_1 = \Omega e^{ik_0 z}$ and $\Omega_2 = \Omega e^{-ik_0 z}$, where $k = 2\pi/\lambda$ is the wave-number of the Raman beams. After adiabatic elimination of $|e\rangle$ original Hamiltonian is reduced to the effective one

$$H_{eff} = \begin{pmatrix} \frac{\hat{p}_z^2}{2m} - \frac{\hbar\delta_{RF}}{2} & \frac{\hbar\Omega_0^2}{2\Delta} e^{i2k_0 \cdot z} \\ \frac{\hbar\Omega_0^2}{2\Delta} e^{-i2k_0 \cdot z} & \frac{\hat{p}_z^2}{2m} + \frac{\hbar\delta_{RF}}{2} \end{pmatrix}, \quad (2.4)$$

where δ is a two-photon detuning. The strength of the interaction is characterized now by 2-photon Rabi frequency $\frac{\hbar\Omega_0^2}{\Delta}$. Thus, we obtained a Hamiltonian of a two-level system driven by an optical field with the wave number $2k_0$.

After applying a position-dependent transformation $\hat{R}_z = e^{-ik_0 z \hat{\sigma}_z}$ the effective Hamiltonian H_{eff} is transformed into 1D spin-orbit coupling Hamiltonian $H_{SOC} = \hat{R}_z H_{eff} \hat{R}_z^\dagger$, where

$$H_{SOC} = \frac{(p_z + k_0 \hat{\sigma}_z)^2}{2m} + \frac{\delta}{2} \hat{\sigma}_z + \frac{\Omega_R}{2} \hat{\sigma}_x \quad (2.5)$$

The fact that the Hamiltonians 2.4 and 2.5 are equivalent up to the unitary transformation gives us a hint how to interpret spin-orbit coupling. It is intrinsically related to the recoil momentum. Transition from one state to another is carried out by absorbing a photon from one of the Raman beams and reemitting a photon into another Raman beam in a stimulated way. The momentum of atom changes by $2k_0$. Depending on the direction of the process the atom gains or loses $2k_0$. As a result, the parabolas of the dispersion relation for spin-up and spin-down are shifted by $2k_0$ (Fig.2-1). The two-photon Rabi frequency characterizing the strength of transition between $|g_\downarrow\rangle$ and $|g_\uparrow\rangle$ enters the spin-orbit coupling Hamiltonian in $\hat{\sigma}_x$ term and opens the gap between the parabolas.

One has to notice that adding another pair of Raman beams in a different direction does not create the "missing" term to make 2D spin-orbit coupling out of 1D. It merely

changes the direction of recoil momentum. In order to fundamentally change the type of the gauge field and make it non-Abelian one needs to consider more complicated systems such as, for instance, tripod level configurations [28].

Chapter 3

Spin-Orbit Coupling in a Superlattice

As was discussed in the previous chapter, spin-orbit coupling is a profound interaction mechanism relevant for various phenomena such as topological insulators, Majorana fermions, and spintronics. Realization of SOC with ultracold atoms enables exploration of new phases of matter and allows control of the motional degree of freedom by the internal degree of freedom of an atom, or the other way around. For example, in quantum dots, by talking to the motional degree of freedom, one can control its spin [29].

Spin-orbit coupling makes the atom's motion spin-dependent. Rather trivial regimes without spin-flips can be achieved with far detuned light [30, 31]. In principle, this is, for example, enough to emulate Spin Quantum Hall effect.

However, in order to simulate Rashba or Dresselhaus spin-orbit coupling, we need to bring in σ_x and σ_y terms, and therefore, there must be an implementation of a spin-flip in some form. In the pioneering work of Ian Spielman's group, spin-orbit coupling was engineered using hyperfine states of ^{87}Rb [27]. Coupling of the two states was achieved by a 2-photon Raman process and the atomic spin-orbit interaction in the excited state. Without fine-structure splitting, caused by the $\mathbf{L} \cdot \mathbf{S}$ interaction, changing the hyperfine state in the ground $l = 0$ manifold would not be possible. Therefore, the experiments using Raman transitions between different hyperfine states faces two contradicting requirements: for the strong coupling through the $\mathbf{L} \cdot \mathbf{S}$ interaction, one needs to minimize the detuning from the excited states, but

to reducing the heating, the detuning must be as large as possible. The strength of the coupling and heating through the spontaneous emission from the excited state scales the same way with the two-photon detuning, i.e. $1/\Delta^2$ [32].

Our goal is to create a transition between spin-states which is accompanied by momentum transfer. Two-photon Raman transitions, when the Raman beams have different orientations, seem to be a perfect choice for the source of the momentum transfer. A photon \mathbf{k}_1 is absorbed from one beam and reemitted into another beam with a wave-vector \mathbf{k}_2 . Then the momentum transfer is $\mathbf{k}_2 - \mathbf{k}_1$. The order can be different: a photon is absorbed with wave-vector \mathbf{k}_2 and reemitted with \mathbf{k}_1 in a stimulated way. The momentum transfer then has the opposite sign. Since the two-photon process and different hyperfine states as a choice of pseudo-spin do not really work well together, there are two passes towards improving already existing spin-orbit coupling schemes.

First, one could keep two-photon Raman process but choose different pseudo-spin states which would not require resonant light to be coupled — for instance, left and right states in a double-well, or different bands in an optical lattice with atoms staying in the same hyperfine state.

Second, one could continue using hyperfine states as pseudo-spins, but not rely on Raman process for momentum transfer. The hyperfine states can be easily coupled with an RF signal, but then one needs to come up with another mechanism to impart recoil, since an RF photon does not have one (for instance, Floquet engineering). The problem of coupling different hyperfine states along with providing momentum transfer can also be eliminated by using species that have nonzero angular momentum in the ground state, like Dy [33], and do not require near-resonant light.

Our lab has explored both strategies for alkali atoms: a different choice of the pseudo-spin, and a different source of recoil. In the present chapter, I would like to overview our experiments based on the first strategy [34, 35]. In order to avoid the problem of spontaneous emission, we decided to consider the two lowest states in the asymmetric double-well potential as pseudo-spin states Fig.5-1. In the tight-binding regime, when the barrier between the wells can be treated perturbatively, the lowest

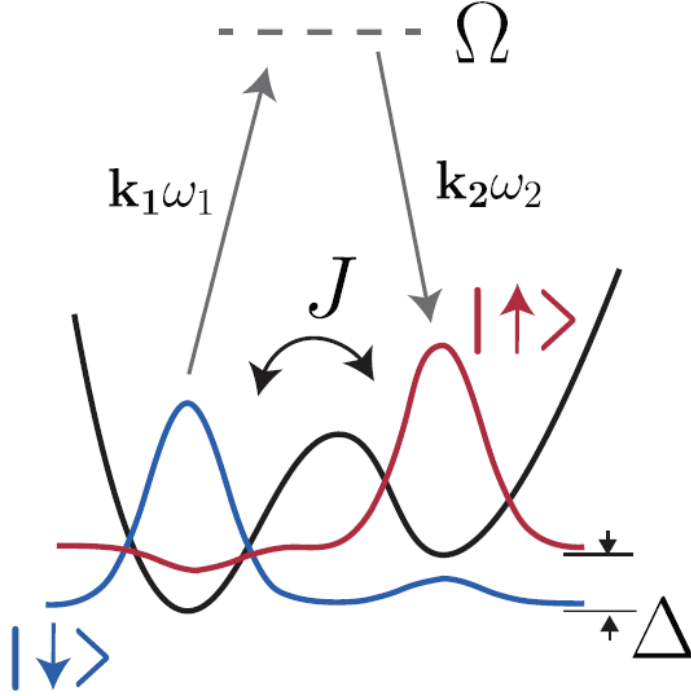


Figure 3-1: A schematic plot of the pseudo-spin states in an asymmetric double-well potential. The overlap between the pseudo-spin-down (the state localized in the left well) and the pseudo-spin-up (the state localized in the right well) is controlled by the tunneling through the barrier J and the offset between the wells Δ .

eigenstates can be written as

$$|\downarrow\rangle = |l\rangle + (J/\Delta) |r\rangle, \quad |\uparrow\rangle = |r\rangle - (J/\Delta) |l\rangle, \quad (3.1)$$

where $|l\rangle$ and $|r\rangle$ are the state, localized in the left and right wells respectively. Since both states belong to the same hyperfine states, there would be no need for resonant light to couple them with the Raman process. Another important advantage of such choice of pseudo-spins is that we can control interactions between them. The collision rate between atoms in left and right wells of double-well potential is determined by the overlap of their wave-functions and can be adjusted by the height of the barrier. In such systems, intra-spin collisions naturally prevail over inter-spin collisions. The collisions between the atoms in left and right wells are suppressed by a factor $\sim (J/\Delta)^2$

with respect to on-site collisions of atoms. Such a relation between the collision rates makes the system miscible. This property is important, since we want to realize and probe many-body Hamiltonians and explore new, unconventional phases of matter.

One of the most intriguing predictions for the spin-orbit coupled Bose gas is the existence of ground state with a density modulation, called stripe phase [36, 37, 38]. In the regime where the intra-spin interactions dominate, $g_{\uparrow\downarrow}^2 < g_{\uparrow}g_{\downarrow}$, i.e. when the system remains miscible, a spontaneous density modulation forms. This phase of matter meets the definition of a supersolid [39], a long-awaited phenomenon which was sought in superfluid helium [40, 41] and eventually was realized in our lab with Bose-Einstein condensates [35] and in the Esslinger group [42].

Our scheme addresses the major challenges of spin-orbit coupling: it does not require resonant light which solves the problem with the heating due to spontaneous emission and the interactions can be controlled so that the system favors miscibility.

In the actual experiment, we created a lattice of double-wells - an optical superlattice. So, the correct model for our system is a sequence of replicated double-wells along the \hat{z} axis, and free space in the transverse direction. This approach creates a number of technical advantages. First, it is more convenient to work with a stack of coherently coupled double wells because of the improved signal-to-noise ratio. Second, the interference between the unit cells of superlattice helps to distinguish pseudo-spin states - since we work with the same hyperfine state of sodium, a traditional method of distinguishing spins, such as Stern-Gerlach experiment, does not work.

3.1 States in a superlattice

The Hamiltonian for a one-dimensional superlattice, created by overlapping standing waves of infrared and green light with relative phase ϕ_{SL} , is

$$H_{lattice} = \frac{\hat{p}_z^2}{2m} + \frac{\hat{p}_{\perp}^2}{2m} + V_{Gr} \sin^2(k_{Gr}z) + V_{IR} \sin^2(k_{IR}z + \phi_{SL}) \quad (3.2)$$

Here the first term describes motion along the lattice direction, the second term describes the motion in orthogonal plane in free space, and the third and fourth terms

are the potentials created by the green and IR lattice respectively.

We can use a basis of $|l_n(r_n)\rangle$ states, localized in the left(right) double well of the unit cell with the number n , so that in the tight-binding approximation the Hamiltonian can be rewritten as

$$H_{lattice} = \frac{\hat{p}_\perp^2}{2m} + \frac{1}{2}\Delta_0 \sum_n (|r_n\rangle \langle r_n| - |l_n\rangle \langle l_n|) - J \sum_n (|l_n\rangle \langle r_n| + h.c.) - \sum_n \sum_{\substack{t=l,r \\ t'=l,r}} (J'_{tt'} |t_n\rangle \langle t'_{n+1}| + h.c.), \quad (3.3)$$

where $|l_n(r_n)\rangle$ is a wavefunction localized in the left(right) well of the n^{th} unit cell, Δ_0 is the energy separation between the right and the left wells. \hbar is taken to be 1.

Tunneling between neighboring unit cells is important for maintaining coherence in the superlattice: eventually what we observe experimentally is the interference patterns of matter waves coming from different nodes of the lattice, but not relevant for describing spin-orbit coupling with double-well states. Thus, all the tunneling terms beyond one unit cell with $J'_{tt'}$ in the Hamiltonian can be neglected for the purpose of describing the pseudo-spin flip and momentum transfer.

When instead of considering an isolated double well we look at the stack of coherently coupled double wells in a superlattice. We have to take lattice band structure into account (Fig.3-2). The lowest state of the double potential will turn into the lowest band of the superlattice. The minimum energy state of the lowest band occurs at zero quasimomentum $q = 0$. The first excited state state of the doublewell will now become the first excited band. But in contrast to the ground band, the first excited band has an inverted structure in qasimomentum space, i.e. its energy minimum is located at the edge of the Brillouin zone at $q = \pi/d$, where d is the period of the lattice.

It is going to be more convenient to use eigenstates of a double-well instead of localized states for further description. To first order in the small parameter $\frac{J}{\Delta_0} \ll 1$,

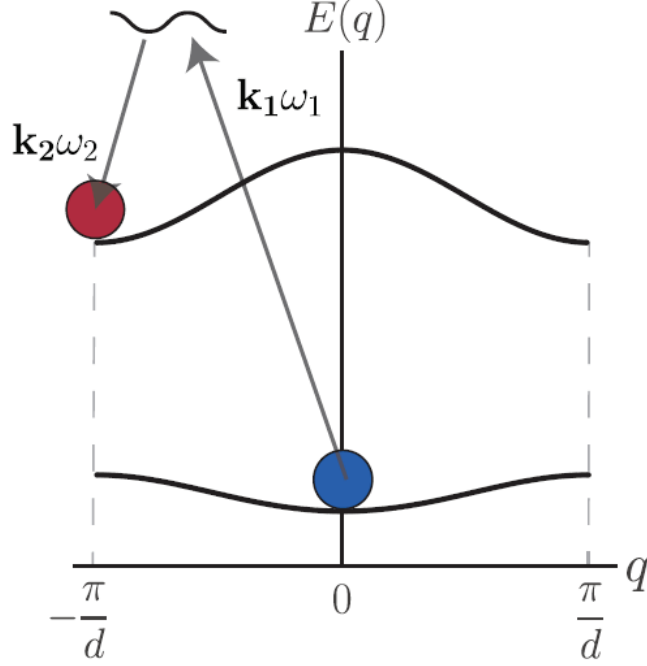


Figure 3-2: Two lowest bands of the superlattice. A Raman process couples the $q = 0$ state of the ground band with edge of the Brillouin zone of the first excited band.

they can be written as

$$|\downarrow_n\rangle = |l_n\rangle + \frac{J}{\Delta_0} |r_n\rangle, \quad |\uparrow_n\rangle = |r_n\rangle - \frac{J}{\Delta_0} |l_n\rangle. \quad (3.4)$$

If the system in our experiment is initially prepared in the lower wells of double-wells, which corresponds to the $q = 0$ of the lowest band of the superlattice,

$$|\psi_{q=0}^{(\downarrow)}\rangle = \sum_{n=1}^N \frac{1}{\sqrt{N}} |\downarrow_n\rangle, \quad (3.5)$$

where N is the number of unit cells in the lattice. When all the atoms are confined in the upper wells, the lowest state is the $q = \frac{\pi}{d}$ state of the first excited band due, to the inverted dispersion relation:

$$|\psi_{q=\pi/d}^{(\uparrow)}\rangle = \sum_{n=1}^N \frac{1}{\sqrt{N}} e^{i\frac{\pi}{d}(z_n + \frac{d}{2})} |\uparrow_n\rangle \quad (3.6)$$

With $z_n = nd$, the state becomes:

$$|\psi_{q=\pi/d}^{(\uparrow)}\rangle = \sum_{n=1}^N \frac{1}{\sqrt{N}} i(-1)^n |\uparrow_n\rangle \quad (3.7)$$

Now, we want to establish coupling between these to states $|\psi_{q=0}^{(\downarrow)}\rangle$ and $|\psi_{q=\pi/d}^{(\uparrow)}\rangle$. For that we turn on the Raman potential V_{Raman} and treat it as perturbation. The complete Hamiltonian of the system is

$$H = H_{lattice} + V_{Raman}, \quad (3.8)$$

where $V_{Raman} = \Omega \cos(k_z z + k_x x - \delta t)$ is a moving lattice potential. One of the Raman beams is aligned along the lattice direction \hat{z} , and is responsible for the quasimomentum transfer from $q = 0$ to the edge of the Brillouin zone $q = \pi/d$. The quasimomentum transfer from this IR beam k_{IR} matches half of the reciprocal vector of the periodic structure, which is $\pi/d = \pi/(\lambda_{IR}/2)$. The second Raman beam is aligned in the orthogonal direction to the lattice \hat{x} (Fig.3-3). After absorbing its photon, the x -component of the wave function of the atom becomes a plane wave with wave number $k = k_{IR}$. For the purpose of our experiment, the initial phase of the Raman potential is not relevant, and is taken to be zero.

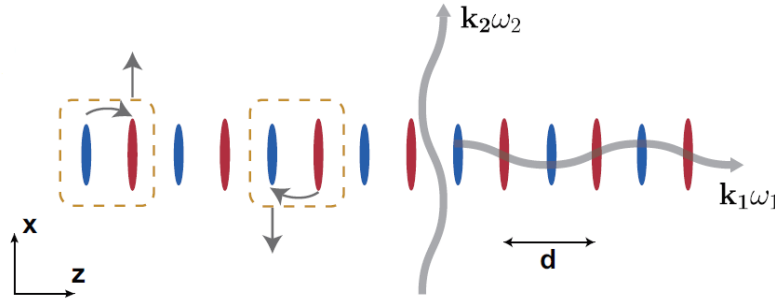


Figure 3-3: A schematic plot of the superlattice and Raman beams. The periodicity of the superlattice is $d = 523$ nm. One of the Raman beams (\mathbf{k}_1, ω_1) is along the superlattice, while another Raman beam (\mathbf{k}_2, ω_2) is in the transverse direction. Atoms that have experienced a 2-photon transition acquire a momentum in transverse direction equal to \mathbf{k}_2 and quasimomentum transfer along \hat{x} equal to k_1 .

We expand the Hamiltonian 3.8 in the new basis 3.4 with $\Delta = \Delta_0 + 2\frac{J^2}{\Delta_0} \approx \Delta_0$:

$$\begin{aligned}
H = & \frac{\hat{p}_\perp^2}{2m} + \frac{1}{2}\Delta \sum_n (|\uparrow_n\rangle \langle \uparrow_n| - |\downarrow_n\rangle \langle \downarrow_n|) + \\
& \sum_{p_\perp, p'_\perp} |p_\perp\rangle \left(\sum_n \sum_{\substack{i=\downarrow, \uparrow \\ i'=\downarrow, \uparrow}} |i_n\rangle \langle i_n| \langle p_\perp| \Omega \cos(k_z z + k_x x - \delta \cdot t) |p'_\perp\rangle |i'_n\rangle \langle i'_n| \right) \langle p'_\perp| \quad (3.9)
\end{aligned}$$

In our experiment $k_z \approx k_x \approx k_{IR} = \frac{\pi}{d}$, where d is a period of the superlattice. In order to consider the effect of the Raman potential with arbitrary phase using first order perturbation theory, one needs to calculate overlap integrals for $\cos(k_{IR} \cdot (z - z_n))$ and $\sin(k_{IR} \cdot (z - z_n))$ to first order in $\frac{J}{\Delta}$:

$$\langle \downarrow_n | \cos(k_{IR} \cdot (z - z_n)) | \uparrow_n \rangle \approx \langle l_n | - \frac{J}{\Delta} | l_n \rangle = -\frac{J}{\Delta}, \quad (3.10)$$

$$\langle \downarrow_n | \cos(k_{IR} \cdot (z - z_n)) | \downarrow_n \rangle \approx 1, \langle \uparrow_n | \cos(k_{IR} \cdot (z - z_n)) | \uparrow_n \rangle \approx 0, \quad (3.11)$$

$$\langle \downarrow_n | \sin(k_{IR} \cdot (z - z_n)) | \uparrow_n \rangle \approx \langle r_n | \frac{J}{\Delta} | r_n \rangle = \frac{J}{\Delta}, \quad (3.12)$$

$$\langle \downarrow_n | \sin(k_{IR} \cdot (z - z_n)) | \downarrow_n \rangle \approx 0, \langle \uparrow_n | \sin(k_{IR} \cdot (z - z_n)) | \uparrow_n \rangle \approx 1, \quad (3.13)$$

where $z_n = nd$ is a coordinate of the left well in the n^{th} unit cell.

Thus, the Raman potential can be expanded in the basis of double-well eigenstates:

$$\begin{aligned}
& \sum_{\substack{i=a,b \\ i'=a,b}} |i_n\rangle \langle i_n| \Omega \cos(k_z(z - z_n) + k_x x - \delta \cdot t) |i'_n\rangle \langle i'_n| = \\
& = \Omega \cos \phi_n \left\{ -\frac{J}{\Delta} (|\downarrow_n\rangle \langle \uparrow_n| + |\uparrow_n\rangle \langle \downarrow_n|) + |\downarrow_n\rangle \langle \downarrow_n| \right\} + \\
& \quad - \Omega \sin \phi_n \left\{ |\uparrow_n\rangle \langle \uparrow_n| + \frac{J}{\Delta} (|\downarrow_n\rangle \langle \uparrow_n| + |\uparrow_n\rangle \langle \downarrow_n|) \right\}, \quad (3.14)
\end{aligned}$$

where $\phi_n = \pi n + k_x x - \delta t$. Later, we will calculate how x as an operator acts on the momentum states $|p_\perp\rangle$.

$$\hat{V}_{Raman} = \sum_n \Omega(-1)^n \cos(k_x x - \delta t) |\downarrow_n\rangle \langle \downarrow_n| - \Omega(-1)^n \sin(k_x x - \delta t) |\uparrow_n\rangle \langle \uparrow_n| + \quad (3.15)$$

$$-\sqrt{2}\Omega \frac{J}{\Delta} (-1)^n \cos(k_x x - \delta t - \frac{\pi}{4}) \{|\downarrow_n\rangle \langle \uparrow_n| + |\uparrow_n\rangle \langle \downarrow_n|\} \quad (3.16)$$

The factor $(-1)^n$ represents the phase of the Raman beams. This factor is present because the wavelength of the Raman beams $\lambda = 1064$ nm, is two times the length of the unit cell. In our experiment, the atomic sample is prepared in the zero-momentum state. When the Raman perturbation is applied, the atoms experience a kick in the x -direction. In the y -direction atoms remain unperturbed, i.e. $\hat{p}_y = 0$. Since the confinement along x is weak, we can use the basis $|\uparrow(\downarrow), k\rangle = |\uparrow(\downarrow)\rangle \otimes e^{ikx}$. Here the states $|\uparrow(\downarrow), k\rangle$ correspond not to the individual double wells, but to the lowest and first excited band of the lattice. They include all the factors needed for a Bloch wave to reflect the symmetry of the Hamiltonian. The Raman interaction gives rise to intra-band coupling terms (3.14), and to the spin-orbit coupling term (3.16).

In addition to coupling the ground band to the first excited band with Raman potential, we also inevitably create some intra-band excitations, which we refer to as "onsite coupling". Atom only keep the same Bloch function, but acquire quasimomentum along the lattice direction and momentum in the orthogonal plane in order to fulfil the conservation laws.

The intra-band coupling terms are

$$\begin{aligned} \left\langle \psi_{q=\pi/d}^{(\downarrow)} \left| \hat{V}_{Raman} \right| \psi_{q=0}^{(\downarrow)} \right\rangle &= \sum_{n,n'} \frac{1}{N} (-1)^n \langle \downarrow_{n'} | \Omega \cos(k_z z + k_x x - \delta t) | \downarrow_n \rangle \\ &= \Omega \sum_n \frac{1}{N} \cos(\phi_n) (-1)^n = \Omega \cos(k_x x - \delta t) \quad (3.17) \end{aligned}$$

$$\begin{aligned}
\langle \psi_{q=0}^{(\uparrow)} | \hat{V}_{Raman} | \psi_{q=\pi/d}^{(\uparrow)} \rangle &= \sum_{n,n'} \frac{1}{N} \langle \uparrow_{n'} | \Omega \cos(k_z z + k_x x - \delta t) i (-1)^n | \uparrow_n \rangle \\
&= \Omega \sum_n \frac{1}{N} i (-1)^n (-\sin(\phi_n)) = -i\Omega \sin(k_x x - \delta t) \quad (3.18)
\end{aligned}$$

While the spin-orbit coupling matrix elements are

$$\begin{aligned}
\langle \psi_{q=\pi/d}^{(\uparrow)} | \hat{V}_{Raman} | \psi_{q=0}^{(\downarrow)} \rangle &= \sum_{n,n'} \frac{1}{N} (-i) (-1)^{n'} \langle \uparrow_{n'} | \Omega \cos(k_z z + k_x x - \delta t) | \downarrow_n \rangle \\
&= -i\Omega \sum_n \frac{1}{N} (-1)^n \langle \uparrow_n | \cos(k_z(z - z_n)) \cos(\phi_n) - \sin(k_z(z - z_n)) \sin(\phi_n) | \downarrow_n \rangle, \quad (3.19)
\end{aligned}$$

$$\begin{aligned}
\langle \psi_{q=\pi/d}^{(\uparrow)} | \hat{V}_{Raman} | \psi_{q=0}^{(\downarrow)} \rangle &= i \frac{J}{\Delta} \Omega \sum_n (-1)^n \frac{1}{N} (\cos(\phi_n) + \sin(\phi_n)) \\
&= i \frac{J}{\Delta} \Omega (\cos(k_x x - \delta t) + \sin(k_x x - \delta t)) \quad (3.20)
\end{aligned}$$

The intra-band coupling matrix elements (3.17) and (3.18) provide recoil kick in x -direction with recoil energy $E_r = \frac{k_x^2}{2m}$ and along the superlattice, changing the quasimomentum by half a reciprocal vector. If the system is initially at $|\psi_{q=0}^{(\downarrow)}, 0\rangle$, the new adiabatically connected eigenstate in first order perturbation theory is:

$$\begin{aligned}
|\Psi_1\rangle &= |\psi_{q=0}^{(\downarrow)}, 0\rangle - \frac{1}{2} \frac{\Omega}{E_r - \delta} e^{-i\delta t} |\psi_{q=\pi/d}^{(\downarrow)}, k_x\rangle - \frac{1}{2} \frac{\Omega}{E_r + \delta} e^{i\delta t} |\psi_{q=\pi/d}^{(\downarrow)}, -k_x\rangle \\
&\quad - i \frac{e^{-i\frac{\pi}{4}}}{\sqrt{2}} \frac{J\Omega/\Delta}{E_r + \Delta - \delta} e^{-i\delta t} |\psi_{q=\pi/d}^{(\uparrow)}, k_x\rangle - i \frac{e^{i\frac{\pi}{4}}}{\sqrt{2}} \frac{J\Omega/\Delta}{E_r + \Delta + \delta} e^{i\delta t} |\psi_{q=\pi/d}^{(\uparrow)}, -k_x\rangle \quad (3.21)
\end{aligned}$$

If the system is prepared in $|\psi_{q=\pi/d}^{(\uparrow)}, 0\rangle$, instead we find

$$\begin{aligned} |\Psi_2\rangle &= e^{-i\Delta t} |\psi_{q=\pi/d}^{(\uparrow)}, 0\rangle - \frac{1}{2} \frac{\Omega}{E_r - \delta} e^{-i(\delta+\Delta)t} |\psi_{q=0}^{(\uparrow)}, k_x\rangle + \frac{1}{2} \frac{\Omega}{E_r + \delta} e^{i(\delta-\Delta)t} |\psi_{q=0}^{(\uparrow)}, -k_x\rangle \\ &+ i \frac{e^{-i\frac{\pi}{4}}}{\sqrt{2}} \frac{\Omega J/\Delta}{E_r - \Delta - \delta} e^{-i(\delta+\Delta)t} |\psi_{q=0}^{(\downarrow)}, k_x\rangle + i \frac{e^{i\frac{\pi}{4}}}{\sqrt{2}} \frac{\Omega J/\Delta}{E_r - \Delta + \delta} e^{i(\delta-\Delta)t} |\psi_{q=0}^{(\downarrow)}, -k_x\rangle \quad (3.22) \end{aligned}$$

Our goal in the experiment was to map the resonances by sweeping the detuning of the Raman beams. In the vicinity of the spin-orbit coupling resonances $\delta = \Delta + E_r$ ($|\psi_{q=0}^{(\downarrow)}, 0\rangle \rightarrow |\psi_{q=\pi/d}^{(\uparrow)}, k_x\rangle$) and $\delta = \Delta - E_r$ ($|\psi_{q=\pi/d}^{(\uparrow)}, 0\rangle \rightarrow |\psi_{q=0}^{(\downarrow)}, k_x\rangle$) the onsite (intra-band) coupling is suppressed and spin-orbit coupling terms dominate. For $\delta = \Delta$, which is slightly away from the actual resonance by recoil energy, the spin-orbit coupling terms form stationary density modulations: the term $|\psi_{q=0}^{(\downarrow)}, 0\rangle$ from equation 3.21 with the term $i \frac{e^{i\frac{\pi}{4}}}{\sqrt{2}} \frac{\Omega J/\Delta}{E_r - \Delta + \delta} e^{i(\delta-\Delta)t} |\psi_{q=0}^{(\downarrow)}, -k_x\rangle$ from 3.22, and the term $-i \frac{e^{-i\frac{\pi}{4}}}{\sqrt{2}} \frac{J\Omega/\Delta}{E_r + \Delta - \delta} e^{-i\delta t} |\psi_{q=\pi/d}^{(\uparrow)}, k_x\rangle$ from equation 3.21 with the term $e^{-i\Delta t} |\psi_{q=\pi/d}^{(\uparrow)}, 0\rangle$ from equation 3.22. The density modulations arising from the interference of these states manifest the stripe phase in the language of pseudo-spins.

3.2 Spin-orbit-coupling Hamiltonian

Omitting all the off-resonant and counter-rotating terms from (3.21) (or similar with (3.22)) we can rewrite the Hamiltonian describing the system as

$$H_{SOC} = \begin{pmatrix} \frac{\hat{p}_x^2}{2m} - \frac{\Delta}{2} & \frac{-ie^{i\pi/4} J}{\sqrt{2}} \frac{\Omega}{\Delta} e^{-i(k_x x - \delta t)} \\ \frac{ie^{-i\pi/4} J}{\sqrt{2}} \frac{\Omega}{\Delta} e^{i(k_x x - \delta t)} & \frac{\hat{p}_x^2}{2m} + \frac{\Delta}{2} \end{pmatrix} \quad (3.23)$$

After a position-dependent unitary transformation, $\hat{U} = e^{(-ik_x x + i\delta t - i\frac{\pi}{4})\sigma_z/2}$, the Hamiltonian turns into $H'_{SOC} = U^\dagger H_{SOC} U - iU^\dagger \frac{\partial U}{\partial t}$.

$$H'_{SOC} = \frac{(\hat{p}_x + \alpha\sigma_z)^2}{2m} + \beta\sigma_x + \delta_0\sigma_z, \quad (3.24)$$

where $\alpha = -\frac{1}{2}k_x$, $\beta = \frac{J\Omega}{\sqrt{2}\Delta}$ and $\delta_0 = \frac{1}{2}(\delta - \Delta)$. This Hamiltonian corresponds to equal contributions of Rashba and Dresselhaus interactions. The parameter α defines

the momentum transfer. It can be tuned by the angle between the Raman beams. The parameter β is the strength of spin-orbit coupling, which can be tuned by the two-photon Rabi frequency of the Raman beams.

3.3 Antiferromagnetic spin texture

A spin-1/2 aligned along the $\cos \phi \hat{x} + \sin \phi \hat{y}$ direction has the wavefunction $|\downarrow\rangle + e^{i\phi} |\uparrow\rangle$. In our experiment, atoms can be prepared in the left and right sites of the double-wells with equal population. The wave function is then proportional to

$$|\psi\rangle = \sum_n |\downarrow_n\rangle + (-1)^n e^{i\theta} e^{-i\Delta t} |\uparrow_n\rangle,$$

which corresponds to spin-states aligned in the x-y plane with opposite directions on neighboring sites, showing x-y antiferromagnetic ordering. The expectation values of spin evolve as $\langle \sigma_x \rangle = (-1)^n \cos(\theta - \Delta t)$, $\langle \sigma_y \rangle = (-1)^n \sin(\theta - \Delta t)$ and $\langle \sigma_z \rangle = 0$.

Tunneling between wells within a unit cell causes a density modulation. Local populations in the n^{th} cell acquire a density imbalance:

$$|\langle l_n | \psi \rangle|^2 \sim \left(1 - (-1)^n \frac{J}{\Delta} \cos(\theta - \Delta t)\right),$$

$$|\langle r_n | \psi \rangle|^2 \sim \left(1 + (-1)^n \frac{J}{\Delta} \cos(\theta - \Delta t)\right)$$

Translating by one superlattice period flips the sign of the imbalance. This shows that r_n and l_{n+1} wells, and r_{n-1} and l_n wells have the same change in density, but oscillate out of phase. Therefore, this density wave has twice the wavelength of the superlattice and is shifted spatially by half a unit cell.

One can say that the state with both bands in $q = 0$, $\sum_n |\uparrow_n\rangle + |\downarrow_n\rangle$ demonstrates a ferromagnetic spin-texture. After the excited bands relaxes to $q = \pi/d$, the resulted state $|\psi\rangle = \sum_n |\downarrow_n\rangle + (-1)^n e^{i\theta} e^{-i\Delta t} |\uparrow_n\rangle$ shows an antiferromagnetic texture. This state has a reduced symmetry with respect to the superlattice.

3.4 Phase of the Superlattice

In the experiment, we observed how the optical superlattice — and spin-orbit coupling on top of it — affected the momentum structure of a BEC. The set-up we created had two major ingredients: the optical superlattice and the Raman beams. The superlattice is produced by an overlap of two standing waves, the infrared and green ones. Combined 1064 nm and 532 nm light propagate together and reflect from a retro-mirror, forming standing waves with 532 nm and 266 nm respectively. The superlattice has to be deep enough, with a barrier sufficient to suppress tunneling within the unit cell. It has to have fast dynamic control: the asymmetry of the double-well potential has to be manipulated on a time scale faster than the atomic motion. Basically, we had to be capable to go from symmetric double well to asymmetric double well before atoms could see the difference.

The shape of the double well was determined by the relative phase ϕ_{SL} between 1064 nm and 532nm light. In our experiment ϕ_{SL} , was controlled by a dispersive glass plate and by a small shift of the frequency of the IR light. The motion of the glass plate was relatively slow, and was used to preset the initial phase of the superlattice. We made it possible to rotate the plate by a galvo on a time scale of 2-3 ms, but eventually it turned out to be too slow for our needs. Fast control of the phase was achieved by a frequency shift of the IR light, using a double-pass AOM. The retro-reflecting mirror sets the boundary condition for the superlattice (Fig.3-4). Both green and IR light must have a node on it. If the frequency of green is not exactly 2 times the frequency of IR, but shifted a small amount (in our case 70 MHz) then a phase shift ϕ_{SL} accumulates between the lattices on the way from the common node at the mirror to the atoms. Using this method, the phase ϕ_{SL} can be changed very quickly at sub-microsecond times.

If we want to go from the symmetric to the antisymmetric double-well potential, we have to change the superlattice phase by π . We have to generate a relative shift of 133 nm between the green lattice lattice and the IR lattice, which corresponds to half the period of green lattice and qartter period of the IR lattice.

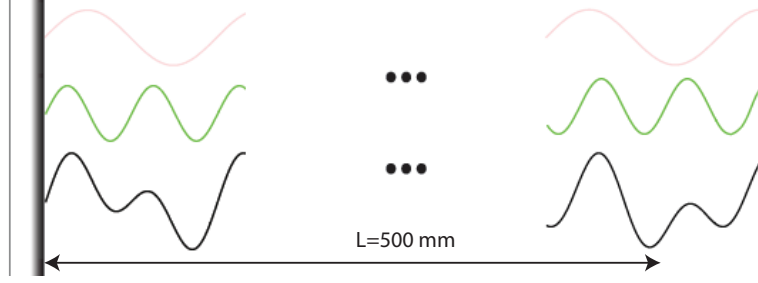


Figure 3-4: The relative phase between green and IR light at the location of the atoms determines the shape of the double-well cell.

The number of nodes in a standing wave between the retro-mirror and the atoms is

$$N = \frac{L}{\lambda/2}, \quad (3.25)$$

where $L \approx 0.5$ m is the distance from retro-mirror to the center of the vacuum chamber. The change of the number of nodes due to the frequency detuning of the beam is

$$\frac{\Delta N}{N} = \frac{\Delta f}{f} \quad (3.26)$$

The required ΔN for green light is $\frac{1}{2}$, and for IR is $\Delta N = \frac{1}{4}$. Thus, we either have to shift the frequency of the green light by 140 MHz, or shift the IR by 70 MHz. It was more convenient for us to shift the IR light frequency, which was easily achieved by a double-pass AOM.

Another important aspect of the superlattice is to make 1064 nm and 532 nm light phase-locked. Without this feature the green lattice would jitter with respect to the IR and the consecutive runs of the experiment would not be reproducible.

3.5 Green light generation

Our experiment with an optical superlattice requires high-power single-mode light sources for fundamental and doubled frequencies. The BEC2 lab is equipped with a stable 2 W seed laser of 1064 nm light (Mephisto from Coherent) and two 50

W Nufern fiber amplifiers. Thus, there's no lack of IR power in the lab, so instead of buying another single-mode green laser, we decided to use some of the IR light and generate 532 nm light using a frequency-doubling crystal. One Nufern is used to provide light for IR lattice, while the output of another one is used for generating a green light by passing it through a nonlinear crystal. Both of the Nuferns use common seed beam. Thus, the current setup has an advantage that the frequency doubled green and fundamental IR are phase-locked when obtained from common seed, whereas two independent lasers would require additional electronic phase-locking for the purpose of our experiment.

Second-harmonic generation (SHG) is a well known and commonly used method of generating light in the blue-green range of the EM spectrum. The general idea of SHG is to utilize the nonlinear polarizability of crystals. A beam of frequency ω passes through the crystal and generates a beam of frequency 2ω via a nonlinear interaction. Since the nonlinear response of the system is a process of "second-order", based on a two-photon interaction, it is supposed to be weak in comparison to linear effects. This intrinsic weakness has led to the development of several methods to boost the efficiency of SHG, such as guided-wave interactions, intra-cavity doubling and resonant enhancement.

3.5.1 Generation of double-frequency wave

In Gaussian units, Maxwell's equations in non-magnetic medium with no free charge and currents give

$$\nabla^2 \vec{E} - \frac{1}{c^2} \frac{\partial^2 \vec{D}}{\partial t^2} = 0 \quad (3.27)$$

The electric displacement vector is

$$\vec{D} = \vec{E} + 4\pi\vec{P} \quad (3.28)$$

The wave equation transforms into

$$\nabla^2 \vec{E} - \frac{1}{c^2} \frac{\partial^2}{\partial t^2} \vec{E} = \frac{4\pi}{c^2} \frac{\partial^2}{\partial t^2} \vec{P} \quad (3.29)$$

Any component P_k of the polarization induced by the electric field \vec{E} can be expanded in a series

$$P_k = \chi^{(1)} E_i + \chi_{ijk}^{(2)} E_i E_j + \chi_{ijmk}^{(3)} E_i E_j E_m + \dots \quad (3.30)$$

The system is driven by monochromatic field at fundamental frequency ω

$$\mathbf{E} = E_i \hat{e}_i = (\mathcal{E}_i e^{i\omega t} + \mathcal{E}_i^* e^{-i\omega t}) \hat{e}_i \quad (3.31)$$

We are most interested in the second-order contribution to the polarization

$$P_i^{(2)} = \chi_{jii}^{(2)} (\mathcal{E}_i^2 e^{i2\omega t} + \mathcal{E}_i^{*2} e^{-i2\omega t} + 2\mathcal{E}_i \mathcal{E}_i^*) \quad (3.32)$$

One can see that the second order polarization also gives rise to a constant term $2\mathcal{E}_i \mathcal{E}_i^*$, which is the reason for the phenomenon of optical rectification.

3.5.2 Plane wave passing through the crystal

The problem of the beam passing through a nonlinear medium is very complicated and requires tedious derivations. However, some intuitive features and scaling laws can be obtained from a simple model of a plane wave (find references).

We will search for the solution of the wave equation in the form $E_k^{(2)}(z, t) = \mathcal{E}_{2\omega} e^{-i2\omega t} + c.c.$. Since we decided to neglect the dynamics of the green beam in the transverse direction, we can employ slowly-varying envelope approximation.

$$\mathcal{E}_{2\omega}^{(2)} = A(z) e^{ik_z z} \quad (3.33)$$

This approximation is valid as long as $\nabla A \ll k_z A$. Substituting this representation of green light into the wave equation 3.27 and omitting the quadratic terms, we are

left with the equation for the envelope

$$-k^2 A(z)e^{ikz} + 2ik e^{ikz} \frac{\partial}{\partial z} A(z) + \frac{4\omega^2}{c^2} A(z)e^{ikz} = \frac{16\pi\omega^2}{c^2} \chi^{(2)} \mathcal{E}_\omega^{*2} e^{i2k_0 z}, \quad (3.34)$$

where k_0 corresponds to the principle wave vector of the IR light. The first and the third terms cancel out and the resulting equation describes the growth of doubled frequency amplitude as a function of fundamental field and distance.

$$i \frac{\partial}{\partial z} A(z) = 2\pi k \chi^{(2)} \mathcal{E}_i^{*2} e^{i(2k_0 - k)z} \quad (3.35)$$

Integrating from $z = 0$ to $z = l$ we come to the result

$$iA(l) = 2\pi k \chi^{(2)2} \mathcal{E}_i^{*2} l e^{i\frac{(2k_0 - k)l}{2}} \text{sinc}\left(\frac{(2k_0 - k)l}{2}\right) \quad (3.36)$$

Thus, the intensity of the output green beam is

$$I(l) = |A(z)|^2 = 4\pi^2 k^2 \chi^{(2)2} l^2 I_0^2 \text{sinc}^2\left(\frac{2k_0 - k}{2} l\right) \quad (3.37)$$

In the experiment, the quantity we deal with is power, rather than intensity. So, putting all the constant factors together and introducing the beam waist w_0 , which stays constant for a plane wave, we can rewrite the previous equation in terms of power:

$$P(l) = Cl^2 \frac{P_0^2}{w_0^2} \text{sinc}^2\left(\frac{2k_0 - k}{2} l\right) \quad (3.38)$$

An important condition to maximize doubled frequency power is phase matching $2k_0 = k$. This equation basically expresses the conservation of momentum. However, in practice, it is not so easy to meet this condition. In addition to careful alignment, one needs to keep in mind that the wave vectors for green and IR beams depend on refractive indexes for frequencies ω and 2ω

$$2k_0 - k = 2n(\omega) \frac{\omega}{c} - n(2\omega) \frac{2\omega}{c} = 0 \quad (3.39)$$

One needs to carefully adjust temperatures and employ some tricks based on crystal birefringence or periodically polling to meet the condition $n(\omega) = n(2\omega)$. For optimal phase-matching,

$$P(l) = C \frac{P_0^2}{w_0^2} l^2 \quad (3.40)$$

This result does not take into account many additional effects. First of all, it contradicts conservation of energy, because the depletion of the fundamental beam is not included in the model. More accurate analysis including the decrease of the IR power on the way through the crystal would give [43]

$$P(l) = \tilde{C} \frac{P_0^2}{w_0^2} \tanh^2(\alpha l) \quad (3.41)$$

3.5.3 Phase-matching

In the previous chapter, we saw how important it is to meet the phase-matching condition to reach a high efficiency of SHG. From formula 3.38, one can see that maximum power is achieved when $k = 2k_0$, i.e. when $n(\omega) = n(2\omega)$. Generated green light must travel at the same phase velocity as the fundamental IR. This condition is impossible to meet in materials with normal dispersion, where the refractive index usually increases with the frequency. One of the possible ways to get around this problem is to use the birefringence of the crystal. If the polarization of the incident fundamental beam is along one axis of the crystal, and the polarization of the second-harmonic beam is aligned in orthogonal direction, then the refractive indices for the normal and anomalous beam could be matched at some temperature or some angle.

However, sometimes it is hard to find materials with sufficient adjustability for some wavelengths. Another more universal technique is quasi-phase-matching or periodic poling. Quasi-phase-matching relies on artificial structure in the crystal [44] and can be implemented in materials even without birefringence.

The physical idea behind phase-matching can be explained in the following way. While traveling through an elongated crystal, the fundamental wave excites secondary radiation sources to emit at double frequency. The amplitudes of the secondary

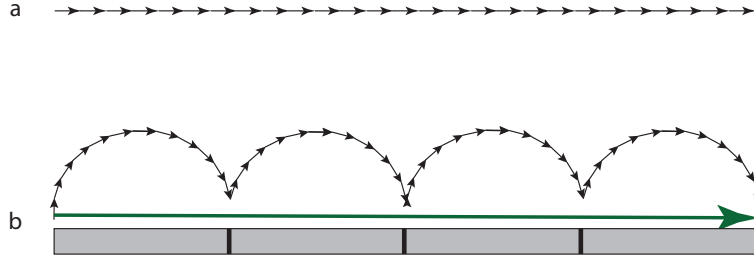


Figure 3-5: a. Phase-vectors add up constructively. b. Periodically-poled crystal; when phase-vectors add up to the maximum amplitude the structural insertion in the crystal adds a π phase shift and the spiral continues to grow, instead of rolling down.

radiation add up with the phase factors corresponding to the relative wave pass. In order to have a strong SHG output of the crystal these amplitudes should add in constructively. When we calculate the total amplitude from all the spatially separated SHG sources, we need to calculate an integral $\int_0^l e^{i\Delta kx} dx$. This type of integral arises in optics very often. We can utilize the diagram technique of Fresnel optics to visualize the summation over the secondary emitters with different phases.

In the case of $\Delta k = 0$ all the sources interfere constructively and all the "phase-vectors" add in a straight line giving the maximum total amplitude Fig.3-5.a. If we don't meet phase-matching condition, then there will be an angle $\Delta k\Delta z$ between "phase-vectors" of two neighboring emitters and the resultant interference amplitude will not be maximal.

For nonzero Δk , one can find a length realizing the π phase shift and equal to $l_\pi = \frac{\pi}{\Delta k}$ for which the resultant amplitude vector is the longest. If we can break into the crystal structure and bring extra π shift at the length l_π , then the spiral will keep building up (Fig. 3-5.b) instead of falling off to the 2π phase and zero total amplitude. Thus, if we can insert this extra π phase every l_π , the resultant amplitude will be less than in perfect constructive interference case, but still pretty big and will be proportional to the number of l_π lengths that we can fit into crystal.

3.5.4 Gaussian beam analysis

The plane wave model is very attractive in its simplicity. However, in practice we usually deal not with plane waves, but Gaussian beams. In their 1968 paper, Boyd and Kleinman [45] studied Gaussian beams passing through nonlinear crystal media. Their research took into account birefringent "walk-off" of the beam, which occurs when the direction of propagation of the beam does not coincide with the axis of the crystal. Our case is much simpler, because in periodically-poled crystals (PPLN, PPSLT) the phase-matching does not rely on the birefringence phenomenon. It can be considered as a special case of the Boyd-Kleinman problem when the birefringent "walk-off" is set to zero.

The plane wave model showed that the second-harmonic intensity scales quadratically with the intensity of the fundamental beam. Thus, if a beam of fixed power is focused tighter, the efficiency of SHG is expected to be higher. However, we know that the tighter we confine the beam, the faster it will diverge. So, even though we are winning in the minimum waist region, we may be losing more around the Rayleigh range of the beam.

Boyd and Kleinman examined loose vs tight focusing and realized that there is an optimal geometry of the beam which gives maximum efficiency of the SHG. For the simplest case of a phase-matched Gaussian beam focused at the center of the crystal and propagating without losses and birefringent "walk-off", the second-harmonic power is given by a formula:

$$P = \frac{16\pi^2 d_{eff}^2}{\epsilon c \lambda^3 n_1 n_3} P_1^2 l h(\xi, B) \quad (3.42)$$

Variable ξ , defined as $\frac{l}{2z_R}$, characterizes the extent of the focusing. Fig.3-6 adopted from the paper [45] shows the family of curves for different values of the "walk-off" parameter B . The upper curve corresponds to the case of no "walk-off" ($B = 0$), in which we are particularly interested in. One can see that the curve $h(\xi, 0)$ has a zero maximum at the value $\xi_m = 2.84$. Thus the optimal efficiency of SHG is achieved when the Rayleigh range is 5.68 times shorter than the length of the crystal. For a

given power of the IR beam P_1 , the maximum of green light power is

$$P_{opt} = 1.068 \frac{16\pi^2 d_{eff}^2}{\epsilon c \lambda^3 n_3 n_1} P_1^2 l \quad (3.43)$$

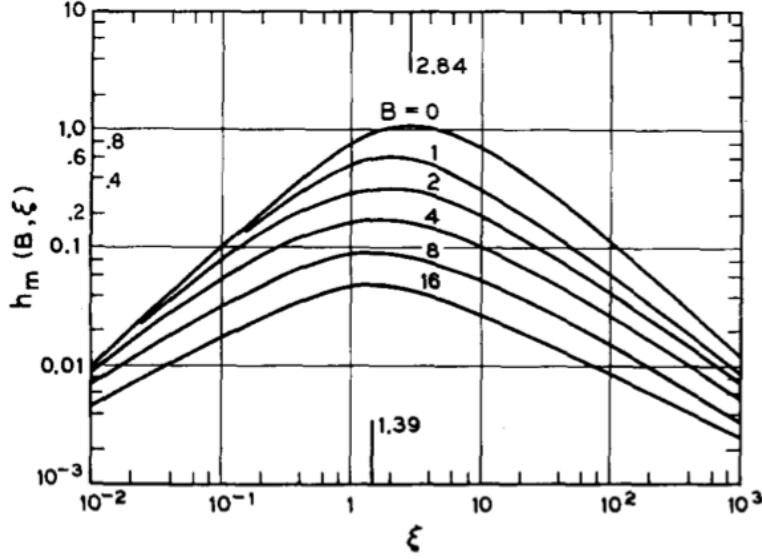


Figure 3-6: A family of SHG power dependences of parameter ξ for different values of the walk-off parameter B . The case we are interested is depicted by the upper curve ($B = 0$). The figure is adopted from [45].

One needs to point out that the maximum green power for a given input IR power scales linearly with the length of the crystal, unlike the result obtained for the plane wave. To confirm the correctness of these results we can consider the limit $\xi \ll 1$ of the formula (15). This limit will give us output green power for the case of very loose focusing, i.e. a plane wave. From reference [45] $h(\xi, 0) \rightarrow \xi$ which leads to the output power

$$P = \frac{8\pi d_{eff}^2}{\epsilon c \lambda^2 n_3 n_1^2 w_0^2} P_1^2 l^2, \quad (3.44)$$

which agrees with the plane wave model.

3.5.5 Operation of SHG

In the previous section, we concluded that neither a plane wave nor very tight focusing give us maximum SHG efficiency, and there is an optimal focusing $\xi = 2.84$ which

maximizes the power output. At the same time we should keep in mind that we want to keep the intensity of light below the damage threshold of the crystal. The typical value of the damage threshold for SLT crystals is $1 \frac{MW}{cm^2}$ (ref. HC-photonics). Therefore, the minimum spot size one could afford, using 50 W beam, is $w_0^* = 40\mu m$. This beam waist corresponds to the Rayleigh range $z_R = 4.7mm$. If the crystal length is $l = 30mm$ then the focusing parameter $\xi \approx 3.2 > \xi_{opt} = 2.84$. Therefore, it appears that we can focus the beam even a little tighter than the optimal focusing and we still would not reach the damage threshold of SLT crystal. This estimation is very promising and means that we should not be excessively careful with operating crystal at high power. The optimal Rayleigh range and beam waist for a 30 mm long crystal are $z_R^* \approx 5.3mm$ and $w_0^* \approx 42\mu m$

The parameters of the optical setup were chosen to match the optimal minimum waist and divergence of the beam for SHG. The use of the variable beam expander allowed us to carefully tune the beam waist and optimize the power of SHG. The optimal beam parameter appeared to be in a very good match with the theoretical prediction.

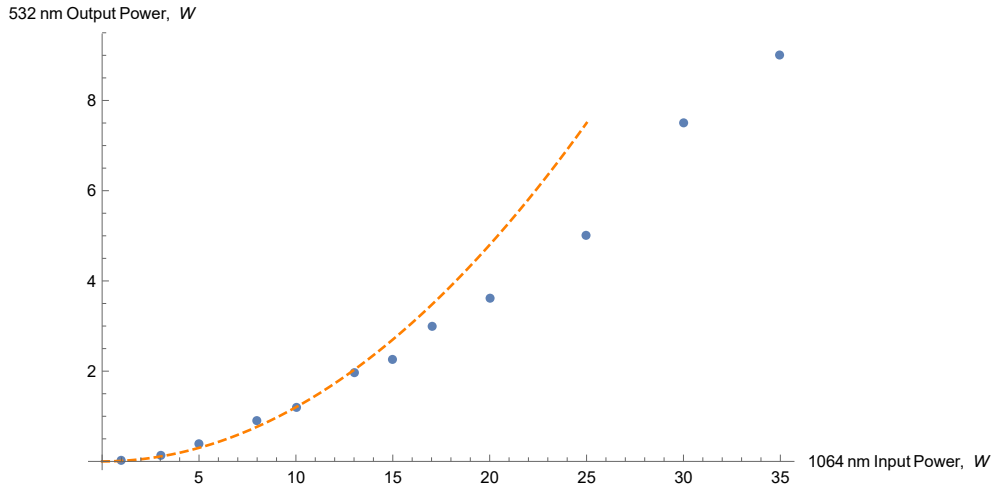


Figure 3-7: Green power generated as a function of the input IR power. As a two-photon process, second-harmonic generation scales quadratically at low powers. At high powers the output was not stable and the points characterize momentary maximum values.

3.5.6 Buyer's catalog

During the upgrade of our SHG setup I had to reach many sellers and collect information from companies which manufacture or sell nonlinear optics. Our old green light setup had been using a 30 mm long PPMgSLT crystal (MgO: Stoichiometric LiTaO₃) along with an oven and temperature controller from Taiwanese company **HC-photonics**. Unfortunately, this company no longer sells this kind of crystals. When I contacted them regarding backup crystals, they offered PPLN crystals, which have higher efficiency than PPSLT, but lower photorefractive damage threshold. We would not be able to obtain more than 3 W of green out of 20 mm crystal on a single pass (according to HC-photonics). Another acknowledged company in our community is **Covesion** (from the UK). However, their crystals have a low damage threshold as well. Covesion offered 40 mm long PPLN crystals which are supposed to provide 2 W of green with 10 W of IR input. Their customers claimed they could obtain up to 5 W of green light without observable signs of photorefractive damage, but that power would still not be sufficient for our applications. Even though Covesion crystals would not work well for our experiment, I decided to buy an oven (PV40) and temperature controller (COV461) from this company. The temperature resolution of the oven+controller was 0.01°, which was a step forward from the old BEC2 oven (0.1° resolution). One cannot overstate the importance of stabilizing the temperature along the crystal. This is highly important for maintaining the phase-matching condition and keeping the efficiency of SHG high. After a search, we realized the company **Oxide** from Japan sells exactly what our lab needed: PPMgSLT crystals (part Q-STD-1064C-S01) with high damage threshold. The unit price for them is around \$2000, which is a lot cheaper than typical purchases from HC-photonics and Covesion. We successfully operated their crystals in BEC2 for several years and were quite satisfied with their performance. Other companies which were explored and may be found useful in the future include **Raicol crystals** from Israel, **Deltronic** from California, **Alphalas** from Germany.

At the end of the day, after having a lot of experience with operating nonlinear

crystals, I must say that the choice of the oven I made was not optimal. The Covesion's oven would do the job well for the normal operating regime of their crystals (2 W of green out of 10 W of IR). We worked in the different range of parameters (10W of green out of 30 W of IR). At such high input power of IR, a phenomenon known as Green Induced Infrared Absorption (GRIIRA) [46] becomes important. Basically, a lot of heat is deposited from the strong IR beam and the crystal's temperature grows without assistance from the oven. The temperature of the crystal and the output green power never stabilizes. It can grow as high as 12 W but then after several seconds it can drop down to 2-3 W. The temperature of the crystal was determined by the thermal equilibrium of the deposited heat from the IR beam and through the oven cover and input/output holes. The active stabilization practically did not work, since the oven could only heat and could not cool the crystal. Thus, it was more convenient to operate the crystal in the more stable medium power range of (8-10 W of green output). Ideally, I should have considered buying an oven which would also have a cooling option through Peltier thermoelectric effect, such ovens are available on the market.

3.6 Experimental Results

The spin-orbit coupling experiment was done with a sodium BEC in $|F = 1, m_F = -1\rangle$ state. The BEC was adiabatically loaded within 250 ms from an optical dipole trap to the lowest band of the superlattice, which is pseudo-spin down of our effective two-level system $|\psi_{q=0}^{(\downarrow)}\rangle = \sum_{n=1}^N \frac{1}{\sqrt{N}} |\downarrow_n\rangle$. The pseudo-spin-up state $|\psi_{q=\pi/d}^{(\uparrow)}\rangle = \sum_{n=1}^N \frac{1}{\sqrt{N}} (-1)^n |\uparrow_n\rangle$, at the edge of the Brillouin zone, has an alternating sign pattern. In time-of-flight (TOF), where we look at the state in momentum space, the interference patterns for $|\psi_{q=0}^{(\downarrow)}\rangle$ and $|\psi_{q=\pi/d}^{(\uparrow)}\rangle$ will be different Fig.(3-8).

After atoms are loaded in the lowest band, we can quickly change the phase of the superlattice, creating an offset Δ and lifting the atoms from the ground band to the first excited band. The quasimomentum of the atoms will remain the same ($q = 0$), so they will be at highest point of the the first excited band and then will relax to the

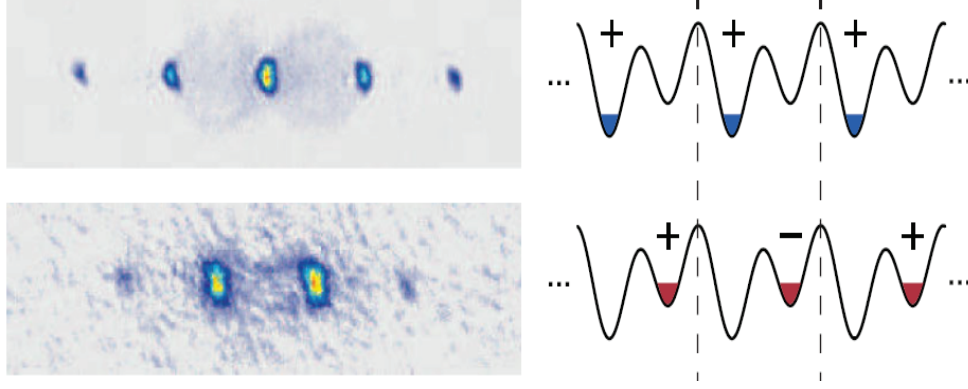


Figure 3-8: patterns for $|\psi_{q=0}^{(\downarrow)}\rangle$ (top) and $|\psi_{q=\pi/d}^{(\uparrow)}\rangle$ (bottom). The state at the edge of the Brillouin zone $q = \pi/d$ is characterized by alternating sign pattern.

edge of the Brillouin zone. The process of relaxation will be reflected in TOF images 3-9.

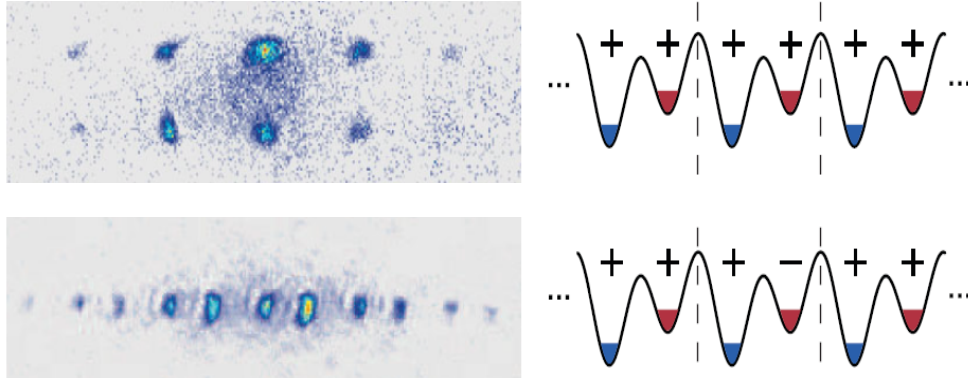


Figure 3-9: The top pattern shows a TOF image for equal populations of atoms prepared in the ground and first excited state with the same quasimomentum $q = 0$. $|\downarrow\rangle$ and $|\uparrow\rangle$ are deliberately vertically displaced by an analog of the Stern-Gerlach effect. After the $|\uparrow\rangle$ state relaxes to $q = \pi/d$, the periodicity of the wavefunction doubles, and therefore the momentum peaks in the inverse space two times as frequent. The relaxation time is about 2 ms.

When atoms are prepared in both ground and excited band at the same quasimomentum $q = 0$ the periodicity of the wave function is going to be 532nm, i.e. the length of the unit cell of the superlattice. After atoms in the excited band relax to $q = \pi/d$ the periodicity of the wavefunction changes to 1064nm. In the TOF image, the number of momentum peaks will double.

The adiabatically ramped Raman coupling $V_{Raman} = \Omega \cos(k_x x + k_z z - \delta t)$ makes

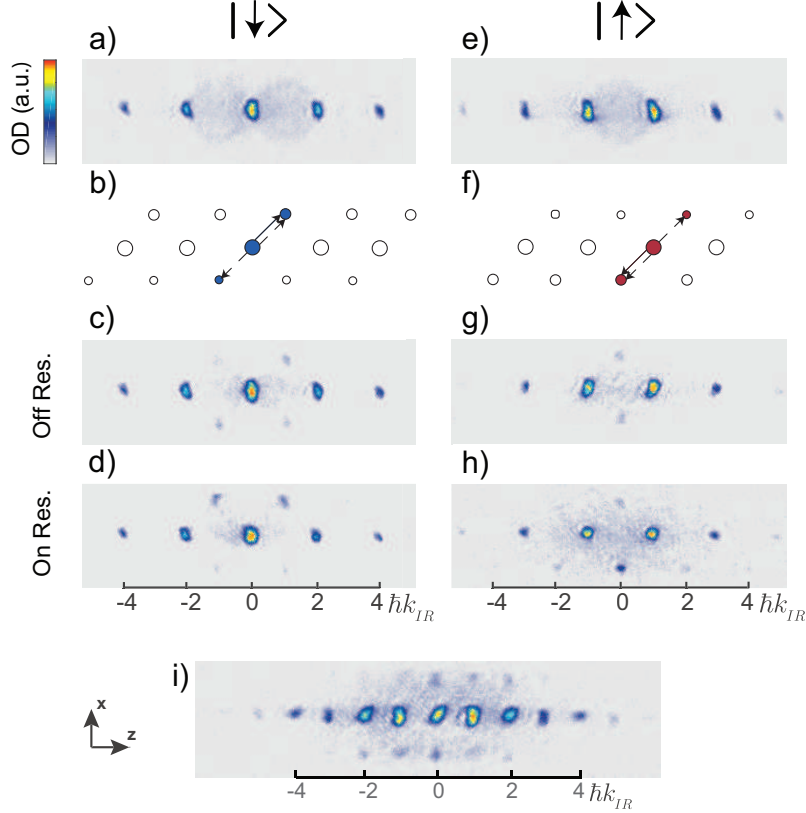


Figure 3-10: TOF interference for atoms loaded in (a) lower wells and (b) upper wells. Schematic plots for the expected SOC signal for atoms prepared in (c) pseudo-spin-down state and in (g) pseudo-spin-up state. Observed signal for both initially prepared states resonant (c, g) and off-resonant (d, h) Raman two-photon detuning. Interference pattern for atoms equally loaded in both pseudo-spin states with Raman interaction tuned between two resonances.

the wavefunction acquire satellites according to equations 3.21 and 3.22. Because of the momentum kick in the direction orthogonal to the superlattice, in TOF the momentum satellites will be displaced along \hat{x} .

We can describe the wave function as $|\downarrow, q, k_x\rangle = |\psi_q^{\downarrow(\uparrow)}\rangle \otimes e^{ik_x x}$ — a tensor product of a Bloch wave (characterized by the quasimomentum q and quasi-spin) and the plane wave in the transverse direction \hat{x} . In the experiment we studied three regimes: (1) atoms loaded in the lower well $|\downarrow, 0, 0\rangle$, where the Raman potential creates spin-orbit side peak $|\uparrow, \pi/d, k_x\rangle$ along with other off-resonant terms; (2) atoms prepared in $|\uparrow, \pi/d, 0\rangle$ with the corresponding spin-orbit coupling satellite is $|\downarrow, 0, -k_x\rangle$; (3) equal population of atoms loaded in the lower and upper wells, wher both types of

spin-orbit peaks are observed simultaneously. All three scenarios are depicted in the Fig.3-10.

The momentum components created by 2-photon Raman processes are displaced along \hat{x} by an amount of the IR photon recoil $\hbar k_{IR}$. The off-resonant peaks are symmetric for $+x$ and $-x$. The resonant spin-orbit coupling peaks are one sided: we are either tuned to the resonance in forward direction from the lower to the upper well, $\delta = \Delta + E_r$, or to the backward direction from upper to lower well $\delta = \Delta - E_r$. The two resonances are supposed to be separated by $2E_r = 15.3$ kHz. One can see that the forward and backward resonances are indeed displaced with respect to each other: Fig.3-11 shows a plot of the normalized population imbalance, where the fractions of atoms with $k_x = +k_{IR}$ and $k_x = -k_{IR}$ are mapped as a function of the Raman detuning δ . The discrepancy from the $2E_r$ values can be explained by the mean field shift $\sim 2\mu \approx 5$ kHz.

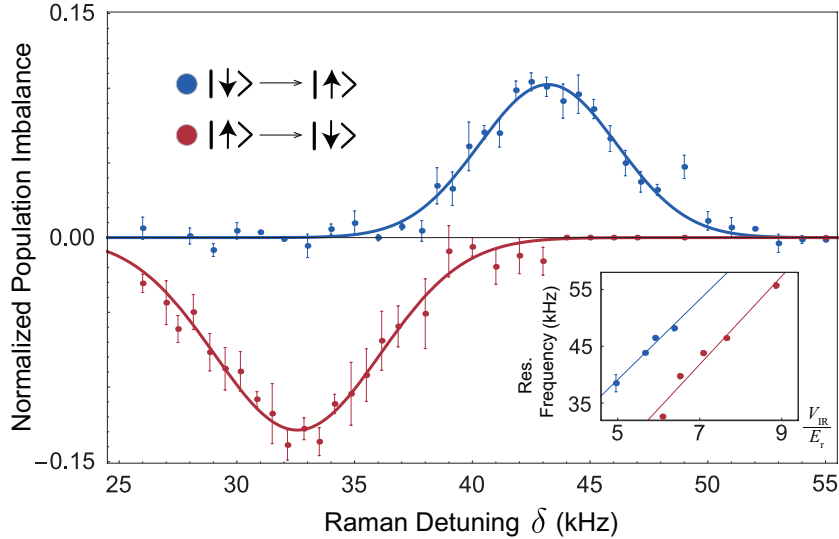


Figure 3-11: Mapped out spin-orbit coupling resonances as a function of Raman detuning. The population imbalance is plotted for forward (blue) and backward (red) spin flips. The inset is the resonance the center frequency of the resonances as a function of the IR lattice depth V_{IR}

The offset Δ can be measured by observing a beat note between the atoms in $|\uparrow\rangle$ and $|\downarrow\rangle$. The condensate was loaded with equal populations into the symmetric double well and then the potential was rapidly changed to the asymmetric one. De-

pending on the hold time in that potential, atoms in the first excited band acquired a time-dependent phase which can be observed through oscillations of the interference pattern in TOF. This beat note measurement must be completed before atoms in the excited band relax in quasimomentum to the edge of Brilluan zone. The offset used for the final data taking was 23 kHz, so the period of oscillation was 44 μs . The relaxation from $q = 0$ to $q = \pi/d$ happens within 2 ms.

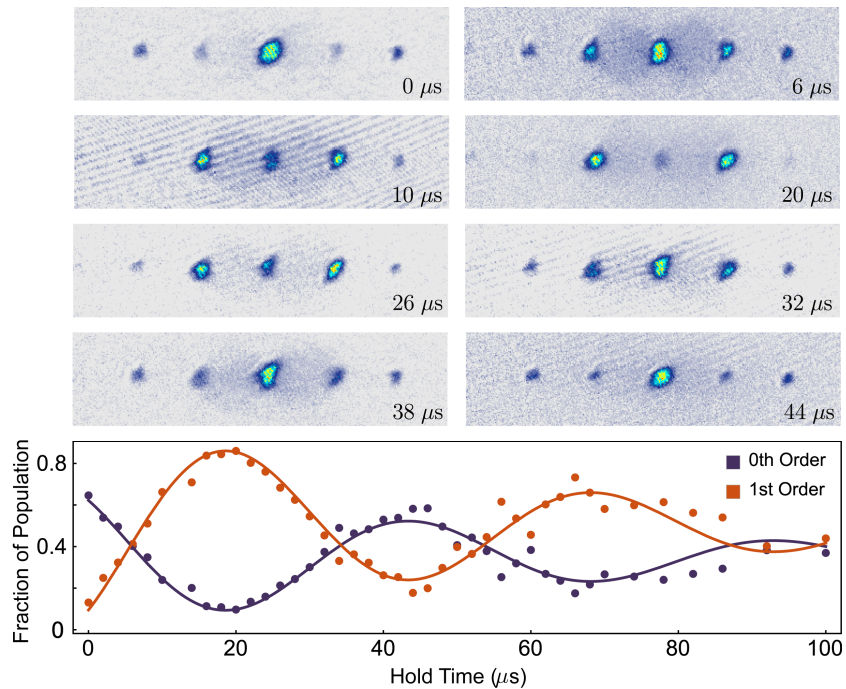


Figure 3-12: Calibration of the offset Δ between lower and upper wells. On a short time scale (relative to 2ms of relaxation in the excited band) the atoms in the upper well have a phase accumulated linearly with time, $e^{-i\Delta t}$. From the period of the oscillation of the interference pattern $\Delta \approx 23$ kHz was deduced.

The presence of satellites for the wavefunctions localized in the left or right wells not only provides possibility for interference between them and future Raman coupling, but also gives a source of heating through collisions. The lifetime observed for the $|\uparrow\rangle$ state and for the state with 50/50 population in $|\uparrow\rangle$ and $|\downarrow\rangle$ was about 200ms for both cases. However, the collision rate for the 50/50 state should have been suppressed by a factor of $4(J/\Delta)^2$. The similarity in the lifetimes indicates that the main heating mechanism comes not from the collisions between spin-up and spin-down, but from rather some technical noise.

3.7 Stripe phase detection

As explained in the previous paragraph, the adiabatically ramped Raman potential dresses the atoms in the left and right wells with momentum satellites according to (3.21) and (3.22).

The states $|\Psi_1\rangle$ and $|\Psi_2\rangle$ produce interference and density modulations. The state $|\downarrow, 0, 0\rangle$ in $|\Psi_1\rangle$ interferes with $\sim e^{i(\delta-\Delta)t} |\downarrow, 0, -k_x\rangle$, resulting in a stationary density modulation at $\delta = \Delta$ along \hat{x} (orthogonal to the superlattice direction), and this density modulation is the sought-for stripe phase (Fig.3-13). $|\downarrow, 0, 0\rangle$ also interferes with the on-site terms $M_1 e^{-i\delta t} |\downarrow, \pi/d, k_x\rangle$ and $M'_1 e^{i\delta t} |\downarrow, -\pi/d, -k_x\rangle$ giving rise to moving density modulations. In the geometry of our experiment $k_x = \pi/d$, so these stripes are formed at 45 degrees to the lattice and move with a phase velocity of $v = \frac{\delta}{\sqrt{2}\pi/d}$. Similarly, the term $e^{-i\Delta t} |\uparrow, \pi/d, 0\rangle$ from $|\Psi_2\rangle$ interferes with $K_1 e^{-i\delta t} |\uparrow, \pi/d, k_x\rangle$, $M_2 e^{i(\delta-\Delta)t} |\uparrow, 0, -k_x\rangle$ and $M'_2 e^{-i(\delta+\Delta)t} |\uparrow, 0, k_x\rangle$. As a result of this interference, there is one stationary density modulation (stripe phase) at $\delta = \Delta$ and two moving modulations.

Thus, the stationary stripe phase occurs at the same detuning $\delta = \Delta$ for both spin-up and spin-down in direction perpendicular to the superlattice with the periodicity inverse to the momentum transfer $2\pi/k_x$, and can be detected by Bragg spectroscopy.

The experimental conditions for stripe phase detection followed the parameters mentioned in the previous chapter. A Bragg probe beam to detect the stripes was added to the existing setup. The Bragg detection had to be done with sodium resonant light $\lambda_{Bragg} = 589nm$ at an incident angle of $\theta = 16^\circ$ in order to meet the Bragg condition $\lambda_{Bragg} = 4d \sin \theta$.

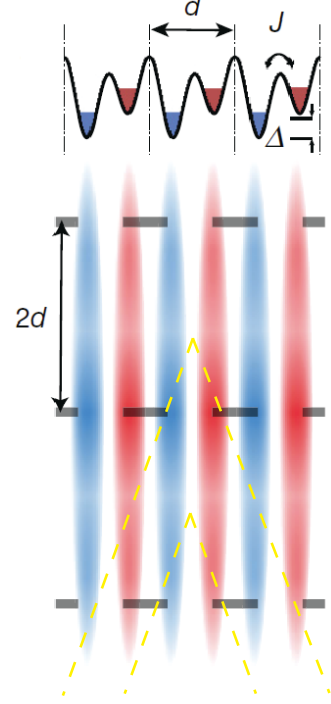


Figure 3-13: A stationary density modulation and the probe meeting the Bragg condition.

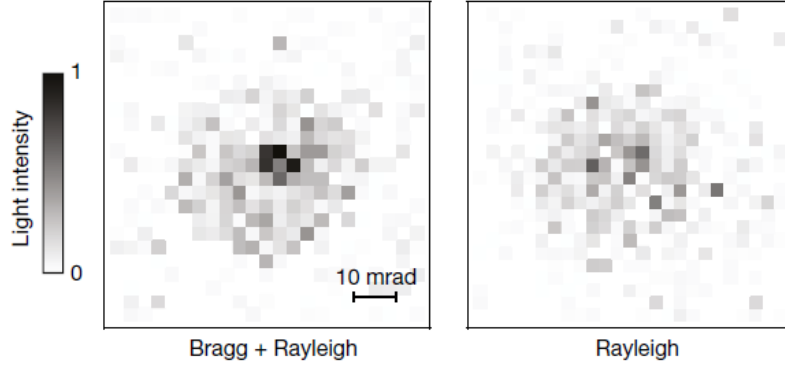


Figure 3-14: Anlge-resolved Bragg signal. The density modulation gives a sharp feature in the center on the top of diffuse Rayleigh scattering. Without spin-orbit coupling there is no density modulation and only the Rayleigh scattering is observed.

The Fig.3-14 shows the angular distribution of Rayleigh-scattered resonant light. Due to the stripe phase formation, the scattering is enhanced in the direction of the Bragg condition. A sharp feature in the angular distribution of the scattered light with zero detuning is a direct proof of the existence of the stationary density modulation.

The FWHM of the observed peak is 9 ± 1 mrad, which is consistent with the diffraction limit λ_{Bragg}/D , where D is the size of the cloud. For the same experimental parameters we observed superfluid peaks of the BEC in TOF images, which suggests that the state of matter we have been working with is superfluid. Thus, we can conclude that the observed phase is a superfluid with a long-range order. This state of matter is referred to as a supersolid.

Since the stripe phase is not the only density modulation formed in our system, we have to make sure that other periodic structures do not contribute to the detected Bragg signal. The other density modulations emerging from the onsite coupling are oriented at 45° to the superlattice, parallel to $\hat{x} + \hat{z}$ direction, whereas the stationary stripes form with the wave vector along x . The Bragg condition cannot be fulfilled for them simultaneously, and therefore the detected signal is background-free.

The detected Bragg signal can be quantified. The contrast of the stripes is estimated to be $\eta = 2\beta/E_r$, which is about 8% for $\beta = 300$ Hz. Denoting the Raleigh-scattering isotropic rate per atom per solid angle as γ , the enhanced Bragg signal is

going to be $\gamma(\eta N_{BEC}^2/4)$, where $1/4$ comes from Debye-Waller factor for a sinusoidal modulation. The detected signal confirmed the anticipated scaling with the BEC number $\sim N_{BEC}^2$.

One can also look at the Bragg signal as "gain" of the Raleigh intensity. We varied the BEC fraction $f = N_{BEC}/N_{total}$ and confirmed that the Bragg intensity scales as $N_{total}(f\beta/E_r)^2$, which also proves that the Bragg enhancement comes only from the superfluid component.

We also mapped the detuning dependence of Bragg and Raleigh signals. By sweeping the detuning of the Raman beams we saw the effect of resonant coupling between spin-up and spin down — the broad resonance separated by $2E_r$ and the sharp Bragg resonance from the stationary stripes at $\delta_0 = 0$.

The periodicity of the stripes depends not only on external parameters such as the momentum transfer from Raman beams but also on the interactions between the atoms. The length of the period is modified to be $2d/\sqrt{1 - (\beta/F)^2}$, where β is the spin gap and $F = (2E_r + n(g + g_{\uparrow\downarrow}))/4$ reflects the effect of interactions. However, in our schemes this correction is only 0.4% and can be neglected.

Chapter 4

Introduction to periodically driven systems

In this chapter I'll review the basic theory describing the behavior of periodically driven systems, both classical and quantum. Dynamics of classical systems, moving in rapidly oscillating fields, splits into slow and fast motion. Fast motion (or micromotion) averages into effective potential which in turn affects the slow variables of the system. These effects do not have a profound connection with discrete time translational symmetry, so Floquet treatment, applicable to quantum systems, is not necessary for them. However, they provide a lucid example of separation of time scales, of what micromotion is, and how important its impact can be. In quantum mechanics, the time-periodicity of Hamiltonian imposes constraints on the wave function. The knowledge about the symmetry of Hamiltonian allows to reduce the time-dependent problem of evolution of quantum system to a time independent one. The quantum picture is more complicated than the classical, however, the main idea is very similar. The system's evolution splits into two types of dynamics: fast micromotion and slow time-averaged evolution. The method of controlling the slow dynamics of the system by time-dependent fields is called Floquet engineering. The variety of the phenomena which can be realized by this technique is really impressive ref.. The goal of this chapter is to show a powerful application of the Floquet engineering and endow a low energy radio-frequency photon with peculiar paradoxical properties: enhance its

momentum by orders of magnitude.

4.1 Classical systems

There are two paradigmatic examples of classical systems where micromotion contributes to the slow dynamics of the systems in a nontrivial way: Kapitza pendulum and Paul trap. The former is well described in [47] along with the classical theory of motion in rapidly oscillating fields.

Let's consider a particle moving in an external potential U and driven by a rapidly oscillating force

$$f(t) = f_1 \cos \omega t + f_2 \sin \omega t \quad (4.1)$$

The force has to be much faster than particle's motion in the potential U , i.e. $2\pi/\omega \ll \sqrt{m/2} \int \frac{dx}{E-U(x)}$. We will imply that the displacement χ caused by the force f is only a small perturbation to the particle's trajectory X in the time-independent potential U . The equation of motion of the particle is

$$m\ddot{x} = -\frac{d}{dx}U + f(t) \quad (4.2)$$

We will seek the solution in the form

$$x(t) = X(t) + \chi(t) \quad (4.3)$$

assuming that the fast periodic force causes some jittering $\chi(t)$ on the top of slow motion $X(t)$ given by the potential U . The average of $\chi(t)$ over drive period $2\pi/\omega$ is zero and $X(t)$ during the same time barely changes, so $\bar{x}(t) = X(t)$, and $X(t)$ describes slow smooth motion averaged over fast oscillations. After substituting equation 4.3 into 4.2 and grouping separately fast oscillating terms and smooth terms we arrive to

$$m\ddot{\chi} = f(X, t) \quad (4.4)$$

Since f is a harmonic function the equation is easily integrated, and the instantaneous value of the fast oscillatory variable is determined by the value of the force $\chi(t) = -\frac{1}{m\omega^2}f(t)$.

The equation of motion for the smooth variable X averaged over drive period is

$$m\ddot{X} = -\frac{d}{dX}U_{eff}, \quad (4.5)$$

where $U_{eff} = U + \frac{1}{2m\omega^2}\bar{f}^2 = U + \frac{m}{2}\bar{\chi}^2$. One can see that when averaged over the fast oscillations the particle moves in a potential which is a sum of the initial time-independent potential and the kinetic energy associated with rapid oscillations - the micromotion energy.

4.1.1 Kapitza pendulum

One of the mechanical systems every physicist has known since the school is a simple pendulum: a body suspended from a support, moving under the force of gravity. If the pendulum is reclined from its equilibrium position at $\phi = 0$ to some small angle ϕ and then released, it starts doing small harmonic oscillations around the equilibrium position. If some friction is added to the system, then eventually the pendulum will stop at its equilibrium point $\phi = 0$ - this is why we say that this equilibrium is stable. Another equilibrium position $\varphi = \pi$ is unstable. When deflected from it, the pendulum first shows large-amplitude unharmonic oscillations, which then die out, and the pendulum eventually finds its stable equilibrium at $\varphi = 0$. All of that is trivial and very intuitive. What is not trivial is that the unstable equilibrium $\varphi = \pi$ can change its character and become stable — after we make the support jitter! By driving the system fast enough we can actually make it more stable. Isn't it amazing? Following one of the examples in [47] the Lagrangian of the pendulum with vertically oscillating support point with position $a \cos \gamma t$ can be written as

$$L = \frac{ml^2}{2}\dot{\varphi}^2 + mgl \cos \varphi + mla\gamma^2 \cos \gamma t \cos \varphi \quad (4.6)$$

The generalized oscillating force is $f = -mla\gamma^2 \cos \gamma t \sin \varphi$. Then the the effective

potential that includes micromotion energy is going to be

$$U_{eff} = mgl \left(-\cos \varphi + \frac{a^2 \gamma^2}{4gl} \cos^2 \varphi \right) \quad (4.7)$$

Under the condition that $a^2 \gamma^2 > 2gl$ the upper unstable equilibrium point $\varphi = \pi$ changes its character and becomes stable. Physically, when the body is deflected from the $\varphi = \pi$ the reduction in potential energy in the gravity field is smaller than the acquired kinetic energy due to micromotion. It is interesting to point out that if the support point jitters horizontally the character of the equilibrium does not change — it remains unstable. This happens because the upper point $\varphi = \pi$ is also the point of maximum micromotion and deviation from it reduces both potential energy of gravity and the kinetic energy of micromotion.

Kapitsa pendulum is a good transparent example of how counterintuitive the behavior of periodically driven system could be. By employing the micromotion and taking it under control we can engineer the systems which do not naturally happen in the real life.

4.1.2 Paul trap

Another paradigmatic example of the importance of micromotion is Paul trap [48], a powerful technique of trapping charged particles. From Maxwell's equations in the absence of charge we know that the divergence of the field must be zero $div \vec{E} = 0$, which implies that the static electric field cannot confine ions in all the directions. If the created potential is trapping along x and y , then it must be untrapping in the remaining direction z . It seems that trapping of charged particles is facing a very fundamental obstacle. However, if the electric field oscillates fast enough the emerging micromotion will help to trap ions and produce confining potential in all the directions.

It is enough to see the role of micromotion in one dimension. The Hamiltonian of a particle in a quadratic potential which oscillates at the frequency γ is

$$H = \frac{p^2}{2m} + \frac{1}{2}m\omega_0^2 x^2 \sin \gamma t \quad (4.8)$$

Using the same approach as for the Kapitza pendulum we decompose particle's motion into a sum of smooth motion $X(t)$ and fast oscillations around it $\chi(t)$. The average of χ over the drive period is zero: $\langle \chi(t) \rangle_{2\pi/\gamma} = 0$

$$x(t) = X(t) + \chi(t) \quad (4.9)$$

The equation of motion splits into two for the fast and the slow variables:

$$\frac{d^2 \chi}{dt^2} = -\omega_0^2 X \sin \gamma t \quad (4.10)$$

$$\frac{d^2 X}{dt^2} = -\omega_0^2 \langle \chi \sin \gamma t \rangle_{2\pi/\gamma} \quad (4.11)$$

After integrating of the first equation and plugging the result for χ into the second one we arrive at

$$\frac{d^2 X}{dt^2} = -\omega_0^2 \cdot \frac{\omega_0^2}{2\gamma^2} X \quad (4.12)$$

From this equation one can conclude that the slow dynamics of the particle follows the motion in a harmonic potential $U_{eff} = \frac{1}{2}m\left(\frac{\omega_0^2}{\sqrt{2}\gamma}\right)^2 X^2$

The idea of oscillating ion trap also found an application in transverse strong focusing (also called alternating-gradient focusing) of the beams of charged particles in accelerator physics. To prevent transverse divergence of the beam in an accelerator engineers use, so called, FODO systems. They alternate the focusing and defocusing lenses (quadrupoles) on the beam path. From the particles' point of view, they see how the attractive potential flips its sign and becomes repulsive: changes from focusing to defocusing, then to focusing again and so on. Eventually, it results in effective overall confining transverse potential for the moving particles [49]

4.2 Quantum systems

In this chapter we investigate quantum systems that have time-periodic Hamiltonians

$$H(t) = H(t + T) \tag{4.13}$$

The discrete time translational symmetry allows us to apply Floquet formalism to the problem of finding the evolution of the system. The Floquet theory was first developed in as a mathematical theory. In the second half of the 20th century it was revisited in the context of solving time-dependent Schrodinger equation [50].

In the literature there are two ways how the main statement of the Floquet theory is formulated. First, since the Hamiltonian possesses discrete time translational symmetry its eigen states can be written as

$$|\psi_n(t)\rangle = e^{-i\epsilon_n t} |u_n(t)\rangle, \tag{4.14}$$

where $u_n(t)$ is called Floquet mode, and it's periodic in time $u_n(t) = u_n(t + T)$, and ϵ_n is called quasienergy. After the period time T passes the wave-function acquires a phase factor $e^{-i\epsilon_n T}$, just like for a Bloch state in spatially periodic potential: the wave function acquires a phase factor, when the particle travels a period of distance. This formulation of the Floquet theory is almost trivial, it simply reflects the symmetry of the Hamiltonian and it is a direct analog of the Bloch theorem in solids.

Another formulation of the Floquet theorem is that the evolution of the system under time-periodic Hamiltonian can be decomposed into initial kick, evolution under some effective time-independent Hamiltonian and final kick

$$U(t_f, t_i) = e^{-i\hat{K}(t_f)} e^{-i\hat{H}_{eff}(t_f - t_i)} e^{i\hat{K}(t_i)} \tag{4.15}$$

The kick (micromotion) operator \hat{K} is periodic in time $\hat{K}(t) = \hat{K}(t + T)$ and describes the initial kick and the subsequent micromotion.

This formulation of the Floquet theorem is less trivial than the first one. Here it is guaranteed the existence of such time-independent Hamiltonian \hat{H}_{eff} and the

kick operator $K(t)$. The proof of this theory along with the perturbative methods of determining \hat{H}_{eff} and \hat{K} and comprehensive review of the Floquet formalism can be found in the references [51, 52].

In this chapter I'm going to show how these two formulations are interconnected. While the Floquet state (the quasienergy and the Floquet mode) is defined as a solution of time-dependent Schrodinger equation, it may be more convenient to refer to an eigen value problem in order to have another view on the definition of Floquet states. One can easily see that the Floquet state is the eigen state of the evolution operator over a period of the drive T :

$$\hat{U}(t_0 + T, t_0) |\psi_n(t_0)\rangle = e^{-i\epsilon_n T} |\psi_n(t_0)\rangle \quad (4.16)$$

The starting time t_0 is a parameter which defines the gauge: the evolution operator for one period and the Floquet state are interconnected. However, the eigenvalue $e^{-i\epsilon_n T}$ does not depend on choice of the starting time t_0 . So, the quasienergy spectrum can be determined from diagonalizing the evolution operator $\hat{U}(t_0 + T, t_0)$ for arbitrary t_0 . Also one can see that even though the eigenvalue $e^{-i\epsilon_n T}$ itself is well-defined, the quasienergy ϵ_n is only known by modulo $\omega = 2\pi/T$. Quasienergies separated by a driving frequency correspond to the same eigenvalue of the evolution operator.

In the basis of Floquet states 4.15 the evolution operator can be written as

$$\hat{U}(t_2, t_1) = \sum_n e^{-i\epsilon_n(t_2-t_1)/\hbar} |u_n(t_2)\rangle \langle u_n(t_1)| \quad (4.17)$$

The Floquet states form a complete basis states, and generally the time evolution of a state is given by

$$|\psi(t)\rangle = \sum_n c_n e^{-i\epsilon_n(t-t_0)} |u_n(t)\rangle. \quad (4.18)$$

The time-independent coefficients c_n can be deduced from $c_n = \langle u_n(t_0) | \psi(t_0) \rangle$. To add a little more intuition into this description, one can say that if the system is prepared in a single Floquet mode, i.e. $|\psi(t)\rangle = e^{-i\epsilon_n t} |u_n(t)\rangle$, it's time evolution is going to be periodic disregarding the obvious phase factor $e^{-i\epsilon_n t}$. Evolution of the

system prepared in a superposition of several Floquet states is no longer periodic, but it can be formulated in terms of two constituents. First is the periodic time-dependence of the Floquet mode $u_n(t)$ is associated with micromotion. On top of that the dynamics of the system is governed by quasienergies, as though we would have an evolution of an eigenstate of a time-independent Hamiltonian. So, the second constituent is the deviation from periodic evolution described by dephasing factors $e^{-i\epsilon_n t}$.

4.3 Effective Hamiltonian

Now let's approach this problem from a little different direction. In the reference [53] it is proved that $\hat{U}(t) = \hat{\mathcal{P}}(t)e^{-it\hat{G}/\hbar}$, where \hat{G} is self-adjoint operator and $\hat{\mathcal{P}}$ is unitary operator periodic in time with the same periodicity as the Hamiltonian.

Let's find a unitary gauge transformation $e^{i\hat{F}(t)}$ where $\hat{F}(t)$ is a Hermitian operator periodic in time, such that in the new gauge the Hamiltonian becomes time-independent. Applying the gauge transformation to the time-dependent Schrodinger equation:

$$i\hbar \frac{\partial}{\partial t} (e^{i\hat{F}} \psi) = e^{i\hat{F}} \hat{H}(t) + i\hbar \left(\frac{\partial}{\partial t} e^{i\hat{F}} \right) \psi \quad (4.19)$$

In the new gauge the wave function is $\phi = e^{i\hat{F}} \psi$. With the new Hamiltonian

$$\hat{H}_{eff} = e^{i\hat{F}} \hat{H} e^{-i\hat{F}} + i\hbar \left(\frac{\partial}{\partial t} e^{i\hat{F}} \right) e^{-i\hat{F}} \quad (4.20)$$

Let's assume that such transformation \hat{F} , that makes \hat{H}_{eff} time-independent, exists, then the eigenstates of \hat{H}_{eff} are also time-independent. We will call them $|v_n(x)\rangle$ and the corresponding eigenvalues ϵ_n . They evolve according to $|\phi(t, x)\rangle = e^{-i\epsilon_n t} v(x)$. In the original gauge the corresponding states are going to be

$$|\psi_n(x, t)\rangle = e^{-i\hat{F}} |\phi_n(x, t)\rangle = e^{-i\epsilon_n t/\hbar} \underbrace{e^{-i\hat{F}} |v_n(x)\rangle}_{|u(x, t)\rangle} \quad (4.21)$$

Here's the state $e^{-i\hat{F}} |v_n(x)\rangle$ is the Floquet mode $|u_n(x, t)\rangle$ introduced earlier in

the text. The evolution operator after transformed from the new gauge to the original is

$$\hat{U}(t_2, t_1) = e^{-i\hat{F}(t_2)} e^{-i\hat{H}_{eff}t/\hbar} e^{i\hat{F}(t_1)}. \quad (4.22)$$

The review paper [51] along with the references [54, 53, 55] discuss how to find the gauge transformation $e^{i\hat{F}}$ and corresponding effective Hamiltonian and its uniqueness. The reference [52] derives it from the stroboscopic evolution and stroboscopic Hamiltonian. It is important to emphasize that approach of effective Hamiltonian is more generic since it does not depend on the phase of the drive or initial time. There exist a class of stroboscopic Hamiltonians connected through the transformation ??, but there is only one effective Hamiltonian related to this class.

4.4 Extended Hilbert space

Another prospective on Floquet formalism which may provide more intuition on periodically driven system is based on idea that we can treat time just like other independent variables of the Hamiltonian. The time-dependent Schrodinger equation

$$(\hat{H}(t) - i\hbar\partial_t) |u_n(t)\rangle = \epsilon |u_n(t)\rangle \quad (4.23)$$

can be viewed as an eigenvalue problem in extended Hilbert space $\mathcal{F} = \mathcal{H} \otimes \mathcal{L}_T$

The hermitian operator $\hat{Q} = \hat{H}(t) - i\hbar\partial_t$ is called quasienergy operator. Its eigenstate are the Floquet modes and eigenvalues are the quasienergies

$$\hat{Q} |u_{nm}\rangle = \epsilon_{nm} |u_{nm}\rangle \quad (4.24)$$

Diagonalization of the quasienergy operator is another way of approaching the problem of finding the evolution of periodically driven system.

The description in terms of quasienergies and Floquet modes is crucial for studying the excitation of the systems or collisional properties. However, the direct methods of deducing the effective Hamiltonian and the micromotion operators can be more helpful for the purpose of Floquet engineering: the simulation of some effective

Hamiltonian with system's slow evolution. In the case of our scheme the effective Hamiltonian and the micromotion operators can be obtained by employing several methods. These methods, both perturbative and exact are discussed in the next chapter.

Chapter 5

Floquet Engineering of Recoil-dressed Photons

5.1 Magnetic shaking experiment

Our initial motivation was to demonstrate a laser-free spin-orbit coupling scheme. The scheme which would inherently avoid the problem of heating due to spontaneous emission. However, while working on this project we realized that the ideas we were developing are more general than just the context of spin-orbit coupling. The scheme we experimentally realized provides a transparent and insightful view on rapidly developing field of Floquet engineering and its application of creating artificial gauge-fields [24] for quantum gases.

A photon is an object which carries energy (frequency) and momentum. How do we know that? An atom, playing a role of a frequency filter, can absorb a photon at certain frequency and experience a recoil kick to conserve momentum brought with the photon. The frequency of the absorbed photon must be detuned from the level spacing frequency of the atom by the amount of Doppler shift and recoil shift.

$$\omega = \omega_0 + kv + \frac{\hbar k^2}{2m} \quad (5.1)$$

This condition is a direct consequence of the energy conservation during atom-

photon interaction. For a given photon the Doppler shift and the recoil energy are strictly determined by the conservation laws. For example, if we take RF (MHz) photon, it's intrinsic momentum is tiny and the associated Doppler and recoil shifts are negligible. Is there a loophole which we can use to tune the recoil and enforce Doppler shift even on RF photon? It turns out, yes. We should sacrifice with the conservation of energy. But how can we get rid of one of the most universal ubiquitous conventions which follows us through out our entire journey in physics? In fact, in a fairly easy way. One can say that conservation of energy comes from the invariance of time translation [47], from uniformity of time. If the invariance of translation of time is broken, the energy is no longer conserved, it is not an integral of the system anymore. It may sound trivial: if the Hamiltonian explicitly depends on time, then the energy is changing. But even for a Hamiltonian which periodically depends on time (when the energy averaged over period does not change, but the time translational symmetry is still reduced) the energy is not an integral of motion.

5.2 Our scheme

Our scheme has two ingredients: an oscillating magnetic force and the sequence of the RF pulses. The time sequence is shown on Fig.5-1. Atoms are driven by a sinusoidal spin-dependent force $f(t) = g_F \mu_B B'_0 \sin(2\pi/T \cdot t + \phi_{RF}) \hat{\sigma}_z$. The RF pulses are fired at times $0, T, 2T, \dots$. The relative phase between the oscillating force and the RF is defined by ϕ_{RF} . Each of the RF pulses couples spin-up and spin-down with the same instantaneous velocity. Both of the ingredients do not provide a momentum kick: the integral of the magnetic force of the period is zero, so there is no net momentum transfer, and momentum associated with the RF photon is negligible in comparison to any relevant atomic scale. However, the beauty of the Floquet engineering is that when these two ingredients are put together and properly synchronized, the result is going to be a an RF photon endowed with tunable momentum. Our experiment demonstrates not only the power of Floquet engineering, but also a lucid semiclassical interpretation of the physics of a periodically driven atom.

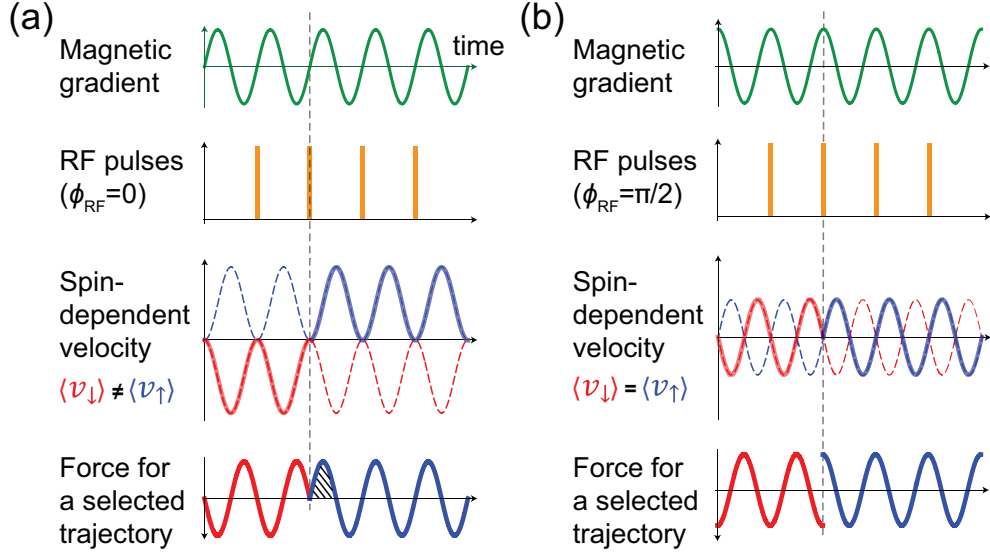


Figure 5-1: Illustration of our scheme for creating a tunable atomic recoil momentum with RF transitions using magnetic forces. (a) & (b) shows the experimental conditions for $\phi_{RF} = 0$ and $\phi_{RF} = \pi/2$, respectively. The spin-dependent forces and velocities are shown (as thick solid lines) for the amplitude of the wavefunction which is transferred from spin down (red) to up (blue) by the RF pulse marked by the gray dashed line. For $\phi_{RF} = 0$, the average velocities $\langle v_{\downarrow} \rangle$ and $\langle v_{\uparrow} \rangle$ are different, which implies a finite recoil associated with the spin-flip. In contrast, $\langle v_{\downarrow} \rangle = \langle v_{\uparrow} \rangle$ for $\phi_{RF} = \pi/2$ and there is no recoil.

Each of the RF pulses couples spin-up and spin-down with the same instantaneous velocity, so atoms while being spin-flipped do not change their velocity. However, they make a "jump" from one velocity trajectory to another, and the average velocity for these trajectory can be different. It is like passengers in metro: on the station, when they change the trains their velocities along the track are not changing. The spin flip happens when a passenger walks out of the doors of one train, goes across the platform and sits into the train which will move in the opposite direction. The instantaneous velocities of the trains were the same, otherwise the passenger would not be able get from one train to another. But after this connection the second train will have different average velocity than the first one.

The velocity trajectories for two cases ($\phi_{RF} = 0$ and $\phi_{RF} = \pi/2$) are shown on the Fig. 5-1. The moment $t = 0$ happens at the first RF pulse, and the synchronization phase ϕ_{RF} determines how we are going to drive atoms with the oscillating force.

One can easily see that ϕ_{RF} determines the difference between the average velocities for spin-up and spin-down. For ϕ_{RF} the difference $\langle v_{\uparrow} \rangle - \langle v_{\downarrow} \rangle$ is maximal, whereas for $\phi_{RF} = \pi/2$ it is zero. So, if we imagine a spin-flip, for the case on the Fig.5-1.(a) from the atoms point of view they have experienced two positive half-periods of a spin-dependent force back to back. For the case depicted on the Fig.5-1.(b) the spin-dependent force is discontinuous, but still does not provide extra kick. So, we can conclude that depending on the phase of the drive the spin-dependent force may provide a momentum transfer in terms of the average values.

So, even if we have a single π -pulse, the atoms will experience a recoil and will be transferred in a state with different average velocity. However, our goal is not only to simulate recoil, but also a Doppler shift to exactly replicate the properties of atom-photon interaction in time-independent systems. With a single RF pulse the frequency of RF is not any different from the case when the shaking is off. To observe the effects we intend to simulate having only one RF pulse is not enough. The "magic" of Floquet engineering will work only if the Hamiltonian is truly periodic in time, and a single-pulse example would break the discrete time translation symmetry. Only when the RF-pulses happen every period one can apply the Floquet formalism and describe the dynamics of the system with the effective Hamiltonian.

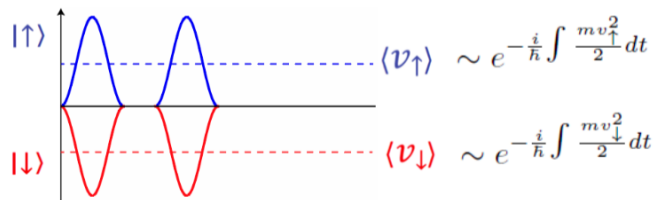


Figure 5-2: Phase accumulation between the spins due to magnetic shaking. On the figure the average velocity for spin up is larger than the average velocity for spin-down. Difference in average kinetic energies during a period of shaking results in phase accumulation between the spins.

A period of magnetic shaking results in relative phase accumulation between spin-up and spin-down. The spin-up and spin down atoms which start from the same velocity after a period of shaking return back to the same velocity since the integral of the force is zero over the period. However, the spin-up and spin-down

had different histories of their motion during that period of time. If the spin-up was first accelerated and then decelerated back to its original velocity, the spin-down was first decelerated and then accelerated. Therefore, the average kinetic energy for spin-up was higher than for spin-down. Quantum mechanically it means that a relative phase being accumulated during a period of motion. This phase can be calculated semiclassically as the integral of the difference of kinetic energies $\alpha = 1/\hbar \int_0^T (E_{\uparrow}^{kin}(t) - E_{\downarrow}^{kin}(t)) dt$. Here we choose integration limits as 0 and T , assuming that the timing of the RF pulses sets the zero of time, and the synchronization of the shaking force with respect to the RF is defined through the phase ϕ_{RF} . The accumulated relative phase between spin-up and down depends on the synchronization phase as $\delta\alpha = \frac{1}{\hbar}(m(\langle v_{\uparrow} \rangle - \langle v_{\downarrow} \rangle)v_{RF})T = k_0 \cos \phi_{RF} v_{RF} T$, where $k_0 = (g_F \mu_B / \pi \hbar) B_0' T$ and v_{RF} is the common velocity for spin-up and spin-down at $t = 0, T, 2T, \dots$. It's already here in the semiclassical treatment one can see that if we enforce RF detuning to be equal to the rate of phase accumulation $\delta = \delta\alpha/T$ then the expression for it will look like Doppler shift $\delta = k v_{RF}$. If the common velocity v_{RF} is rewritten as $v_{RF} = \langle v_{\downarrow} \rangle + \hbar k / 2m$ then we recover the Doppler relation we have seen in atom-photon interaction

$$\delta = k \langle v_{\downarrow} \rangle + \hbar k^2 / 2m \quad (5.2)$$

The RF detuning compensates the Doppler shift and recoil shifts in the time-averaged picture. It is important to emphasize the role of the synchronization between the shaking and the RF pulses parametrized as ϕ_{RF} . The momentum transfer $k = k_0 \cos \phi_{RF}$ is determined by the strength of the drive and by timing of the RF pulses. For a given magnitude of the drive, the momentum transfer is maximized when the RF pulses are fired at the zeros of the force ($\phi_{RF} = 0$) and it is equal to zero when RF is fired at the points of maximum force ($\phi_{RF} = \pi/2$).

5.2.1 Bloch sphere representaiton

The semiclassical approach can be visualized on the Bloch sphere. A period of magnetic shaking does not change the spin populations and results only in the relative

phase accumulation $\frac{1}{\sqrt{2}}(|\downarrow\rangle + |\uparrow\rangle) \rightarrow \frac{1}{\sqrt{2}}(|\downarrow\rangle + e^{i\delta\alpha} |\uparrow\rangle)$, i.e. σ_z -rotation in the frame rotating at the frequency of the spin-splitting ω_0 (RF-resonant frequency). The RF pulses coupling the spins rotate the Bloch vector with $\hat{\sigma}_y$ around the instantaneous $\hat{y}(t)$ axis. In the current frame the \hat{y} -axis rotates with the rate of RF detuning δ around \hat{z} -axis. If the rate of precession of \hat{y} -axis delta compensate the phase accu-

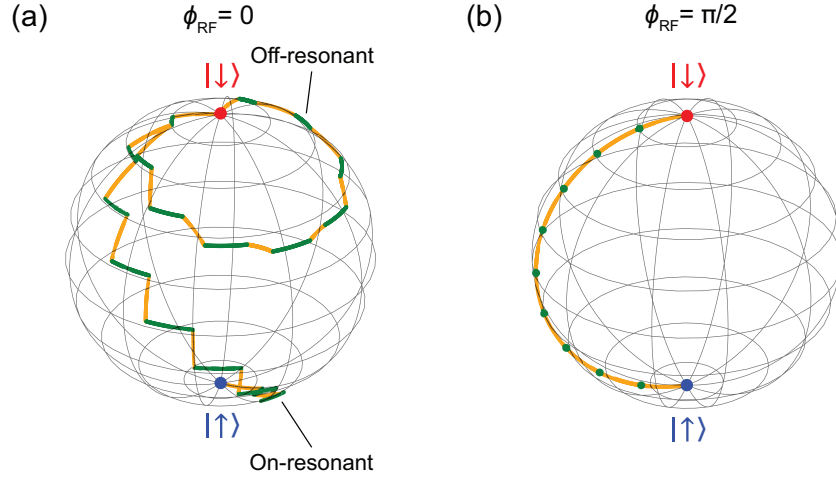


Figure 5-3: Bloch sphere representation of magnetic shaking and RF pulses. (a) & (b) Trajectories on the Bloch sphere for several periods of magnetic shaking (green solid lines representing α) and RF pulses for $\phi_{RF} = 0$ and $\phi_{RF} = \pi/2$, respectively. Fig. (a) shows the trajectories for atoms with a finite initial velocity when the RF frequency is at ω_0 , the atomic resonance, and when it is detuned by the Doppler and recoil shift. In (b), the RF frequency is at ω_0 , the trajectory is independent of the atomic velocity, and there is no net rotation around the z-axis during a magnetic shaking cycle. The red (blue) dot represents the initial (final) spin state.

mulation during the magnetic shaking, then the subsequent RF pulses will move the Bloch vector along the meridians, transferring population to the south pole in the most "efficient" way. Since the phase accumulation due during shaking depends on the velocity of the atoms, the spin flip is going to be efficient for some velocity group of atoms (when RF pulses add up constructively), and for some velocities the Bloch vector will come back to the north pole. This is the way we impose Doppler selectivity on RF photons. For a given RF detuning, the RF signal will match Doppler condition for some velocity group and these atoms will experience resonant Rabi oscillations.

When we fire RF pulses at the maxima of the periodic force, then the momentum transfer is 0. It means that in the frame rotating with ω_0 the shaking does not move

the Bloch vector. Then the RF pulses will add up constructively when the RF is resonant with the spin-splitting for all the velocity groups. The Doppler selectivity is completely lost in this case.

5.2.2 Floquet treatment

According to Floquet theory, the evolution of a system with time-periodic Hamiltonian can be factorized as

$$\hat{U}(t_f, t_i) = e^{-i\hat{K}(t_f)} e^{-i\hat{H}_{eff}(t_f-t_i)} e^{i\hat{K}(t_i)}, \quad (5.3)$$

where $K(t)$ is a micromotion operator, which describes the initial and final kick due to turn on and turn off, and \hat{H}_{eff} is time-independent effective Hamiltonian, which governs slow time evolution of the system averaged over fast micromotion with period T . A powerful formalism of Floquet theory provides us with methods to determine the H_{eff} and the micromotion operator K , and solve the evolution of the system.

The time-dependent Hamiltonian for our scheme in the frame rotating with the RF drive after the rotating-wave approximation is

$$\hat{H} = \frac{\hat{p}_z^2}{2m} + \hbar k_0 \hat{z} \frac{\pi}{T} \sin(2\pi t/T + \phi_{RF}) \hat{\sigma}_z - \frac{1}{2} \hbar \delta_{RF} \hat{\sigma}_z + \hbar \Omega \hat{\sigma}_x T \sum_n \delta(t - nT), \quad (5.4)$$

where δ_{RF} is the RF detuning with respect to the atomic resonant frequency. The short RF pulses are represented as a series of delta-functions with effective Rabi frequency Ω .

The choice of RF pulses to be short and approximated with the delta-functions is consistent with our experimental settings (a typical RF pulse duration is 4 μs , whereas the period T is usually set to be 100 or 200 μs) and the reason of this choice will be discussed later.

We now rederive the same effective Hamiltonian and micromotion operator using a rigorous high-frequency $1/\omega$ expansion. Appendix K of the reference [51] discusses

Hamiltonians of a general form

$$\hat{H}(t) = \hat{H}_0 + \hat{A}f(t) + \omega\hat{B}g(t) \quad (5.5)$$

and derives expansions for an effective Hamiltonian \hat{H}_{eff} and the kick operator \hat{K} .

$$\hat{H}_{eff} = \sum_{n=0}^{\infty} \frac{1}{\omega^n} \hat{H}_{eff}^{(n)}, \quad \hat{K}(t) = \sum_{n=0}^{\infty} \frac{1}{\omega^n} \hat{K}^{(n)}(t) \quad (5.6)$$

The Hamiltonian \hat{H} in equation 5.5 is of this form with

$$\hat{H}_0 = \frac{p^2}{2m} - \frac{1}{2}\delta_{RF} + \Omega\hat{\sigma}_x, \quad \hat{B} = \frac{1}{2}k_0z\hat{\sigma}_z, \quad \hat{A} = \Omega\sigma_x, \quad (5.7)$$

$$g(t) = \sin(\omega t + \phi_{RF}), \quad f(t) = T \sum_n \delta(t - nT) - 1 \quad (5.8)$$

Functions $f(t)$ and $g(t)$ meet the requirement of having zero mean value over a period T .

The kick operator is in 0-th order:

$$\hat{K}^{(0)} = \hat{B}G(t), \quad G(t) = \omega \int_0^t g(\tau)d\tau = -\cos(\omega t + \phi_{RF}) \quad (5.9)$$

The effective Hamiltonian to the lowest order in $1/\omega$ can be expanded as

$$\hat{H}_{eff} = \hat{H}_0 + \sum_{n=1} \frac{i^n}{n!} \overline{G^n f} [\underbrace{B \dots [B, A]}_n] + \sum_{n=1} \frac{i^n}{n!} \overline{G^n} [\underbrace{B \dots [B, H_0]}_n] + O(1/\omega) \quad (5.10)$$

After calculating all commutators and time-averaged coefficients before them, and grouping the terms proportional to $\hat{\sigma}_x$ and $\hat{\sigma}_y$, the expansion reduces to

$$\hat{H}_{eff} = \frac{\hat{p}_z^2}{2m} - \frac{1}{2}\delta_{RF}\hat{\sigma}_z + \Omega \cos(k_0z \cos \phi_{RF})\hat{\sigma}_x + \Omega \sin(k_0z \cos \phi_{RF})\hat{\sigma}_y + \frac{1}{16} \frac{k_0^2}{m} + O(1/\omega) \quad (5.11)$$

It can be rewritten in the matrix form as

$$\hat{H}_{eff} = \begin{pmatrix} \frac{\hat{p}_z^2}{2m} + \frac{1}{16} \frac{\hbar^2 k_0^2}{m} - \frac{\hbar \delta_{RF}}{2} & \hbar \Omega e^{-ik_0 \cos \phi_{RF} \cdot z} \\ \hbar \Omega e^{ik_0 \cos \phi_{RF} \cdot z} & \frac{\hat{p}_z^2}{2m} + \frac{1}{16} \frac{\hbar^2 k_0^2}{m} + \frac{\hbar \delta_{RF}}{2} \end{pmatrix} \quad (5.12)$$

The corresponding micromotion operator is

$$\hat{K}(t) = -ik_0 z \hat{\sigma}_z \cos\left(\frac{2\pi}{T}t + \phi_{RF}\right). \quad (5.13)$$

This effective Hamiltonian describes a two-level atom with energy spacing ω_0 driven by a photon field at frequency ω_{RF} with a wave-vector $k \cos \phi_{RF}$. The common term $\hbar^2 k_0^2/2m$ is associated with the kinetic energy of micromotion. The form of the effective Hamiltonian is a solid proof that our scheme simulates an RF photon with tunable recoil.

The effective Hamiltonian is one step away from the Spin-orbit Coupling Hamiltonian. If we apply an spatially-dependent unitary transformation

$$\hat{R}_{z1} = \exp(-izk_0 \cos \phi_{RF} \hat{\sigma}_z/2) \quad (5.14)$$

The transformed Hamiltonian becomes translationally invariant and acquires the standard form of H_{SOC} for one-dimensional spin-orbit coupling:

$$\hat{H}_{SOC} = \frac{1}{2m} (\hat{p}_z - \frac{1}{2} k_0 \cos \phi_{RF} \hat{\sigma}_z)^2 + \Omega \hat{\sigma}_x - \frac{\delta_{RF}}{2} \hat{\sigma}_z, \quad (5.15)$$

where the spin-orbit coupling strength is described by the momentum shift $k_0 \cos \phi_{RF}/2$.

With the new kick operator

$$\hat{K}_{SOC}(t) = -k_0 z \hat{\sigma}_z \left[\cos\left(\frac{2\pi}{T}t + \phi_{RF}\right) - \cos \phi_{RF} \right] \quad (5.16)$$

the time evolution can be written as

$$U(t_2, t_1) = e^{-i\hat{K}_{SOC}(t_2)} e^{-i\hat{H}_{SOC}(t_2-t_1)} e^{i\hat{K}_{SOC}(t_1)}. \quad (5.17)$$

In that case the operator $\hat{K}_{SOC}(t)$ has a non-zero temporal average, so it cannot

be treated as a pure micromotion operator. Similarly \hat{H}_{SOC} can not be considered as an effective Hamiltonian for the time-periodic Hamiltonian (5.4). It is rather a Hamiltonian related to the true effective Hamiltonian by the unitary transformation: $\hat{H}_{SOC} = \hat{R}_{z1}^\dagger \hat{H}_{eff} \hat{R}_{z1}$. Note that reference [56] has obtained \hat{H}_{SOC} as a stroboscopic Floquet Hamiltonian.

5.2.3 Evolution of the system

In the previous section we solved the evolution of the system by summing infinite number of terms in the expansion given us by Floquet theory. The reference [51] proves that the result of this summation is the effective Hamiltonian which is unique with respect to time transformations. The perturbative methods are typical for the treatment of periodically driven systems. However, our example is very special because it is exactly solvable. We can find the evolution of the system and deduce the effective Hamiltonian from it by regrouping time-depend terms in the evolution operator.

We start with the same Hamiltonian describing our system 5.5. The reason why we can't integrate it to find the evolution operator is that it has both momentum and position-dependent terms, so the Hamiltonian does not commute with itself at different times $[\hat{H}(t), \hat{H}(t')] \neq 0$. However, it is not hard to find a position-dependent spin rotation $\hat{R}_z(t)$ such that in the new frame $|\psi(\tilde{t})\rangle = \hat{R}_z^\dagger(t) |\psi(t)\rangle$ the transformed Hamiltonian $\hat{\tilde{H}}(t)$ will still be time-dependent, but without non-commuting terms: $[\hat{\tilde{H}}(t), \hat{\tilde{H}}(t')] = 0$.

Let's applying a position-dependent spin rotation

$$\hat{R}_z(t) = \exp[-ik_0 z \gamma(t) \hat{\sigma}_z / 2] \quad (5.18)$$

where the rotation angle γ is

$$\gamma(t) = \omega \int_0^t \sin\left(\frac{2\pi}{T}t' + \phi_{RF}\right) dt' - C = -\cos\left(\frac{2\pi}{T}t + \phi_{RF}\right) \quad (5.19)$$

The integration constant C entering $\gamma(t)$ has been taken to be $C = \cos \phi_{RF}$, so that $\gamma(t)$ averages to zero over a period. The reason for this choice will be discussed later on.

At the RF pulses where $t = nT$ the transformation $\hat{R}_z(nT) = \exp[ik_0z \cos \phi_{RF} \hat{\sigma}_z/2]$ describes a spin rotation by an angle $k_0z \cos \phi_{RF}$ around the z axis. As a result, the transformed Hamiltonian $\hat{H}(t) = \hat{R}_z^\dagger(t) \hat{H} \hat{R}_z(t) - i\hat{R}_z^\dagger(t) \partial_t \hat{R}_z(t)$ takes the form

$$\hat{H}(t) = \frac{1}{2m} \left(\hat{p}_z - \frac{1}{2} k_0 \gamma(t) \hat{\sigma}_z \right)^2 - \frac{1}{2} \delta_{RF} \hat{\sigma}_z + \Omega [\cos(k_0z \cos \phi_{RF}) \hat{\sigma}_x + \sin(k_0z \cos \phi_{RF}) \hat{\sigma}_y] T \sum_n \delta(t - nT) \quad (5.20)$$

Note that unlike the spin-dependent potential gradient featured in the original Hamiltonian (5.5), the oscillating momentum shift term $k_0\gamma(t) \hat{\sigma}_z/2$ is no longer proportional to the driving frequency and hence can be considered as a small perturbation in the limit of high frequency driving where $k_0\gamma(t) \ll \omega$ and also $\Omega \ll \omega$. In that case it is appropriate to describe the evolution of the system in terms of the zero-order effective Hamiltonian obtained by time averaging of $\hat{H}(t)$ over a single driving period, i.e. by the zero frequency component of the Hamiltonian $\hat{H}(t)$, giving

$$\hat{H}_{eff} = \frac{\hat{p}_z^2}{2m} - \frac{1}{2} \delta_{RF} \hat{\sigma}_z + \Omega \cos(k_0z \cos \phi_{RF}) \hat{\sigma}_x + \Omega \sin(k_0z \cos \phi_{RF}) \hat{\sigma}_y + \frac{1}{16} \frac{k_0^2}{m}, \quad (5.21)$$

where the momentum shift has averaged to zero. The obtained effective Hamiltonian \hat{H}_{eff} is in exact agreement with 5.12.

The full dynamics includes also the micromotion. In the present situation there are two origins of the micromotion. The first kind comes from the time-dependence of the transformed Hamiltonian $\hat{H}(t)$. However, in the limit of the large driving frequency this kind of micromotion is negligibly small compared to the second type of micromotion emerging due to the time-dependence of the unitary transformation $\hat{R}_z(t)$. In fact, returning to the original representation $|\psi(t)\rangle = \hat{R}_z(t) |\tilde{\psi}(t)\rangle$, one arrives at the following time-evolution of the state-vector from the initial to the final

time

$$|\psi(t_2)\rangle = \hat{U}(t_2, t_1) |\psi(t_1)\rangle, \quad \text{where} \quad \hat{U}(t_2, t_1) = \hat{R}_z(t_2) e^{-i\hat{H}_{eff}(t_2-t_1)} \hat{R}_z^\dagger(t_1), \quad (5.22)$$

where the unitary transformation $\hat{R}_z(t)$ represents a micro-motion operator.

The time evolution operator can be rewritten as

$$\hat{U}(t_2, t_1) = e^{-i\hat{K}(t_2)} e^{-i\hat{H}_{eff}(t_2-t_1)} e^{i\hat{K}(t_1)}, \quad (5.23)$$

where

$$\hat{K}(t) = -k_0 z \hat{\sigma}_z \cos\left(\frac{2\pi}{T}t + \phi_{RF}\right) \quad (5.24)$$

is a Hermitian micromotion (kick) operator. The choice of the integration constant $C = \cos \phi_{RF}$ in the unitary transformation (5.19) ensures that the micromotion operator $\hat{K}(t)$ averages to zero over the driving period. Thus, the effective Hamiltonian and the micromotion operators are defined in a unique way through the condition $C = \cos \phi_{RF}$.

5.2.4 Canonical vs mechanical momenta

In the presence of the vector potential two important variables are distinguished: canonical momentum and mechanical momentum. Canonical momentum is conjugate to the coordinate, mechanical momentum is quantity needed to evaluate kinetic energy in the system. Our scheme provides a lucid interpretation of what the difference between canonical and mechanical momenta is. The spin-orbit coupling Hamiltonian $\hat{H}_{SOC} = \frac{1}{2m}(\hat{p}_z - \frac{1}{2}A\hat{\sigma}_z)^2 + \hbar\Omega\hat{\sigma}_x - \frac{\hbar\delta_{RF}}{2}\hat{\sigma}_z$ is an example of spin-dependent gauge field. Spin-dependent vector potential $\frac{1}{2}A\hat{\sigma}_z$ shifts the mechanical momentum for spin-up and spin-down from the canonical momentum.

In our scheme the canonical momentum is the instantaneous momentum at the moment of RF pulse $p_z = mv_{RF}$, which is the same for spin-up and spin-down. The mechanical momenta for spin-up and spin-down is the average momenta $p_{\uparrow(\downarrow)}^{kin} = m\langle v_{\uparrow(\downarrow)} \rangle$. The mechanical momenta for spin-up and spin-down $p_z \pm \frac{1}{2}A$ are shifted by

the vector potential $A = k_0 \cos \phi_{RF}$, i.e. momentum transfer which depends on the relative phase between the RF pulses and the magnitude of shaking force.

The difference between canonical and mechanical momenta can be seen on the dispersion relation (Fig.5-4). Using canonical momentum as the coordinate of horizontal axis, all couplings and transitions between the two spin states are vertical. The dashed lines illustrate the transitions observed in our experiment. Away from the spin gap the energy separation is dominated by Doppler and recoil shifts.

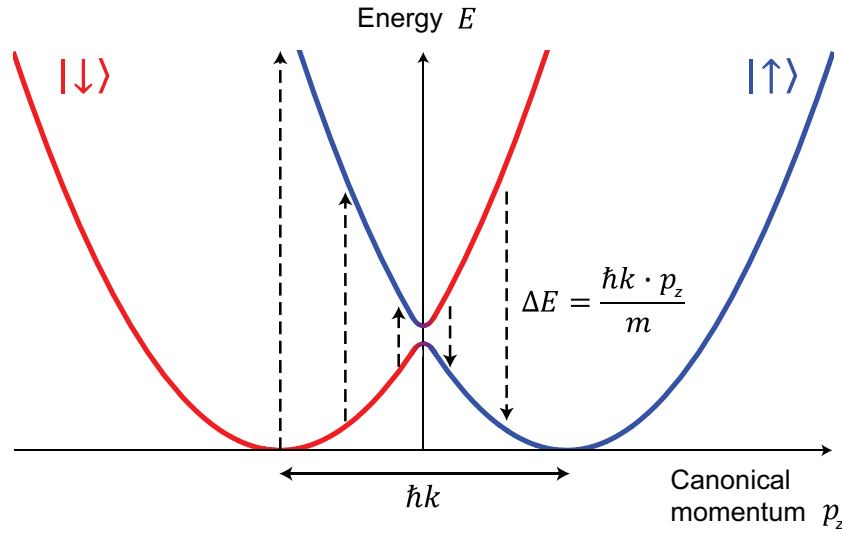


Figure 5-4: Energy-momentum dispersion relations for spin-orbit coupled spin 1/2 states. The two minima are separated by the recoil momentum $\hbar k$. The vertical dashed arrows show spinflip transitions. Their lengths are given by the Doppler and recoil shifts.

5.3 Experimental realization

Experimentally what we wanted to do is to demonstrate that the RF transition can be made velocity-selective. In a thermal cloud different velocity groups of atoms acquire velocity-dependent phase due to magnetic shaking. This accumulated phase can be addressed by the RF detuning $\delta = kv$. One can also view this effect in the following way. The sequence of the RF pulses results in a Ramsey fringe in Fourier space. The thermal cloud velocity distribution can be mapped out through the $\delta = kv$ relation. We convolute the Ramsey fringe with the velocity distribution, the major peaks of

the fringe cut a slice out of the thermal cloud (Fig.5-5). By changing the detuning of the RF signal we move the Ramsey fringe across the velocity distribution, resonantly exciting different velocity groups of atoms. In TOF, after the cloud is released from the trap, we should see how the slice of the atoms in the excited states moves as a function of the RF detuning. The stronger we can shake the atoms, the higher momentum transfer k is, which means the wider thermal cloud distribution looks in the frequency space. Thus, we can cut more slices with a given Ramsey fringe from the thermal cloud velocity distribution, if we shake stronger. Alternative way of improving resolution is to shake slower (since $k_0 \sim B'/\omega$), but then we soon hit the constraint of limited coherence time. We do not want to have the sequence of the RF pulses to be much longer than 1 ms, and if the shaking frequency ω is too small we would not be able to fit many periods of shaking into this time duration.

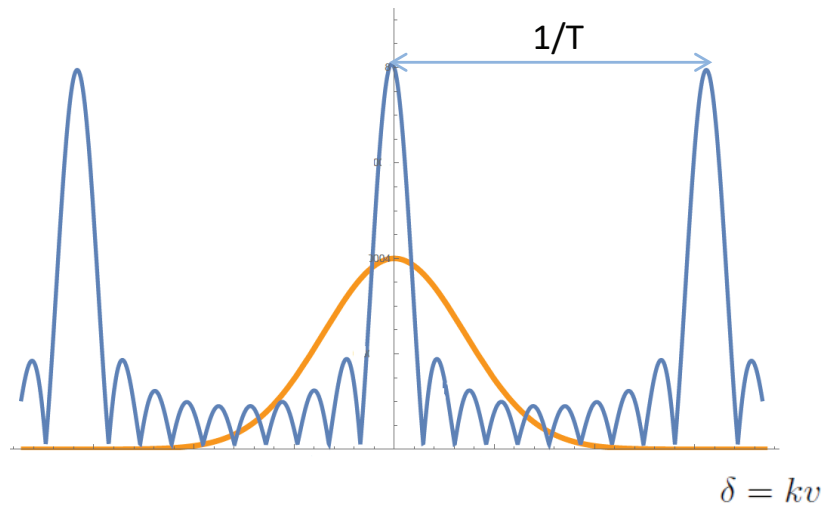


Figure 5-5: Ramsey fringe of the sequence of the RF pulses - blue, thermal cloud distribution mapped through the enforced Doppler relation $\delta = kv$ - yellow. By changing the detuning of the RF we make the Ramsey fringe move through the velocity distribution.

We prepared a thermal cloud of approximately 10^5 ^{23}Na atoms at the temperature 380 nK - close to the onset of condensation. If the atoms were prepared at higher temperature it would, of course, allow us to cut more of the velocity slices out of the cloud, but at the same time it would reduce the signal-to-noise ratio. So, for

the purpose of cleaner detection we preferred to prepare atoms right above the Bose-condensation.

Atoms were loaded into a shallow optical dipole trap with trapping frequencies $(\omega_x, \omega_y, \omega_z) = 2\pi(98, 94, 25)$ Hz, corresponding to Gaussian radii of 19.5, 20 and 68 μm , respectively. The trap was made shallow in the shaking direction \hat{z} because it was important to separate the time scales of the dynamics in the trap and the experimental sequence. In the trap the momentum distribution is converted to spatial distribution every quarter period. For us it was important to address only momentum information and prevent any coordinate-dependent phase accumulation. So, the duration of the sequence of the Floquet engineering (1-2 ms) was deliberately made much shorter than the trap period 40 ms.

As pseudospin-1/2 system we used $|m_F = -1\rangle$ and $|m_F = 0\rangle$ of the $F = 1$ hyperfine manifold of the atoms. The state $|\downarrow\rangle = |m_F = 0\rangle$ is magnetically insensitive, it does not see any oscillating force. So, when atoms were prepared in $|\downarrow\rangle$ they were not affected by any transient magnetic effect such as "pre-shaking", when it takes a few periods for the ac-current generating circuit to stabilize. In the experiment we did not have two states moving out of phase with respect to each other as it was described in the theory part. Instead we had a $|\downarrow\rangle$ state standing still, and $|\uparrow\rangle$ state shaken around it. So, the maximum momentum transfer $\hbar k_0$ was reduced by a factor of 2 compared to example discussed above. The third hyperfine state of the $F = 1$ manifold $|m_F = +1\rangle$ was decoupled from the two-level system via quadratic Zeeman effect.

The oscillating magnetic force was created by a time-dependent 3D quadrupole field $B'(t)(z\hat{z} + y\hat{y} - 2x\hat{x})$. The direction of the effective 1D force was determined by the bias field B_0 along \hat{z} . Orthogonal to the bias field, the periodic potential is quadratic, which only creates a small modulation to the confinement:

$$U = \mu_B \sqrt{(B_0 + B'(t)z)^2 + (B'(t)y)^2 + (4B'(t)x)^2} \approx \mu_B (B_0 + B'(t)z + \frac{B'^2(t)}{2B_0}(x^2 + 4y^2)) \quad (5.25)$$

In the presented results the amplitude of the magnetic field was 48 G/cm at a frequency of 5 kHz, which led to the momentum transfer $k_0 = 0.07k_L$, where $\hbar k_L$ is the recoil of the $\lambda = 589$ nm Na transition with the recoil velocity $\hbar k_L/m = 2.9$ cm/s.

We pulsed a sequence of 9 RF pulses at 8 MHz. The duration of the single pulse was $4 \mu\text{s}$. The Rabi frequency of the RF signal in CW regime was 10 kHz. The effective Rabi frequency with the duty cycle (4μ out of $200 \mu\text{s}$) was $\Omega = 200$ Hz. Each single $4\mu\text{s}$ pulse resulted in approximately $\pi/12$ rotation on a Bloch sphere.

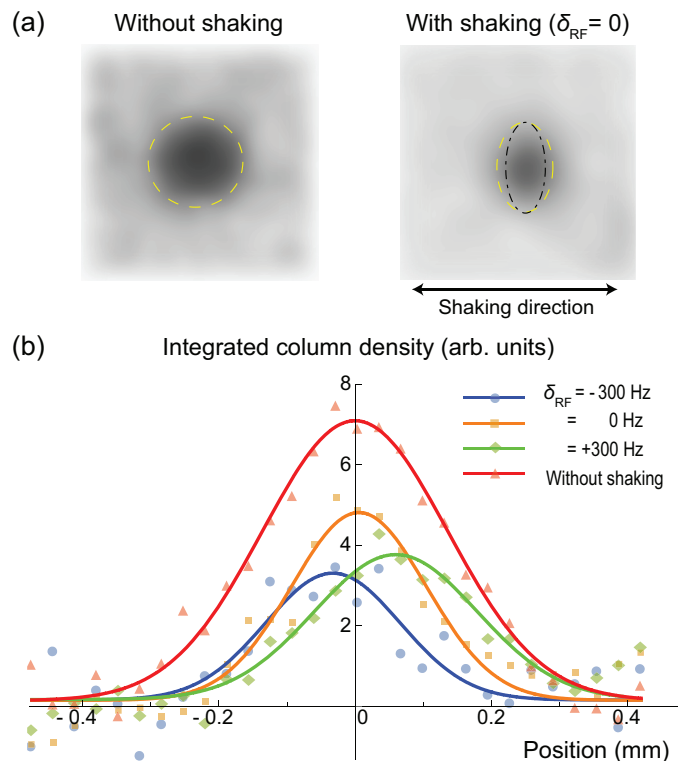


Figure 5-6: (a) images of the atoms in the excited state after being spin-flipped by the sequence of the RF pulses. Without shaking the cloud is isotropic (a feature of thermal cloud expansion). With shaking the cloud is narrowed, because the atoms were chosen to be excited based on their velocities. The yellow line dashed ellipses have their major and minor axes according to FWHM of a Gaussian fit. The dashed-dotted line corresponds to a Gaussian fit with the effect of the induced currents taken into account. (b). Integrated column densities for different detunings of RF pulses fired at the positive slope of the magnetic force ($\phi_{RF} = 0$). The asymmetry between the ± 300 Hz profiles most likely comes from the field drifts estimated to be ~ 70 Hz or small residual magnetic field gradients.

The Doppler width of the thermal cloud due to the momentum transfer $k = 0.07k_L$ was 3 kHz (FWHM), whereas the Fourier width of the central feature in the Ramsey

fringe was 625 Hz (given the total duration of the pulse sequence 1.6 ms). Thus, according to our estimation we could resolve 5 velocity slices out of the thermal cloud velocity distribution.

In the cold atoms experiments the standard way to probe momentum distribution of the atomic sample is long TOF expansion. In the limit of long expansion time the spatial information is lost and only momentum distribution is revealed. However, since we worked with the thermal cloud we could not really afford using long TOF, because of the quality of the images being deteriorated. The presented data were taken at $\tau = 12$ ms TOF (only twice the inverse of ω_z).

For such relatively short TOF the size of the cloud is mainly determined by the original spatial size. So, instead of seeing a sharp slice we could only see the partial narrowing of the width of the spin-flipped atoms Fig.5-6.(a).

However, even for short TOF the displacement of the center of the spin-flipped atoms is still exactly $v\tau$. So as long as we could do a reliable fit into the image of spin flipped atoms and resolve $v\tau$ displacement for different velocity groups Fig.5-6.(b) we could still claim that we enforced Doppler sensitivity of RF.

The dependence of the RF detuning on the center-velocity of the slice is shown on the Fig.5-7. The slope of the line gave the momentum transfer which was in a good agreement with the predicted $k = 0.07k_L$. The dependence of the momentum on the synchronization of the RF pulses with the oscillating force was checked for ϕ_{RF} , i.e. when the RF pulses were fired at the negative slope of the magnetic force. Effectively it flipped the sign of the momentum transfer $k = -0.07k_L$ and the corresponding dependance of the RF detuning on the velocity of the atoms is on the Fig.5-7(b). It was impossible to explore phases ϕ_{RF} besides 0 and π due to technical reasons discussed further in the section.

5.3.1 High current

In order to dress RF photon with momentum comparable to the recoil from optical photon we had to generate relatively high currents at audio frequencies (5-10 kHz). The benchmark was 100A at the frequency of 10 kHz. It was clear that if we can reach

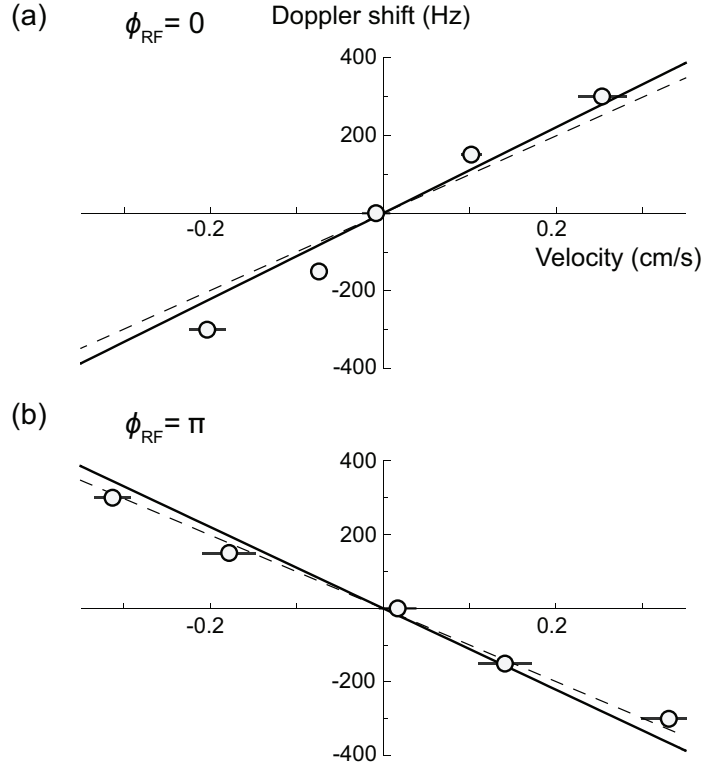


Figure 5-7: Doppler shift mapped for different velocity groups. (a) RF detuning as a function of the target resonant center-velocity of the atoms for the case of RF fired at positive slope $\phi_{RF} = 0$. (b) The same for negative slope $\phi_{RF} = \pi$. The solid lines represent the predicted Doppler shifts based on the calibration of recoil momentum. The dashed line takes into account the model of induced currents. The error bars are purely statistical and correspond to 1σ . The inferred field fluctuation from 1σ is 70 Hz

it, then we can simulate recoil on the order of $0.1k_L$. The main challenge we faced was that at audio frequencies the impedance of the coils turned out to be much higher than for dc current, 1 Ohm in contrast to 0.06 Ohm. Such dramatic increase of the impedance came from eddy currents induced in the stainless still vacuum chamber. It turned out that we had to work in the regime which was quite different from the typical settings of atomic physics experiment. We usually use high current low voltage power supplies in the lab to create strong gradients and bias fields. To generate high current at audio frequency we had use high-current high voltage source. We had to efficiently use output power, i.e. ideally to make power supply to be both current and voltage limited. Also in order to produce ac current from dc power supply we had to

build our own H-bridge, which can tolerate high power and work as a fast switch.

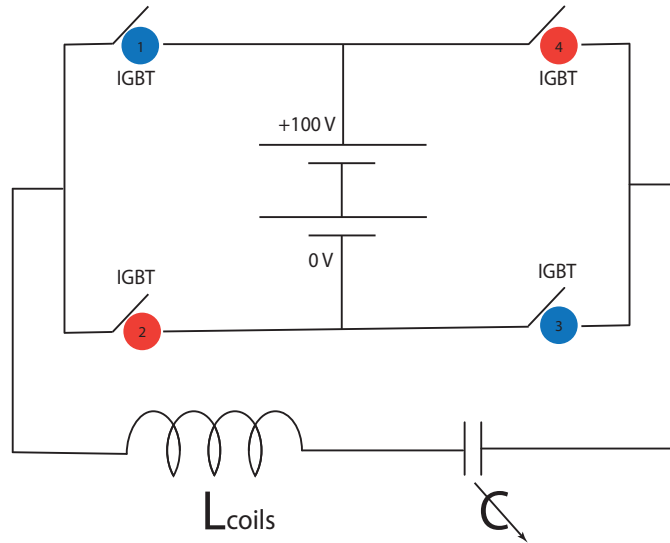


Figure 5-8: Scheme of the coils circuit. Two DC power supplies connected in series and placed in the "bar" of the H-bridge. IGBTs are triggered in pairs: 1 and 3, 2 and 4. Triggering of the pairs is out of phase. When pair 1-3 is on, pair 2 and 4 is off. The resonant frequency of the circuit is controlled by the capacitor C . The IGBTs are triggered at twice the frequency of the circuit thus realizing parametric pumping.

As power supplies we used model RST-5000-48 from Mean Well. Two power supplies were connected in series to produce the voltage of 100V. For the H-bridge we used four IGBT switches, which met both requirements: they switched fast and they stand high currents. IGBTs and power supplies were protected by varistors. To tune the resonance of the circuit we had to add the μF capacitors compatible with ac current (model ..). It is a pleasure to acknowledge that during extensive use of our homemade ac-current generator at the limit of its capacity it worked reliably and never failed.

5.3.2 Stability of magnetic field and gradient

Coherent manipulation of hyperfine-states requires substantial stability of magnetic field. Our first attempts to do the experiment convinced us that the control of magnetic fields in our apparatus was not sufficient. Initially we used audio amplifiers

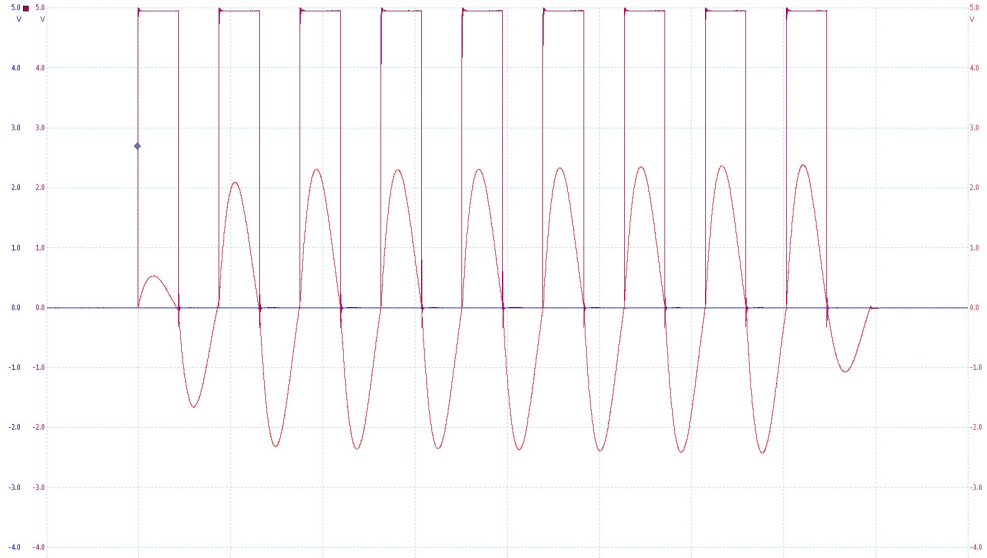


Figure 5-9: An example of a typical trace of Hall probe measuring the current generated by the H-bridge parametric triggering. Our benchmark is 120 A at 5 kHz (on the plot), 90 A at 10 kHz

model Behringer EP4000, which seemed to work in desirable for us regime. However, they appeared to be the major sources of the 60 Hz noise, which for the time scale of our experiment cannot be viewed only as a dc shift of magnetic field (the duration of the quantum simulation was 1-2 ms in comparison to 13 ms of the 60Hz noise period). The instabilities in operation of the audio amplifiers were hard to fix due to the absence of documentation and control of the non-scientific equipment. Even though the audio amplifiers proved to be not suitable for for generation of the accurate symmetric oscillating gradient, they still potentially can be used for implementing our scheme in the TOP-trap configuration. Instead of sending oscillating current through the anti-Helmholtz coil and creating dc bias field which polarizes the spin and defines the direction of the force one can, in principle, run dc current through the anti-Helmholtz pair and rotate the bias field by driving oscillating currents through two other perpendicular Helmholtz pairs with a $\pi/2$ phase shift. In this scheme there are less requirements on the symmetry of the ac-current since it only sets the instantaneous direction of the polarizing bias. The symmetry of the magnetic force will depend on the stability of the dc current through the anti-Helmholtz pair, which is much easier to accomplish than for the ac-current. For this application the audio-amplifiers may

be a good choice.

The observation of Doppler shifts at the 200 Hz level required careful control of Zeeman shifts. Three critical adjustments were done.

We had to protect our system from the potential causes of the false signal. Inhomogeneous Zeeman shift was one of our most dangerous enemies. We had to make sure the signal we observe comes from Doppler shift. In principle the phase acquired by atoms may be not only velocity dependent, but also position dependent. Unless we would go to infinite TOF these two mechanisms cannot be fully separated. Thus, we put a lot of effort in minimizing all the position-dependent effects in order to observe a pure Doppler signal.

Here're the precautions we took to eliminate the false Zeeman effect. The RF pulses can be safely fired only in the vicinity of the zero crossing of the time-dependent gradient, i.e. for the phases $\phi_{RF} = 0$ and $\phi_{RF} = \pi$. Since the clouds' size is finite a non-zero gradient across the cloud leads to inhomogeneous Zeeman effect, which is very undesirable for us. It may sound like this circumstance limits the tunability of scheme, that the momentum transfer in SOC cannot be changed continuously by changing the timing of the Rf pulses. However, this constraint is only technical. The shorter RF pulses, the broader their Fourier width, and if the Fourier broadening prevails over the inhomogeneous Zeeman shift the RF pulses can be fired not only at the zero crossings, but also at finite gradients. The duration of the RF pulse itself is limited only by the RF power (in the case of our experiment) and the switching electronics. We found that the optimal pulse duration in the experiment was $4\mu s$. It was short enough for the Fourier width to be broader than than the inhomogeneous Zeeman effect, and long enough to transfer substantial population of atoms in 9-10 pulses.

An important requirement on the field control is the symmetry of the gradient. The absence of it would hurt the velocity-dependent Doppler effect. If the magnetic gradient is asymmetric in time it averages over the period T as the dc-gradient $\langle B' \rangle_T$ which again leads to inhomogenous Zeeman effect.

Another side effect comes from the imperfection of the anti-Helmholtz coils. In

addition to the oscillating gradient, we at the same time excite small oscillating bias magnetic field. The bias field quickly sweeps through the resonance during the RF pulse and effectively shortens its duration. Also when the induced bias is not perfectly symmetric in time, it again results in unwanted phases accumulation due to Zeeman effect.

The most peculiar and unexpected side effect came from the current induced in the surrounding stainless steel vacuum chamber. The eddy currents caused shaking of atoms at doubled frequency in the perpendicular direction with respect to the chosen axis, which tilted the velocity slice in TOF. This effect is going to be discussed further.

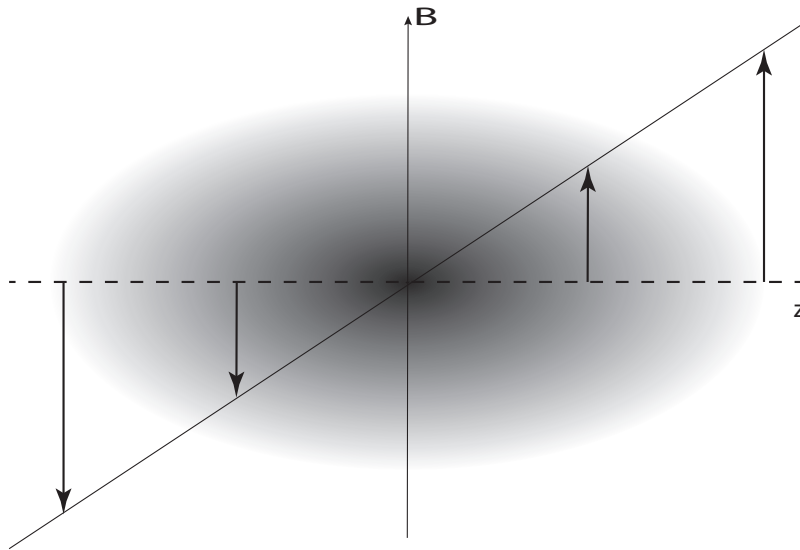


Figure 5-10: Atomic cloud is center with respect to the zero of the quadrupole. Due to the finite size of the cloud atoms displaced from the origin of the quadrupole experience oscillating bias magnetic field.

5.3.3 Symmetry of the modulated magnetic field gradient

If inhomogeneous Zeeman shifts across the cloud (Fig.5-10) are comparable or larger than Doppler shifts, the spinflips are no longer velocity selective since there is always a local Zeeman shift to compensate for the Doppler shift. Therefore, the magnetic field gradient averaged over one modulation cycle $\langle B' \rangle$, had to be zeroed: $g_F \mu_B \langle B' \rangle D \ll$

kv , where D is the length of the cloud. To avoid transient asymmetries from the turn-on process of the periodic magnetic gradient, we added a pre-shaking period of 3 ms before the spectroscopic sequence. This didn't affect the trapped atom cloud, since the atoms were initially in the non-magnetic $|m_F = 0\rangle$ state. After the pre-shaking, we achieve $\langle B' \rangle \approx 20$ mG/cm, implying a time-averaged differential Zeeman shift across the cloud of less than 100 Hz. $\langle B' \rangle$ was determined from converting the measurement of time-averaged current asymmetry to the time-averaged magnetic gradient asymmetry using the Stern-Gerlach calibration. As a final check, we added asymmetries (Fig.5-11) on either the positive or negative side of the sinusoidal current to create $\langle B' \rangle \approx \pm 100$ mG/cm, and for both cases observed a slight increase in the width of the velocity-selected atom slice confirming that the residual asymmetry of the magnetic gradient modulation was negligibly small.

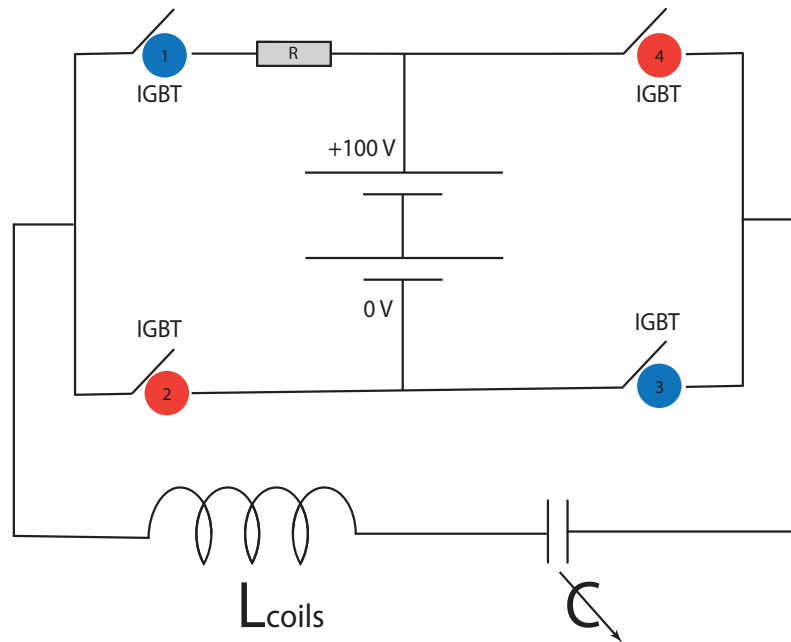


Figure 5-11: An H-bridge with built-in asymmetry. A resistor in one of the legs controlled the asymmetry of current at the per cent level.

The following two adjustments addressed the issue that the RF pulses were not delta functions, but had a duration of $4 \mu\text{s}$. The presence of Zeeman shifts comparable

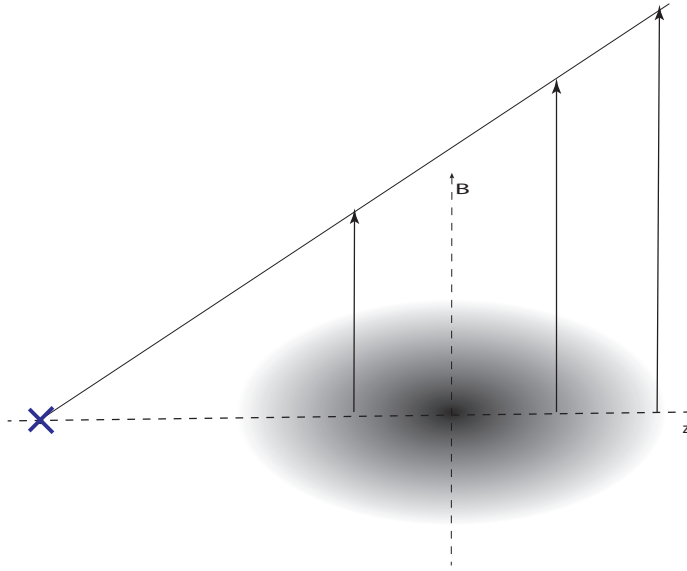


Figure 5-12: Atomic cloud displaced from the origin of the quadrupole. Magnetic fields experienced by the atoms sweeps through larger range of values and effectively shortens the duration of the RF pulses.

or larger than the Fourier width of a single pulse would reduce the RF pulse area. For our parameters, a 45 kHz detuning will reduce the pulse area by 5 percent (and therefore the single pulse excitation probability by 10 percent).

5.3.4 Minimize modulation of magnetic bias field

The time-dependent gradient creates also a time-dependent bias field given by the gradient times the displacement of the atoms from the origin of the magnetic quadrupole field. $60 \mu\text{m}$ away from the origin, the bias field changes by 30 mG during the $4 \mu\text{s}$ RF pulse. To minimize the reduction of the RF pulse area, the optical trap was aligned with the center of the quadrupole field to within $1 \mu\text{m}$ like on Fig.5-10 (a situation which we wanted to avoid is depicted on the Fig. 5-12). This was done by minimizing the shift in the RF resonant frequency when a stationary gradient field was added to the constant magnetic bias field. In addition, the eddy currents created a time-dependent bias field, which was compensated by RF detuning. The detuning and the timing of the RF pulses (described below) were adjusted together in order to

maximize the fraction of spin-flipped atoms.

5.3.5 Timing of the RF pulses with respect to the magnetic modulation

The goal was to pulse on the RF while the magnetic field gradient crosses zero. A $5 \mu\text{s}$ offset would imply a gradient of 7.5 G/cm and a differential magnetic field along the cloud of 50 mG . In the presence of strong gradients, the short RF pulse is resonant only for a small part of the cloud. Therefore, we could find the optimum condition by scanning both the timing and the detuning of the RF pulses until the measured total fraction of the spin-flipped atoms is maximized. The optimum time was offset by $2 \mu\text{s}$ from the zero-crossing of the current through the gradient coils, possibly due to eddy currents.

To summarize, we optimized three parameters, which are trap position, timing of the RF pulse, and RF detuning. The optimal position minimizes temporal variation of the bias field, optimal timing of RF minimizes B' during the pulse, and optimal detuning compensates for any bias field at the time of the pulse.

5.3.6 Induced shaking

One of the striking features of our experiment was that the narrowing of the atoms in the excited state of the TOF happened not in the direction we expected to see it. The slicing of the cloud happened not in the shaking direction \hat{z} which was defined by the bias field, but at the some angle to it (Fig.5-13).

It looked like the Doppler effect we simulated was

$$\delta = k_y v_y + k_z v_z$$

The tilt angle we first observed was $\theta = \arctan(k_y/k_z) \approx 60^\circ$ (Fig. 5-14). So, we had to find out what may cause Doppler selectivity in the \hat{y} direction with the magnitude of the effective momentum transfer comparable to one along \hat{z} .

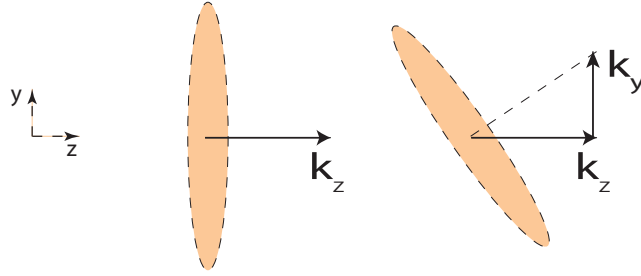


Figure 5-13: Slicing of the momentum distribution at an angle.

The first check we did was changing the RF phase to $\phi_{RF} = \pi$, i.e. fire the RF pulses at zero crossing on the negative slope of the magnetic drive. The change of the phase to π flips the sign of the momentum transfer. So, we had an expectation to simulate Doppler shift $\delta\omega = -k_y v_y - k_z v_z$. It would keep the orientation of the slice the same. However, to our surprise, in the experiment the orientation of the slice changed. After fitting the data we realized that k_z has changed to $-k_z$ as we expected, but k_y stayed the same, so the new tilt was $\theta = -60^\circ$. This peculiar observation led us to a possible model which provided qualitatively accurate explanation to the effect.

We inferred that in addition to the bias field B_0 we created along \hat{z} , the eddy currents in the stainless steel vacuum chamber induce oscillating bias field along \hat{y} . This magnetic field from the eddy currents should oscillate at the same frequency ω as magnetic gradient we create (and as the current we drive through the coils), and may have some phase shift ϕ with respect to it $\vec{B}_{ec}(t) = B_{ec} \sin(\omega t + \phi) \hat{y}$.

This assumption has the following intuition behind it. In order to produce shaking in the \hat{y} -direction there must a component of oscillating force in the same direction. While the magnitude of the force is determined by the amplitude of the oscillating gradient, the direction of the force comes from the polarization of the spin, i.e. from the instantaneous direction of bias magnetic field (Fig.5-15). If the bias field has only dc component along \hat{y} it causes some polarization of the spin along \hat{y} and therefore a component of the force oscillating at the same frequency ω as the gradient. That

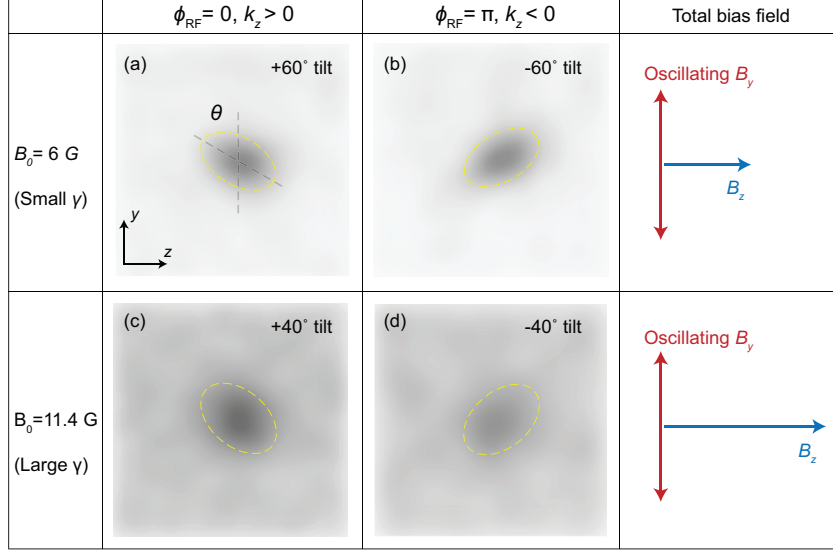


Figure 5-14: Effect of eddy currents on observed velocity-selected atom slices. The induced bias field along \mathbf{e}_y led to a y -component of the oscillating force, resulting in velocity selectivity in \mathbf{e}_y and therefore tilting of the resonant velocity slice in the $y-z$ plane. The tilt angle depends on the static bias field B_0 and the RF phase ϕ_{RF} . The dashed lines are guides to the eye.

would explain a tilt of the slice we cut in TOF, but would not agree with the observation that for the pulses at the negative slope the tilt changes from θ to $-\theta$. If we imagine that there is an oscillating bias field at frequency ω along \hat{y} , the polarization of the spin, its projection on \hat{y} , will also oscillate at ω . The force along \hat{y} , which is proportional to the product of the spin-projection (oscillating at ω) and the gradient (oscillating at ω) will rectify and have a component oscillating at 2ω . Well, so now we have atoms being shaken at ω along \hat{z} and 2ω along \hat{y} . The RF pulses are fired every $T = 2\pi/\omega$, i.e. every period for the \hat{z} force and every other period for y -force. When we change the phase of the the RF to π and fire it on the negative slope for z -force, with respect to the y -force the phase does not change. In turns out that k_y does not change whereas k_z changed to $-k_z$. Thus, shaking at double frequency caused by the bias oscillating at the single frequency may explain the observed reflection of the slice with respect to \hat{y} .

Here's a more quantitative analysis of the model. The total magnetic field expe-

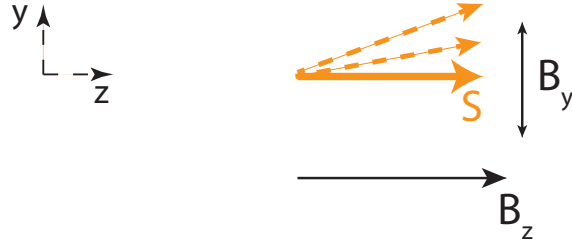


Figure 5-15: Due to the induced bias field along \hat{y} oscillating at the drive frequency ω the polarized spin is steered along the instantaneous direction of the total bias field, i.e. $B_0\hat{z} + B_{ef}(t)\hat{y}$

rienced by the atoms comes from the two bias components and the gradient:

$$\vec{B} = [B_0 + B'_0 \sin(\omega t)z] \hat{z} + [B_{ec} \sin(\omega t + \phi) + B'_0 \sin(\omega t)y] \hat{y} - 2B'_0 \sin(\omega t)x \hat{x}, \quad (5.26)$$

with a magnetic field strength

$$\begin{aligned} |\vec{B}| &= \sqrt{[B_0 + B'_0 \sin(\omega t)z]^2 + [B_{ec} \sin(\omega t + \phi) + B'_0 \sin(\omega t)y]^2 + [2B'_0 \sin(\omega t)x]^2} \\ &\approx B_0 \sqrt{1 + \gamma^2 \sin^2(\omega t + \phi)} + \frac{B'_0 z + \gamma \sin(\omega t + \phi) B'_0 y}{\sqrt{1 + \gamma^2 \sin^2(\omega t + \phi)}} \sin(\omega t) \end{aligned} \quad (5.27)$$

here $\gamma = B_{ec}/B_0$. The first term corresponds to a time varying homogeneous bias field resulting in a *velocity-independent* effective detuning of the RF transition. The oscillating magnetic field gradients along the z and y directions are

$$\begin{aligned} \frac{\partial |\vec{B}|}{\partial z} &= \frac{B'_0}{\sqrt{1 + \gamma^2 \sin^2(\omega t + \phi)}} \sin(\omega t), \\ \frac{\partial |\vec{B}|}{\partial y} &= \frac{\gamma B'_0}{\sqrt{1 + \gamma^2 \sin^2(\omega t + \phi)}} \sin(\omega t) \sin(\omega t + \phi). \end{aligned} \quad (5.28)$$

The gradient in \hat{y} oscillates at 2ω , twice the frequency of the driving. The phase delay ϕ is determined by the magnetic properties of the vacuum chamber. We modeled the chamber as an LC circuit with a self inductance L_{Ch} and a resistance R_{Ch} , and obtain

$\phi = \arctan(\omega L_{\text{Ch}}/R_{\text{Ch}}) + \pi/2$. Our observations imply $R_{\text{Ch}} \gg \omega L$, $\phi \approx \pi/2$, resulting in an effective recoil component in the y direction with

$$\begin{aligned} k_{\text{so},y} &= \frac{1}{T} \int_0^T \left(\int_0^t \frac{\gamma B'_0}{\sqrt{1 + \gamma^2 \cos^2(\omega t')}} \sin(\omega t') \cos(\omega t') dt' \right) dt \\ &= \frac{1}{T} \int_0^T \left(\int_0^t \frac{\gamma B'_0}{2\sqrt{1 + \gamma^2 \cos^2(\omega t')}} \sin(2\omega t') dt' \right) dt. \end{aligned} \quad (5.29)$$

Consequentially, the Doppler shift is modified as

$$\delta = k_y v_y + k_z v_z, \quad (5.30)$$

directly observed as a rotation of the velocity slice with an angle $\theta = \arctan(k_y/k_z)$ in the time-of-flight images, as shown in Fig. .

A natural way to verify these assumption is to reduce the effect of the transverse shaking by stronger polarizing the spin along \hat{z} . We increased the bias field B_0 from 6 Gs to 11.4 Gs and saw how the angle θ of the rotation decreased with stronger static bias to $\theta \approx 40^\circ$. Due to the 2ω oscillating frequency of the y force, k_y did not change sign when the RF phase ϕ_{RF} was shifted from 0 to π in contrast to k_z , and therefore the rotation angle flipped from θ to $-\theta$, as suggested by and shown in Fig.5-14 .

The effects of the induced currents can be completely eliminated if the experiment is conducted in a glass cell. In our apparatus, which was design for optical lattices experiments, and has a stainless steel chamber we could only suppress the effects by ramping the bias field B_0 further up. However, using higher bias fields has its own incidental problems. First of all, using higher bias fields means that we need to change the frequency of the radio signal resonant with the level splitting of the hyperfine states. Higher frequency would lead to the loss of the efficiency of the antenna and therefore a decrease in Rabi frequency of the RF transition. Also, our bias coils were not water-cooled, so eventually we would also be limit by the power we dissipate in them at high currents.

What we have described so far applies to free space or to an isotropic trap.

However, the optical trap in the experiment is anisotropic. For zero time-of-flight, in the $y - z$ plane, the minor axis of the ellipsoidal cloud is oriented along y , $\theta = \pi/2$. For long time-of-flight, the angle is solely determined by the velocity selection $\theta = \arctan(k_y/k_z)$. For intermediate time-of-flight, as used in the experiment, the observed angle interpolates between these values. We calculate that the observed tilt angles of 60° and 40° correspond to tilt angles of the bias field $\arctan(k_y/k_z)$ of 53° and 32° , respectively.

5.4 Heating due to collisions between the spin states

One of the advantages of magnetically generated spin-orbit coupling is that it inherently does not suffer from spontaneous emission, since no lasers are used to produce it. Since the scheme we realized is laser-free, it is promising as an experimental tool and may potentially make the experiments realizing spin-dependent gauges easier to build and maintain.

However, instead of heating via spontaneous emission like in two-photon schemes, the use of periodic drive brings another heating mechanism: heating due to collisions. Micromotion of the different spin states can be transferred into secular motion and heat the sample. Our experiment was done with rather humble momentum transfer $k \sim 0.7k_L$, characterizing the strength of the drive. The lifetime of the two colliding condensates in $|F = 1, m = 0\rangle$ and $|F = 1, m = -1\rangle$ states was very long — about 8 s.

The follow-up theoretical study [57] describes heating due to collisions in the presence of periodic drive for various system. In this work it was shown that energy pumping into the system of two colliding species can be expressed as $\dot{E} \sim \rho v_{col} E_0$, where v_{col} reflects an effective density of states, ρ is the density and σ is two-body s -scattering cross section. For instance, in the case of colliding condensates $v_{col} = \sqrt{\hbar\omega/m}$ for large modulation frequencies ω . It was estimated that if the momentum transfer is scaled to the optical recoil k_0 , the collisional heating will increase significantly unless the density of atoms is reduced to $\sim 10^{12} \text{ cm}^{-3}$. Otherwise it will not be possible to

reach long lifetime of the order of 100 ms. For degenerate Fermi gas the expectations are more optimistic. Due to Pauli blocking in s -wave collisions for driving frequency below the Fermi energy $\hbar\omega < E_F$ the heating is suppressed by a factor of $(\hbar\omega/E_F)^2$.

Chapter 6

Conclusions and Outlook

Two methods of generating one-dimensional spin-orbit coupling were presented in this thesis. In the first approach, we used a two-photon Raman process as a source of momentum transfer and applied it to couple pseudo-spin states, defined as the ground and first excited state of a double-well potential. In the second approach we picked conventional hyperfine states of sodium as pseudo-spin states, but developed a completely new mechanism of momentum transfer: we took a low-energy RF transition, which inherently does not carry any recoil momentum, and endowed it with tunable momentum in the time-averaged picture.

Both schemes shared as a motivation the goal of simulating spin-orbit coupling with minimal heating. In addition, the first approach was targeted to explore a new point on the phase diagram – the stripe phase, a long-awaited supersolid state of matter.

The method based on dressing RF photons with recoil was conceived in the context of spin-orbit coupling, but in fact, goes beyond it. It also provided a lucid pedagogical interpretation of what Floquet engineering is. This technique can also be used for velocimetry and accelerometry. The new fundamental concept of recoil-dressed photons can become a new building block for future quantum simulations. Our experiment was carried out in an apparatus which was not perfectly suitable for the use of high oscillating fields. The humble value of momentum transfer that we generated $\sim 0.1k_L$ was only technically limited by the induced eddy currents in the

stainless steel chamber. If the same scheme would be realized in a glass cell, this limitation would be lifted. Also, much higher magnetic gradients than ours could be realized in atom-chip experiments, which would also allow one to boost the momentum transfer. Thus, seeing our work as the first step and proof-of-principle result, I hope it has provided a new look at the quantum mechanics of periodically driven systems. This work can inspire future development in the next-generation of quantum simulation experiments. Application of the scheme to fermionic gases was found to be particularly promising in the follow-up theoretical study [57].



Spin-Orbit Coupling and Spin Textures in Optical Superlattices

Junru Li, Wujie Huang, Boris Shteynas, Sean Burchesky, Furkan Çağrı Top, Edward Su, Jeongwon Lee, Alan O. Jamison, and Wolfgang Ketterle

Research Laboratory of Electronics, MIT-Harvard Center for Ultracold Atoms, Department of Physics, Massachusetts Institute of Technology, Cambridge, Massachusetts 02139, USA

(Received 10 June 2016; revised manuscript received 17 August 2016; published 27 October 2016)

We propose and demonstrate a new approach for realizing spin-orbit coupling with ultracold atoms. We use orbital levels in a double-well potential as pseudospin states. Two-photon Raman transitions between left and right wells induce spin-orbit coupling. This scheme does not require near resonant light, features adjustable interactions by shaping the double-well potential, and does not depend on special properties of the atoms. A pseudospinor Bose-Einstein condensate spontaneously acquires an antiferromagnetic pseudospin texture, which breaks the lattice symmetry similar to a supersolid.

DOI: 10.1103/PhysRevLett.117.185301

Spin-orbit coupling is the mechanism for many intriguing phenomena, including \mathbb{Z}_2 topological insulators, the spin quantum Hall effect [1,2], Majorana fermions [3], and spintronics devices [4]. Realizing controllable spin-orbit coupling with ultracold atoms should make it feasible to explore fundamental aspects of topology in physics and applications in quantum computing [5].

Spin-orbit coupling requires the atom's motion to be dependent on its spin state. Spin-orbit coupling without spin flips is possible for schemes that are diagonal in the spin component σ_z . Such spin-dependent vector potentials, which are sufficient for realizing quantum spin Hall physics and topological insulators, can be engineered using far-detuned laser beams to completely suppress spontaneous emission [6,7].

However, spin flips (i.e., spin-orbit coupling terms involving σ_x or σ_y operators) are necessary for Rashba [8] and Dresselhaus [9] spin-orbit coupling [10]. Experiments with ultracold atoms couple pseudospin states using optical dipole transitions, which couple only to the orbital angular momentum of the atom. Most realizations, including the first demonstration [11], use hyperfine states of an alkali atom as pseudospins. In this case, the coupling of the two states occurs due to internal spin-orbit coupling in the excited state of the atom, which causes the fine-structure splitting between the D_1 and D_2 lines. The optimum detuning of the lasers is comparable to this splitting, leading to heating. Special atomic species with orbital angular momentum in the ground state can avoid this problem, as recently realized with dysprosium [12]. Here, we present a new method that can be applied to any atomic species, using an external orbital degree of freedom as the pseudospin to avoid the need for near-resonant light.

An external degree of freedom as the pseudospin could be realized for a two-dimensional system by using the ground and first excited states of the confinement along the third dimension as pseudospin states. However, the

excited state would rapidly relax due to elastic collisions, typically on a millisecond time scale [13]. This is also the case for the recent implementation of spin-orbit coupling (SOC) with hybrid s - p Floquet bands in a one-dimensional optical lattice [14]. To solve this issue, we choose an asymmetric double-well potential (Fig. 1). Pseudospins up and down are realized as the two lowest eigenstates of the double-well potential. For $J/\Delta \ll 1$, they can be expressed by the tight-binding states $|l\rangle$ and $|r\rangle$ localized in the left and right wells, respectively: $|\downarrow\rangle = |l\rangle + (J/\Delta)|r\rangle$ and

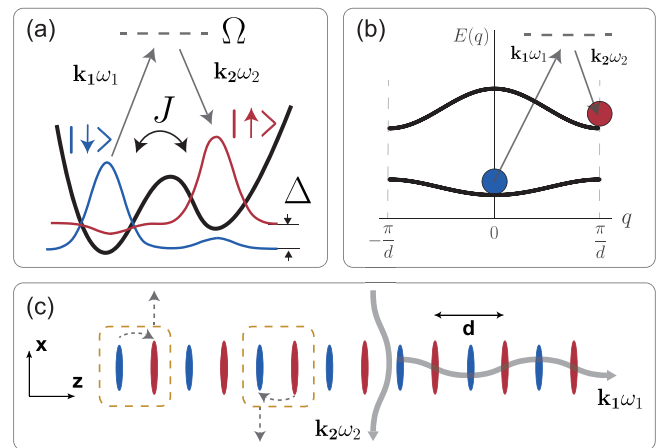


FIG. 1. Realization of orbital pseudospins in a superlattice. (a) The unit cell of the superlattice is a double well with offset Δ and tunneling J . The two lowest eigenstates (pseudospin up and down) are coupled via a two-photon Raman process. (b) Raman process in the band structure of the superlattice. The ground state with quasimomentum $q = 0$ is coupled to the edge of the Brillouin zone $q = (\pi/d)$ of the first excited band. (c) Top view of the superlattice with period $d = \lambda_{\text{IR}}/2 = 532$ nm. Raman coupling is implemented by two λ_{IR} beams: one along the superlattice (z direction), the other along the x direction. SOC (curved arrows) transfers transverse recoil in the x direction to the atoms (dashed arrows).

$|\uparrow\rangle = |r\rangle - (J/\Delta)|l\rangle$. The tunneling J and offset Δ between the two wells are used to adjust the overlap—and therefore the interactions and the collisional relaxation rate—between the two pseudospin states. We couple the two states via a two-photon Raman transition with large detunings to achieve SOC with spin flips. (For convenience, we will refer to pseudospin as spin in this Letter.) Recent work on two-leg ladders can be mapped to SOC between the two legs of the ladder [15,16]. Our scheme is qualitatively different from other realizations of orbital pseudospin since it realizes spin-orbit coupling in free space as compared to lattice models.

An intriguing prediction for spin-orbit coupled Bose-Einstein condensates (BECs) is the existence of a stripe phase [17–19], a spontaneous density modulation that realizes a supersolid [20]. However, when the interspin ($g_{\uparrow\downarrow}$) and intraspin ($g_{\uparrow\uparrow}, g_{\downarrow\downarrow}$) interaction strengths are the same, the increased interaction energy of the density modulation drives spatial phase separation, eliminating the stripes. The system can be kept in the miscible phase when interspin interactions are weaker than intraspin interactions, $g_{\uparrow\downarrow}^2 < g_{\uparrow\uparrow}g_{\downarrow\downarrow}$ [19]. In our realization, $g_{\uparrow\downarrow}$ is proportional to the overlap squared of the wave functions on the two sides of the double well. An analogous scheme can be realized with hyperfine pseudospins and spin-dependent lattices [21], but requires near-resonant light. Our scheme does not depend on specific atomic properties and addresses three challenges to realizing the stripe phase: (1) spin-orbit coupling without near resonant light, (2) a miscible system with adjustable interspin interactions, (3) a long lifetime against collisional relaxation.

Instead of one double-well system, we create a lattice of double wells using an optical superlattice [Fig. 1(c)]. The advantages of working with a stack of coherently coupled double wells are twofold: the increased signal to noise ratio and the use of interference between the double wells to separately observe the two spin states. In the present work, the degree of freedom along the superlattice direction is purely an aid to observation [22].

Our main result is the observation of the momentum structure of a BEC modified by a superlattice and spin-orbit coupling. We first describe the effects of the superlattice without adding SOC. A one-dimensional superlattice of double wells was realized by combining lattices of $\lambda_{\text{IR}} = 1064$ nm light and $\lambda_{\text{Gr}} = 532$ nm light obtained by frequency doubling the $\lambda_{\text{IR}} = 1064$ nm light. The shape of the double-well unit cell is determined by the relative strength and spatial phase ϕ_{SL} between the two lattices. The phase is controlled by a rotatable dispersive glass plate and an acousto-optical modulator for rapidly switching the IR lattice frequency.

The experiment starts with a BEC of $\sim 3 \times 10^5$ ^{23}Na atoms in the $|F = 1, m_F = -1\rangle$ state in a crossed optical dipole trap. The superlattice is adiabatically ramped up within 250 ms. For an offset $\Delta \gg J$, all the atoms

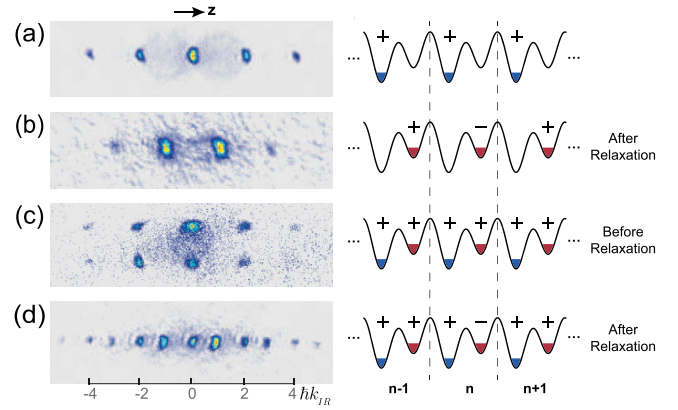


FIG. 2. Spontaneous formation of an antiferromagnetic spin texture. (a),(b) Time-of-flight (TOF) pattern of atoms in the ground (first excited) band of the superlattice. After preparation of the $|\uparrow\rangle$ state with quasimomentum $q = 0$, it relaxes to the bottom of the band at $q = \pi/d$. (c) An equal mixture of spin states is prepared by rapidly switching the superlattice parameters. The two spin states can be separated in the TOF by a pseudospin Stern-Gerlach effect [23]. The figure shows that both spin states are in $q = 0$ before the relaxation. (d) After relaxation, spinor BECs with states $|\downarrow\rangle, q = 0$ and $|\uparrow\rangle, q = \pi/d$ are observed. The momentum pattern implies a periodic structure at $2d$, twice the lattice constant, indicating that an antiferromagnetic spin structure with a doubled unit cell has formed. The plus and minus signs indicate (one possible choice for) the phase of the BEC wave function. n is the site index.

equilibrate at the band minimum $q = 0$ of the lowest superlattice band, putting 100% of the population in the $|\downarrow\rangle$ state. The relative population of the two spin states can be controlled by first adjusting Δ for the loading stage to achieve a desired state population and then rapidly lifting one well up to the final offset [23]. The upper well corresponds to the first excited band, which has its minimum energy at quasimomentum $q = \pi/d$ with $d = \lambda_{\text{IR}}/2$ [Figs. 2(a) and 2(b)]. Since the lowest energy $|\uparrow\rangle$ and $|\downarrow\rangle$ states have different quasimomenta and experience different transverse confinement, they can be separately observed in ballistic expansion images without the band-mapping techniques [23].

The π/d quasimomentum difference also leads to an interesting spin texture for an equal population of the $|\uparrow\rangle$ and $|\downarrow\rangle$ states. For this, atoms are prepared in both bands with $q = 0$ [Fig. 2(c)], corresponding to a wave function periodicity of 532 nm, i.e., the lattice constant. However, after relaxation, the periodicity has doubled to 1064 nm, as indicated by the doubled number of momentum components in ballistic expansion images [Fig. 2(d)]. Specifically, the system was prepared in the symmetric state $\sum_n (|\downarrow_n\rangle + |\uparrow_n\rangle)$, where n denotes the lattice site, which is a ferromagnetic spin state in the x - y plane. After relaxation into the state $\sum_n [|\downarrow_n\rangle + (-1)^n e^{i\theta} e^{-i\Delta t} |\uparrow_n\rangle]$ an antiferromagnetic spin texture has developed, which reduces the translational symmetry of the lattice. This

TABLE I. The amplitudes of the wave functions in Eqs. (1) and (2) obtained from first order perturbation theory ($i = 1, 2$).

States	M_i	M'_i	K
$ \Psi_1\rangle$	$-\frac{1}{2}(\Omega/E_r - \delta)$	$-\frac{1}{2}(\Omega/E_r + \delta)$	$-i[e^{-i(\pi/4)}/\sqrt{2}](J/\Delta)(\Omega/E_r + \Delta - \delta)$
$ \Psi_2\rangle$	$+\frac{1}{2}(\Omega/E_r + \delta)$	$-\frac{1}{2}(\Omega/E_r - \delta)$	$+i[e^{i(\pi/4)}/\sqrt{2}](J/\Delta)(\Omega/E_r - \Delta + \delta)$

system breaks both U(1) symmetry (the phase of the BEC) and the translational symmetry of the superlattice. In addition to the spin-density wave, it also has a density wave with the same period due to the interference of the $|\uparrow\rangle$ and $|\downarrow\rangle$ satellites. The position of the spin and density modulations is determined by the spontaneous phase θ and oscillates at frequency Δ [23]. It is a simple system fulfilling one definition of supersolidity [25–27].

The small satellites allow spin-orbit coupling, but also lead to the collisional decay of the $|\uparrow\rangle$ state. We observed lifetimes on the order of 200 ms for both the $|\uparrow\rangle$ and equally mixed states at a density of $n \approx 2.5 \times 10^{14} \text{ cm}^{-3}$. The similar lifetimes for both states and the sensitivity to daily alignment indicate the lifetime being limited by technical noise and the misalignment of the lattice rather than by collisions. Collisions would lead to a shorter lifetime for the mixed state by a factor of $4(J/\Delta)^2$. Adding Raman beams (with the parameters presented in Fig. 4) increases the loss rate by $\sim 10/s$, probably caused by technical issues. While previous work with ^{87}Rb reports a lifetime of seconds [11], the Raman hyperfine spin flip scheme is not promising for lighter atoms because of the substantially higher heating rates compared with ^{87}Rb , which are 10^3 (10^5) times higher for ^{23}Na (^6Li) [28]. Even without major improvements, the lifetimes achieved in our work are longer than any relevant dynamic time scale and should be sufficient for further studies, including the observation of the stripe phase [29].

Coupling between the two spin states is provided by two λ_{IR} beams: one along the superlattice direction z , the other orthogonal to it (along x). The frequency difference of the two beams is close to the offset in the double well, allowing near-resonant population transfer. The recoil k_z along the lattice is necessary to couple the two orthogonal spin states in the double well, and was chosen to be $k_z = \pi/d$. The recoil kick k_x in the transverse plane provides the coupling between the free-space motion in the transverse plane and the spin. It has opposite signs for the transition $|\downarrow\rangle$ to $|\uparrow\rangle$ and the reverse transition.

The Raman coupling can be described as a moving potential $V_{\text{Raman}} = \Omega \cos(k_x x + k_z z - \delta t)$, characterized by a two-photon Rabi frequency Ω , a detuning of Raman beams δ , and a wave vector $(k_x, 0, k_z)$. We characterize the states by their spin, quasimomentum q , and x momentum k_x (the y momentum is always zero).

If the system is initially prepared in the state $|\downarrow, q = 0, k_x = 0\rangle$, the adiabatically ramped Raman beams will transfer it to a new eigenstate:

$$|\Psi_1\rangle = |\downarrow, 0, 0\rangle + K_1 e^{-i\delta t} |\uparrow, \pi/d, k_x\rangle + M_1 e^{-i\delta t} |\downarrow, \pi/d, k_x\rangle + M_1' e^{i\delta t} |\downarrow, -\pi/d, -k_x\rangle. \quad (1)$$

If prepared in $|\uparrow, \pi/d, 0\rangle$, the new state will be

$$|\Psi_2\rangle = e^{-i\Delta t} |\uparrow, \pi/d, 0\rangle + K_2 e^{i(\delta-\Delta)t} |\downarrow, 0, -k_x\rangle + M_2 e^{i(\delta-\Delta)t} |\uparrow, 0, -k_x\rangle + M_2' e^{-i(\delta+\Delta)t} |\uparrow, 0, k_x\rangle. \quad (2)$$

The amplitudes obtained from first order perturbation theory appear in Table I. The spin-orbit coupling is described by the second term in Eqs. (1) and (2). In addition, the Raman beams act as a comoving lattice and (in the limit $\delta \gg E_r$) create a moving density modulation in the two spin states, described by the third and fourth terms. The spin-orbit coupling shows a resonant behavior for $\delta \approx \Delta$ —the range of interest for SOC—where the moving density modulation is nonresonant. Both contributions are proportional to Ω/Δ . The off-resonant counterrotating spin flip term is proportional to Δ^{-2} and has been neglected. For $\delta \gg E_r$, all off-resonant amplitudes M_i, M'_i become $\approx \Omega/\delta$. For $\delta = \Delta$ and both spin states populated, the spin-orbit admixture of $|\Psi_1\rangle$ is expected to form a stationary interference pattern with $|\Psi_2\rangle$ along x with wave vector k_x , and vice versa, which constitutes the stripe phase of spin-orbit coupled BECs in the perturbative limit. (In general, the periodicity of the stripes depends on β and the atoms' interactions [19].)

The resonant Raman coupling leads to the standard spin-orbit Hamiltonian [23]:

$$\hat{H}_{\text{SOC}} = \frac{(\hat{p} + \alpha \hat{\sigma}_z)^2}{2m} + \beta \hat{\sigma}_x + \delta_0 \hat{\sigma}_z, \quad (3)$$

which can be considered as equal contributions of Rashba and Dresselhaus interactions. The parameters $\alpha = -k_x/2$, $\beta = (1/\sqrt{2})\Omega J/\Delta$, and $\delta_0 = (\delta - \Delta)/2$ are independently tunable in our experiment.

To characterize all the components of the wave functions above, the Raman coupling was adiabatically switched on by ramping up the intensity of the two Raman beams. The momentum space wave function was observed by suddenly switching off the lattice and trapping beams and measuring the resulting density distribution with absorption imaging after 10 ms of ballistic expansion (Fig. 3).

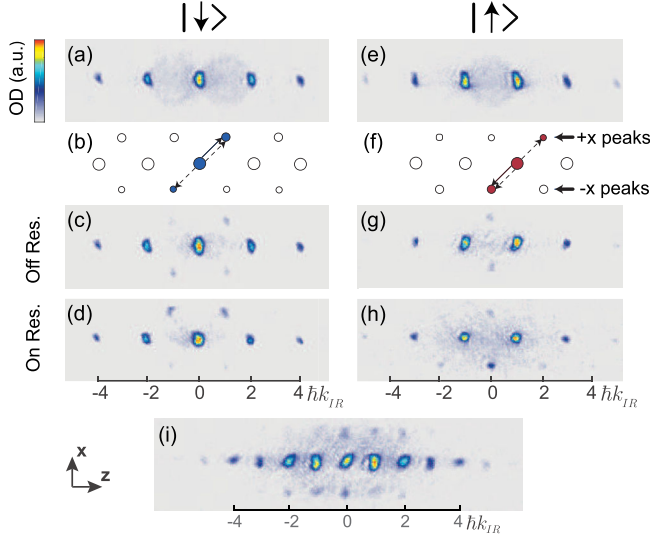


FIG. 3. Characterization of spinor BECs through their momentum distributions. (a),(e) TOF images of the $|\downarrow\rangle$ and $|\uparrow\rangle$ states, respectively. (b),(f) Schematics of the momentum peaks for $|\downarrow\rangle$ and $|\uparrow\rangle$ with Raman coupling. Both the SOC (solid arrows) and the density modulation (dashed arrows) are shown. The main peak (filled circle) is equal to the quasimomentum of the state. Extra peaks (open circles) appear due to the periodic potential. (c),(d),(g),(h) Same as in (a) and (e), but now with Raman coupling at different detunings δ . The momentum components created by the Raman process are vertically shifted compared to (a) and (e) due to the transverse momentum kick. The momentum shift along the superlattice (z direction) reflects the π/d quasimomentum of the Raman lattice. The off-resonant density modulation creates momentum peaks that are symmetric along $+x$ and $-x$ [(c) and (g)], whereas resonant spin-orbit coupling creates unidirectional momentum transfer resulting in asymmetry [(d) and (h)]. (i) Spin-orbit coupled BEC with equal population in the spin up and spin down states.

The momentum components created by the Raman beams are displaced in the x direction by the recoil shift $\hbar k_{\text{IR}}$. For off-resonant Raman beams, the pattern is symmetric for the $+x$ and $-x$ directions—signifying the moving density modulation [see Eqs. (1) and (2)]. The resonant spin-orbit coupling is one sided, with opposite transfer of x momentum for the two spin states—as observed in Fig. 3. We separate the momentum peaks due to the moving density modulation from SOC by evaluating the difference between the momentum peaks along the $+x$ and $-x$ directions. Figure 4 shows the resonance feature of the SOC when the Raman detuning was varied. The resonances for the two processes $|\downarrow\rangle \rightarrow |\uparrow\rangle$ and $|\uparrow\rangle \rightarrow |\downarrow\rangle$ should be separated by $2E_r \approx 15.3$ kHz. The observed discrepancy is consistent with mean field interactions, which reduce the separation by $\sim 2\mu \approx 5$ kHz, where μ is the single site chemical potential. The observed widths of the resonances are probably dominated by the inhomogeneity of Δ due to the Gaussian beam profile of the IR lattice laser [23].

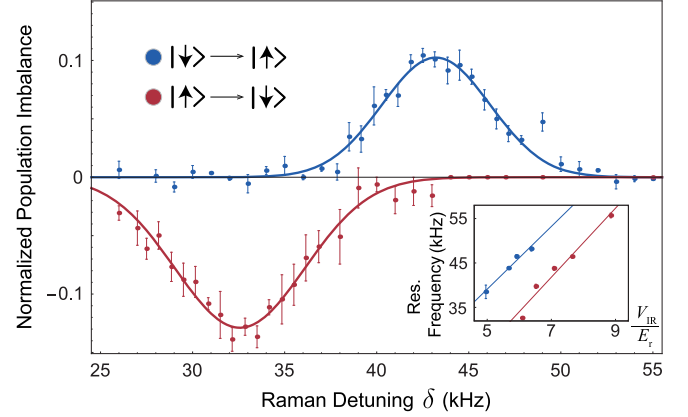


FIG. 4. Spin-orbit coupling resonances. Shown is the population imbalance between the “ $+x$ ” and “ $-x$ ” momentum peaks versus Raman detuning for the $|\downarrow\rangle \rightarrow |\uparrow\rangle$ (blue) and $|\uparrow\rangle \rightarrow |\downarrow\rangle$ (red) processes. The two sets of data were measured for the same superlattice parameters $V_{\text{IR}} = 7.5(2)E_r$, $V_{\text{Gr}} = 20(2)E_r$, and $\phi_{\text{SL}} \approx 0.22(1)\pi$, which gives $\Delta \approx 37(1)$ kHz. The spin-orbit coupling strength β was calculated to be $0.40(5)$ kHz. The solid lines are Gaussian fits to the resonances centered at $32.2(3)$ and $43.2(3)$ kHz. The Gaussian profile of the IR lattice inhomogeneously broadens the resonances. The error bars represent 1σ statistical uncertainty. Inset: resonance center frequencies versus the IR lattice depth V_{IR} for fixed ϕ_{SL} . The resonances are linear in V_{IR} with a constant split equal to twice the recoil energy. The slope of the linear fit reveals ϕ_{SL} . The error bars are the uncertainties of the fit.

Having established spin-orbit coupling at the single-particle level, the next step is to explore the phase diagram of spin-orbit coupled Bose-Einstein condensates with interactions [17,19,21], particularly the stripe phase. The clear signature of the stripe phase is the stationary, periodic density modulation on the BEC mentioned above. The periodicity is tunable through the spin-orbit coupling strength and can be directly observed via Bragg scattering [30]. In contrast to experiments carried out with ^{87}Rb , which has similar inter- and intraspin scattering lengths, our system has an adjustable interspin interaction $g_{\downarrow\uparrow} \approx (J/\Delta)^2 g_{\downarrow\downarrow} = (J/\Delta)^2 g_{\uparrow\uparrow}$. Small values of $g_{\downarrow\uparrow}/g_{\uparrow\uparrow}$ lead to a large window of β for observing the stripe phase and enable higher contrast stripes [19]. Figure 3(i) shows the momentum distribution of an equal spin mixture with SOC. We observed an ~ 40 ms lifetime for the parameters presented in Fig. 4. After adding Bragg detection, the observation of the stripe phase is in reach.

In conclusion, we proposed and demonstrated a new scheme for realizing spin-orbit coupling using superlattices. An asymmetric double-well potential provides attractive features for pseudospins, including long lifetimes, adjustable interactions, and easy detection. This scheme can be applied to a wide range of atoms including lithium and potassium, which suffer from strong heating when hyperfine pseudospins are coupled. On the other hand, by

combining multiple hyperfine states with the orbital degree of the double well, our scheme can realize two-dimensional Rashba spin-orbit coupling [31] and suggestions made for alkaline-earth atoms, for example, synthetic non-Abelian gauge potentials [32,33], and Kondo lattice models [34–36].

We acknowledge helpful discussions with S. Stringari, E. Mueller, and N. Cooper. We thank A. Keshet for contributions to building the experiment and J. Amato-Grill, C. J. Kennedy, and P. N. Jepsen for suggestions and a critical reading of the manuscript. We acknowledge support from the NSF through the Center for Ultracold Atoms and by Grant No. 1506369, from Army Research Office –Multidisciplinary University Research Initiative Non-equilibrium Many-body Dynamics (Grant No. W911NF-14-1-0003), and from Air Force Office of Scientific Research – Multidisciplinary University Research Initiative Quantum Phases of Matter (Grant No. FA9550-14-1-0035).

J. L. and W. H. contributed equally to this work.

-
- [1] M. Z. Hasan and C. L. Kane, *Rev. Mod. Phys.* **82**, 3045 (2010).
- [2] X.-L. Qi and S.-C. Zhang, *Rev. Mod. Phys.* **83**, 1057 (2011).
- [3] R. Wei and E. J. Mueller, *Phys. Rev. A* **86**, 063604 (2012).
- [4] I. Žutić, J. Fabian, and S. Das Sarma, *Rev. Mod. Phys.* **76**, 323 (2004).
- [5] J. Alicea, Y. Oreg, G. Refael, F. von Oppen, and M. P. A. Fisher, *Nat. Phys.* **7**, 412 (2011).
- [6] H. Miyake, G. A. Siviloglou, C. J. Kennedy, W. C. Burton, and W. Ketterle, *Phys. Rev. Lett.* **111**, 185302 (2013).
- [7] M. Aidelsburger, M. Atala, M. Lohse, J. T. Barreiro, B. Paredes, and I. Bloch, *Phys. Rev. Lett.* **111**, 185301 (2013).
- [8] Y. A. Bychkov and E. I. Rashba, *J. Phys. C* **17**, 6039 (1984).
- [9] G. Dresselhaus, *Phys. Rev.* **100**, 580 (1955).
- [10] A. Manchon, H. C. Koo, J. Nitta, S. M. Frolov, and R. A. Duine, *Nat. Mater.* **14**, 871 (2015).
- [11] Y.-J. Lin, K. Jimenez-Garcia, and I. B. Spielman, *Nature (London)* **471**, 83 (2011).
- [12] N. Q. Burdick, Y. Tang, and B. L. Lev, *Phys. Rev. X* **6**, 031022 (2016).
- [13] I. B. Spielman, P. R. Johnson, J. H. Huckans, C. D. Fertig, S. L. Rolston, W. D. Phillips, and J. V. Porto, *Phys. Rev. A* **73**, 020702 (2006).
- [14] M. A. Khomehchi, C. Qu, M. E. Mossman, C. Zhang, and P. Engels, *Nat. Commun.* **7**, 10867 (2016), article.
- [15] D. Hügél and B. Paredes, *Phys. Rev. A* **89**, 023619 (2014).
- [16] M. Atala, M. Aidelsburger, M. Lohse, J. T. Barreiro, B. Paredes, and I. Bloch, *Nat. Phys.* **10**, 588 (2014).
- [17] T. L. Ho and S. Zhang, *Phys. Rev. Lett.* **107**, 150403 (2011).
- [18] C. Wang, C. Gao, C.-M. Jian, and H. Zhai, *Phys. Rev. Lett.* **105**, 160403 (2010).
- [19] Y. Li, L. P. Pitaevskii, and S. Stringari, *Phys. Rev. Lett.* **108**, 225301 (2012).
- [20] M. Boninsegni and N. V. Prokof'ev, *Rev. Mod. Phys.* **84**, 759 (2012).
- [21] G. I. Martone, Y. Li, and S. Stringari, *Phys. Rev. A* **90**, 041604 (2014).
- [22] More specifically, our scheme realizes 1D SOC in the 2D free space orthogonal to the superlattice.
- [23] See Supplemental Material at <http://link.aps.org/supplemental/10.1103/PhysRevLett.117.185301> for derivations and experimental details, which includes Ref. [24].
- [24] J. Stenger, S. Inouye, A. P. Chikkatur, D. M. Stamper-Kurn, D. E. Pritchard, and W. Ketterle, *Phys. Rev. Lett.* **82**, 4569 (1999).
- [25] An alternative view is that this system is a superposition of two BECs with two spontaneously broken U(1) symmetries (the overall phase, and the relative phase θ). The phase θ determines the orientation of the antiferromagnetic pseudospin texture in the spin x - y plane. The spin texture breaks the lattice symmetry by doubling the lattice constant. This system therefore does not fulfill a stronger definition of supersolidity that demands breaking a continuous translational symmetry.
- [26] K. Baumann, C. Guerlin, F. Brennecke, and T. Esslinger, *Nature (London)* **464**, 1301 (2010).
- [27] Y. Chen, J. Ye, and G. Tian, *J. Low Temp. Phys.* **169**, 149 (2012).
- [28] X. Luo, L. Wu, J. Chen, Q. Guan, K. Gao, Z. Xu, L. You, and R. Wang, *Sci. Rep.* **6**, 18983 (2016).
- [29] Collisional losses could be further diminished by reducing the overlap between the pseudospin states. The consequently reduced spin-orbit coupling strength can be compensated by higher intensity Raman beams up to the point where higher order effects and additional heating occur due to nonperturbative driving. The parameters of Fig. 4 were close to this limit.
- [30] H. Miyake, G. A. Siviloglou, G. Puentes, D. E. Pritchard, W. Ketterle, and D. M. Weld, *Phys. Rev. Lett.* **107**, 175302 (2011).
- [31] S.-W. Su, S.-C. Gou, Q. Sun, L. Wen, W.-M. Liu, A.-C. Ji, J. Ruseckas, and G. Juzeliūnas, *Phys. Rev. A* **93**, 053630 (2016).
- [32] J. Dalibard, F. Gerbier, G. Juzeliūnas, and P. Öhberg, *Rev. Mod. Phys.* **83**, 1523 (2011).
- [33] K. Osterloh, M. Baig, L. Santos, P. Zoller, and M. Lewenstein, *Phys. Rev. Lett.* **95**, 010403 (2005).
- [34] A. Gorshkov, M. Hermele, V. Gurarie, C. Xu, P. Julienne, J. Ye, P. Zoller, E. Demler, M. Lukin, and A. Rey, *Nat. Phys.* **6**, 289 (2010).
- [35] M. Foss-Feig, M. Hermele, and A. M. Rey, *Phys. Rev. A* **81**, 051603 (2010).
- [36] M. Nakagawa and N. Kawakami, *Phys. Rev. Lett.* **115**, 165303 (2015).

Supplemental Material for “Spin-Orbit Coupling and Spin Textures in Optical Superlattices”

Junru Li,* Wujie Huang,* Boris Shteynas, Sean Burchesky,
Furkan Çağrı Top, Edward Su, Jeongwon Lee, Alan O. Jamison, and Wolfgang Ketterle
*Research Laboratory of Electronics, MIT-Harvard Center for Ultracold Atoms, Department of Physics,
Massachusetts Institute of Technology, Cambridge, Massachusetts 02139, USA*
(Dated: August 17, 2016)

SUPERLATTICE HAMILTONIAN WITH RAMAN COUPLING

The Hamiltonian for a one-dimensional superlattice, created by standing waves of infrared and green light with relative phase ϕ_{SL} is

$$H_{lattice} = \frac{\hat{p}_z^2}{2m} + \frac{\hat{p}_\perp^2}{2m} + V_{Gr} \sin^2(k_{Gr}z) + V_{IR} \sin^2(k_{IR}z + \phi_{SL})$$

In the tight-binding limit, it can be rewritten as

$$H_{lattice} = \frac{\hat{p}_\perp^2}{2m} + \frac{1}{2}\Delta_0 \sum_n (|r_n\rangle \langle r_n| - |l_n\rangle \langle l_n|) - J \sum_n (|l_n\rangle \langle r_n| + h.c.) - \sum_n \sum_{\substack{t=l,r \\ t'=l,r}} (J'_{tt'} |t_n\rangle \langle t'_{n+1}| + h.c.),$$

where $|l_n(r_n)\rangle$ is a wavefunction localized in the left(right) well of the n^{th} unit cell, Δ_0 is the energy separation between the right and the left wells. \hbar is taken to be 1. Tunneling between neighboring unit cells is important for maintaining of coherence in the superlattice, but not relevant for the physics of spin-orbit coupling. Thus, tunneling terms with $J'_{tt'}$ in the Hamiltonian can be neglected.

The complete Hamiltonian of the system is

$$H = H_{lattice} + V_{Raman},$$

where $V_{Raman} = \Omega \cos(k_z z + k_x x - \delta t)$ is a moving lattice potential. For the purpose of our experiment, the initial phase of the Raman potential is not relevant and taken to be zero.

We prefer to use eigenstates of a double well for the description. To first order in small parameter $\frac{J}{\Delta_0} \ll 1$ they can be written as

$$|\downarrow_n\rangle = |l_n\rangle + \frac{J}{\Delta_0} |r_n\rangle, \quad |\uparrow_n\rangle = |r_n\rangle - \frac{J}{\Delta_0} |l_n\rangle$$

We expand the Hamiltonian in the new basis with $\Delta = \Delta_0 + 2\frac{J^2}{\Delta_0} \approx \Delta_0$:

$$H = \frac{\hat{p}_\perp^2}{2m} + \frac{1}{2}\Delta \sum_n (|\uparrow_n\rangle \langle \uparrow_n| - |\downarrow_n\rangle \langle \downarrow_n|) + \sum_{p_\perp, p'_\perp} |p_\perp\rangle \left(\sum_n \sum_{\substack{i=\downarrow, \uparrow \\ i'=\downarrow, \uparrow}} |i_n\rangle \langle i_n| \langle p_\perp| \Omega \cos(k_z z + k_x x - \delta \cdot t) |p'_\perp\rangle |i'_n\rangle \langle i'_n| \right) \langle p'_\perp|$$

In our experiment $k_z \approx k_x \approx k_{IR} = \frac{\pi}{d}$, where d is a period of the superlattice. In order to estimate the effect of the Raman potential with arbitrary phase we need to know the overlap integrals for $\cos(k_{IR} \cdot (z - z_n))$ and $\sin(k_{IR} \cdot (z - z_n))$. To first order in $\frac{J}{\Delta}$:

$$\langle \downarrow_n | \cos(k_{IR} \cdot (z - z_n)) | \uparrow_n \rangle \approx \langle l_n | - \frac{J}{\Delta} | l_n \rangle = -\frac{J}{\Delta},$$

$$\langle \downarrow_n | \cos(k_{IR} \cdot (z - z_n)) | \downarrow_n \rangle \approx 1, \quad \langle \uparrow_n | \cos(k_{IR} \cdot (z - z_n)) | \uparrow_n \rangle \approx 0,$$

$$\langle \downarrow_n | \sin(k_{IR} \cdot (z - z_n)) | \uparrow_n \rangle \approx \langle r_n | \frac{J}{\Delta} | r_n \rangle = \frac{J}{\Delta},$$

$$\langle \downarrow_n | \sin(k_{IR} \cdot (z - z_n)) | \downarrow_n \rangle \approx 0, \langle \uparrow_n | \sin(k_{IR} \cdot (z - z_n)) | \uparrow_n \rangle \approx 1,$$

where $z_n = nd$ is a coordinate of the left well in the n^{th} unit cell.

Thus, the Raman potential can be expanded in the basis of double-well eigenstates:

$$\begin{aligned} \sum_{\substack{i=a,b \\ i'=a,b}} |i_n\rangle \langle i_n| \Omega \cos(k_z(z - z_n) + k_z z_n + k_x x - \delta \cdot t) |i'_n\rangle \langle i'_n| = \\ = \Omega \cos \phi_n \left\{ -\frac{J}{\Delta} (|\downarrow_n\rangle \langle \uparrow_n| + |\uparrow_n\rangle \langle \downarrow_n|) + |\downarrow_n\rangle \langle \downarrow_n| \right\} + \\ - \Omega \sin \phi_n \left\{ |\uparrow_n\rangle \langle \uparrow_n| + \frac{J}{\Delta} (|\downarrow_n\rangle \langle \uparrow_n| + |\uparrow_n\rangle \langle \downarrow_n|) \right\}, \end{aligned}$$

where $\phi_n = \pi n + k_x x - \delta t$. Later, we will calculate how x as an operator acts on the momentum states $|p_\perp\rangle$.

$$\hat{V}_{Raman} = \sum_n \Omega (-1)^n \cos(k_x x - \delta t) |\downarrow_n\rangle \langle \downarrow_n| - \Omega (-1)^n \sin(k_x x - \delta t) |\uparrow_n\rangle \langle \uparrow_n| + \quad (1)$$

$$-\sqrt{2}\Omega \frac{J}{\Delta} (-1)^n \cos(k_x x - \delta t - \frac{\pi}{4}) \{ |\downarrow_n\rangle \langle \uparrow_n| + |\uparrow_n\rangle \langle \downarrow_n| \} \quad (2)$$

The factor $(-1)^n$ represents the phase of the Raman beams, which have a wavelength two times the length of the unit cell. In our experiment the atomic sample is prepared in the zero-momentum state. When the Raman perturbation is applied the atoms experience a kick in the x -direction. In the y -direction atoms remain unperturbed, i.e. $\hat{p}_y = 0$. Since the confinement along x is weak, we can use the basis $|\uparrow(\downarrow), k\rangle = |\uparrow(\downarrow)\rangle \otimes e^{ikx}$. The Raman interaction gives rise to intra-band coupling terms (1), and to the spin-orbit coupling term (2).

The system in our experiment initially prepared in the lower wells, which corresponds to the $q = 0$ of the lowest band of the superlattice:

$$|\psi_{q=0}^{(\downarrow)}\rangle = \sum_{n=1}^N \frac{1}{\sqrt{N}} |\downarrow_n\rangle$$

N is the number of unit cells in the lattice. When all the atoms are confined in the upper wells, the lowest state is the $q = \frac{\pi}{d}$ state of the first excited band, due to the inverted dispersion relation:

$$|\psi_{q=\pi/d}^{(\uparrow)}\rangle = \sum_{n=1}^N \frac{1}{\sqrt{N}} e^{i\frac{\pi}{d}(z_n + \frac{d}{2})} |\uparrow_n\rangle$$

With $z_n = nd$, the state becomes:

$$|\psi_{q=\pi/d}^{(\uparrow)}\rangle = \sum_{n=1}^N \frac{1}{\sqrt{N}} i (-1)^n |\uparrow_n\rangle$$

For the calculation of matrix elements we assume that overlap is nonzero only for $n = n'$.

Intra-band coupling terms:

$$\begin{aligned} \langle \psi_{q=\pi/d}^{(\downarrow)} | \hat{V}_{Raman} | \psi_{q=0}^{(\downarrow)} \rangle = \sum_{n,n'} \frac{1}{N} (-1)^n \langle \downarrow_{n'} | \Omega \cos(k_z z + k_x x - \delta t) | \downarrow_n \rangle \\ = \Omega \sum_n \frac{1}{N} \cos(\phi_n) (-1)^n = \Omega \cos(k_x x - \delta t) \quad (3) \end{aligned}$$

$$\begin{aligned}
\langle \psi_{q=0}^{(\uparrow)} | \hat{V}_{Raman} | \psi_{q=\pi/d}^{(\uparrow)} \rangle &= \sum_{n,n'} \frac{1}{N} \langle \uparrow_{n'} | \Omega \cos(k_z z + k_x x - \delta t) i (-1)^n | \uparrow_n \rangle \\
&= \Omega \sum_n \frac{1}{N} i (-1)^n (-\sin(\phi_n)) = -i\Omega \sin(k_x x - \delta t) \quad (4)
\end{aligned}$$

Spin-orbit coupling matrix element:

$$\begin{aligned}
\langle \psi_{q=\pi/d}^{(\uparrow)} | \hat{V}_{Raman} | \psi_{q=0}^{(\downarrow)} \rangle &= \sum_{n,n'} \frac{1}{N} (-i) (-1)^{n'} \langle \uparrow_{n'} | \Omega \cos(k_z z + k_x x - \delta t) | \downarrow_n \rangle \\
&= -i\Omega \sum_n \frac{1}{N} (-1)^n \langle \uparrow_n | \cos(k_z(z - z_n)) \cos(\phi_n) - \sin(k_z(z - z_n)) \sin(\phi_n) | \downarrow_n \rangle,
\end{aligned}$$

$$\langle \psi_{q=\pi/d}^{(\uparrow)} | \hat{V}_{Raman} | \psi_{q=0}^{(\downarrow)} \rangle = i \frac{J}{\Delta} \Omega \sum_n (-1)^n \frac{1}{N} (\cos(\phi_n) + \sin(\phi_n)) = i \frac{J}{\Delta} \Omega (\cos(k_x x - \delta t) + \sin(k_x x - \delta t))$$

Intra-band coupling matrix elements (3) and (4) provide recoil kick in x -direction with recoil energy $E_r = \frac{k_x^2}{2m}$ and along the superlattice, changing the quasimomentum by half a reciprocal vector. If the system is initially at $|\psi_{q=0}^{(\downarrow)}\rangle$, the new adiabatically connected eigenstate in first order perturbation theory is:

$$\begin{aligned}
|\Psi_1\rangle &= |\psi_{q=0}^{(\downarrow)}, 0\rangle - \frac{1}{2} \frac{\Omega}{E_r - \delta} e^{-i\delta t} |\psi_{q=\pi/d}^{(\downarrow)}, k_x\rangle - \frac{1}{2} \frac{\Omega}{E_r + \delta} e^{i\delta t} |\psi_{q=\pi/d}^{(\downarrow)}, -k_x\rangle + \\
&\quad - i \frac{e^{-i\frac{\pi}{4}}}{\sqrt{2}} \frac{J\Omega/\Delta}{E_r + \Delta - \delta} e^{-i\delta t} |\psi_{q=\pi/d}^{(\uparrow)}, k_x\rangle - i \frac{e^{i\frac{\pi}{4}}}{\sqrt{2}} \frac{J\Omega/\Delta}{E_r + \Delta + \delta} e^{i\delta t} |\psi_{q=\pi/d}^{(\uparrow)}, -k_x\rangle
\end{aligned}$$

If the system is prepared in $|\psi_{q=\pi/d}^{(\uparrow)}, 0\rangle$:

$$\begin{aligned}
|\Psi_2\rangle &= e^{-i\Delta t} |\psi_{q=\pi/d}^{(\uparrow)}, 0\rangle - \frac{1}{2} \frac{\Omega}{E_r - \delta} e^{-i(\delta+\Delta)t} |\psi_{q=0}^{(\uparrow)}, k_x\rangle + \frac{1}{2} \frac{\Omega}{E_r + \delta} e^{i(\delta-\Delta)t} |\psi_{q=0}^{(\uparrow)}, -k_x\rangle + \\
&\quad + i \frac{e^{-i\frac{\pi}{4}}}{\sqrt{2}} \frac{\Omega J/\Delta}{E_r - \Delta - \delta} e^{-i(\delta+\Delta)t} |\psi_{q=0}^{(\downarrow)}, k_x\rangle + i \frac{e^{i\frac{\pi}{4}}}{\sqrt{2}} \frac{\Omega J/\Delta}{E_r - \Delta + \delta} e^{i(\delta-\Delta)t} |\psi_{q=0}^{(\downarrow)}, -k_x\rangle
\end{aligned}$$

For δ close to Δ intra-band coupling is off-resonant and both co- and counter-rotating terms contribute at comparable strengths, whereas for spin-orbit coupling the co-rotating term is resonant and, therefore, much stronger than the counter-rotating term.

SPIN-ORBIT-COUPLING HAMILTONIAN

Keeping only the near-resonant spin-orbit coupling term, the Hamiltonian describing the system is

$$H_{SOC} = \begin{pmatrix} \frac{\hat{p}_x^2}{2m} - \frac{\Delta}{2} & \frac{-ie^{i\pi/4}}{\sqrt{2}} \frac{J}{\Delta} \Omega e^{-i(k_x x - \delta t)} \\ \frac{ie^{-i\pi/4}}{\sqrt{2}} \frac{J}{\Delta} \Omega e^{i(k_x x - \delta t)} & \frac{\hat{p}_x^2}{2m} + \frac{\Delta}{2} \end{pmatrix}$$

After a unitary transformation with a position-dependent rotation, $\hat{U} = e^{(-ik_x x + i\delta t - i\frac{\pi}{4})\sigma_z/2}$, the Hamiltonian turns into $H'_{SOC} = U^\dagger H_{SOC} U - iU^\dagger \frac{\partial U}{\partial t}$.

$$H'_{SOC} = \frac{(\hat{p}_x + \alpha\sigma_z)^2}{2m} + \beta\sigma_x + \delta_0\sigma_z,$$

where $\alpha = -\frac{1}{2}k_x$, $\beta = \frac{J\Omega}{\sqrt{2}\Delta}$ and $\delta_0 = \frac{1}{2}(\delta - \Delta)$. For the total Hamiltonian we have to add the intra-band coupling, which causes a density modulation.

PSEUDOSPIN STERN-GERLACH EFFECT

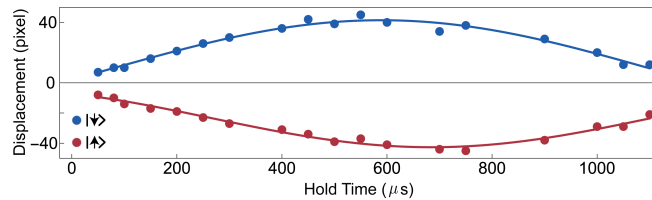


FIG. 1: (color) Stern-Gerlach separation of the spin states. Atoms are loaded into the green lattice, then the IR lattice is suddenly ramped up. After different hold times, the vertical displacements of atoms in different spin states is measured with 10ms ballistic expansion. $y = 0$ corresponds to the position of atoms without the sudden ramp. The spin states are displaced due to of transverse oscillations in the superlattice. The oscillating frequencies are equal to the transverse trapping frequencies which the spins experience in the superlattice. In the data shown, atoms in $|\uparrow\rangle$ and $|\downarrow\rangle$ oscillates with frequencies of 356 Hz and 417 Hz correspondingly.

Atoms in different pseudospin states can be spatially separated by a pseudospin Stern-Gerlach effect. The two spin states experience different transverse confinement from the 1064 nm lattice. When this lattice beam is displaced from the green lattice, the atoms in the two spin states experience different momentum kicks in the $x - y$ plane when the IR lattice is suddenly increased. This leads to transverse oscillations of the two spin states relative to each other and can be used to separate them in ballistic expansion (Fig.1). The frequency of the oscillation is equal to the corresponding transverse trapping frequency of each spin state.

SUPERLATTICE CALIBRATION

The superlattice potential $V(x) = V_{\text{IR}} \sin^2(k_{\text{IR}}z + \phi_{\text{SL}}) + V_{\text{Gr}} \sin^2(k_{\text{Gr}}z)$ was produced by overlapping two one-dimensional lattices with spacing $\lambda_{\text{IR}}/2 = 532$ nm (long) and $\lambda_{\text{Gr}}/2 = 266$ nm (short). The 532 nm light was generated by frequency doubling a high power $\lambda = 1064$ nm laser seeded by the same seed laser as the laser for the long lattice. This eliminated the need for any phase or frequency locking of two independent lasers. The long and short lattice also shared the same retroreflective mirror to minimize noise and drifts in the relative phase ϕ_{SL} .

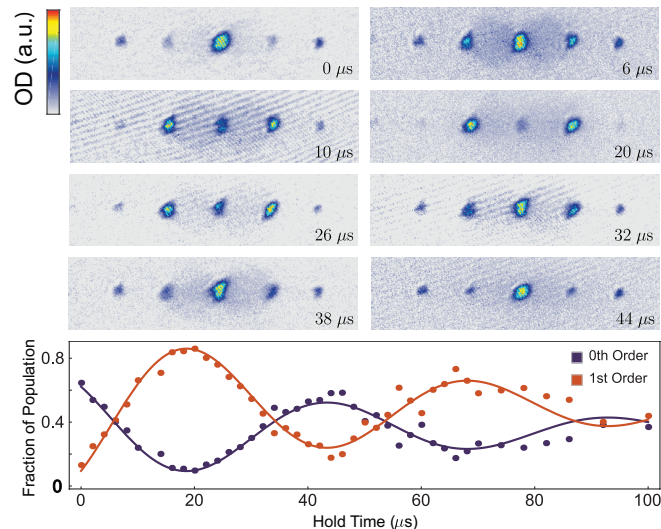


FIG. 2: (color) Calibration of the superlattice offset Δ . The relative phase between atoms in the lower and upper wells accumulated linearly with time and results in periodic changes in the time-of-flight interference pattern. The period of the oscillation is equal to Δ which is ~ 23 kHz for the data shown.

The relative phase ϕ_{SL} was controlled by introducing different phase shifts for the $\lambda = 1064$ nm and 532 nm lattice lights from a rotatable dispersive glass plate and by switching the frequency of the 1064 nm light with an acousto-optical modulator. The glass plate allowed a wide tuning range for ϕ_{SL} . This design minimizes the optical path

length, reducing the sensitivity to atmospheric pressure changes. The frequency switching allowed rapid but small phase shifts. For our geometry, a 70 MHz shift for the 1064 nm light corresponded to a $\pi/4$ change in ϕ_{SL} .

The offset Δ was directly calibrated by observing a beat note within a single double-well. Condensates with equal population of atoms in the left and right well were prepared by pre-setting the glass plate to the desired value and then rapidly ramping up the IR lattice to the final offset. Interference patterns for atoms sitting in the lower and upper well overlap and therefore interfere with each other before they relax to orthogonal quasi-momentum states. The interference pattern evolves periodically with frequency $\omega = \Delta$ (Fig.2).

The relaxation to the band minimum occurs in less than 2 ms as shown in Figure 3. The observation of the relaxation also indicates the population to be transferred to the first excited band.

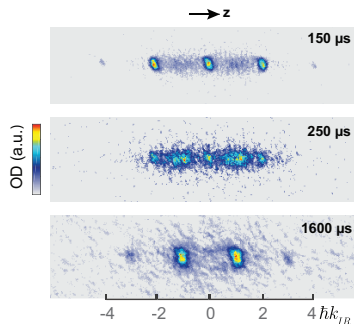


FIG. 3: Relaxation process for atoms in the first excited band of the superlattice. After preparation of the $|\uparrow\rangle$ state with quasimomentum $q = 0$, it relaxes to the bottom of the band at $q = \pi/d$ within a time scale of 2 ms.

ANTIFERROMAGNETIC SPIN TEXTURE

A spin-1/2 aligned along the $\cos \phi \hat{x} + \sin \phi \hat{y}$ direction has the wavefunction $|\downarrow\rangle + e^{i\phi} |\uparrow\rangle$. In our experiment atoms can be prepared in left and right sites of the double wells with equal population. The wave function is proportional to

$$|\psi\rangle = \sum_n |\downarrow_n\rangle + (-1)^n e^{i\theta} e^{-i\Delta t} |\uparrow_n\rangle,$$

which corresponds to spin-states aligned in the x-y plane with opposite direction on neighboring sites, showing x-y antiferromagnetic ordering. The expectation values of spin evolve as $\langle \sigma_x \rangle = (-1)^n \cos(\theta - \Delta t)$, $\langle \sigma_y \rangle = (-1)^n \sin(\theta - \Delta t)$ and $\langle \sigma_z \rangle = 0$.

Tunneling between wells within a unit cell causes a density modulation. Local populations in the n^{th} cell acquire a density imbalance:

$$|\langle l_n | \psi \rangle|^2 \sim \left(1 - (-1)^n \frac{J}{\Delta} \cos(\theta - \Delta t)\right),$$

$$|\langle r_n | \psi \rangle|^2 \sim \left(1 + (-1)^n \frac{J}{\Delta} \cos(\theta - \Delta t)\right)$$

Translating by one superlattice period flips the sign of the imbalance. This shows that r_n and l_{n+1} wells, and r_{n-1} and l_n wells have the same change in density, but oscillate out of phase. Therefore, this density wave has twice the wavelength of the superlattice and is shifted spatially by half a unit cell.

RESONANCE LINE BROADENING

The spin-orbit coupling shows resonant behavior as a function of the frequency difference between the Raman beams. We attribute the broadening of the resonant line shape to 1) Doppler broadening due to the finite size of the trapped condensate 2) inhomogeneous mean-field shift due to inhomogeneous condensate density 3) inhomogeneous shift of the superlattice offset Δ due to the Gaussian beam profile.

First, the finite size of the condensate implies a distribution of momenta along the transverse direction which Doppler broadens the resonance. A momentum \mathbf{p} along x direction will shift the resonance by $\mathbf{k}_{\text{IR}} \cdot \mathbf{p}/\mathbf{m}$ considering the geometry of our setup. Therefore a condensate size x_0 results in a broadening of $\sim k_{\text{IR}}\hbar/mx_0$. Assuming a Thomas-Fermi distribution in the transverse direction, we obtain an rms width of [1]

$$\delta\nu_D = \sqrt{\frac{21}{8}} \frac{k_{\text{IR}}}{2\pi} \frac{\hbar}{mx_0}$$

where $x_0 = \sqrt{2\mu/m(2\pi\nu_x)^2}$. This gives a broadening of ~ 400 Hz.

The resonance is also broadened by the inhomogeneous density distribution of the condensate as

$$\delta\nu_M = \sqrt{\frac{8}{147}} \frac{\mu}{\hbar}$$

with μ being the chemical potential. This effect broadens the resonance by ~ 600 Hz.

The Gaussian beam profile of the long lattice implies an inhomogeneous offset Δ within the sample, therefore broadening the transition. The resulted shift is estimated to be

$$\delta\nu_I \approx 2\Delta\left(\frac{x_0}{\sigma}\right)^2$$

where σ is the Gaussian beam waist parameter. This effect broadens the resonance line by ~ 1.10 kHz. However, the broadening can be much larger for small displacement between the green and IR lattice.

The three widths add up quadratically to a value of 1.30 kHz.

The linewidth of the frequency difference of the Raman beams was negligible — it was monitored through a beat note and was ~ 50 Hz without actively phase-locking the two. We conclude that observed resonance width of 2 kHz is most likely dominated by the spread in Δ due to slight misalignment of lattice beams.

* These two authors contributed equally.

[1] J. Stenger, S. Inouye, A. P. Chikkatur, D. M. Stamper-Kurn, D. E. Pritchard, and W. Ketterle, Phys. Rev. Lett. **82**, 4569 (1999).

A stripe phase with supersolid properties in spin–orbit–coupled Bose–Einstein condensates

Jun-Ru Li^{1*}, Jeongwon Lee^{1*}, Wujie Huang¹, Sean Burchesky¹, Boris Shteynas¹, Furkan Çağrı Top¹, Alan O. Jamison¹ & Wolfgang Ketterle¹

Supersolidity combines superfluid flow with long-range spatial periodicity of solids¹, two properties that are often mutually exclusive. The original discussion of quantum crystals² and supersolidity focused on solid ⁴He and triggered extensive experimental efforts^{3,4} that, instead of supersolidity, revealed exotic phenomena including quantum plasticity and mass supertransport⁴. The concept of supersolidity was then generalized from quantum crystals to other superfluid systems that break continuous translational symmetry. Bose–Einstein condensates with spin–orbit coupling are predicted to possess a stripe phase^{5–7} with supersolid properties^{8,9}. Despite several recent studies of the miscibility of the spin components of such a condensate^{10–12}, the presence of stripes has not been detected. Here we observe the predicted density modulation of this stripe phase using Bragg reflection (which provides evidence for spontaneous long-range order in one direction) while maintaining a sharp momentum distribution (the hallmark of superfluid Bose–Einstein condensates). Our work thus establishes a system with continuous symmetry-breaking properties, associated collective excitations and superfluid behaviour.

Supersolids are defined as systems that spontaneously break two continuous U(1) symmetries: the global phase of the superfluid breaks the internal gauge symmetry, and a density modulation breaks the translational symmetry of space. Starting from superfluid Bose–Einstein condensates (BECs), several forms of supersolidity have been predicted to occur when the condensates feature dipolar interactions¹³, Rydberg interactions¹⁴, superradiant Rayleigh scattering¹⁵, nearest-neighbour interaction in lattices¹⁶ or spin–orbit interactions^{5–7}. Work simultaneous with ours used light scattering into two cavities to realize a BEC with supersolid properties¹⁷. For fermions, the predicted Fulde–Ferrell–Larkin–Ovchinnikov states have supersolid properties^{18,19}. Several of these proposals lead to solidity along a single spatial direction maintaining gaseous or liquid-like properties along the other directions. These systems are different from quantum crystals, but share the symmetry-breaking properties.

Spin–orbit coupling occurs in solid-state materials when an electron moving at velocity \mathbf{v} through an electric field \mathbf{E} experiences a Zeeman energy term $-\mu_B \boldsymbol{\sigma} \cdot (\mathbf{v} \times \mathbf{E})$ owing to the relativistic transformation of electromagnetic fields. Here $\boldsymbol{\sigma}$ is the spin vector and μ_B is the Bohr magneton. The Zeeman term can be written as $\alpha_{ij} v_j \sigma_i / 4$, where the strength of the coupling α has the units of momentum. The $v_x \sigma_z$ term, together with the transverse magnetic Zeeman term $\beta \sigma_x$, leads to the Hamiltonian $H = ((P_x + \alpha \sigma_z)^2 + P_y^2 + P_z^2) / 2m + \beta \sigma_x$, where m is the atomic mass. A unitary transformation can shift the momenta by $\alpha \sigma_z$, resulting in

$$H = \frac{P^2}{2m} + \begin{pmatrix} 0 & \beta e^{2i\alpha x} \\ \beta e^{-2i\alpha x} & 0 \end{pmatrix} \quad (1)$$

The second term represents a spin-flip process with a momentum transfer of 2α , which is therefore equivalent to a form of spin–orbit

coupling. Such a spin-flip process can be directly implemented for ultracold atoms using a two-photon Raman transition between the two spin states^{10,20}.

Without spin–orbit coupling, a BEC populating two spin states shows no spatial interference, owing to the orthogonality of the states. With spin–orbit coupling, each spin component has now two momentum components (0 and either $+2\alpha$ or -2α , where the sign depends on the initial spin state), which form a stationary spatial interference pattern with a wavevector of 2α (Fig. 1a). Such spatial periodicity of the atomic density can be directly probed with Bragg scattering²¹, as shown in Fig. 1b. The position of the stripes is determined by the relative phase of the two condensates. This spontaneous phase breaks continuous translational symmetry. The two broken U(1) symmetries are reflected in two long-wavelength collective excitations (the Goldstone modes), one for density (or charge), the other one for spin transport⁹. Adding a longitudinal Zeeman term $\delta_0 \sigma_z$ to equation (1) leads to a rich phase diagram^{6,22} as a function of δ_0 and β . For sufficiently large $|\delta_0|$, the ground state is in a plane-wave phase. This phase has a roton gap^{9,11}, which decreases when $|\delta_0|$ is reduced, causing a roton instability and leading to a phase transition into the stripe phase.

Most experimental studies of spin–orbit coupling with ultracold atoms used two hyperfine ground states coupled by a two-photon Raman spin-flip process^{10–12,23–26}. So far direct evidence of the spatial modulation pattern has been missing, possibly suppressed by stray magnetic fields detuning the Raman transitions and low miscibility between the hyperfine states used (see Methods). Both limitations were recently addressed by a new spin–orbit coupling scheme in which orbital states (the lowest two eigenstates in an asymmetric double-well potential) are used as the pseudospins²⁷. Since the eigenstates mainly populate different wells, their interaction strength g_{\perp} is small and can be adjusted by adjusting their spatial overlap, improving the miscibility (see Methods). Furthermore, since both pseudospin states have the same hyperfine state, there is no sensitivity to magnetic fields. The scheme is realized with a coherently coupled array of double wells using an optical superlattice, a periodic structure with two lattice sites per unit cell with intersite tunnelling J (Fig. 2a). The superlattice has two low-lying bands, split by the energy difference Δ between the double wells, each hosting a BEC in the respective band minima. The BECs in the lower and upper band minima are the pseudospin states in our system. Spin–orbit coupling and the supersolid stripes are created for the free-space motion in the two-dimensional plane orthogonal to the superlattice. The physics in a single two-dimensional plane is not modified in a stack of coherently coupled double wells. However, this increases the signal-to-noise ratio and suppresses the background to the Bragg signal (see below).

Experiments started with approximately 1×10^5 ²³Na atoms forming a BEC loaded into the optical superlattice along the z direction, equally split between the two pseudospin states with a density $n \approx 1.5 \times 10^{14} \text{ cm}^{-3}$. The superlattice consists of laser beams at

¹Department of Physics, MIT-Harvard Center for Ultracold Atoms, and Research Laboratory of Electronics, MIT, Cambridge, Massachusetts 02139, USA.

*These authors contributed equally to this work.

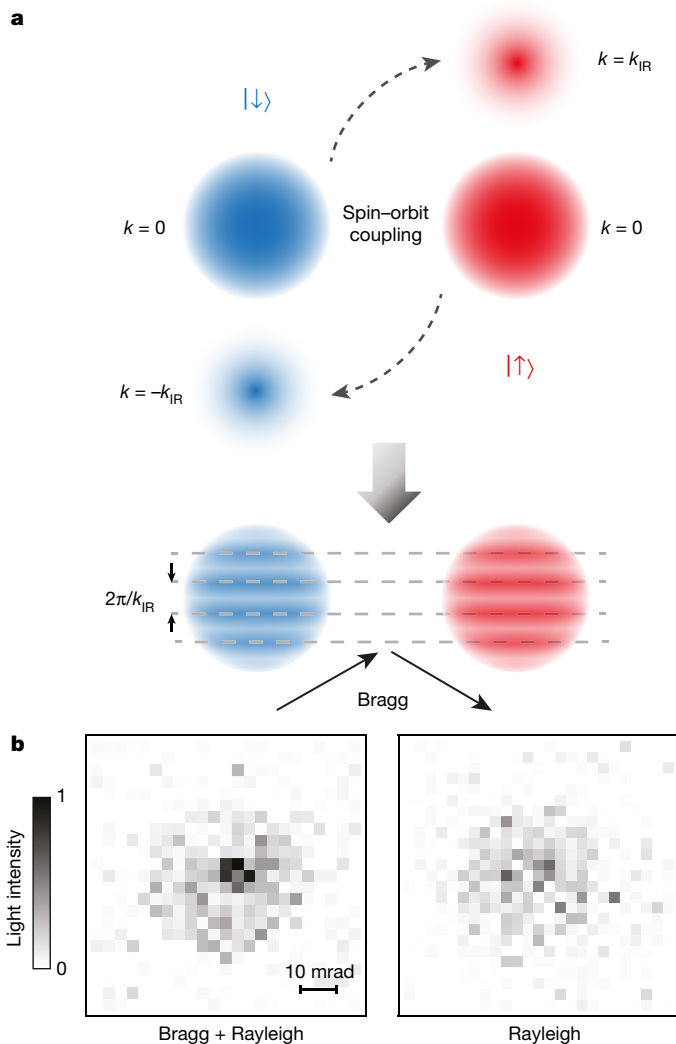


Figure 1 | Origin of supersolid stripes and detection via Bragg scattering. **a**, Supersolid stripes from spin-orbit coupling. Spin-orbit coupling adds momentum components $+\hbar k_{\text{IR}}$ or $-\hbar k_{\text{IR}}$ of the opposite spin state to the spin-up and spin-down BECs (at the top are spin states in momentum space). Matter wave interference leads to a spatial density modulation of period $2\pi/k_{\text{IR}}$ (at the bottom are spin states in real space). The spatial periodicity can be directly probed by Bragg scattering. **b**, Angle-resolved Bragg signal. The supersolid stripe phase is detected by angle-resolved light scattering. A sharp specular feature in the left panel is the Bragg signal due to the periodic density modulation. The diffuse signal is Rayleigh scattering filling the round aperture of the imaging system. Without spin-orbit coupling, only Rayleigh scattering is observed (right panel). The figure is the average over seven shots.

wavelengths of 1,064 nm and 532 nm, resulting in a lattice constant of $d = 532$ nm. Spin-orbit coupling was induced by two infrared (IR) Raman laser beams $\lambda_{\text{IR}} = 1,064$ nm along the x and z axes, providing a momentum transfer $\hbar \mathbf{k}_{\text{Raman}} = \hbar(k_{\text{IR}}, 0, k_{\text{IR}})$ and spin flip from one well to the other with two-photon Rabi frequency Ω . Here $\hbar k_{\text{IR}} = 2\pi\hbar/\lambda_{\text{IR}}$ is the recoil momentum from a single infrared photon (see ref. 27 and Methods). The scheme realizes the spin-orbit Hamiltonian in equation (1) with $\alpha = k_{\text{IR}}/2$, $\beta = (1/\sqrt{2})J\Omega/\Delta$, and an extra Zeeman term $\delta_0\sigma_z = (\delta - \Delta)/2\sigma_z$, depending on the Raman-beam detuning δ and the superlattice offset Δ . The parameters J , Ω and Δ are determined from calibration experiments²⁷. A separate laser beam was added in the x - y plane to enable detection of the stripes, which form perpendicularly to the superlattice with a periodicity of approximately $2d = 1,064$ nm. Their detection requires near-resonant yellow light (Bragg probe light wavelength $\lambda_{\text{Bragg}} = 589$ nm) at an incident angle $\theta = 16^\circ$, fulfilling the Bragg condition $\lambda_{\text{Bragg}} = 4d\sin\theta$.

Figure 1b shows the angular distribution of the Rayleigh-scattered light induced by the 589-nm laser at $\delta_0 = 0$ in the Bragg direction (see Methods). The spin-orbit coupling leads to supersolid stripes and causes a specular reflection of the Bragg beam, observed as a sharp feature in the angular distribution of the Rayleigh-scattered light (Fig. 1b). The angular width (full-width at half-maximum, FWHM) of the observed peak of 9 ± 1 mrad is consistent with the diffraction limit of λ_{Bragg}/D , where D is the FWHM size of the cloud, demonstrating phase coherence of the stripes throughout the whole cloud. This observation of the Bragg-reflected beam is our main result, and constitutes a direct observation of the stripe phase with long-range order. For the same parameters, we observe sharp momentum peaks in time of flight²⁷—the signature of BECs—which implies superfluidity.

Our detection of the stripe phase is almost background-free, since all other density modulations have different directions, as depicted in Fig. 2a. The superlattice is orthogonal to the stripes, along the z axis. The Raman beams form a moving lattice and create a propagating density modulation at an angle of 45° to the superlattice, parallel to $\hat{x} + \hat{z}$. The pseudospin state in the upper band of the superlattice forms at the minimum of the band at a quasimomentum of $q = \pi/d$. The wavevector of the stripes is the sum of this quasimomentum and the momentum transfer that accompanies the spin-flip of the spin-orbit coupling interaction²⁷, resulting in a stripe wavevector in the x direction. Since the difference in the wavevectors between the off-resonant density modulation and the stripes is not a reciprocal lattice vector, the Bragg condition cannot be simultaneously fulfilled for both density modulations. This background-free Bragg detection of the stripes uniquely depends on the realization of a coherent array of planar spin-orbit-coupled systems.

For a pure condensate, the contrast of the density modulation is predicted^{5,6} to be $\eta = 2\beta/E_r$, which is about 8% for $\beta \approx 300$ Hz. Here $E_r = 7.6$ kHz is the ^{23}Na recoil energy for a single 1,064-nm photon. A sinusoidal density modulation of ηN_{BEC} (where N_{BEC} is the number of atoms in the BEC) atoms gives rise to a Bragg signal equivalent to $\gamma(\eta N_{\text{BEC}})^2/4$, where γ is the independently measured Rayleigh scattering signal per atom per solid angle, and the factor $1/4$ is the Debye-Waller factor for a sinusoidal modulation. In Fig. 2b, we observed the expected behaviour of the Bragg signal to be proportional to N_{BEC}^2 with the appropriate pre-factors. The prediction for the signal assumes that the stripes are long-range-ordered throughout the whole cloud. If there were m domains, the signal would be m times smaller. Therefore, the observed strength of the Bragg signals confirms the long-range coherence already implied by the sharpness of the angular Bragg peak. Another way to quantify the Bragg signal is to define the ratio of the peak Bragg intensity to the Rayleigh intensity as ‘gain’, which is calculated to be $N_{\text{total}}(f\beta/E_r)^2$, where $f = N_{\text{BEC}}/N_{\text{total}}$ is the condensate fraction. The inset of Fig. 2b shows the normalized gain as a function of condensate fraction squared. The linear fit to the data points is consistent with a y -axis intercept of zero. This shows that the observed gain comes only from the superfluid component of the atomic sample. Figure 2c shows that the Bragg signal increases with larger spin-orbit-coupling strength up to $\beta \approx 300$ Hz, and starts to decrease owing to heating from the Raman driving (see Methods).

Figure 3a shows the phase diagram for spin-orbit-coupled BECs for the parameters implemented in this work. The stripe phase is wide, owing to the high miscibility of the two orbital pseudospin states. Our spin-orbit coupling scheme and the one previously used^{10,11} with ^{87}Rb are complementary. In ^{87}Rb , the phase-separated and the single-minimum states were easily observed^{10,11}, whereas our scheme favours the stripe phase.

Exploring the phase diagram in the vertical direction requires varying δ_0 with the two Raman beams detuned. For $\delta_0 = 0$, spin-orbit coupling leads to two degenerate spin states. For sufficiently large values of $|\delta_0|$, the ground state is the lower spin state. The vertical width of the stripe phase in Fig. 3a depends on the miscibility of the two spin components^{6,22}. However, population relaxation between the two spin states is very slow¹⁰. For our parameters, the equal population of the two pseudospin states is constant during the lifetime of the system for

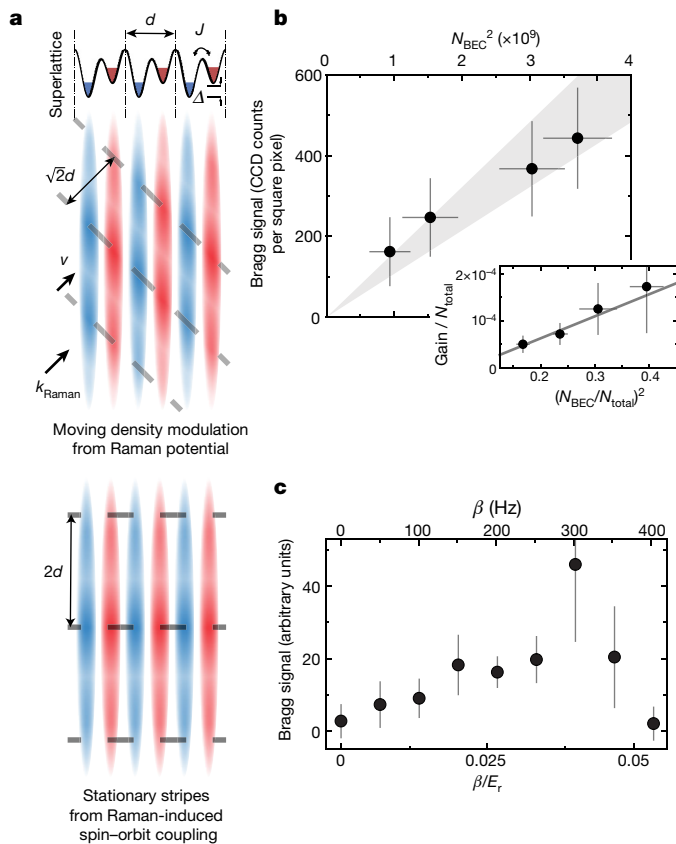


Figure 2 | Density modulations from Raman beams, and quantitative studies of the supersolid stripes. **a**, Effect of Raman beams. The two lowest bands of the superlattice are mapped into orbital pseudospins, where the pseudospin down state (localized in the left wells of the superlattice) is shown in blue and the pseudospin up state (localized in the right wells of the superlattice) is shown in red. Coupling the pseudospins with Raman laser beams causes two different types of density modulations; one is a moving density modulation caused by the moving lattice potential, and the other is the stationary stripes from Raman-induced spin-orbit coupling between the pseudospins. The stationary stripes along the free-space x direction break the continuous translational symmetry. **b**, BEC number dependence. Bragg signal is plotted versus the BEC number, showing the count rate integrated over the Bragg peak. The grey wedge is the theoretical prediction without any adjustable parameters, using independently measured values of β and γ (and the corresponding 1σ errors) along with the theoretical Debye–Waller factor, assuming full phase coherence of the stripes. The simple theory (see main text) predicts the peak angular amplitude of the Bragg signal. To compare it to the total count rate, we assumed a Gaussian lineshape with a constant linewidth. The linewidth was obtained by averaging the widths obtained from two-dimensional Gaussian fits to the data for each condensate number. The inset shows the normalized gain as the BEC fraction is varied. The grey solid line is a linear fit, where the y -axis intercept is consistent with zero, within 2σ fitting error. **c**, Spin-orbit-coupling dependence. Bragg signal versus Raman coupling strength β at zero Raman detuning is shown. Error bars represent 1σ standard error of the mean with a sample size of 3 to 4.

all detunings $|\delta_0|$ studied (up to ± 10 kHz). Therefore, detection of the stripes is possible even for large detuning.

We observed peaked Bragg reflection at $\delta_0 \approx \pm 0.7E_r$, which was characterized previously as spin-flip resonances coupling $|\uparrow, P=0\rangle$ to $|\downarrow, P=-\hbar k_{\text{IR}}\rangle$ and $|\downarrow, P=0\rangle$ to $|\uparrow, P=-\hbar k_{\text{IR}}\rangle$ (Fig. 3b). These peaks show that density modulations are resonantly created in either the $|\uparrow\rangle$ or $|\downarrow\rangle$ states. In addition, we observed a third peak around $\delta_0=0$, where the stripe pattern is stationary. For finite δ_0 , it moves at a velocity of δ_0/k_{IR} . Our observation shows that the stationary stripe pattern is either more stable or has higher contrast compared to a moving stripe. Since the tunnel coupling along the superlattice direction is weak (about 1 kHz) it seems possible that the alignment of moving stripe patterns

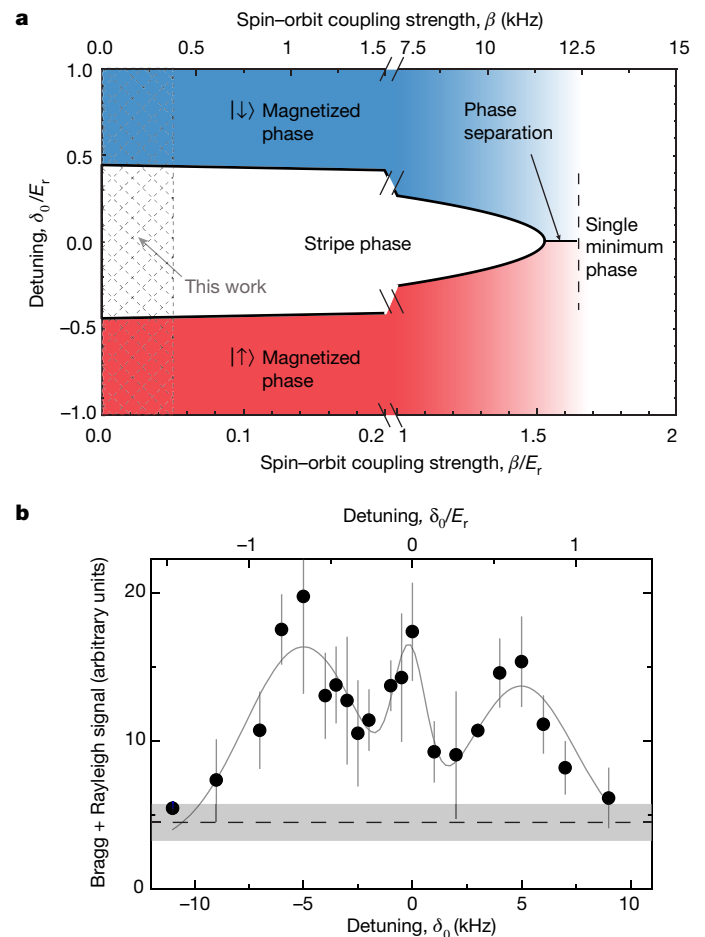


Figure 3 | Phase diagram for spin-orbit-coupled BECs, and effect of Raman detuning on the supersolid stripes. **a**, Mean-field phase diagram of spin-orbit-coupled BECs as a function of detuning and spin-orbit-coupling strength with $n \approx 1.5 \times 10^{14} \text{ cm}^{-3}$. The parameter space explored in this work is crosshatched in grey. However, owing to metastability, our effective detuning is always zero (see text). **b**, Detuning dependence. Black filled circles show the total light scattering signal (Bragg and Rayleigh) as a function of the frequency detuning. The light was detected within a solid angle of 10 mrad. The grey dashed line and shaded area show the mean and standard deviation of the Rayleigh scattered light for the same conditions. The light-grey solid line is a triple Gaussian fit to the total light scattering where the widths and centre positions of the two outer peaks are constrained to be identical to the spin-flip resonances studied in our previous work²⁷. Error bars represent 1σ standard error of the mean with a sample size of 3 to 6.

is more sensitive to perturbations than for stationary stripes and leads to a reduced Debye–Waller factor for moving stripes.

The periodicity of the supersolid density modulation can depend on external, single-atom, and two-atom parameters. In the present case, the periodicity is given by the wavelength and geometry of the Raman beams. It is then further modified by the spin gap parameter β and the interatomic interactions^{5,6} to become $2d/\sqrt{1-(\beta/F)^2}$, where $F=(2E_r+n(g+g_{\perp}))/4$. For $\beta \approx 300$ Hz, the correction due to the interactions is only 0.4% and was not detected in our work. In contrast, for the dipolar supersolid¹³ and a quantum crystal with vacancies^{1,2}, the periodicity dominantly depends on atomic interactions.

So far, we have presented a supersolid that breaks the continuous translational symmetry in the free-space x direction (Fig. 2a). Unrelated to the presence of spin-orbit coupling, our superlattice system also breaks a discrete translational symmetry along the lattice direction \hat{z} by forming a spatial period that is twice that of the external lattice owing to the interference between atoms in the two pseudospin states with quasimomentum difference $\Delta q = \pi/d$ (Fig. 4a) (see ref. 27). This fulfils the definition of a lattice supersolid^{19,28}. This 1,064-nm-period

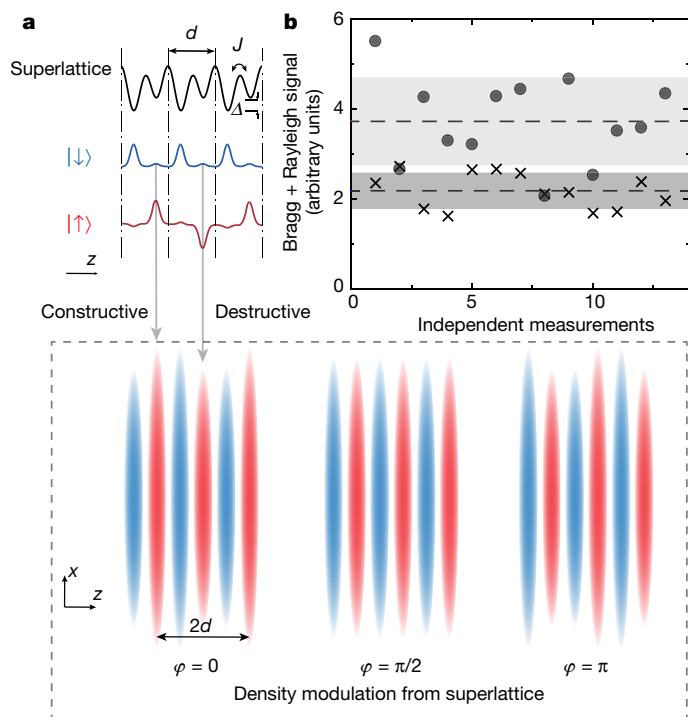


Figure 4 | Bragg detection of a lattice supersolid caused by an antiferromagnetic spin texture. **a**, Phase-sensitive density modulation of the lattice supersolid. The interference between the pseudospin down and up states alternates between constructive and destructive for adjacent unit cells in the lattice. This generates an oscillating density modulation, which has a spatial periodicity of $2d$ along the superlattice direction \hat{z} and depends on the relative phases between the orbital pseudospins as $\varphi = \varphi_0 + \Delta t$, with φ_0 as the spontaneous phase. The density modulations at different phase conditions are shown below (in the dashed box). This breaks the discrete symmetry of the lattice potential. **b**, The Bragg signal for independent measurements with $n \approx 1.5 \times 10^{14} \text{ cm}^{-3}$. The Bragg signal, which is set up for detection of a spatial periodicity of $2d$ along the superlattice, depends on the relative phase φ when the Bragg pulse width is shorter than $1/(2\Delta)$. Black crosses show the Rayleigh-scattered background integrated over 40 mrad before the antiferromagnetic spin texture develops. Grey filled circles show Bragg-enhanced scattering. The Bragg enhancement fluctuated between zero and a factor of two, which indicates variations of the spontaneous phase φ_0 between independent measurements.

density modulation has a maximum amplitude of (J/Δ) and oscillates at frequency 2Δ temporally with spontaneous initial phase and can be detected with the same geometry of the Bragg beam and camera, but rotated to the y - z plane. Figure 4b shows the observed enhanced light scattering due to Bragg reflection. The enhancement was absent immediately after preparing an equal mixture of the two pseudospin states, both in $q = 0$, and appeared spontaneously after the upper pseudospin state relaxed to the band minimum at $q = \pi/d$. With the Bragg pulse duration shorter than $1/(2\Delta)$, the Bragg signal varied between 0% and 100%, depending on the phase of the oscillation of the density modulation when probed. The increased fluctuation in Fig. 4b shows the random nature of the initial phase, which is consistent with spontaneous symmetry breaking.

In conclusion, we have observed the long-predicted supersolid stripe phase of spin-orbit-coupled BECs. This realizes a system that simultaneously has off-diagonal and diagonal long-range order. In the future, it will be interesting to characterize this system's collective excitations⁹ and to find ways to extend it to two-dimensional spin-orbit coupling, which leads to a different and rich phase diagram²⁹. Another direction for future research is the study of vortices and the effects of impurities and disorder in different phases of spin-orbit-coupled condensates³⁰.

Online Content Methods, along with any additional Extended Data display items and Source Data, are available in the online version of the paper; references unique to these sections appear only in the online paper.

Received 26 October 2016; accepted 14 January 2017.

- Boninsegni, M. & Prokof'ev, N. V. Supersolids: what and where are they? *Rev. Mod. Phys.* **84**, 759–776 (2012).
- Chester, G. V. Speculations on Bose-Einstein condensation and quantum crystals. *Phys. Rev. A* **2**, 256–258 (1970).
- Kim, E. & Chan, M. H. W. Probable observation of a supersolid helium phase. *Nature* **427**, 225–227 (2004).
- Kuklov, A. B., Pollet, L., Prokof'ev, N. V. & Svistunov, B. V. Quantum plasticity and supersolid response in helium-4. *Phys. Rev. B* **90**, 184508 (2014).
- Li, Y., Pitaevskii, L. P. & Stringari, S. Quantum tricriticality and phase transitions in spin-orbit-coupled Bose-Einstein condensates. *Phys. Rev. Lett.* **108**, 225301 (2012).
- Ho, T.-L. & Zhang, S. Bose-Einstein condensates with spin-orbit interaction. *Phys. Rev. Lett.* **107**, 150403 (2011).
- Wang, C., Gao, C., Jian, C.-M. & Zhai, H. Spin-orbit coupled spinor Bose-Einstein condensates. *Phys. Rev. Lett.* **105**, 160403 (2010).
- Han, W., Juzeliūnas, G., Zhang, W. & Liu, W.-M. Supersolid with nontrivial topological spin textures in spin-orbit-coupled Bose gases. *Phys. Rev. A* **91**, 013607 (2015).
- Li, Y., Martone, G. I., Pitaevskii, L. P. & Stringari, S. Superstripes and the excitation spectrum of a spin-orbit-coupled Bose-Einstein condensate. *Phys. Rev. Lett.* **110**, 235302 (2013).
- Lin, Y.-J., Jiménez-García, K. & Spielman, I. B. Spin-orbit-coupled Bose-Einstein condensates. *Nature* **471**, 83–86 (2011).
- Ji, S.-C. *et al.* Softening of roton and phonon modes in a Bose-Einstein condensate with spin-orbit coupling. *Phys. Rev. Lett.* **114**, 105301 (2015).
- Ji, S.-C. *et al.* Experimental determination of the finite-temperature phase diagram of a spin-orbit coupled Bose gas. *Nat. Phys.* **10**, 314–320 (2014).
- Giovannazzi, S., O'Dell, D. & Kurizki, G. Density modulations of Bose-Einstein condensates via laser-induced interactions. *Phys. Rev. Lett.* **88**, 130402 (2002).
- Henkel, N., Nath, R. & Pohl, T. Three-dimensional roton excitations and supersolid formation in Rydberg-excited Bose-Einstein condensates. *Phys. Rev. Lett.* **104**, 195302 (2010).
- Ostermann, S., Piazza, F. & Ritsch, H. Spontaneous crystallization of light and ultracold atoms. *Phys. Rev. X* **6**, 021026 (2016).
- Wessel, S. & Troyer, M. Supersolid hard-core bosons on the triangular lattice. *Phys. Rev. Lett.* **95**, 127205 (2005).
- Léonard, J. *et al.* Supersolid formation in a quantum gas breaking a continuous translational symmetry. *Nature* <http://dx.doi.org/10.1038/nature21067> (2017).
- Bulgac, A. & Forbes, M. M. Unitary Fermi supersolid: the Larkin-Ovchinnikov phase. *Phys. Rev. Lett.* **101**, 215301 (2008).
- Chen, Y., Ye, J. & Tian, G. Classification of a supersolid: trial wavefunctions, symmetry breaking and excitation spectra. *J. Low Temp. Phys.* **169**, 149–168 (2012).
- Stanescu, T. D., Anderson, B. & Galitski, V. Spin-orbit coupled Bose-Einstein condensates. *Phys. Rev. A* **78**, 023616 (2008).
- Miyake, H. *et al.* Bragg scattering as a probe of atomic wave functions and quantum phase transitions in optical lattices. *Phys. Rev. Lett.* **107**, 175302 (2011).
- Martone, G. I. Visibility and stability of superstripes in a spin-orbit-coupled Bose-Einstein condensate. *Eur. Phys. J. Spec. Top.* **224**, 553–563 (2015).
- Burdick, N. Q., Tang, Y. & Lev, B. Long-lived spin-orbit-coupled degenerate dipolar Fermi gas. *Phys. Rev. X* **6**, 031022 (2016).
- Cheuk, L. W. *et al.* Spin-injection spectroscopy of a spin-orbit coupled Fermi gas. *Phys. Rev. Lett.* **109**, 095302 (2012).
- Wang, P. *et al.* Spin-orbit coupled degenerate Fermi gases. *Phys. Rev. Lett.* **109**, 095301 (2012).
- Song, B. *et al.* Spin-orbit coupled two-electron Fermi gases of ytterbium atoms. *Phys. Rev. A* **94**, 061604(R) (2016).
- Li, J. *et al.* Spin-orbit coupling and spin textures in optical superlattices. *Phys. Rev. Lett.* **117**, 185301 (2016).
- Baumann, K., Guerlin, C., Brennecke, F. & Esslinger, T. Dicke quantum phase transition with a superfluid gas in an optical cavity. *Nature* **464**, 1301–1306 (2010).
- Sun, Q., Wen, L., Liu, W.-M., Juzeliūnas, G. & Ji, A.-C. Tunneling-assisted spin-orbit coupling in bilayer Bose-Einstein condensates. *Phys. Rev. A* **91**, 033619 (2015).
- Zhai, H. Degenerate quantum gases with spin-orbit coupling. *Rep. Prog. Phys.* **78**, 026001 (2015).

Acknowledgements We thank S. Stringari for discussions and W. C. Burton for reading the manuscript. We acknowledge support from the NSF through the Center for Ultracold Atoms and from award 1506369, from ARO-MURI Non-equilibrium Many-body Dynamics (grant W911NF-14-1-0003) and from AFOSR-MURI Quantum Phases of Matter (grant FA9550-14-1-0035).

Author Contributions J.-R.L., W.H., J.L., B.S., S.B., F.C.T. and A.O.J. contributed to the building of the experiment. J.-R.L. led the experimental efforts. J.L. led the data analysis and simulations. W.H., J.-R.L. and W.K. conceived the experiment. All authors contributed to the writing of the manuscript.

Author Information Reprints and permissions information is available at www.nature.com/reprints. The authors declare no competing financial interests. Readers are welcome to comment on the online version of the paper. Correspondence and requests for materials should be addressed to J.-R.L. (junruli@mit.edu).

Reviewer Information Nature thanks K. Hazzard and the other anonymous reviewer(s) for their contribution to the peer review of this work.

METHODS

Experimental setup and sample preparation. The superlattice (SL) potential $V(z) = V_{\text{IR}} \sin^2(k_{\text{IR}}z + \phi_{\text{SL}}) + V_{\text{Green}} \sin^2(k_{\text{Green}}z)$ was generated by overlapping two one-dimensional lattices with spacing $\lambda_{\text{IR}}/2 = 532$ nm (long) and $\lambda_{\text{Green}}/2 = 266$ nm (short). The relative phase ϕ_{SL} is controlled by the frequency of the 1,064-nm lattice light for rapid switching and a rotatable dispersive glass plate in the lattice beam path. The offset Δ is determined by V_{IR} and ϕ_{SL} and is calibrated by observing the oscillation of the interference pattern between atoms released from the two wells²⁷. We estimate the fluctuations of the offset parameter Δ to be within 1 kHz, caused by drifts in the air pressure that affect the relative phase ϕ_{SL} between the two lattices.

The two Raman beams were generated from the same laser and then split into two parts. The relative frequency was tuned by two independent acousto-optic modulators in each path. We prepared $N \approx 4 \times 10^5$ ²³Na atoms in a crossed optical dipole trap. An equal mixture of spin-up and spin-down states was created by first adiabatically ramping up the superlattice with an offset $\Delta = 0$ and then rapidly setting Δ to the final value by a fast frequency change of the infrared lattice²⁷. Subsequently, the Raman lasers inducing the spin-orbit coupling are adiabatically ramped up within about 10 ms followed by a variable hold time, after which the Bragg probe beam is applied.

Miscibility and the stripe phase. Achieving stable and high-contrast stripes requires miscibility of the two spin components. The difference in energy density between a BEC in the stripe phase and a phase-separated phase is $g\delta n^2 - (g - g_{\perp})n^2$ where $g = 4\pi\hbar^2 a/m$ and $g_{\perp} = 4\pi\hbar^2 a_{\perp}/m$ parameterize the interaction energy strengths between atoms in the same and in different spin states, respectively. Here a (a_{\perp}) is the interspin (intraspin) s -wave scattering length. The extra mean-field energy due to a modulation of the density n with amplitude δn leads to phase separation when the contrast of the stripes $\eta = \delta n/n$ exceeds $\sqrt{(g - g_{\perp})/g}$. All previous studies with bosons used ⁸⁷Rb atoms^{10–12}. For ⁸⁷Rb atoms in the $|F = 1, m_F = 0\rangle$ and $|F = 1, m_F = -1\rangle$ states, $(g - g_{\perp})/g = 10^{-3}$ is extremely small. In addition, the full width in δ_0 for stable stripes is $W = 2n(g - g_{\perp})$, which is about 10 Hz for ⁸⁷Rb and requires extreme control of ambient magnetic field fluctuations. For these reasons the stripe phase has not yet been observed in previous studies of spin-orbit-coupled rubidium atoms^{10–12}.

Using the orbital degree of freedom as pseudospin, Raman lights can be far-detuned from atomic transitions, suppressing spontaneous emission heating. In addition, the orbital overlap controls the intra-spin interaction $g_{\perp} \approx (J/\Delta)g$, where J is the

interwell tunnelling and Δ is the well offset²⁷. For typical experimental parameters with $(J/\Delta) \approx 1/20$, $(g - g_{\perp})/g \approx 1$. The highly imbalanced interaction enhances the miscibility and therefore allows higher contrast and more stable stripes.

Bragg beam parameters and detection. The Bragg beam was chosen to be blue-detuned about 1,030 MHz from the sodium $|3S_{1/2}, F = 1\rangle$ to $|3P_{3/2}, F = 2\rangle$ transition with a linear polarization along the superlattice direction. The detuning was chosen such that the Bragg beam can propagate through the entire condensate without much absorption or wave-front distortion.

The alignment of the Bragg beam required accurate prealignment by triangulation. A major challenge was the alignment of this beam to an accuracy of better than about 0.5° , the angular width of the Bragg signal, without any auxiliary density modulation at the same periodicity, given that creating such a density modulation would have required a standing wave of laser light at 2,128 nm. Experimentally, the lattice supersolid is more robust than the stripe phase while having the same periodicity of the density modulation. Therefore, the alignment procedure was first developed for the lattice supersolid. The same setting was rotated around the axis \hat{y} by 90° to probe for the stripe phase.

The Bragg reflected beam and the Rayleigh fluorescence were recorded with an electron multiplying charge-coupled device (CCD) camera. The angular distribution was recorded by first focusing an imaging system onto the camera and then moving the camera out of focus. The signal was normalized for fluctuating atom numbers using the fluorescence intensity monitored by a photomultiplier using a separate viewport. The Bragg signal was obtained by integrating the counts of the CCD pixels around the Bragg-matched angle. The Rayleigh signal was obtained from fitting the diffuse background with a two-dimensional Gaussian fit. The detected Bragg signal was of the order of only ten photons.

We observed a lifetime of about 20 ms for the Bragg signal after ramping up the spin-orbit coupling, accompanied by a clearly visible reduction in the number of atoms in the BEC. We believe that it is limited by the heating due to the Raman driving²⁷. At values of $\beta \approx 300$ Hz, the moving Raman lattice has a depth of about $3E_p$, which is comparable to the stationary lattice at around $10E_p$. When the spin-orbit coupling was increased further, the Bragg signal decreased, as shown in Fig. 2c, with noticeable atom loss. In addition, the observed heating may still have a contribution from technical sources, since the observed lifetime is sensitive to alignment.

Data availability. The data that support the findings of this study are available from the corresponding author upon reasonable request.

How to Dress Radio-Frequency Photons with Tunable Momentum

Boris Shteynas,^{1,‡} Jeongwon Lee,^{1,*;‡} Furkan Çağrı Top,¹ Jun-Ru Li,^{1,†} Alan O. Jamison,¹
Gediminas Juzeliūnas,² and Wolfgang Ketterle¹

¹*Research Laboratory of Electronics, MIT-Harvard Center for Ultracold Atoms, Department of Physics, Massachusetts Institute of Technology, Cambridge, Massachusetts 02139, USA*

²*Institute of Theoretical Physics and Astronomy, Vilnius University, Saulėtekio 3, Vilnius 10257, Lithuania*



(Received 18 July 2018; published 16 July 2019)

We demonstrate how the combination of oscillating magnetic forces and radio-frequency (rf) pulses endows rf photons with tunable momentum. We observe velocity-selective spin-flip transitions and the associated Doppler shift. Recoil-dressed photons are a promising tool for measurements and quantum simulations, including the realization of gauge potentials and spin-orbit coupling schemes which do not involve optical transitions.

DOI: 10.1103/PhysRevLett.123.033203

The field of cooling and trapping atoms depends on mechanical forces exerted by light through photon recoil [1]. Since photons can be scattered only by admixing electronically excited states, the mechanical forces due to light always involve dissipation by spontaneous emission. This is desirable in laser cooling but causes heating and atom loss in other situations where it is often suppressed by using far off resonant light (e.g., in optical lattices).

In this work we show how to dress radio-frequency (rf) photons with tunable recoil momentum by combining rf pulses with an oscillating magnetic force. This is a new application of Floquet engineering: periodically driven systems can have time-averaged properties which cannot be achieved with constant fields. Well-known examples are the Kapitza pendulum, Paul traps for ions, and the realization of Hamiltonians with complex tunneling matrix elements for ultracold atoms in optical lattices [2–4].

The question of how to replace photon recoil by other forces was raised in the context of spin-orbit coupling for ultracold atoms [5]. The well-established two-photon scheme is limited by heating due to spontaneous emission of photons. This limitation has motivated the development of alternative schemes which use time-dependent magnetic fields [6–9] to realize spin-dependent synthetic gauge fields. Some of those schemes are fairly complex, and have motivated the following question: Is it possible to Floquet engineer a rf or microwave transition between two spin states in such a way that it shows all aspects of recoil momentum?

With this motivation, we propose and demonstrate the new concept of recoil-dressed rf photons. This scheme allows us to conduct Doppler-sensitive spectroscopy and velocimetry of molecules when suitable optical transitions are not available. It is a building block for quantum simulations and offers a new approach for spin-orbit coupling using time-dependent magnetic forces. In our scheme, we drive rf

transitions between two different hyperfine states in the presence of an alternating magnetic field gradient. The time-averaged evolution is a rf transition where recoil momentum is transferred. The sign and magnitude of the momentum kick is adjustable via the magnetic fields, and we observe a recoil momentum for the dressed photon which is 6×10^6 higher than the (usually negligible) momentum of a bare rf photon around 8 MHz frequency.

Our scheme shows the power of Floquet engineering: we combine a rf transition, which has negligible momentum transfer, with a sinusoidally oscillating magnetic field gradient, which has no time-averaged momentum transfer, and the result is a rf photon with recoil, depending on how rf pulses are synchronized with the time-dependent magnetic field gradient.

Figure 1 shows the time sequence of our scheme, which consists of a sinusoidal spin-dependent force $f(t) = g_F \mu_B B'_0 \sin[(2\pi/T)t + \phi_{\text{rf}}] \sigma_z$, where g_F is the Lande factor, μ_B is the Bohr magneton, and B'_0 is the magnitude of the magnetic gradient, and a synchronized sequence of short rf pulses at times $t = 0, T, 2T, \dots$. The timing of the pulses with respect to the periodic force is described by the phase ϕ_{rf} which determines the magnitude of the photon recoil. Each of the rf pulses couples spin-up and spin-down states with the same momentary (i.e., at the time of the rf pulse) velocity v_{rf} . For $\phi_{\text{rf}} = 0$, the velocities averaged over a full cycle of the oscillating force, $\langle v_{\uparrow} \rangle$ and $\langle v_{\downarrow} \rangle$, are different. By flipping the spin, atoms experience an “extra” half-cycle of the magnetic acceleration [hatched area in Fig. 1(a)], which transfers them to the state with a different averaged velocity, and, therefore, provides recoil. For the case $\phi_{\text{rf}} = \pi/2$, the time-averaged velocities for spin-up and spin-down are identical to v_{rf} . Therefore, a rf transition will not change the time-averaged velocities, and there is no recoil.

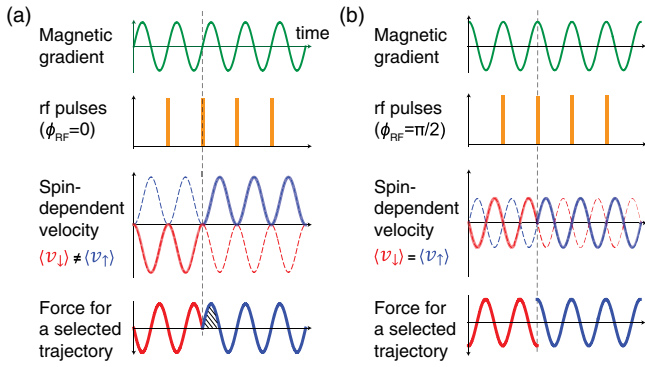


FIG. 1. Illustration of our scheme for creating a tunable atomic recoil momentum with rf transitions using magnetic forces. Panels (a) and (b) show the experimental conditions for $\phi_{\text{rf}} = 0$ and $\phi_{\text{rf}} = \pi/2$, respectively. The spin-dependent forces and velocities are shown (as thick solid lines) for the amplitude of the wave function which is transferred from spin-down (red) to -up (blue) by the rf pulse marked by the gray dashed line. For $\phi_{\text{rf}} = 0$, the average velocities $\langle v_{\downarrow} \rangle$ and $\langle v_{\uparrow} \rangle$ are different, which implies a finite recoil associated with the spin flip. In contrast, $\langle v_{\downarrow} \rangle = \langle v_{\uparrow} \rangle$ for $\phi_{\text{rf}} = \pi/2$, and there is no recoil.

Using this semiclassical picture, we obtain for the amount of momentum transfer $\hbar k = m(\langle v_{\uparrow} \rangle - \langle v_{\downarrow} \rangle) = \hbar k_0 \cos \phi_{\text{rf}}$, where $k_0 = (g_F \mu_B / \pi \hbar) B'_0 T$. Next we discuss where the change in kinetic energy comes from. For an optical transition with recoil $\hbar k$ and an atom moving at initial velocity v_{in} , the resonance frequency is shifted by the Doppler shift $k v_{\text{in}}$ and recoil shift $(\hbar k)^2 / 2m$, which ensures energy conservation. However, in the current situation, energy can also come from the time-dependent magnetic force. Indeed, if we would apply a single rf π pulse at phase $\phi_{\text{rf}} = 0$, the time-averaged velocity would change by $\hbar k_0 / m$, but the rf resonance frequency would be independent of velocity and k_0 . However, if a series of rf pulses is used, as in (Fig. 1), the resonance is Doppler shifted and becomes velocity selective. This can be seen by regarding the pulses as Ramsey pulses and considering the phase evolution of the wave function between two pulses. The rf pulses create a superposition of spin-up and spin-down. Between pulses, the phase evolution for spin-up or -down is solely determined by the kinetic energy $\alpha_{\uparrow\downarrow} = (1/\hbar) \int (m v_{\uparrow\downarrow}^2 / 2) dt$, leading to a phase difference $\delta\alpha = (1/\hbar) (m(\langle v_{\uparrow} \rangle - \langle v_{\downarrow} \rangle) v_{\text{rf}}) T = k v_{\text{rf}} T$ after one period of shaking, where $v_{\text{rf}} = (v_{\uparrow} + v_{\downarrow}) / 2$ is the common velocity at the moment of the rf pulse. With $\langle v_{\downarrow} \rangle = v_{\text{rf}} - \hbar k / 2m$, we find that for resonant excitation, the rf has to compensate for this phase shift by the Doppler detuning $k \langle v_{\downarrow} \rangle$ and the recoil shift $(\hbar k)^2 / 2m$ (see Supplemental Material for more details [13]).

Periodic Hamiltonians are formally treated by Floquet theory [2,3,15–17], which provides an expression for an effective Hamiltonian \hat{H}_{eff} describing the slow time evolution of the system averaged over the fast micromotion with period T . However, in the standard treatment the effective

Hamiltonian is not unique and may depend on the initial time when the periodic drive is switched on. We adopt the approach of Ref. [2], where the evolution of the quantum system with periodic drive is expressed by an effective Hamiltonian independent of initial and final times t_i, t_f and a kick (micromotion) operator \hat{K} , which describes the initial kick due to a sudden switch on and the subsequent micromotion, shown as $\hat{U}(t_f, t_i) = e^{-i\hat{K}(t_f)} e^{-i\hat{H}_{\text{eff}}(t_f - t_i)} e^{i\hat{K}(t_i)}$.

For our scheme, the time-dependent Hamiltonian of the system in the frame rotating with the rf drive after the rotating-wave approximation is

$$\hat{H} = \frac{\hat{p}_z^2}{2m} + \hbar k_0 \hat{z} \frac{\pi}{T} \sin(2\pi t/T + \phi_{\text{rf}}) \hat{\sigma}_z - \frac{1}{2} \hbar \delta_{\text{rf}} \hat{\sigma}_z + \hbar \Omega \hat{\sigma}_x T \sum_n \delta(t - nT), \quad (1)$$

where δ_{rf} is the rf detuning with respect to the atomic resonant frequency and m is the atomic mass. The short rf pulses are represented as a series of delta functions with effective Rabi frequency Ω .

Through the derivation shown in the Supplemental Material [13], we obtain an explicit expression for the effective Hamiltonian and the kick operator defined above:

$$\hat{H}_{\text{eff}} = \begin{pmatrix} \frac{\hat{p}_z^2}{2m} + \frac{1}{16} \frac{\hbar^2 k_0^2}{m} - \frac{\hbar \delta_{\text{rf}}}{2} & \hbar \Omega e^{-ik_0 \cos \phi_{\text{rf}} z} \\ \hbar \Omega e^{ik_0 \cos \phi_{\text{rf}} z} & \frac{\hat{p}_z^2}{2m} + \frac{1}{16} \frac{\hbar^2 k_0^2}{m} + \frac{\hbar \delta_{\text{rf}}}{2} \end{pmatrix},$$

$$\hat{K}(t) = -ik_0 z \hat{\sigma}_z \cos\left(\frac{2\pi}{T} t + \phi_{\text{rf}}\right). \quad (2)$$

The effective Hamiltonian is identical to the one for a two-level atom driven by a photon field at frequency ω_{rf} and with wave vector k , which confirms our discussion above about recoil momentum and Doppler shift. The term $\hbar^2 k_0^2 / 16m$ is the kinetic energy due to micromotion.

We implemented this scheme using a thermal cloud of approximately 1×10^5 ^{23}Na atoms at 380 nK in a crossed optical dipole trap with trapping frequencies $(\omega_x, \omega_y, \omega_z) = 2\pi(98, 94, 25)$ Hz corresponding to Gaussian radii of 19.5, 20, and 68 μm , respectively. The $|m_F = -1\rangle$ and $|m_F = 0\rangle$ states of the $F = 1$ hyperfine manifold of the atoms were used to form a pseudospin-1/2 system, which will be referred to as $|\uparrow\rangle$ and $|\downarrow\rangle$ states, respectively. The $|m_F = 1\rangle$ state was decoupled from this two-level system through the quadratic Zeeman effect at a bias field of 11.4 G. Since there is no micromotion in the “nonmagnetic” $|m_F = 0\rangle$ state, the maximum momentum transfer $\hbar k_0$ is reduced by a factor of 2 compared to the discussion above.

The oscillating magnetic force was created by a time-dependent 3D quadrupole field. Along the bias field direction z , this provides a 1D periodic force. Orthogonal to the bias field, the periodic potential is quadratic—there is no net force, only a (negligible) modulation of the confinement.

The amplitude of the magnetic field gradient was 48 G/cm at a frequency of 5 kHz, implying a recoil $k_0 = 0.07k_L$, where $\hbar k_L$ is the recoil of the resonant transition at 589 nm, with a recoil velocity $(\hbar k_L/m) = 2.9$ cm/s.

To resolve Doppler shifts of 200 Hz, sub-mG stability was needed. Any asymmetry of the periodic magnetic field gradient leads to a time-averaged dc field gradient resulting in an inhomogeneous Zeeman shift which had to be suppressed at the 100 Hz level. Finally, the applied magnetic fields were modified by eddy currents in the stainless steel chamber, which had to be accounted for (see Supplemental Material [13]).

The goal of the experimental demonstration was to show that the rf transition is now Doppler sensitive due to the recoil transfer. The spin-flip transitions were driven by 4 μ s long rf pulses at 8 MHz with a Rabi frequency of 10 kHz resulting in approximately $\pi/12$ pulses and an average Rabi frequency of $\Omega = 200$ Hz, which is defined as the Rabi frequency of the pulse times the duty cycle. Since it was not possible to switch off the shaking coils on microsecond timescales, the rf pulses had to be applied with the magnetic shaking present, which required several steps of spatial and temporal alignments (see Supplemental Material [13]).

The rf pulses and the shaking were applied while the atoms were trapped to ensure that the velocity distribution is independent of position. In time of flight (TOF), this is no longer the case, and any residual Zeeman shift gradients could lead to velocity selection. To avoid broadening of the Doppler selected velocity groups by the trapping potential, the total interrogation was chosen to be 1.6 ms, much shorter than the trap period along the z direction. This time is also comparable to the coherence time due to the ambient magnetic field stability. Based on these considerations, we applied a pulse sequence of 2 ms consisting of 10 magnetic shaking cycles with 9 rf pulses across them.

The temperature of the cloud was chosen to be high enough that the Doppler width of 3 kHz (FWHM) was larger than our spectral resolution, mainly Fourier limited to 625 Hz by the 1.6 ms pulse sequence. Because of the Doppler shift, different detunings of the rf selected different velocity groups which were observed in ballistic expansion (Fig. 2). The width of the observed spin-flipped slices is almost completely determined by the original spatial size of the cloud since the expansion time of $\tau = 12$ ms was only twice the inverse of ω_z . The TOF was limited by the signal-to-noise ratio, given the constraints discussed above. Fortunately, even for small TOF, the displacement of the center of the spin-flipped atoms is exactly $v\tau$, which could be accurately measured as a function of rf detuning, as shown in Fig. 3. The observed Doppler shift is in agreement with the theoretical treatment above and confirms that rf photons have been Floquet engineered to have recoil of $k = 0.07k_L$.

The dependence of the recoil on the rf phase was demonstrated by shifting the rf phase from 0 to π [Fig. 3(b)]. The Doppler shift and therefore the direction

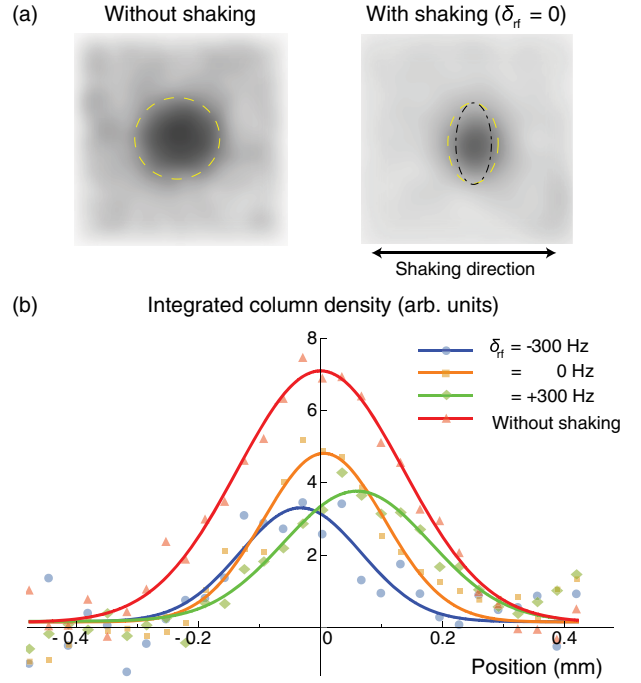


FIG. 2. Observation of velocity-selective rf transitions. (a) Absorption images of the spin-flipped atoms (i.e., in the $|m_F = -1\rangle$ state) after 12 ms of TOF with and without magnetic shaking. The yellow dashed ellipses have major and minor axes obtained as FWHM of Gaussian fits. After TOF, the thermal cloud could expand by a factor of 2.13; thus, a single-velocity class is narrower than the thermal cloud by $1/2.13 \approx 0.47$. The Fourier limit of our velocity selection increases this to 0.50, and inclusion of eddy currents further modifies it to 0.45 (dash-dotted line). The field of view is 1×1 mm². (b) Integrated column density distribution obtained from absorption images like those in (a), for different rf detunings. The solid lines are Gaussian fits to the data points. The rf phase was at $\phi_{rf} = 0$ to maximize Doppler sensitivity. The asymmetry between the ± 300 Hz is most likely caused by bias field drifts (estimated in Fig. 3 to be 70 Hz) or small residual magnetic field gradients.

of the recoil changed sign. This observation confirmed that the selection of slices in Fig. 2 is not due to time-averaged magnetic field gradients, which do not depend on the rf phase. We could not experimentally explore $\phi_{rf} = \pi/2$, since this would have required to pulse on the rf at the maximum field gradient, which would have caused large spatially dependent detunings.

Our scheme can be used to implement one-dimensional spin-orbit coupling of ultracold atoms with magnetic forces and without lasers. The Hamiltonian [Eq. (3)] which we have implemented is, by a unitary transformation, equivalent to a Hamiltonian with spin-dependent gauge fields [4]:

$$\hat{H}_{\text{SOC}} = \frac{1}{2m} \left(\hat{p}_z - \frac{1}{2} A \hat{\sigma}_z \right)^2 + \hbar \Omega \hat{\sigma}_x - \frac{\hbar \delta_{\text{rf}}}{2} \hat{\sigma}_z. \quad (3)$$

We note that Ref. [14] obtains the same Hamiltonian as the stroboscopic Floquet Hamiltonian. The gauge field

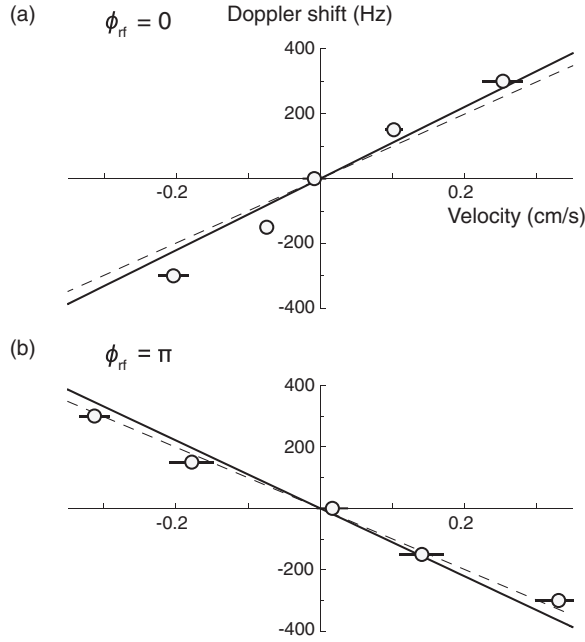


FIG. 3. Observation of rf transitions with Doppler shifts. (a), (b) Central velocities of the spin-flipped atomic distribution [as in Fig. 2(b)] are shown as a function of rf detuning for $\phi_{\text{rf}} = 0$ and $\phi_{\text{rf}} = \pi$, respectively. Shifting the rf phase changes the sign of the Doppler shift and therefore the direction of the recoil momentum. The solid line represents the predicted Doppler shifts based on the calibration of recoil momentum. The dashed line takes into account the effects of eddy currents (see Supplemental Material [13]). The error bars are purely statistical based on five data points and correspond to 1 standard deviation. The inferred 1σ fluctuations for the frequency are 70 Hz.

$A = \hbar k_0 \cos \phi_{\text{rf}}$ is equal to the recoil momentum transfer $\hbar k$, which depends on the rf phase ϕ_{rf} . Previous experimental studies claimed the realization of spin-orbit coupling and gauge fields purely by magnetic shaking, without rf transitions [8,18]. These claims are ambiguous based on our discussion here: without rf coupling, the momentum transfer and the gauge field are not defined and can be transformed away with a gauge transformation. According to Eqs. (1) and (3), pure magnetic shaking leads only to a kick operator for the micromotion, and the effective Hamiltonian is the free-particle Hamiltonian. Therefore, all observations in Refs. [8,18] are related to an initial kick and micromotion and not to a modified effective Hamiltonian.

In the presence of gauge fields, there are two momenta: the mechanical or kinetic momentum ($p_z \pm \frac{1}{2}A$) and the canonical momentum $p_z = mv_{\text{rf}}$. In our scheme, they can both be directly observed and have a very transparent meaning: the kinetic momenta are the time-averaged momenta $m\langle v_{\uparrow} \rangle$, $m\langle v_{\downarrow} \rangle$. The canonical momentum is the instantaneous momentum during the rf pulse (see Supplemental Material [13]).

Our demonstration of rf dressed photons was done with a modest recoil k_0 of $0.07k_L$ due to technical limitations

(see Supplemental Material [13]). The recoil could have been increased by using a glass cell, miniature coils, or atomic chips for which 12 times larger magnetic field gradients have been assumed [6]. Given the small value of k_0 , we did not look for recoil effects in Bose-Einstein condensates, as in Ref. [19], and rather focused on Doppler shifts in thermal clouds.

Dressed-photon recoil has several features different from optical photon recoil: The maximum recoil of a dressed photon is only technically limited, and can be tuned via the strength of the magnetic gradient and in principle also via the rf phase, whereas the recoil in a two-photon transition can be tuned via the angle between the two laser beams. Heating for optical recoil transfer is independent of momentum transfer and depends on the Rabi frequency, whereas the reverse applies to the magnetic scheme.

As in any Floquet schemes, micromotion can lead to heating when the associated kinetic energy is transferred to the secular motion by elastic collisions between the two spin states (which is equivalent to transitions between Floquet states of different quasienergies). In Ref. [20], we describe various cases (high and low temperature limit, bosons, and fermions) and conclude that the energy transfer can be expressed by $\dot{E} \propto \rho \sigma v_{\text{col}} E_0$, where v_{col} reflects an effective density of states. For Bose-Einstein condensates, $v_{\text{col}} = \sqrt{\hbar\omega/m}$ for large modulation frequencies ω , implemented in our experiments, and $v_{\text{col}} = \hbar k_0/m$ in the semiclassical regime. Here, ρ is the density and σ is the two-body s -wave scattering cross section. For a sodium condensate with two spin components and density $\rho \sim 10^{14} \text{ cm}^{-3}$, we observed a condensate lifetime of $\sim 8 \text{ s}$ at $k_0 = 0.05k_L$, consistent with weak Floquet heating [20]. If the momentum transfer k_0 is scaled up to k_L , losses increase proportional to the second or third power of k_0 , depending on the regime [20]. For momentum transfers of k_L , lifetimes larger than 100 ms will require low density clouds on the order of $\sim 10^{12} \text{ cm}^{-3}$ or small scattering lengths. For degenerate Fermi gases with $E_F \gg \hbar\omega$, heating is Pauli suppressed by a factor of $(\hbar\omega/E_F)^2$.

There are possible extensions of generating magnetic recoil. One is to use the time-averaged, orbiting potential (TOP) trap configuration [21], where a constant gradient is combined with a rotating bias field in the x - y plane, which creates a rotating force. A sequence of rf pulses generates “dressed photons” with recoil k along the $\cos \phi_{\text{rf}} \mathbf{e}_x + \sin \phi_{\text{rf}} \mathbf{e}_y$ direction. The rf phase now controls the direction of the recoil. The concept of dressed rf photons should be useful for a more general class of quantum simulations. For instance, it applies to spin-dependent forces created by the vector ac Stark shift. Using focused laser beams or lattices to create spin-dependent potentials, the effective recoil is spatially localized, and can easily be time modulated. In comparison to magnetic field gradients, the forces due to the vector ac Stark shift can be larger, and much faster modulation frequencies are possible. Using optical spin-dependent

forces instead of magnetic forces may eliminate several limitations of our scheme, especially for atoms like cesium and rubidium, where large spin-dependent optical forces can be realized without major heating by spontaneous scattering.

In conclusion, we demonstrated how magnetic shaking can be used to endow a rf photon with large and tunable recoil. This scheme illustrates many aspects of Floquet engineering, including heating in both the quantum and classical limit. This technique is a building block for quantum simulations including spin-dependent gauge fields and measurements such as Doppler velocimetry. It can be applied to any atom or molecule with nonzero spin in the ground state, and is independent of the structure of electronically excited states.

We would like to acknowledge Will Lunden for experimental assistance, Ivana Dimitrova for critical reading of the manuscript, and Viktor Novičenko for discussions. We acknowledge support from the NSF through the Center for Ultracold Atoms and Grant No. 1506369, from ARO-MURI Non-equilibrium Many-body Dynamics (Grant No. W911NF-14-1-0003), from AFOSR-MURI Quantum Phases of Matter (Grant No. FA9550-14-1-0035), from ONR (Grant No. N00014-17-1-2253), and a Vannevar-Bush Faculty Fellowship. Part of this work was performed at the Aspen Center for Physics, which is supported by NSF Grant No. PHY-1607611.

*jwlee0705@gmail.com

Present address: The Institute for Advanced Study, The Hong Kong University of Science and Technology, Clear Water Bay, Kowloon, Hong Kong.

†Present address: JILA, NIST and University of Colorado, 440 UCB, Boulder, Colorado 80309, USA.

‡B. S. and J. L. contributed equally to this work.

- [1] C. Cohen-Tannoudji, J. Dupont-Roc, and G. Grynberg, *Atom-Photon Interactions: Basic Process and Applications* (Wiley, New York, 2008).

- [2] N. Goldman and J. Dalibard, *Phys. Rev. X* **4**, 031027 (2014).
- [3] M. Bukov, L. D'Alessio, and A. Polkovnikov, *Adv. Phys.* **64**, 139 (2015).
- [4] J. Dalibard, F. Gerbier, G. Juzeliūnas, and P. Öhberg, *Rev. Mod. Phys.* **83**, 1523 (2011).
- [5] V. Galitski and I. B. Spielman, *Nature (London)* **494**, 49 (2013).
- [6] B. M. Anderson, I. B. Spielman, and G. Juzeliūnas, *Phys. Rev. Lett.* **111**, 125301 (2013).
- [7] Z.-F. Xu, L. You, and M. Ueda, *Phys. Rev. A* **87**, 063634 (2013).
- [8] X. Luo, L. Wu, J. Chen, Q. Guan, K. Gao, Z.-F. Xu, L. You, and R. Wang, *Sci. Rep.* **6**, 18983 (2016).
- [9] For relevant work with modulated magnetic field in optical lattices, see Refs. [10–12].
- [10] J. Struck, J. Simonet, and K. Sengstock, *Phys. Rev. A* **90**, 031601(R) (2014).
- [11] G. Jotzu, M. Messer, F. Görg, D. Greif, R. Desbuquois, and T. Esslinger, *Phys. Rev. Lett.* **115**, 073002 (2015).
- [12] J. Yu, Z.-F. Xu, R. Lü, and L. You, *Phys. Rev. Lett.* **116**, 143003 (2016).
- [13] See Supplemental Material at <http://link.aps.org/supplemental/10.1103/PhysRevLett.123.033203> for the derivation of the effective Hamiltonian, which includes Refs. [2,6,14].
- [14] See Supplemental Material in X. Luo, L. Wu, J. Chen, Q. Guan, K. Gao, Z.-F. Xu, L. You, and R. Wang, *Sci. Rep.* **6**, 18983 (2016).
- [15] A. Eckardt and E. Anisimovas, *New J. Phys.* **17**, 093039 (2015).
- [16] V. Novičenko, E. Anisimovas, and G. Juzeliūnas, *Phys. Rev. A* **95**, 023615 (2017).
- [17] A. Eckardt, *Rev. Mod. Phys.* **89**, 011004 (2017).
- [18] L.-N. Wu, X.-Y. Luo, Z.-F. Xu, M. Ueda, R. Wang, and L. You, *Sci. Rep.* **7**, 46756 (2017).
- [19] Y.-J. Lin, K. Jimenez-Garcia, and I. B. Spielman, *Nature (London)* **471**, 83 (2011).
- [20] J.-R. Li, B. Shteynas, and W. Ketterle, [arXiv:1906.08747](https://arxiv.org/abs/1906.08747).
- [21] W. Petrich, M. H. Anderson, J. R. Ensher, and E. A. Cornell, *Phys. Rev. Lett.* **74**, 3352 (1995).

Supplemental Material for “How to dress radio-frequency photons with tunable momentum”

(Dated: June 21, 2019)

EXPERIMENTAL IMPLEMENTATION OF MAGNETIC SHAKING

To realize magnetic shaking, we drove a sinusoidal current through a pair of anti-Helmholtz coils along the x -axis while there was a fixed bias field of 11.4 G aligned to the z -axis. The sinusoidal current was provided by a DC power supply and four insulated gate bipolar transistors connected in an H-bridge configuration. The transistors created a square wave voltage modulation, which resulted in a sinusoidal current due to the frequency response of the coils. A capacitor was connected in series to eliminate the imaginary component of the impedance coming from the inductance of the coils. The amplitudes of the current and the voltage were 70 A and 70 V. The real impedance of 1Ω is mainly due to eddy currents in the stainless steel vacuum chamber and is much larger than the resistance of the coils (0.1Ω). The combined fields result in a periodic 1D magnetic force along the z -axis $B'_z(t) = B'_0 \sin(\omega t + \phi_{RF})$, where $B'_0 = 48$ G/cm, $\omega = 2\pi \times 5$ kHz, and ϕ_{RF} is determined from the relative phase between the magnetic gradient modulation and the radio frequency (RF) pulses. Larger recoil momenta can be realized by either increasing B'_0 or decreasing ω . The field gradient was calibrated using Stern-Gerlach deflection during ballistic expansion of a Bose-Einstein condensate. We also calibrated the recoil k_0 directly by measuring the momentum transfer to a cloud in the $|m_F = -1\rangle$ state during a half-cycle of the magnetic shaking. The two calibrations agreed to within the accuracy of measurement.

ADJUSTMENTS TO THE MAGNETIC FIELD PROFILE

The observation of Doppler shifts at the 200 Hz level required careful control of Zeeman shifts. Three critical adjustments were done.

(1) *Symmetry of the modulated magnetic field gradient*: If inhomogeneous Zeeman shifts across the cloud are comparable or larger than Doppler shifts, the spinflips are no longer velocity selective since there is always a local Zeeman shift to compensate for the Doppler shift. Therefore, the magnetic field gradient averaged over one modulation cycle $\langle B' \rangle$, had to be zeroed: $g_F \mu_B \langle B' \rangle D \ll kv$, where D is the length of the cloud. To avoid transient asymmetries from the turn-on process of the periodic magnetic gradient, we added a pre-shaking period of 3 ms before the spectroscopic sequence. This didn't affect the trapped atom cloud, since the atoms were initially in the non-magnetic $|m_F = 0\rangle$ state. After the pre-shaking, we achieve $\langle B' \rangle \approx 20$ mG/cm, implying a time-averaged differential Zeeman shift across the cloud of less than 100 Hz. $\langle B' \rangle$ was determined from converting the measurement of time-averaged current asymmetry to the time-averaged magnetic gradient asymmetry using the Stern-Gerlach calibration. As a final check, we added asymmetries on either the positive or negative side of the sinusoidal current to create $\langle B' \rangle \approx \pm 100$ mG/cm, and for both cases observed a slight increase in the width of the velocity-selected atom slice confirming that the residual asymmetry of the magnetic gradient modulation was negligibly small.

The following two adjustments addressed the issue that the RF pulses were not delta functions, but had a duration of $4 \mu\text{s}$. The presence of Zeeman shifts comparable or larger than the Fourier width of a single pulse would reduce the RF pulse area. For our parameters, a 45 kHz detuning will reduce the pulse area by 5 percent (and therefore the single pulse excitation probability by 10 percent).

(2) *Minimize modulation of magnetic bias field*: The time-dependent gradient creates also a time-dependent bias field given by the gradient times the displacement of the atoms from the origin of the magnetic quadrupole field. $60 \mu\text{m}$ away from the origin, the bias field changes by 30 mG during the $4 \mu\text{s}$ RF pulse. To minimize the reduction of the RF pulse area, the optical trap was aligned with the center of the quadrupole field to within $1 \mu\text{m}$. This was done by minimizing the shift in the RF resonant frequency when a stationary gradient field was added to the constant magnetic bias field. In addition, the eddy currents created a time-dependent bias field, which was compensated by RF detuning. The detuning and the timing of the RF pulses (described below) were adjusted together in order to maximize the fraction of spin-flipped atoms.

(3) *Timing of the RF pulses with respect to the magnetic modulation*: The goal was to pulse on the RF while the magnetic field gradient crosses zero. A $5 \mu\text{s}$ offset would imply a gradient of 7.5 G/cm and a differential magnetic field along the cloud of 50 mG. In the presence of strong gradients, the short RF pulse is resonant only for a small part of the cloud. Therefore, we could find the optimum condition by scanning both the timing and the detuning of

the RF pulses until the measured total fraction of the spin-flipped atoms is maximized. The optimum time was offset by $2 \mu\text{s}$ from the zero-crossing of the current through the gradient coils, possibly due to eddy currents.

To summarize, we optimized three parameters, which are trap position, timing of the RF pulse, and RF detuning. The optimal position minimizes temporal variation of the bias field, optimal timing of RF minimizes B' during the pulse, and optimal detuning compensates for any bias field at the time of the pulse.

EFFECTS OF INDUCED EDDY CURRENTS

The modulated magnetic field gradient $B'(t) = B'_0 \sin \omega t$ induced eddy currents in the stainless steel vacuum chamber. From our observations, we inferred that the main effect was caused by an induced oscillating bias field $\vec{B}_{ec}(t) = B_{ec} \sin(\omega t + \phi) \mathbf{e}_y$ along y with the same modulation frequency ω and a relative phase delay ϕ . This oscillating bias field led to a y -component of the oscillating force. As a result, the effective recoil and velocity selection are tilted away from the z direction, and the selected velocity slices are rotated in the $y - z$ plane.

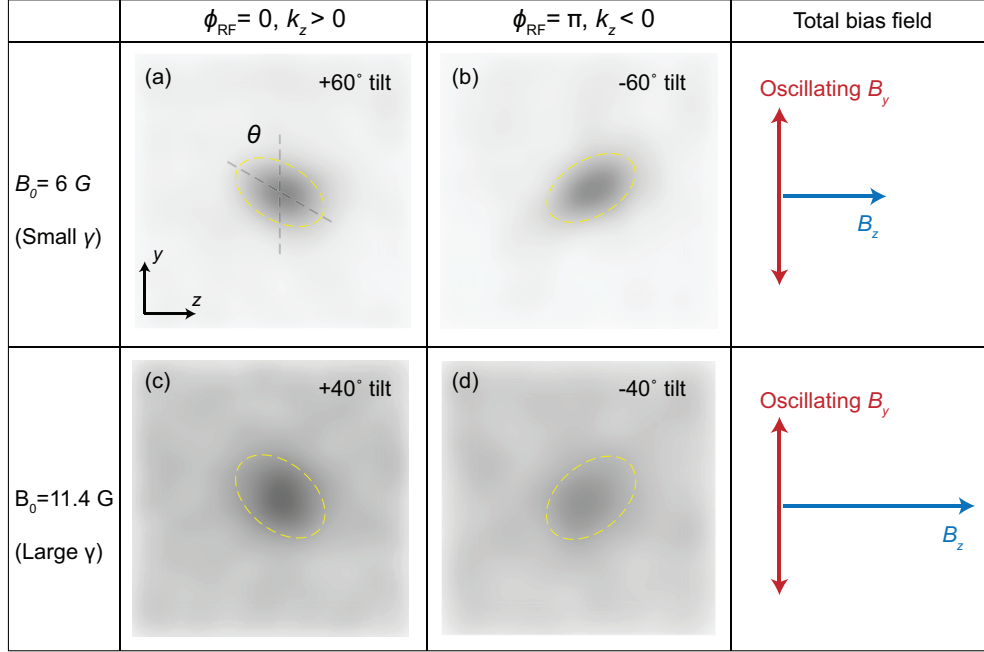


FIG. S1: Effect of eddy currents on observed velocity-selected atom slices. The induced bias field along \mathbf{e}_y led to a y -component of the oscillating force, resulting in velocity selectivity in \mathbf{e}_y and therefore tilting of the resonant velocity slice in the $y - z$ plane. The tilt angle depends on the static bias field B_0 and the RF phase ϕ_{RF} . The dashed lines are guides to the eye.

In a simplified model, the total magnetic field experienced by the atoms is

$$\vec{B} = [B_0 + B'_0 \sin(\omega t)z] \mathbf{e}_z + [B_{ec} \sin(\omega t + \phi) + B'_0 \sin(\omega t)y] \mathbf{e}_y - 2B'_0 \sin(\omega t)x \mathbf{e}_x, \quad (\text{S1})$$

with a magnetic field strength

$$\begin{aligned} |\vec{B}| &= \sqrt{[B_0 + B'_0 \sin(\omega t)z]^2 + [B_{ec} \sin(\omega t + \phi) + B'_0 \sin(\omega t)y]^2 + [2B'_0 \sin(\omega t)x]^2} \\ &\approx B_0 \sqrt{1 + \gamma^2 \sin^2(\omega t + \phi)} + \frac{B'_0 z + \gamma \sin(\omega t + \phi) B'_0 y}{\sqrt{1 + \gamma^2 \sin^2(\omega t + \phi)}} \sin(\omega t) \end{aligned} \quad (\text{S2})$$

here $\gamma = B_{ec}/B_0$. The first term corresponds to a time varying homogeneous bias field resulting in a *velocity-independent* effective detuning of the RF transition. The oscillating magnetic field gradients along the z and y

directions are

$$\begin{aligned}\frac{\partial|\vec{B}|}{\partial z} &= \frac{B'_0}{\sqrt{1+\gamma^2\sin^2(\omega t+\phi)}}\sin(\omega t), \\ \frac{\partial|\vec{B}|}{\partial y} &= \frac{\gamma B'_0}{\sqrt{1+\gamma^2\sin^2(\omega t+\phi)}}\sin(\omega t)\sin(\omega t+\phi).\end{aligned}\tag{S3}$$

It should be noted that the gradient in \mathbf{e}_y oscillates at 2ω , twice the frequency of the driving.

The phase delay ϕ is determined by the magnetic properties of the vacuum chamber. We modeled the chamber as an LC circuit with a self inductance L_{Ch} and a resistance R_{Ch} , and obtain $\phi = \arctan(\omega L_{\text{Ch}}/R_{\text{Ch}}) + \pi/2$. Our observations imply $R_{\text{Ch}} \gg \omega L$, $\phi \approx \pi/2$, resulting in an effective recoil component in the y direction with

$$\begin{aligned}k_{\text{so},y} &= \frac{1}{T} \int_0^T \left(\int_0^t \frac{\gamma B'_0}{\sqrt{1+\gamma^2\cos^2(\omega t')}} \sin(\omega t') \cos(\omega t') dt' \right) dt \\ &= \frac{1}{T} \int_0^T \left(\int_0^t \frac{\gamma B'_0}{2\sqrt{1+\gamma^2\cos^2(\omega t')}} \sin(2\omega t') dt' \right) dt.\end{aligned}\tag{S4}$$

Consequentially, the Doppler shift is modified as

$$\delta\omega = k_y v_y + k_z v_z,\tag{S5}$$

directly observed as a rotation of the velocity slice with an angle $\theta = \arctan(k_y/k_z)$ in the time-of-flight images, as shown in Fig. S1.

We verified two predictions of this model: the angle θ of the rotation decreased with stronger static bias field \vec{B}_0 which lowered γ (Fig.S1a. and Fig.S1 c). Due to the 2ω oscillating frequency of the y force, k_y did not change sign when the RF phase ϕ_{RF} was shifted from 0 to π in contrast to k_z , and therefore the rotation angle flipped from θ to $-\theta$, as suggested by Eq. S5 and shown in Fig. S1.

In the future, the effects of the induced eddy current can be suppressed by using an even stronger static bias field \vec{B}_0 or by conducting the experiment in a glass cell.

What we have described so far applies to free space or to an isotropic trap. However, the optical trap in the experiment is anisotropic. For zero time-of-flight, in the $y-z$ plane, the minor axis of the ellipsoidal cloud is oriented along y , $\theta = \pi/2$. For long time-of-flight, the angle is solely determined by the velocity selection $\theta = \arctan(k_y/k_z)$. For intermediate time-of-flight, as used in the experiment, the observed angle interpolates between these values. We calculate that the observed tilt angles of 60° and 40° (Fig.S1) correspond to tilt angles of the bias field $\arctan(k_y/k_z)$ of 53° and 32° , respectively.

The observed tilt angles were used to infer the induced eddy currents. Equation S4 provided the dashed line for the predicted recoil k in Figure 3 of the main text.

BLOCH SPHERE REPRESENTATION OF MAGNETIC SHAKING AND RF PULSES

The evolution of the quantum system under magnetic shaking and RF pulses can be visualized using the Bloch sphere (Fig. S2). In the frame rotating at the atomic RF resonance frequency ω_0 , each RF pulse of area β rotates the Bloch vector around the y -axis by an angle β . In the absence of magnetic shaking, subsequent pulses would continue the rotation all the way down to the south pole of the Bloch sphere and up again, resulting in Rabi oscillations at a rate $\beta/(2\pi T)$. However, due to the phase evolution discussed in the main text, the Bloch vector rotates around the z axis by an angle $\delta\alpha$, and therefore, the following RF pulse increases the polar angle by less than β . After several cycles, the Bloch vector returns to the north pole without having ever reached the south pole, realizing off-resonant Rabi oscillations (Fig.S2(a)). However, if the RF frequency is shifted by the Doppler and recoil shift, the Bloch vector reaches the south pole again. In contrast, for the phase $\phi_{\text{RF}} = \pi/2$, kinetic energies of the coupled spin up and down states are the same, irrespective of velocity, and therefore all atoms perform resonant Rabi oscillations (Fig. S2(b)). It should be noted that the evolution of the atomic wavefunction is the same if the RF frequency is detuned by an integer multiple of $\frac{2\pi}{T}$, similar to the situation in Ramsey spectroscopy.

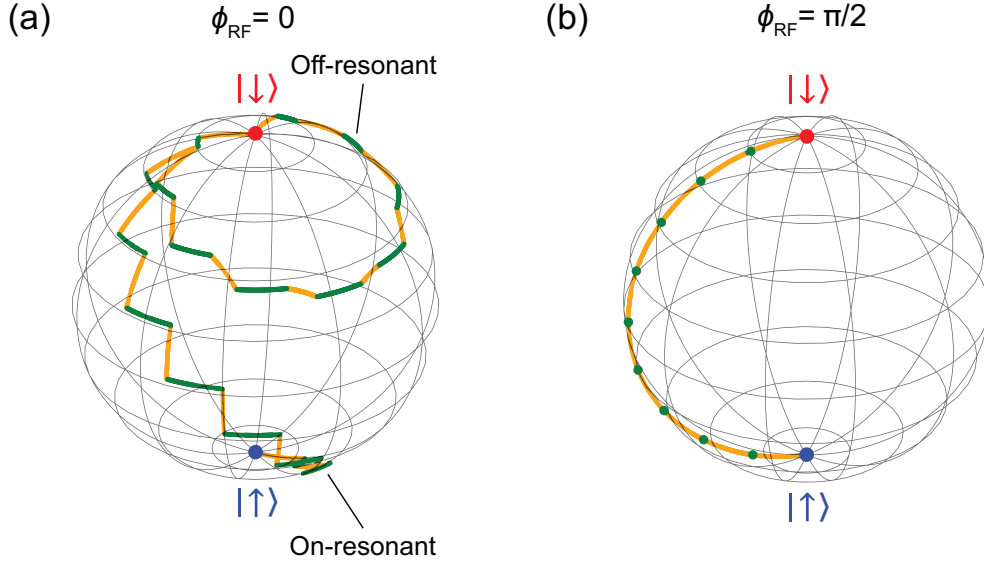


FIG. S2: Bloch sphere representation of magnetic shaking and RF pulses. (a) & (b) Trajectories on the Bloch sphere for several periods of magnetic shaking (green solid lines representing α from the main text) and RF pulses (yellow solid lines representing β) for $\phi_{RF} = 0$ and $\phi_{RF} = \pi/2$, respectively. Fig. (a) shows the trajectories for atoms with a finite initial velocity when the RF frequency is at ω_0 , the atomic resonance, and when it is detuned by the Doppler and recoil shift. In (b), the RF frequency is at ω_0 , the trajectory is independent of the atomic velocity, and there is no net rotation around the z-axis during a magnetic shaking cycle. The red (blue) dot represents the initial (final) spin state.

DERIVATION OF EFFECTIVE HAMILTONIAN

In our scheme, the Hamiltonian in the frame rotating with the RF drive is

$$\hat{H}(t) = \frac{\hat{p}_z^2}{2m} - \frac{1}{2}\delta_{RF}\hat{\sigma}_z + \frac{1}{2}\omega k_0 \hat{z} \sin\left(\frac{2\pi}{T}t + \phi_{RF}\right) \hat{\sigma}_z + \Omega \hat{\sigma}_x T \sum_n \delta(t - nT), \quad (\text{S6})$$

where we have applied the rotating-wave approximation and set $\hbar = 1$. To deal with the dynamics of such a periodically driven system we shall apply two alternative approaches described below.

To eliminate the spin-dependent potential slope featured in the Hamiltonian (S6), we go to the spin-dependent co-moving frame via a time-dependent unitary transformation to the new state-vector $|\psi(t)\rangle = \hat{R}_z^\dagger(t) |\tilde{\psi}(t)\rangle$, similar to the one used in refs. [1, 2]:

$$\hat{R}_z(t) = \exp[-ik_0 z \gamma(t) \hat{\sigma}_z / 2], \quad \gamma(t) = \omega \int_0^t \sin\left(\frac{2\pi}{T}t' + \phi_{RF}\right) dt' - C = -\cos\left(\frac{2\pi}{T}t + \phi_{RF}\right), \quad (\text{S7})$$

where the integration constant C entering $\gamma(t)$ has been taken to be $C = \cos \phi_{RF}$, so that $\gamma(t)$ averages to zero over a period. The reason for this choice will be discussed later on.

At the RF pulses where $t = nT$ the transformation $\hat{R}_z(nT) = \exp[ik_0 z \cos \phi_{RF} \hat{\sigma}_z / 2]$ describes a spin rotation by an angle $k_0 z \cos \phi_{RF}$ around the z axis. As a result, the transformed Hamiltonian $\hat{H}(t) = \hat{R}_z^\dagger(t) \hat{H} \hat{R}_z(t) - i \hat{R}_z^\dagger(t) \partial_t \hat{R}_z(t)$ takes the form

$$\hat{H}(t) = \frac{1}{2m} \left(\hat{p}_z - \frac{1}{2} k_0 \gamma(t) \hat{\sigma}_z \right)^2 - \frac{1}{2} \delta_{RF} \hat{\sigma}_z + \Omega [\cos(k_0 z \cos \phi_{RF}) \hat{\sigma}_x + \sin(k_0 z \cos \phi_{RF}) \hat{\sigma}_y] T \sum_n \delta(t - nT). \quad (\text{S8})$$

Note that unlike the spin-dependent potential gradient featured in the original Hamiltonian (S6), the oscillating momentum shift term $k_0 \gamma(t) \hat{\sigma}_z / 2$ is no longer proportional to the driving frequency and hence can be considered as

a small perturbation in the limit of high frequency driving where $k_0\gamma(t) \ll \omega$ and also $\Omega \ll \omega$. In that case it is appropriate to describe the evolution of the system in terms of the zero-order effective Hamiltonian obtained by time averaging of $\hat{H}(t)$ over a single driving period, i.e. by the zero frequency component of the Hamiltonian $\hat{H}(t)$, giving

$$\hat{H}_{eff} = \frac{\hat{p}_z^2}{2m} - \frac{1}{2}\delta_{RF}\hat{\sigma}_z + \Omega \cos(k_0z \cos \phi_{RF}) \hat{\sigma}_x + \Omega \sin(k_0z \cos \phi_{RF}) \hat{\sigma}_y + \frac{1}{16} \frac{k_0^2}{m}, \quad (\text{S9})$$

where the momentum shift has averaged to zero. The effective Hamiltonian can be represented in a matrix form as:

$$\hat{H}_{eff} = \begin{pmatrix} \frac{\hat{p}_z^2}{2m} + \frac{1}{16} \frac{k_0^2}{m} - \frac{1}{2}\delta_{RF} & \Omega e^{-ik_0z \cos \phi_{RF}} \\ \Omega e^{ik_0z \cos \phi_{RF}} & \frac{\hat{p}_z^2}{2m} + \frac{1}{16} \frac{k_0^2}{m} + \frac{1}{2}\delta_{RF} \end{pmatrix}. \quad (\text{S10})$$

The full dynamics includes also the micromotion. In the present situation there are two origins of the micromotion. The first kind comes from the time-dependence of the transformed Hamiltonian $\hat{H}(t)$. However, in the limit of the large driving frequency this kind of micromotion is negligibly small compared to the second type of micromotion emerging due to the time-dependence of the unitary transformation $\hat{R}_z(t)$. In fact, returning to the original representation $|\psi(t)\rangle = \hat{R}_z(t) |\tilde{\psi}(t)\rangle$, one arrives at the following time-evolution of the state-vector from the initial to the final time

$$|\psi(t_2)\rangle = \hat{U}(t_2, t_1) |\psi(t_1)\rangle, \quad \text{where} \quad \hat{U}(t_2, t_1) = \hat{R}_z(t_2) e^{-i\hat{H}_{eff}(t_2-t_1)} \hat{R}_z^\dagger(t_1), \quad (\text{S11})$$

where the unitary transformation $\hat{R}_z(t)$ represents a micro-motion operator.

The time evolution operator can be rewritten as

$$\hat{U}(t_2, t_1) = e^{-i\hat{K}(t_2)} e^{-i\hat{H}_{eff}(t_2-t_1)} e^{i\hat{K}(t_1)}, \quad (\text{S12})$$

where

$$\hat{K}(t) = -k_0z\hat{\sigma}_z \cos\left(\frac{2\pi}{T}t + \phi_{RF}\right) \quad (\text{S13})$$

is a Hermitian micromotion (kick) operator. The choice of the integration constant $C = \cos \phi_{RF}$ in the unitary transformation (S7) ensures that the micromotion operator $\hat{K}(t)$ averages to zero over the driving period. Thus, the effective Hamiltonian and the micromotion operators are defined in a unique way through the condition $C = \cos \phi_{RF}$.

We now rederive the same effective Hamiltonian and micromotion operator using a rigorous high-frequency $1/\omega$ expansion. Appendix K of ref. [3] discusses Hamiltonians of a general form

$$\hat{H}(t) = \hat{H}_0 + \hat{A}f(t) + \omega\hat{B}g(t) \quad (\text{S14})$$

and derives expansions for an effective Hamiltonian \hat{H}_{eff} and the kick operator \hat{K} .

$$\hat{H}_{eff} = \sum_{n=0}^{\infty} \frac{1}{\omega^n} \hat{H}_{eff}^{(n)}, \quad \hat{K}(t) = \sum_{n=0}^{\infty} \frac{1}{\omega^n} \hat{K}^{(n)}(t) \quad (\text{S15})$$

The Hamiltonian \hat{H} in equation (S6) is of this form with

$$\hat{H}_0 = \frac{p^2}{2m} - \frac{1}{2}\delta_{RF} + \Omega\hat{\sigma}_x, \quad (\text{S16})$$

$$\hat{B} = \frac{1}{2}k_0z\hat{\sigma}_z, \quad g(t) = \sin(\omega t + \phi_{RF}), \quad (\text{S17})$$

$$\hat{A} = \Omega\sigma_x, \quad f(t) = T \sum_n \delta(t - nT) - 1 \quad (\text{S18})$$

Functions $f(t)$ and $g(t)$ meet the requirement of having zero mean value over a period T .

The kick operator is in 0-th order:

$$\hat{K}^{(0)} = \hat{B}G(t), \quad G(t) = \omega \int_0^t g(\tau) d\tau = -\cos(\omega t + \phi_{RF}) \quad (\text{S19})$$

The effective Hamiltonian to the lowest order in $1/\omega$ can be expanded as

$$\hat{H}_{eff} = \hat{H}_0 + \sum_{n=1} \frac{i^n \overline{G^n}}{n!} \underbrace{f[B \dots [B, A]]}_n + \sum_{n=1} \frac{i^n \overline{G^n}}{n!} \underbrace{[B \dots [B, H_0]]}_n + O(1/\omega) \quad (\text{S20})$$

After calculating all commutators and time-averaged coefficients before them, and grouping the terms proportional to $\hat{\sigma}_x$ and $\hat{\sigma}_y$, the expansion reduces to

$$\hat{H}_{eff} = \frac{\hat{p}_z^2}{2m} - \frac{1}{2} \delta_{RF} \hat{\sigma}_z + \Omega \cos(k_0 z \cos \phi_{RF}) \hat{\sigma}_x + \Omega \sin(k_0 z \cos \phi_{RF}) \hat{\sigma}_y + \frac{1}{16} \frac{k_0^2}{m} + O(1/\omega) \quad (\text{S21})$$

The resulting effective Hamiltonian and micromotion operator are in exact agreement with the above equations (S9), (S10) and (S13).

If we apply an additional spatially-dependent unitary transformation $\hat{R}_{z1} = \exp[-izk_0 \cos \phi_{RF} \hat{\sigma}_z/2]$ corresponding to the choice $C = 0$ of the constant in Eq.(S7), the transformed Hamiltonian becomes translationally invariant and acquires the standard form of H_{SOC} for one-dimensional spin-orbit coupling:

$$\hat{H}_{SOC} = \frac{1}{2m} (\hat{p}_z - \frac{1}{2} k_0 \cos \phi_{RF} \hat{\sigma}_z)^2 + \Omega \hat{\sigma}_x - \frac{\delta_{RF}}{2} \hat{\sigma}_z, \quad (\text{S22})$$

where the spin-orbit coupling strength is described by the momentum shift $k_0 \cos \phi_{RF}/2$. With the new kick operator

$$\hat{K}_{SOC}(t) = -k_0 z \hat{\sigma}_z \left[\cos\left(\frac{2\pi}{T} t + \phi_{RF}\right) - \cos \phi_{RF} \right] \quad (\text{S23})$$

the time evolution can be written as

$$U(t_2, t_1) = e^{-i\hat{K}_{SOC}(t_2)} e^{-i\hat{H}_{SOC}(t_2-t_1)} e^{i\hat{K}_{SOC}(t_1)}. \quad (\text{S24})$$

In that case the operator $\hat{K}_{SOC}(t)$ has a non-zero temporal average, so it cannot be treated as a pure micromotion operator. Similarly \hat{H}_{SOC} can not be considered as an effective Hamiltonian for the time-periodic Hamiltonian (S6). It is rather a Hamiltonian related to the true effective Hamiltonian by the unitary transformation: $\hat{H}_{SOC} = \hat{R}_{z1}^\dagger \hat{H}_{eff} \hat{R}_{z1}$. Note that ref. [2] has obtained \hat{H}_{SOC} as a stroboscopic Floquet Hamiltonian after applying a unitary transformation of the form (S7) with $C = 0$.

MECHANICAL AND CANONICAL MOMENTA

The difference between canonical and mechanical momenta can be seen on the dispersion relation (Fig.S3). Using canonical momentum all couplings and transitions between the two spin states are vertical. The dashed lines illustrate

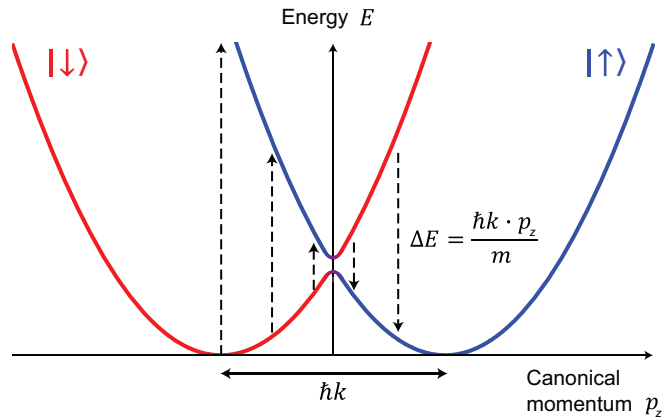


FIG. S3: Energy-momentum dispersion relations for spin-orbit coupled spin 1/2 states. The two minima are separated by the recoil momentum $\hbar k$. The vertical dashed arrows show spinflip transitions. Their lengths are given by the Doppler and recoil shifts.

the transitions observed in our experiment. Away from the spin gap the energy separation is dominated by Doppler and recoil shifts. Energy-momentum dispersion relations for spin-orbit coupled spin 1/2 states. The two minima are separated by the recoil momentum $\hbar k$. The vertical dashed arrows show spinflip transitions. Their lengths are given by the Doppler and recoil shifts.

-
- [1] B. M. Anderson, I. B. Spielman, and G. Juzeliūnas, Phys. Rev. Lett. **111**, 125301 (2013), URL <https://link.aps.org/doi/10.1103/PhysRevLett.111.125301>.
 - [2] X. Luo, L. Wu, J. Chen, Q. Guan, K. Gao, Z.-F. Xu, L. You, and R. Wang, Scientific Reports **6**, 18983 EP (2016), supplementary material, URL <http://dx.doi.org/10.1038/srep18983>.
 - [3] N. Goldman and J. Dalibard, Phys. Rev. X **4**, 031027 (2014), URL <https://link.aps.org/doi/10.1103/PhysRevX.4.031027>.

Floquet Heating in Interacting Atomic Gases with an Oscillating Force

Jun-Ru Li,^{1,*} Boris Shteynas,¹ and Wolfgang Ketterle¹

¹*Research Laboratory of Electronics, MIT-Harvard Center for Ultracold Atoms,
Department of Physics, Massachusetts Institute of Technology, Cambridge, Massachusetts 02139, USA*
(Dated: June 21, 2019)

We theoretically investigate the collisional heating of a cold atom system subjected to time-periodic forces. We show within the Floquet framework that this heating rate due to two-body collisions has a general semiclassical expression $\mathcal{P} \propto \rho \sigma v_{\text{col}} E_0$, depending on the kinetic energy E_0 associated with the shaking, particle number density ρ , elastic collision cross section σ , and an effective collisional velocity v_{col} determined by the dominant energy scale in the system. We further show that the collisional heating is suppressed by Pauli blocking in cold fermionic systems, and by the modified density of states in systems in lower dimensions. Our results provide an exactly solvable example and reveal some general features of Floquet heating in interacting systems.

I. INTRODUCTION

Engineering novel Hamiltonians is central to quantum simulations. In general, Hamiltonians can be implemented directly and statically, or in a time-averaged way. The latter implies periodic driving of the system. If the fast modulation can be neglected, an effective time-averaged static Hamiltonian is realized as formally captured by *Floquet theory* [1, 2]. With proper driving, dynamically generated *Floquet Hamiltonians* can be designed. Such *Floquet systems* potentially exhibit novel properties which are difficult or impossible to be realized in static settings. Examples include synthetic gauge fields [3–6], spin-orbit coupling [7–9], and topological bands and materials [10–13]. Experimental progress includes creation of the Hofstadter-Hamiltonian in optical lattices for neutral atoms [14–17], realization of the topological Haldane model with shaken optical lattice [18], and the demonstration of dressed recoil momentum for radio-frequency photons in ultracold gases with modulated magnetic fields [19].

However, *higher order terms* beyond the time average, related to fast *micromotion*, can cause heating via interactions, limiting experimental studies of many-body physics. In general, a driven system constantly exchanges energy with the driving field. Interactions redistribute this energy into other degrees of freedom, leading to an increase of the total entropy and energy. Although this heating can be suppressed in specific scenarios, e.g. via many-body localization [20–22], a generic closed quantum system will eventually thermalize at infinite temperature when driven [23], limiting the experimental studies of many-body Floquet systems. Therefore, understanding and potentially controlling the heating in Floquet systems has triggered both theoretical [22–28] and experimental efforts [29, 30].

The dynamics of a Floquet system are studied with Floquet theory. Systems heat by absorbing energy from

the driving field in multiples of the energy quanta related to the modulation frequency ω , caused by the scattering of the driven particles [26]. The heating rate reads

$$\mathcal{P} = \sum_n \Gamma_n n \hbar \omega, \quad (1)$$

which is determined by the transition rates Γ_n for the processes of absorption/emission of n energy quanta. In this description, the energy exchange is quantized.

On the other hand, in the limit of low modulation frequency where the system's intrinsic energy scales dominate, the quantization of the driving field should not have a prominent effect. The system's behavior can be described semiclassically. As a result, it is anticipated that the heating dynamics of a Floquet system have a corresponding semiclassical counterpart in this low-frequency regime. Moreover, the quantized and the semiclassical description should exhibit a continuous crossover as a function of the modulation frequency ω and amplitude.

In this work, we investigate the Floquet heating and the crossover between the quantum and semiclassical regimes for systems subjected to periodic forcing in free space, motivated by the recent experimental demonstration of Floquet-dressed recoil momentum for photons in a two-spin mixture of cold gases [19] where the two spins are shaken relative to each other. Such a setting is the key ingredient of many Floquet schemes proposed for generating synthetic gauge fields and topological matter [2, 7–10]. The corresponding semiclassical description of the heating in such a system is the following: the force modulates the particles' velocities and consequently generates extra kinetic energy E_0 . This *micromotion* energy E_0 can be transferred into the *secular* motion of the particles via inter-particle collisions when the micromotion is out-of-phase for the colliding particles, causing an increase of the system's total energy, and consequently heating. The resulting heating rate can be estimated with the two-body elastic collision rate $\rho \sigma v$ and the associated energy E_0 as

$$\mathcal{P} \propto \rho \sigma v E_0 \quad (2)$$

with the atomic density ρ , elastic collisional cross section σ , and the relative speed of the two particles v . This

* Present address: JILA, Department of Physics, University of Colorado, 440 UCB, Boulder, Colorado 80309, USA.; junru.li@colorado.edu

heating rate is continuously variable depending on the strength of the driving, characterized by E_0 , and is independent of the driving frequency ω , which seems to contradict the Floquet description of quantized energy transfer.

In this paper, we calculate the collisional heating rates in periodically shaken atomic gases with a full Floquet treatment. We identify several distinct regimes determined by the energy hierarchies in the system and show that the semiclassical and the Floquet picture are two limiting cases of a unified general description of the heating rate as $\mathcal{P} \sim \rho \sigma v_{\text{col}} E_0$. The key parameter v_{col} is an *effective* collisional velocity parametrizing the final density of states. This can be, for example, the averaged thermal velocity $\sqrt{k_b T/m}$ with k_b being the Boltzmann constant, $\sqrt{\hbar\omega/m}$, or $\sqrt{E_0/m}$, depending on the dominant energy scales. In addition, we show that collisional heating is suppressed in a cold fermionic system by Pauli blocking, and due to the modified density of states in systems in lower dimensions.

The paper is organized as follows: Sec. II is a concise review on the Floquet theory and scattering of Floquet-Bloch states, which serves as the theoretical basis for the main results presented in Sec. III. We first analyze the Floquet heating for two atoms in Sec. III A. We then analyze different regimes of the collisional heating in Sec. III B and subsequently extend the analysis to atomic ensembles in Sec. III C, including a specific discussion on fermionic systems in Sec. III D. A discussion of heating rates in lower-dimensional systems is presented in Sec. III E, followed by a summary and outlook in Sec. IV.

II. FLOQUET THEORY AND FLOQUET HEATING

Our work is based on Floquet theory, which describes the evolution of a periodically driven system. Evolution of a Floquet system has been studied in different scenarios with different approaches, for example through high-frequency expansion [1, 2, 31], Floquet-Magnus expansion [32], and extended Hilbert space [33]. We summarize here the basic concepts and formalism in Floquet theory and the scattering of the Floquet-Bloch states. This section mainly follows the description in Ref. [26]; Comprehensive discussions can be found in Refs. [2, 26, 32, 33].

A. General Aspects of Floquet Theory

Floquet theory describes the behavior of a system governed by a time-periodic Hamiltonian $\hat{H}(t+T_0) = \hat{H}(t)$. This temporal translational symmetry allows simple descriptions of the time evolution. Solutions of the time-dependent Schrödinger equation

$$\hat{H}(t) |\Phi(t)\rangle = i\hbar \partial_t |\Phi(t)\rangle, \quad (3)$$

known as *Floquet-Bloch states*, can be decomposed into Fourier modes as

$$|\Phi(t)\rangle = \sum_l e^{-iEt/\hbar + il\omega t} C_l |\phi_l\rangle. \quad (4)$$

Here, $\omega = 2\pi/T_0$ is the modulation frequency and E is the eigenenergy of the corresponding non-driven system. The amplitude of each of the Fourier modes C_l generally depends on parameters such as the strength and the frequency of the driving.

The system does not conserve energy, due to the external drive. In the literature, two different conventions are adopted to describe the energy structure of such a system [26]. Some authors define *quasienergies* $E^q = E \bmod \hbar\omega$ lying between $(-\hbar\omega/2, \hbar\omega/2)$. Others distinguish between the carrier energy E , describing the *secular motion*, and the energy sidebands $E \pm l\hbar\omega$, describing the *micromotion*. This distinction can be understood by considering an adiabatic ramp of the amplitude of the driving. In this work, we adopt the second convention.

B. Scattering of Floquet-Bloch States

The dressed energy sidebands of the Floquet-Bloch states modify the scattering between two states caused by interactions. Scattering can occur not only between the carriers but also from the carrier of the initial state to the sidebands of the final state. In the latter case, the final and the initial carrier energy are different by multiples of the energy quanta $\hbar\omega$, representing the energy exchange between the driving field and the system via scattering. This process is formulated with the so-called Floquet Fermi's golden rule [26]. The transition amplitude between two Floquet-Bloch states is calculated using time-dependent perturbation theory [26]:

$$\begin{aligned} A(i \rightarrow f, t) &= -\frac{i}{\hbar} \int_0^t dt' \langle \Psi_f(t') | \hat{V} | \Psi_i(t') \rangle \\ &= -\frac{i}{\hbar} \sum_{p,q} \int_0^t dt' e^{i[E_f - E_i + \hbar(p-q)\omega]t'/\hbar} V^{p,q}, \end{aligned} \quad (5)$$

where $V^{p,q} = \langle \phi_f^q | \hat{V} | \phi_i^p \rangle$ is the coupling between two Fourier modes p, q belonging to the final and the initial state respectively via, for example, collisions. The corresponding transition rate is readily obtained as

$$\begin{aligned} \Gamma(i \rightarrow f) &= \lim_{t \rightarrow \infty} \frac{|A(i \rightarrow f, t)|^2}{t} \\ &= \frac{2\pi}{\hbar} \sum_n \left(\sum_{l,m} V^{l,l+n} V^{*m,m+n} \right) \delta(E_f - E_i - n\hbar\omega). \end{aligned} \quad (6)$$

The sum over the index n explicitly reveals an important feature of the scattering between two Floquet-Bloch

states. In the $n = 0$ scattering channel, the initial and final states have the same carrier energy, and therefore no net energy is exchanged between the colliding particles and the driving field (*Floquet elastic processes*), which resembles the conventional elastic scattering. Scattering channels with $n \neq 0$ characterize the processes where the energy of the atomic system is changed by exchanging n quanta with the driving field (*Floquet inelastic processes*), leading to Floquet heating.

C. Heating Rates

We define the heating rate \mathcal{P} of the system as the rate of the average increase in the system's total energy \bar{E}_{tot} , which can be expressed with the scattering rate Γ_n and the related energy transfer $n\hbar\omega$ as

$$\mathcal{P} = \sum_n \Gamma_n n\hbar\omega. \quad (7)$$

As shown above, heating of a periodically driven system originates from the absorption of energy from the driving field through inter-particle interactions. The heating rate of a Floquet system can be calculated by first finding the exact Floquet-Bloch state wave function. Then the energy exchange rate can be obtained by calculating the transition rates for all quantized absorption/emission processes and their associated energy change. Generally, the explicit form of the wave function of the Floquet-Bloch state $|\Phi(t)\rangle$ is obtained by inserting Eq. (4) into Eq. (3) and solving the infinite number of coupled equations for amplitudes C_l . However, for some special cases, the exact solutions have a simple form, such as the system presented in Sec. III.

III. COLLISIONAL HEATING FOR PERIODIC FORCES

We apply the method described in Sec. II to the system of interest: a spin mixture of atoms with different magnetic moments for a periodically modulated magnetic field gradient, as implemented in Ref. [19] (Fig. 1). For simplicity, we assume the two spins to have equal but opposite magnetic moments, such that they experience opposite forces. We first derive the exact analytic form of the corresponding Floquet-Bloch state wave function, then calculate the collisional heating for a single pair of atoms with opposite spins, before generalizing the results to atomic ensembles. In this section, we focus on three-dimensional systems. The results are extended to lower dimensions in Sec. III E.

A. Collisional Heating for Two Atoms

1. Single-particle Floquet-Bloch states

The Hamiltonian we consider is

$$\hat{H}(t) = \frac{\hbar^2 \hat{\mathbf{k}}^2}{2m} + \hbar k_0 \sigma_z \hat{z} \sin(\omega t + \phi), \quad (8)$$

where the time dependent term arises from a spin-dependent periodic force $\mathbf{F} = \hbar k_0 \sigma_z \sin(\omega t + \phi) \hat{\mathbf{e}}_z$. The corresponding Floquet-Bloch states defined in Eq. (3) have the compact and intuitive form

$$\Psi_{\mathbf{k}}(\mathbf{r}, t) = \frac{1}{\sqrt{V}} \exp[i\mathbf{k}(t) \cdot \mathbf{r} - i\Phi(t)], \quad (9)$$

where

$$\hbar\mathbf{k}(t) = \hbar\mathbf{k} + \hbar k_0 \bar{\mathbf{e}}_z \int_0^t \sin \omega t' dt', \quad (10)$$

and

$$\Phi(t) = \int_0^t \frac{\hbar^2 \mathbf{k}(t') \cdot \mathbf{k}(t')}{2m} dt' \quad (11)$$

are the instantaneous momentum and the cumulative dynamic phase at time t . The physical interpretation of the wave function Eq. (9) is made transparent by considering a stationary Gaussian wave packet $|\phi\rangle_{t=0} = \int d\mathbf{k} \exp(-\mathbf{k} \cdot \mathbf{k}/\sigma_{\mathbf{k}}^2) |\phi\rangle_{\mathbf{k}}$ at the origin. The expectation values of the position \mathbf{r} and the momentum $\hbar\mathbf{k}$ of the wave packet at time t under the periodic driving

$$\langle \mathbf{r} \rangle_t = \frac{\hbar}{m} \int_0^t \mathbf{k}(t') dt', \quad \langle \hbar\mathbf{k} \rangle_t = \hbar\mathbf{k}(t) \quad (12)$$

are identical to those of a driven classical particle. We further identify the *secular* motion of the particle with the time average of $\langle \mathbf{r} \rangle_t, \langle \hbar\mathbf{k} \rangle_t$ over a period T_0 .

The periodic modulation at the driving frequency ω appears in both the dynamic phase $\Phi(t)$ and the wave vector $\mathbf{k}(t)$. The amplitude C_l of each Fourier mode defined in Eq. (4) can be readily obtained via the expansion $e^{ia \sin \omega t} = \sum_{n=-\infty}^{\infty} J_n(a) e^{in\omega t}$ as $C_l = \sum_{i+j+2k=l} J_i(k_0 z) J_j(\alpha) J_k(\beta)$ with the First-order Bessel functions J_ν and two parameters defined as

$$\alpha_{\mathbf{k}} = \frac{\hbar k_z k_0}{m\omega}, \quad \beta = \frac{\hbar k_0^2}{8m\omega}. \quad (13)$$

These motional sidebands dressed by the periodic driving have been directly observed via resonant fluorescence spectroscopy in trapped-ion systems [34]. The result is also conceptually similar to an optical modulator where the carrier frequency is dressed with frequency sidebands due to the periodic modulation of the medium's optical properties.

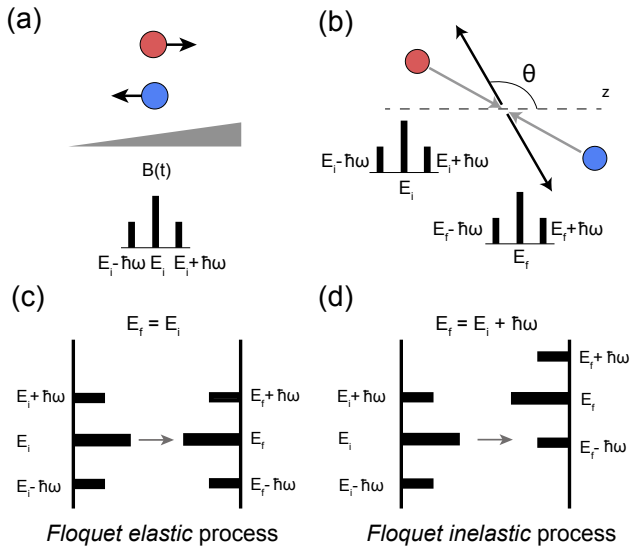


FIG. 1. Scattering between two particles subjected to a periodic force. Atoms with different spins are represented by red and blue. a) The oscillating force dresses each particle with energy sidebands spaced by $\hbar\omega$. The scheme has been implemented in Ref. [19] where atoms with different magnetic moments are driven by a periodic magnetic field gradient. b) Elastic collisions couple two Floquet-Bloch states. Gray and black arrows represent the incoming and the outgoing states respectively and θ is the scattering angle. c - d) Illustration of the *Floquet elastic* (c) and *Floquet inelastic* (d) process. Besides the regular elastic collisions where the final and the initial state have the same carrier energy (*Floquet elastic process*), the existence of the energy sidebands allows transitions between states whose carrier energies are different by a multiple of $\hbar\omega$ (*Floquet inelastic process*), leading to the exchange of energy between the system and the driving field.

2. Two-particle collisions and the heating rates

The two-body problem is reduced to a single particle problem by decomposing the dynamics into relative and center-of-mass parts. The center-of-mass motion is unaffected by collisions and is therefore omitted in further calculations. The two-body Hamiltonian reads

$$\hat{H}(\mathbf{R}, \mathbf{r}, t) = \frac{\hbar^2 \hat{\mathbf{K}}^2}{2M} + \frac{\hbar^2 \hat{\mathbf{k}}^2}{2\mu} + \hbar k_0 \hat{\sigma}_z \mathbf{z} \sin(\omega t + \phi) + g\delta(\mathbf{r}), \quad (14)$$

with $\mu = m/2$ being the reduced mass. $\mathbf{r} = (\mathbf{r}_1 - \mathbf{r}_2)/2$, $\mathbf{k} = (\mathbf{k}_1 - \mathbf{k}_2)/2$ are the relative coordinate and momentum.

The wave functions for the relative motion have the same structure as Eq. (9), except that the mass is replaced by the reduced mass μ and the momentum by the relative momentum $\hbar\mathbf{k}$.

Collisions are captured by the s -wave pseudopotential $\hat{V} = g\delta(\mathbf{r})$ described by Eq. (14). Here $g = 4\pi\hbar^2 a/m$ is the strength of the interaction and a is the s -wave scattering length between the two spin states. The interaction

\hat{V} couples two Floquet-Bloch states in Eq. (9). Without the periodic driving, elastic collisions couple only states with the same kinetic energy $E_{\mathbf{k}} = E_{\mathbf{k}'} = \hbar^2|\mathbf{k}|^2/2\mu$. However, the energy sidebands introduced by the periodic driving, formulated in Eq. (9), allow the scattering between states whose carrier energies differ by a multiple of $\hbar\omega$, giving $E_{\mathbf{k}'} - E_{\mathbf{k}} = n\hbar\omega$ (Fig. 1(b)-(d)). The associated quantized energy change $n\hbar\omega$ is transferred to the secular motion, leading to heating (or cooling). The transition rate from the ingoing state $|\Psi_{\mathbf{k}}^i\rangle$ to the outgoing state $|\Psi_{\mathbf{k}'}^f\rangle$ can be readily calculated from Eq. (6). By combining Eqs. (6) and (9), we derive the coupling matrix element

$$M_n(\mathbf{k} \rightarrow \mathbf{k}') = g \sum_l \int d\mathbf{r} \delta(\mathbf{r}) C_l(\mathbf{k})^* C_{l+n}(\mathbf{k}') \quad (15)$$

$$= g J_n(\alpha_{\mathbf{k}} - \alpha_{\mathbf{k}'}),$$

which gives the total transition rate from $|\Psi_{\mathbf{k}}^i\rangle$ to $|\Psi_{\mathbf{k}'}^f\rangle$

$$\Gamma(\mathbf{k} \rightarrow \mathbf{k}') = \sum_n \Gamma_n(\mathbf{k} \rightarrow \mathbf{k}') \quad (16)$$

$$= \sum_n \frac{2\pi}{\hbar} |M_n(\mathbf{k} \rightarrow \mathbf{k}')|^2 \delta(E_{\mathbf{k}'} - E_{\mathbf{k}} - n\hbar\omega),$$

explicitly showing the scattering rate of channels with different numbers of energy quanta $\hbar\omega$ exchanged. The scattering matrix element M_n reveals the microscopic process of the energy exchange with the driving field ($n \neq 0$ processes): it occurs only when $\alpha_{\mathbf{k}} \neq \alpha_{\mathbf{k}'}$, i.e. when the projection of the relative momentum \mathbf{k} to the shaking axis changes.

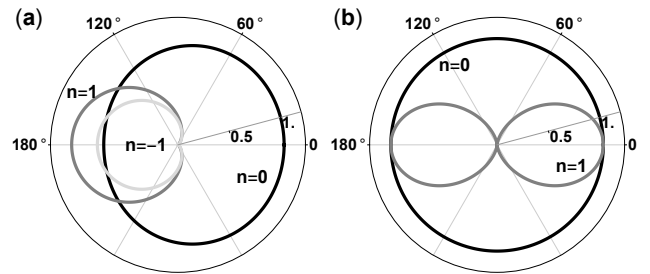


FIG. 2. Differential scattering cross sections for Floquet scattering processes with $n = 0$ (black), $n = 1$ (gray), and $n = -1$ (light gray). The angular coordinate corresponds to θ as depicted in Fig. 1. (a) For $E_{\mathbf{k}} > \hbar\omega$, both absorption ($n > 0$) and emission ($n < 0$) processes are allowed. Scattering between the Floquet-Bloch states is anisotropic in angle due to the sidebands. The figure is plotted for $\alpha = 0.4, \beta = 0.003$. (b) For strong driving the micromotion dominates, and the forward and backward scattering are symmetric as expected. The maximum scattering cross sections are normalized to unity, except for the process with $n = -1$ in (a) which is normalized with the maximal cross section of the $n = 1$ process in (a).

A feature of the scattering between two dressed particles is the anisotropy in the scattering cross section, as

shown in the differential scattering cross section (Fig. 2)

$$\frac{d^2\sigma_n}{d\Omega dE} = \frac{2\sigma}{\sqrt{m}} \frac{|\mathbf{k}'|}{|\mathbf{k}|} |M_n|^2 \delta(E_{\mathbf{k}'} - E_{\mathbf{k}} - n\hbar\omega). \quad (17)$$

Though the potential \hat{V} is isotropic, the scattering cross sections are *anisotropic* for each channel. This anisotropy in the scattering could be potentially observed in the time-of-flight pattern of a spin-mixed driven condensate.

We calculated the heating rate $\mathcal{P} = \sum_n \Gamma_n n\hbar\omega$ for a single pair of colliding particles with a relative momentum $\hbar\mathbf{k}$ by summing over the allowed final states \mathbf{k}' and scattering channels n , leading to

$$\begin{aligned} \mathcal{P}_{\mathbf{k}} &= \sum_n \sum_{\mathbf{k}'} \Gamma_n(\mathbf{k} \rightarrow \mathbf{k}') n\hbar\omega \\ &= \sum_n \frac{2\pi}{\hbar} \frac{g^2}{V} D_{3D}(E_{\mathbf{k}} + n\hbar\omega) \gamma^2(\mathbf{k}, n) n\hbar\omega, \end{aligned} \quad (18)$$

where

$$\begin{aligned} \gamma^2(\mathbf{k}, n) &= \\ \frac{1}{2g^2} \int_0^\pi d\theta \sin\theta |M_n(|\mathbf{k}| \rightarrow \sqrt{|\mathbf{k}|^2 + 2\mu n\omega/\hbar} \cos\theta)|^2 \end{aligned} \quad (19)$$

characterizes the transition amplitude, and $D_{3D}(E) = (2\mu/\hbar^2)^{3/2} \sqrt{E}/(2\pi)^2$ is the three-dimensional density of states of a free particle with energy E . Here we have assumed for simplicity that the initial relative momentum \mathbf{k} is along the direction of modulation.

B. Regimes and Crossovers

One of the major results of this paper is to show the connection between the Floquet picture, where energy transfer is quantized, and the semiclassical picture, where the energy transfer is continuous. The consolidation of the two pictures can be demonstrated already by examining the two-particle calculation presented above.

We recognize three fundamental energy scales in the system: 1) $E_0 = \hbar^2 k_0^2/(4m)$ characterizing the micromotion, and the strength of the modulation. 2) $\hbar\omega$ characterizing the modulation quanta, and 3) $E_{\mathbf{k}}$ characterizing the relative motion between the two colliding particles, e.g. $k_b T$ for a thermal system or E_F for a cold Fermi gas. The heating behavior of the system is qualitatively different depending on the relationship between these quantities.

We identify the following regimes from Eq. (18) :

a. Rapid-modulation Regime $\hbar\omega \gg E_{\mathbf{k}}, E_0$: A system with this condition has three features. First, only energy absorption is allowed. Second, the energy of the final states, $E_{\mathbf{k}} + \hbar\omega$, is now dominated by the modulation energy and $D_{3D}(E_{\mathbf{k}} + \hbar\omega) \sim \sqrt{\hbar\omega}$. Finally, since $M_n \sim 1/\omega^{n/2}$, the transition rate for the multi-quanta processes scales with $1/\omega^n$ and is therefore negligible.

The heating rate can be obtained analytically by considering only the $n = +1$ process and reads

$$\mathcal{P}_{\mathbf{k}} \approx \frac{4}{3} \frac{\sigma}{V} \sqrt{\frac{2\hbar\omega}{\mu}} E_0. \quad (20)$$

This is the regime where the quantum and the semiclassical picture diverge. Though the amplitudes of the sidebands drop with increasing modulation frequency, the system's heating rate increases due to the larger final density of states and the energy transfer $\hbar\omega$.

b. Semiclassical Regime $E_{\mathbf{k}} \gg \hbar\omega, E_0$: In this regime, as realized in Ref. [19], the final density of states is approximated to be $D_{3D}(E_{\mathbf{k}} + n\hbar\omega) \approx \sqrt{E_{\mathbf{k}}}[1 + n\hbar\omega/(2E_{\mathbf{k}})]$. Both the energy absorption (heating) and emission (cooling) processes are allowed. The heating of the system comes from the imbalance between absorption and emission of energy quanta $\hbar\omega$, due to the higher density of states and the larger value of the scattering matrix element for the energy absorption process. If a stronger criterion $E_{\mathbf{k}} \gg \hbar\omega \gg \sqrt{E_0 E_{\mathbf{k}}}$ is fulfilled such that $\alpha_k \ll 1$, only sidebands with $l = \pm 1$ are relevant. In this case, we obtain from Eq. (18)

$$\mathcal{P}_{\mathbf{k}} \approx 8 \frac{\sigma}{V} \sqrt{\frac{2E_{\mathbf{k}}}{\mu}} E_0, \quad (21)$$

showing the same dependence on parameters as the semiclassical picture. The heating of the system can be understood in the semiclassical picture where the collision rate is proportional to the initial relative velocity and the modulation energy gets transferred as heat to the secular motion.

Contributions from multi-quanta transfer processes $|n| > 1$ can be important. Indeed, as shown in Fig. 3, results obtained with the single-quantum transfer assumption deviate at small ω from the results where higher energy transfer processes are considered. However, the heating rate at lower ω with all the higher energy transfer processes included still converges to the semiclassical limit Eq. (21) obtained from the single-sideband approximation.

c. Strong-drive Regime $E_0 \gg \hbar\omega, E_{\mathbf{k}}$: In this limit, the strongly driven oscillation dominates over the particle's initial motion. The scattered particles, therefore, behave as if each particle were moving at velocity $\sqrt{E_0/m}$. Multi-quanta processes contribute significantly to the heating rate due to the large modulation index $\beta \sim \sqrt{E_0}/(\hbar\omega)$ of the final state. The heating rate reads

$$\begin{aligned} \mathcal{P}_{\mathbf{k}=0} &= \frac{2\pi}{\hbar} g^2 \sum_{n=0}^{\infty} \left[D_{3D}(n\hbar\omega) n\hbar\omega \right. \\ &\quad \times \left. \int d\theta \frac{\sin\theta}{2} |J_n \left(4\sqrt{\frac{nE_0}{\hbar\omega}} \cos\theta \right)|^2 \right] \\ &= 3.36 \sigma \sqrt{\frac{E_0}{m}} E_0, \end{aligned} \quad (22)$$

where the coefficient 3.36 is found numerically.

C. Ensemble Heating Rates

We now apply the two-particle results above to thermal ensembles with total atom number N by averaging over the ensemble as

$$\mathcal{P}_{\text{ens}} = \int \frac{d^3\mathbf{k}_1}{(2\pi)^3} \frac{d^3\mathbf{k}_2}{(2\pi)^3} \frac{d^3\mathbf{k}'_1}{(2\pi)^3} \frac{d^3\mathbf{k}'_2}{(2\pi)^3} \delta_{\mathbf{k}_1+\mathbf{k}_2, \mathbf{k}'_1+\mathbf{k}'_2} \quad (23)$$

$$\times f(\mathbf{k}_1)f(\mathbf{k}_2)\mathcal{P}(\mathbf{k}_1, \mathbf{k}_2 \rightarrow \mathbf{k}'_1, \mathbf{k}'_2),$$

where $f(\mathbf{k})$ is the particles' velocity distribution and $\mathcal{P}(\mathbf{k}_1, \mathbf{k}_2 \rightarrow \mathbf{k}'_1, \mathbf{k}'_2) = \mathcal{P}(\mathbf{k} \rightarrow \mathbf{k}')$ with $\mathbf{k} = (\mathbf{k}_1 - \mathbf{k}_2)$, $\mathbf{k}' = (\mathbf{k}'_1 - \mathbf{k}'_2)$. We calculate the heating rates at different regimes for 1) thermal clouds at temperature T , 2) a Bose-Einstein Condensate, and 3) a degenerate Fermi gas.

The analytic results presented in this section are obtained by assuming the single-sideband approximation unless otherwise stated, as justified in the previous Section. Multi-quanta results are presented as numerical results in Fig. 3.

a. Thermal Ensemble For a classical ensemble at a temperature T , the distribution $f(\mathbf{k})$ is the Boltzmann distribution. The resultant ensemble heating rate is

$$\mathcal{P}_{\text{ens}}^{\text{Thermal}} = \frac{2}{3} N n_{3D} \sigma \sqrt{\frac{\hbar\omega}{m}} E_0 \quad (24)$$

for the *rapid-modulation regime*, and

$$\mathcal{P}_{\text{ens}}^{\text{Thermal}} = \frac{16}{3} N n_{3D} \sigma \sqrt{\frac{kT}{\pi m}} E_0 \quad (25)$$

for the *semiclassical regime*. Along with the general expression $\mathcal{P} \sim \rho v_{\text{col}} E_0$, we identify $v_{\text{col}} \propto \sqrt{k_b T/m}$ to be the ensemble averaged thermal velocity, which reproduces the semiclassical picture where the micromotion energy is transferred to the secular motion via elastic collisions at a rate proportional to the thermally averaged relative speed between the two colliding particles.

b. Bose-Einstein Condensates A Bose-Einstein condensate at $T = 0$ is treated as an ensemble with $f(\mathbf{k}) = \delta(0)$. Following Eqs. (20) and (22), the heating rate reads

$$\mathcal{P}_{\text{ens}}^{\text{BEC}} = 3.36 N n_{3D} \sigma \sqrt{\frac{E_0}{m}} E_0 \quad (26)$$

at $E_0 \gg \hbar\omega$ and

$$\mathcal{P}_{\text{ens}}^{\text{BEC}} = \frac{2}{3} N n_{3D} \sigma \sqrt{\frac{\hbar\omega}{m}} E_0 \quad (27)$$

at $E_0 \ll \hbar\omega$, as shown in Fig. 3(b). The result suggests a collisional velocity $v_{\text{col}} \propto \sqrt{E_0/m}$ and $v_{\text{col}} \propto \sqrt{\hbar\omega/m}$ respectively.

To compare with the experimental results in Ref. [19], we numerically calculate the heating rates for various cases by directly calculating the sum Eq. (18) for the experimental parameters (Fig. 3). Our result is consistent with the weak Floquet heating observed.

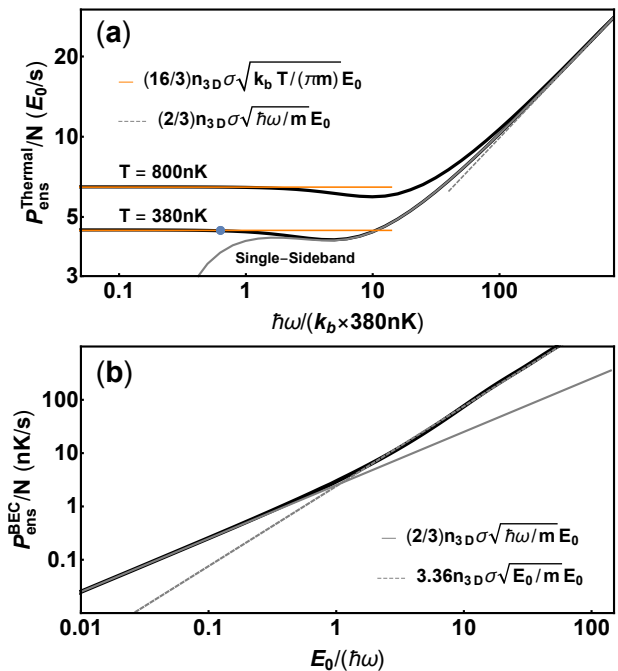


FIG. 3. Numerical calculations of the heating rate involving multi-quanta process $|n| \geq 1$ for a thermal cloud at temperature $T = 380$ nK (experimental condition in [19]), 800 nK and for $T = 0$ (i.e. an ideal Bose-Einstein condensate) at $\omega = 2\pi \times 5$ kHz. a) For the thermal cloud, the heating rates scale with $\sqrt{\omega}$ at high frequencies and become independent of ω around $\hbar\omega \approx 4k_b T$ which is the ensemble averaged $E_{\mathbf{k}}$. The heating rates, then plateau at the semiclassical value given by Eq. (25), illustrated by the orange lines. The solid gray and the dashed gray lines represent the results obtained from the single-sideband approximation Eq. (24) for $T = 380$ nK. The blue dot indicates the parameter implemented in [19]. b) For a condensate, the heating rate scales quadratically with the modulation strength characterized by E_0 when $\hbar\omega \gg E_0$ and shows semiclassical behavior at $\hbar\omega \ll E_0$. The black line is the numerical result, the dashed gray line is the heating rate calculated with the single-sideband approximation which matches the numerical result in the regime $\hbar\omega \gg E_0$. In this calculation we use $n_{3D} = 10^{12} \text{ cm}^{-3}$ and scattering length $a = 53.8a_0$.

D. Fermionic Systems

The heating effect studied in this work relies on atomic collisions which can be affected by particle statistics. For deeply degenerated Fermi gases, Pauli blocking effectively reduces the elastic collisional cross section σ , as experimentally demonstrated in [35–37]. As a result, collisional heating from periodic driving is suppressed in a fermionic system.

Fermi statistics dominates when E_F is the largest energy scale. At this condition, collisions occur on the Fermi surface. More formally, the heating rate for a

fermionic system is expressed as

$$\begin{aligned} \mathcal{P}_{\text{ens}}^F &= \int \frac{d^3\mathbf{k}_1}{(2\pi)^3} \frac{d^3\mathbf{k}_2}{(2\pi)^3} \frac{d^3\mathbf{k}'_1}{(2\pi)^3} \frac{d^3\mathbf{k}'_2}{(2\pi)^3} \delta_{\mathbf{k}_1+\mathbf{k}_2, \mathbf{k}'_1+\mathbf{k}'_2} \\ &\times f_{\downarrow}(\mathbf{k}_1) f_{\uparrow}(\mathbf{k}_2) [1 - f_{\downarrow}(\mathbf{k}'_1)] [1 - f_{\uparrow}(\mathbf{k}'_2)] \\ &\times \mathcal{P}(\mathbf{k}_1, \mathbf{k}_2 \rightarrow \mathbf{k}'_1, \mathbf{k}'_2). \end{aligned} \quad (28)$$

Here, $f = 1/(g_i + 1)$ is the occupation number with $g = \exp[(\hbar^2\mathbf{k} \cdot \mathbf{k}/(2m) - \mu)/k_bT]$, and μ is the chemical potential. Pauli blocking is captured by the extra factor $(1 - f_{\downarrow}(\mathbf{k}'_1))(1 - f_{\uparrow}(\mathbf{k}'_2))$, accounting for the occupation of the final states. Here we consider an equal mixture of spin-up and spin-down atoms.

When $\hbar\omega$ is the largest energy scale in the system, the entire Fermi sea is involved in the collisional heating process since all possible final states are unoccupied. The heating rate scales with ω in a similar way as in the case where Fermi statistics is absent as in Eq. (24).

When $\hbar\omega < E_F$, Pauli blocking occurs. At $T = 0$, f approaches a step function with $\mu = E_F$. Collisions occur in a shell with a thickness of $\sim (\hbar\omega/E_F)k_F$ around the sharp Fermi surface. We show in Appendix B that the heating rate of the 3D system becomes

$$\mathcal{P}_{\text{ens}}^F \approx \frac{\pi}{\sqrt{2}} N n_{3D} \sigma \left(\frac{\hbar\omega}{E_F} \right)^2 \sqrt{\frac{E_F}{m}} E_0 \quad (29)$$

when $\hbar\omega < E_F$, where the factor $(\hbar\omega/E_F)^2$ characterizes the effect of Pauli blocking. The power law of $\hbar\omega$ originates from three effects: 1) scatterings occurs in a shell at the surface of the Fermi sphere, accounting for a factor of $(\hbar\omega/E_F)^3$, 2) the scattering matrix elements contribute $1/(\hbar\omega)^2$, 3) the energy transfer per Floquet inelastic scattering process gives $\hbar\omega$.

For $T \neq 0$, thermal excitations smear the Fermi surface, affecting the number of states involved in the collisional processes. When $k_bT < \hbar\omega$, the modulation energy still dominate the scattering. The result is similar to the $T = 0$ cases, as shown in Fig. 4. When $k_bT > \hbar\omega$, the thickness of the collisional shell in momentum space is on the order of $(k_bT/E_F)k_F$. We show in Appendix B and also numerically that the heating rate scales as

$$\mathcal{P}_{\text{ens}}^F \propto N n_{3D} \sigma \left(\frac{T}{T_F} \right)^2 \sqrt{\frac{E_F}{m}} E_0 \quad (30)$$

at low temperature and is independent of the modulation frequency.

When the micromotion energy E_0 is large compared with both the thermal energy k_bT and the modulation energy $\hbar\omega$, the heating rate of the system becomes

$$\mathcal{P}_{\text{ens}}^F \propto N n_{3D} \sigma \left(\frac{E_0}{E_F} \right)^2 \sqrt{\frac{E_F}{m}} E_0, \quad (31)$$

which can be explained by considering the collision between two Fermi spheres displaced by k_0 from each other. Collisions are only allowed within a Fermi shell with a thickness of k_0 . The number of available states is therefore $\propto (k_0/k_F)^2 N^2$ which implies the Pauli blocking factor $(E_0/E_F)^2$.

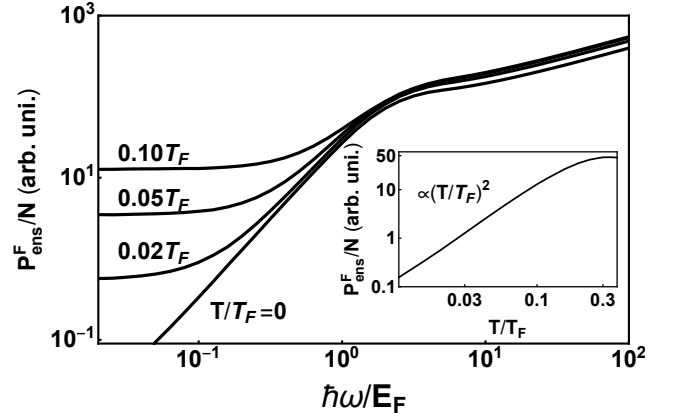


FIG. 4. Collisional heating rates in a periodically driven spin mixture of degenerated Fermi gases at $T = 0.1T_F$, $0.05T_F$, $0.02T_F$. The heating effects are Pauli suppressed for a cold Fermi gas when the energy quantum $\hbar\omega$ is smaller than the Fermi energy E_F . The discrepancies at high modulation frequencies are numerical artifact. Inset: heating rates at $\hbar\omega = 0.016 E_F$ and fixed E_F for various temperatures where $\hbar\omega < k_bT < E_F$. The heating rate is proportional to $(T/T_F)^2$.

E. Lower-Dimension Systems

Though our calculations are done for a specific system, several conclusions are generally valid. The result that $\mathcal{P} \sim \sqrt{\hbar\omega}$ at high frequencies is valid for any three-dimensional systems in free space with quadratic particle dispersion due to the density of states. Since the Floquet elastic collisional rate is bounded, such Floquet systems *cannot* be studied in thermal equilibrium in the limit of fast modulation frequencies. However, it is often desirable to have the modulation energy scale $\hbar\omega$ greater than all the other dynamic energy scales.

One possible solution is to go to lower dimensions, suggested by the observation that heating at high frequency originates from the increased density of states with higher energy $D_{3D} \sim \sqrt{\hbar\omega}$. In a 2D system, the density of states is independent of the energy, so that excessive collisional heating can be suppressed.

We consider here quasi-2D scenarios where the atomic motion is constrained in a two-dimensional pancake but scattering is still described by the 3D s -wave pseudopotential. This can be achieved in the case where the scattering length a is much larger than the interaction range but smaller than the oscillator length $l_0 = \sqrt{\hbar/(m\nu_{\perp})}$ in the strongly confined direction, with trapping frequency ν_{\perp} . The modulation is in-plane.

In these cases, the Floquet-Bloch wave function is written as

$$\Psi(x, \boldsymbol{\rho}, t) = \phi_{\perp}(x) \frac{1}{\sqrt{A}} \exp[i\mathbf{k}(t) \cdot \boldsymbol{\rho} - i\Phi(t)], \quad (32)$$

where $\boldsymbol{\rho} = \{y, z\}$ and $\mathbf{k} = \{k_y, k_z\}$ are the 2D radial vector and wave vectors. A is the system area.

The component along the strongly confined direction x has been explicitly separated as ϕ_{\perp} . We assume that $\phi_{\perp}(x) = \pi^{1/4} l_0^{1/2} \exp(-x^2/2l_0^2)$ and particles stay in the ground state wave function.

With these parameters, results obtained for the 3D case can be readily extended to quasi-2D by replacing the scattering strength g with the effective 2D scattering strength [38]

$$g_{2D} = \frac{2\sqrt{2\pi}\hbar^2 a}{m l_0}. \quad (33)$$

Together with the 2D density of states $D_{2D} = \mu/(2\pi\hbar^2)$ and $\sigma = 4\pi a^2$, the heating rate can be expressed as (see Appendix A 2 for details)

$$\mathcal{P}_{2D} = 16Nn_{2D} \frac{\hbar}{m} \frac{\sigma}{l_0^2} \left(\frac{8k_b T}{\hbar\omega} + 1 \right) E_0 \quad (34)$$

in the *rapid-modulation regime* and

$$\mathcal{P}_{2D} = 32Nn_{2D} \frac{\hbar}{m} \frac{\sigma}{l_0^2} E_0 \quad (35)$$

in the *semiclassical regime*. This can be interpreted as a 3D density $n_{3D} = n_{2D}/l_0 = N/(Al_0)$, and a velocity $v_{col} = \hbar/(ml_0)$. The heating rates are bounded in both regimes.

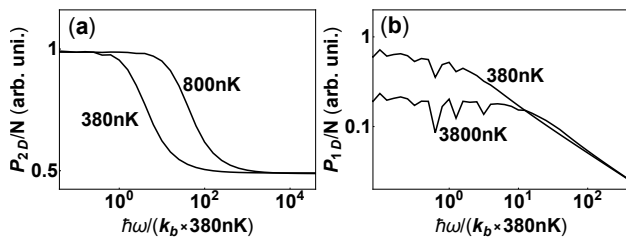


FIG. 5. Numerical calculations for the collisional heating rates in a quasi-2D (a) and quasi-1D system (b). The heating rate is independent of ω at high modulation frequencies in quasi-2D regime, and is suppressed with the increasing modulation frequency $\hbar\omega$ in quasi-1D. The oscillations in (b) are numerical artifacts.

Similarly, for a quasi-1D system with length L , $g_{1D} = \hbar^2 a/(ml_0^2)$ is the interaction strength. We obtained

$$\begin{aligned} \mathcal{P}_{1D} &\propto Nn_{1D} \left(\frac{\hbar}{m} \right)^2 \sqrt{\frac{m}{\hbar\omega}} \frac{\sigma}{l_0^4} E_0 \quad (\hbar\omega \gg k_b T), \\ \mathcal{P}_{1D} &\propto Nn_{1D} \left(\frac{\hbar}{m} \right)^2 \sqrt{\frac{m}{k_b T}} \frac{\sigma}{l_0^4} E_0 \quad (\hbar\omega \ll k_b T), \end{aligned} \quad (36)$$

with $n_{1D} = N/L$. The heating is now suppressed at high frequencies.

However, we note that the modulation frequency ω is assumed to be smaller than the trapping frequency along the direction of the strong confinement $\omega \ll \nu_{\perp}$ to avoid excitations to higher oscillation states. In the opposite

regime, systems are expected to reduce to the 3D case. These effects are addressed in the studies of collisional heating in modulated optical lattices [25, 27, 30], which is beyond the scope of this work.

IV. DISCUSSIONS AND SUMMARY

In this work we have shown how a Floquet system acquires energy from the external drive and heats up via inter-particle interactions. Using the scattering theory of Floquet-Bloch states, we have calculated the collisional heating rates for a cold atomic gas driven by time-periodic oscillating forces. We have shown that the heating of such systems can be described by a general expression by introducing the *effective collisional velocity* v_{col} parametrizing the density of states :

$$\mathcal{P} \propto \rho \sigma v_{col} E_0. \quad (37)$$

The velocity v_{col} is determined by the dominant energy in the system and is summarized in Table I. For fermionic systems, the collisional heating is further suppressed by Pauli blocking. In systems with lower dimensions, collisional heating is also reduced due to the modified density of states.

Our calculation can also help to understand the collisional heating in other similar Floquet systems by using appropriate interparticle potentials and Floquet-Bloch states wave functions. One such system is a *combined* trap for ions and neutral atoms, where ions are sympathetically cooled by atoms, limited by heating effects due to the micromotion of the ions [39–42]

In this work, we considered collisions between particles which are periodically driven by opposite forces. This is different from radio-frequency ion traps or the Time-Orbital Potential (TOP) trap [43], where all particles experience the same periodic force. In those cases, heating occurs due to non-adiabatic motion and the inhomogeneous strength of the drive or long-range Coulomb interactions [44].

A major motivation for studying Floquet heating is to assess the feasibility of preparing interesting Floquet many-body states. An essential question is whether a quantum state can be prepared before excessive heating occurs. This is often captured by a dimensionless parameter η defined as:

$$\eta \sim \frac{\tau}{\tau_{ev}}, \quad (38)$$

which characterizes the number of cycles of evolution the system can experience before the system's total energy increases by its characteristic energy E due to the heating. Here τ_{ev} is the timescale for the system's evolution and $\tau \sim (E/\mathcal{P})$ is the system's lifetime. Floquet engineering of quantum states requires $\eta \gg 1$. We can use the results of this paper to estimate the parameter η for various systems. For a thermal ensemble with

TABLE I. Effective collisional velocities v_{col} for various systems. The heating rates follow an unified description $\mathcal{P} \propto \rho \sigma v_{\text{col}} E_0$ where E_0 is the strength of the drive and ρ is the corresponding particle density.

v_{col}	Condition	Dominating Energy Scale
$\sqrt{\hbar\omega/m}$	$\hbar\omega \gg E_0, k_b T$	<i>Rapid-modulation regime</i> , where $\hbar\omega$ dominates
$\sqrt{k_b T/m}$	$k_b T \gg \hbar\omega, E_0$	<i>Semiclassical regime</i> , where the thermal motion dominates
$\sqrt{E_0/m}$	$E_0 \gg \hbar\omega, k_b T$	<i>Strong-drive regime</i> where micromotion dominates as in, for example, condensates and cold atomic samples.
$\sqrt{E_F/m}$	$E_F \gg \hbar\omega, k_b T, E_0$	Fermi energy dominant as in a degenerate Fermi gas. The heating rate is further suppressed by Pauli blocking with a suppression factor, $(\hbar\omega/E_F)^2$, (E_0/E_F) , or $(k_b T/E_F)^2$, depending on the relation between $\hbar\omega, k_b T, E_0$.
\hbar/ml_0	$\hbar\nu_{\perp} \gg \hbar\omega, k_b T, E_0$	Confinement energy dominant as in systems of lower dimension.

$\tau_{\text{ev}} \sim n_{3\text{D}} \sigma v_{\text{th}}$ and $E = k_b T$, we obtain $\eta \sim k_b T/E_0$ in the *semiclassical regime* and $\eta \sim k_b T/E_0 \sqrt{k_b T/\hbar\omega}$ for rapid modulation. For condensates, evolution of the system is characterized by the mean-field interaction strength $\hbar/\tau_{\text{ev}} \sim U = gn_{3\text{D}}$ in 3D, which leads to $\eta \sim U^2/\mathcal{P} \sim n_{3\text{D}}/k_0^3$ or $\sim \sqrt{\hbar^2/ma^2}/\sqrt{\hbar\omega}(U/E_0)$. For Fermi gases, $\hbar/\tau_{\text{ev}} \sim E_F$, giving $\eta \sim E_F^{1/2}/(\hbar^2\omega^2 E_0)$. This illustrates the benefit of using systems with large Fermi energy.

The purpose of this paper was a transparent treatment of heating in different regimes for a particularly simple Floquet system. Our discussion provides a starting point for more complex systems where we expect similar regimes depending on the hierarchy of the relevant energy scales.

ACKNOWLEDGMENTS

We would like to thank useful discussions with Nigel Cooper, Erich Mueller, Alan O. Jamison, Jeongwon Lee, Furkan Çağrı Top, Yair Margalit, and Gediminas Juzeliūnas. We would like to thank Jesse Amato-Grill for critical reading of the manuscript. We acknowledge support from the NSF through the Center for Ultracold Atoms and award 1506369, from ARO-MURI Non-equilibrium Many-body Dynamics (Grant No. W911NF-14-1-0003), from AFOSR-MURI Quantum Phases of Matter (Grant No. FA9550-14-1-0035), from ONR (Grant No. N00014-17-1-2253) and a Vannevar-Bush Faculty Fellowship.

Appendix A: Ensemble Averaged Heating Rates

1. 3D Systems

We present the detailed calculation for Eq. (25). Rewriting Eq. (23) with the center-of-mass and relative coordinates $\mathbf{K} = (\mathbf{k}_1 + \mathbf{k}_2)/2 = (\mathbf{k}'_1 + \mathbf{k}'_2)/2$, and $\Gamma(\mathbf{k}_1, \mathbf{k}_2 \rightarrow \mathbf{k}'_1, \mathbf{k}'_2) = \Gamma(\mathbf{k} \rightarrow \mathbf{k}')$ with $\mathbf{k} = (\mathbf{k}_1 - \mathbf{k}_2)$, $\mathbf{k}' = (\mathbf{k}'_1 - \mathbf{k}'_2)$ one obtains:

$$\mathcal{P} = \int \frac{d^3\mathbf{K}}{(2\pi)^3} \frac{d^3\mathbf{k}}{(2\pi)^3} \frac{d^3\mathbf{k}'}{(2\pi)^3} f\left(\frac{\mathbf{k}}{2} + \mathbf{K}\right) f\left(-\frac{\mathbf{k}}{2} + \mathbf{K}\right) \mathcal{P}(\mathbf{k} \rightarrow \mathbf{k}') \quad (\text{A1})$$

with the Boltzmann distribution function.

$$f(\mathbf{k}) = N \left(\frac{\hbar^2}{2\pi m k_b T} \right)^{3/2} \exp\left(-\frac{\hbar^2 \mathbf{k} \cdot \mathbf{k}}{2m k_b T}\right)$$

As discussed in Sec. III B, we consider only the processes where $n = \pm 1$. The coupling matrix elements M_n , to the lowest orders in α_k , are shown in Table II.

TABLE II. Approximate coupling matrix elements M_n for various Floquet collision processes.

M_0/g	M_1/g	M_{-1}/g	M_2/g	M_{-2}/g
1	$\frac{\hbar k_0(k_z - k'_z)}{2m\omega}$	$-\frac{\hbar k_0(k_z - k'_z)}{2m\omega}$	$\frac{1}{2} \left[\frac{\hbar k_0(k_z - k'_z)}{2m\omega} \right]^2$	$\frac{1}{2} \left[\frac{\hbar k_0(k_z - k'_z)}{2m\omega} \right]^2$

With the single-sideband assumption, we obtain the analytic expression of Eq. (18) by explicitly calculating $\gamma^2(\mathbf{k}, \pm 1)$:

$$\mathcal{P}_{\mathbf{k}} = 4 \frac{\sigma}{V} \sum_{n=\pm 1} \sqrt{\frac{E_{\mathbf{k}} + n\hbar\omega}{m}} \left(\frac{\hbar^2 k_z^2}{\mu\hbar\omega} + \frac{\hbar^2 |\mathbf{k}|^2}{3\mu\hbar\omega} + \frac{2n}{3} \right) n E_0. \quad (\text{A2})$$

with $n = \pm 1$ for the *semiclassical regime*, and $n = 1$ for the *rapid-modulation regime*. The total heating rate \mathcal{P} can be readily obtained as

$$\mathcal{P} = N^2 \left(\frac{4\pi\hbar^2}{mk_b T} \right)^{3/2} \int \frac{d^3\mathbf{k}}{(2\pi)^3} e^{-\frac{\hbar^2\mathbf{k}\cdot\mathbf{k}}{4mk_b T}} \mathcal{P}_{\mathbf{k}}, \quad (\text{A3})$$

which gives Eq. (20) and Eq. (25) at the corresponding limits.

2. Quasi-2D Systems

We start with the Floquet-Bloch states wave function for quasi-2D system written as Eq. (32). The scattering strength, defined as

$$g = \int d\mathbf{r} \phi_i(\mathbf{r}) V(\mathbf{r}) \phi_f(\mathbf{r}),$$

has the form [38]:

$$g_{2D} = \frac{2\sqrt{2\pi}\hbar^2 a}{m l_0}$$

in quasi-2D. The results obtained for 3D cases can be readily extended to quasi-2D by replacing g with g_{2D} and using the corresponding 2D density. We therefore obtain the coupling matrix element between two quasi-2D Floquet-Bloch states

$$M_n(\mathbf{k} \rightarrow \mathbf{k}') = g_{2D} J_n(\alpha_k - \alpha_{k'}), \quad (\text{A4})$$

and obtain

$$\begin{aligned} \gamma_{2D}^2(\mathbf{k}, n) = & \\ \frac{1}{2g_{2D}^2} \int_0^\pi d\theta & |M_n(\mathbf{k} \rightarrow \sqrt{|\mathbf{k}|^2 + 2\mu n\omega/\hbar} \cos \theta)|^2. \end{aligned} \quad (\text{A5})$$

Following similar procedures as in the 3D calculation, and using the 2D density of states lead to

$$\mathcal{P}_{\mathbf{k}}^{2D} = \frac{\pi\mu g_{2D}^2}{4\hbar^3 A} \sum_{n=\pm 1} \left(\frac{2\hbar^2 k_z^2}{\mu\hbar\omega} + \frac{\hbar^2 |\mathbf{k}|^2}{\mu\hbar\omega} + 2n \right) n E_0. \quad (\text{A6})$$

Together with the 2D Boltzmann distribution $f(\mathbf{k}) = N \left(\frac{2\pi\hbar^2}{mk_b T} \right) \exp\left(-\frac{\hbar^2\mathbf{k}\cdot\mathbf{k}}{2mk_b T}\right)$, we obtain the heating rate of the ensemble

$$\begin{aligned} \mathcal{P}_{2D} &= \int \frac{d^2\mathbf{K}}{(2\pi)^2} \frac{d^2\mathbf{k}}{(2\pi)^2} \frac{d^2\mathbf{k}'}{(2\pi)^2} f\left(\frac{\mathbf{k}}{2} + \mathbf{K}\right) f\left(-\frac{\mathbf{k}}{2} + \mathbf{K}\right) \mathcal{P}(\mathbf{k} \rightarrow \mathbf{k}') \\ &= 2N^2 \left(\frac{2\pi\hbar^2}{mk_b T} \right) \int \frac{d^2\mathbf{k}}{(2\pi)^2} e^{-\frac{\hbar^2\mathbf{k}\cdot\mathbf{k}}{4mk_b T}} \mathcal{P}_{\mathbf{k}}^{2D}, \end{aligned} \quad (\text{A7})$$

which gives Eqs. (34) and (35).

3. Quasi-1D Systems

For a quasi-1D system, we use the 1D wave function, a scattering strength g_{1D} , and M_n

$$\begin{aligned} \Psi(x, y, z, t) &= \phi_\perp(x, y) \frac{1}{\sqrt{L}} \exp[ik(t)z - i\Phi(t)], \\ g_{1D} &= \frac{\hbar^2 a}{ml_0^2}, \\ M_n(k \rightarrow k') &= g_{1D} J_n(\alpha_k - \alpha_{k'}), \\ D_{1D}(E) &= \frac{1}{2\pi\hbar} \sqrt{\frac{\mu}{2E}}, \end{aligned} \quad (\text{A8})$$

to obtain

$$\begin{aligned} \gamma_{1D}^2(k, n) = & \\ \frac{1}{2g_{1D}^2} \left[& |M_n(k \rightarrow \sqrt{k^2 + 2\mu n\omega/\hbar})|^2 \right. \\ & \left. + |M_n(k \rightarrow -\sqrt{k^2 + 2\mu n\omega/\hbar})|^2 \right], \end{aligned} \quad (\text{A9})$$

yielding

$$\mathcal{P}_k^{1D} = \frac{8g_{1D}^2}{\hbar^2\omega L} \sum_n \frac{k^2 + n\mu\hbar\omega/\hbar^2}{\sqrt{k^2 + 2\mu n\hbar\omega/\hbar^2}} n E_0. \quad (\text{A10})$$

With the 1D Boltzmann distribution $f(k) = N \left(\frac{2\pi\hbar^2}{mk_b T} \right)^{1/2} \exp\left(-\frac{\hbar^2 k^2}{mk_b T}\right)$, we calculate the heating rate of the ensemble

$$\begin{aligned} \mathcal{P}_{1D} &= \int \frac{dK}{2\pi} \frac{dk}{2\pi} \frac{dk'}{2\pi} f\left(\frac{k}{2} + K\right) f\left(-\frac{k}{2} + K\right) \mathcal{P}(k \rightarrow k') \\ &= N^2 \left(\frac{\pi\hbar^2}{mk_b T} \right)^{1/2} \int \frac{dk}{2\pi} e^{-\frac{\hbar^2 k^2}{4mk_b T}} \mathcal{P}_k^{1D}, \end{aligned} \quad (\text{A11})$$

which results in Eq. (36).

We add the note that the scaling $\sim 1/\sqrt{k_b T}$ in the regime $\hbar\omega \ll k_b T$ cannot be directly obtained in the same way as for other dimensions. In 1D, terms in zeroth, first, and second order in $\hbar\omega/E_k$ cancel between the $n = \pm 1$ processes if both processes are allowed for two particles with $k^2 > 2\mu n\hbar\omega/h^2$

$$\begin{aligned} & \sum_{n=\pm 1} \frac{k^2 + n\mu\hbar\omega/\hbar^2}{\sqrt{k^2 + 2\mu n\hbar\omega/\hbar^2}} n \\ &= - \left(\frac{\hbar\omega}{E_k} \right)^3 \left(\frac{\hbar^2}{mE_k} \right)^2 + \mathcal{O} \left[\left(\frac{\hbar\omega}{E_k} \right)^4 \right]. \end{aligned} \quad (\text{A12})$$

Therefore, even for $k_b T \gg \hbar\omega$, the leading contribution comes from the regime $k^2 < 2\mu n\hbar\omega/h^2$, where only the

$n = +1$ process is allowed. We obtain

$$\begin{aligned}
\mathcal{P}_{1D} &= N^2 \left(\frac{\pi \hbar^2}{m k_b T} \right)^{1/2} \int \frac{dk}{2\pi} e^{-\frac{\hbar^2 k^2}{4m k_b T}} \mathcal{P}_k^{1D} \\
&\approx N^2 \left(\frac{\hbar}{m} \right)^3 \frac{\sigma}{l_0^4} \frac{E_0}{\pi^2 \omega L} \sqrt{\frac{m\pi}{k_b T}} \\
&\quad \times \int_{-\sqrt{2\mu\hbar\omega/\hbar^2}}^{\sqrt{2\mu\hbar\omega/\hbar^2}} dk e^{-\frac{\hbar^2 k^2}{4m k_b T}} \frac{k^2 + \mu\hbar\omega/\hbar^2}{\sqrt{k^2 + 2\mu\hbar\omega/\hbar^2}} \\
&\sim N^2 \frac{\sqrt{2}}{\pi^2 L} \left(\frac{\hbar}{m} \right)^2 \sqrt{\frac{m\pi}{k_b T}} \frac{\sigma}{l_0^4} E_0 \quad (\hbar\omega \ll k_b T).
\end{aligned} \tag{A13}$$

The obtained scaling is consistent with the numerical results.

Appendix B: Derivation of the Pauli Blocking Factor

1. Zero-Temperature Fermi Gases

In this part we present the calculation for Eq. (29). The interspin collision rate of a two-component Fermi mixture is written as

$$\begin{aligned}
\mathcal{P}_{\text{ens}}^F &= \int \frac{d^3\mathbf{k}_1}{(2\pi)^3} \frac{d^3\mathbf{k}_2}{(2\pi)^3} \frac{d^3\mathbf{k}'_1}{(2\pi)^3} \frac{d^3\mathbf{k}'_2}{(2\pi)^3} \delta_{\mathbf{k}_1+\mathbf{k}_2, \mathbf{k}'_1+\mathbf{k}'_2} \\
&\quad \times f_{\downarrow}(\mathbf{k}_1) f_{\uparrow}(\mathbf{k}_2) (1 - f_{\downarrow}(\mathbf{k}'_1)) (1 - f_{\uparrow}(\mathbf{k}'_2)) \\
&\quad \times \mathcal{P}(\mathbf{k}_1, \mathbf{k}_2 \rightarrow \mathbf{k}'_1, \mathbf{k}'_2).
\end{aligned} \tag{B1}$$

We denote $\epsilon_i = \hbar^2 |\mathbf{k}_i|^2 / 2m$, $\epsilon'_i = \hbar^2 |\mathbf{k}'_i|^2 / 2m$, and rewrite the integral in spherical coordinates with $\mathbf{k}_i = k_i (\sin \theta_i \cos \phi_i, \sin \theta_i \sin \phi_i, \cos \theta_i)$, $\mathbf{k}'_i = k'_i (\sin \theta'_i \cos \phi'_i, \sin \theta'_i \sin \phi'_i, \cos \theta'_i)$.

Momentum conservation $\mathbf{k}_1 + \mathbf{k}_2 = \mathbf{k}'_1 + \mathbf{k}'_2$ gives

$$\begin{aligned}
\mathcal{P}(\mathbf{k}_1, \mathbf{k}_2 \rightarrow \mathbf{k}'_1, \mathbf{k}_1 + \mathbf{k}_2 - \mathbf{k}'_1) \\
&= C_{\Gamma} \left[\frac{(\mathbf{k}_1 - \mathbf{k}_2)_z - (\mathbf{k}'_1 - \mathbf{k}'_2)_z}{4} \right]^2 \delta(\epsilon_1 + \epsilon_2 + \hbar\omega - \epsilon'_1 - \epsilon'_2) \\
&= C_{\Gamma} \left[\frac{k_1 \cos \theta_1 - k'_1 \cos \theta'_1}{2} \right]^2 \delta(\epsilon_1 + \epsilon_2 + \hbar\omega - \epsilon'_1 - \epsilon'_2),
\end{aligned} \tag{B2}$$

where $C_{\Gamma} = \frac{2\pi}{\hbar} \frac{g^2 \hbar^3 k_0^2}{\mu^2 \omega}$ is a constant, and $\epsilon'_2 = \frac{\hbar^2}{2m} |\mathbf{k}_1 +$

$\mathbf{k}_2 - \mathbf{k}'_1|^2$. The heating rate Eq. (B1) now has the form

$$\begin{aligned}
\mathcal{P}_{\text{ens}}^F &= \int \frac{d^3\mathbf{k}_1}{(2\pi)^3} \frac{d^3\mathbf{k}_2}{(2\pi)^3} \frac{d^3\mathbf{k}'_1}{(2\pi)^3} \delta(\epsilon_1 + \epsilon_2 + \hbar\omega - \epsilon'_1 - \epsilon'_2) \\
&\quad \times f_{\downarrow}(\mathbf{k}_1) f_{\uparrow}(\mathbf{k}_2) (1 - f_{\downarrow}(\mathbf{k}'_1)) (1 - f_{\uparrow}(\mathbf{k}_1 + \mathbf{k}_2 - \mathbf{k}'_1)) \\
&\quad \times C_{\Gamma} \left[\frac{k_1 \cos \theta_1 - k'_1 \cos \theta'_1}{2} \right]^2 \\
&= C_{\Gamma} \left[\frac{(2m)^{3/2}}{2\hbar^3} \right]^3 \int \frac{\sqrt{\epsilon_1 \epsilon_2 \epsilon'_1}}{(2\pi)^9} d\epsilon_1 d\epsilon_2 d\epsilon'_1 d\Omega_1 d\Omega_2 d\Omega'_1 \\
&\quad \times f_{\downarrow}(\epsilon_1) f_{\uparrow}(\epsilon_2) (1 - f_{\downarrow}(\epsilon'_1)) (1 - f_{\uparrow}(\epsilon_1 + \epsilon_2 + \hbar\omega - \epsilon'_1)) \\
&\quad \times \left[\frac{k_1 \cos \theta_1 - k'_1 \cos \theta'_1}{2} \right]^2 \\
&\quad \times \delta(\epsilon_1 + \hbar\omega - \epsilon'_1 - \frac{\hbar^2 q^2}{2m} + \frac{\hbar^2}{m} \mathbf{q} \cdot \mathbf{k}_2),
\end{aligned} \tag{B3}$$

where $\mathbf{q} = \mathbf{k}_1 - \mathbf{k}'_1$ and $q = |\mathbf{q}|$. Integrating over the solid angle $d\Omega_2 = \sin \theta_2 d\theta_2 d\phi_2$ gives

$$\begin{aligned}
\mathcal{P}_{\text{ens}}^F &= (2\pi) C_{\Gamma} \left[\frac{(2m)^{3/2}}{2\hbar^3} \right]^3 \int \frac{\sqrt{\epsilon_1 \epsilon_2 \epsilon'_1}}{(2\pi)^9} d\epsilon_1 d\epsilon_2 d\epsilon'_1 d\Omega_1 d\Omega'_1 \\
&\quad \times f_{\downarrow}(\epsilon_1) f_{\uparrow}(\epsilon_2) (1 - f_{\downarrow}(\epsilon'_1)) (1 - f_{\uparrow}(\epsilon_1 + \epsilon_2 + \hbar\omega - \epsilon'_1)) \\
&\quad \times \left[\frac{k_1 \cos \theta_1 - k'_1 \cos \theta'_1}{2} \right]^2 \\
&\quad \times \frac{m}{\hbar^2 q \sqrt{\epsilon_2}} \int_{-1}^1 dx \delta(x - \frac{-\epsilon_1 - \hbar\omega + \epsilon'_1 + \frac{\hbar^2 q^2}{2m}}{\frac{\hbar^2}{m} q \sqrt{\epsilon_2}}),
\end{aligned} \tag{B4}$$

with $x = \cos \theta_2$. We subsequently integrate over Ω_1 and Ω'_1 . When $\mathbf{k}_1, \mathbf{k}'_1$ vary over their respective solid angles Ω_1, Ω'_1 with fixed lengths $k_1 = \sqrt{\epsilon_1}, k'_1 = \sqrt{\epsilon'_1}$, the differential vector \mathbf{q} also varies over the entire solid angle Ω_q with the length varying from $\sqrt{\epsilon'_1} - \sqrt{\epsilon_1}$ to $\sqrt{\epsilon'_1} + \sqrt{\epsilon_1}$. Therefore, we have the equivalence

$$d\Omega_1 d\Omega_2 = C_q q^2 dq \sin \theta_q d\theta_q d\phi_q d\phi_l,$$

where $C_q = 6/(\sqrt{\epsilon'_1} + \sqrt{\epsilon_1})^3$ is the normalization factor, and ϕ_l is the angle between the planes expanded by

$\{\mathbf{k}_1, \mathbf{k}'_1\}$ and $\{\mathbf{q}, \mathbf{e}_z\}$. The heating rate follows as

$$\begin{aligned}
\mathcal{P}_{\text{ens}}^{\text{F}} &= (2\pi)^3 C_{\Gamma} \left[\frac{(2m)^{3/2}}{2\hbar^3} \right]^3 \int \frac{C_q \sqrt{\epsilon_1 \epsilon_2 \epsilon'_1}}{(2\pi)^9} d\epsilon_1 d\epsilon_2 d\epsilon'_1 \\
&\times q^2 dq \sin \theta_q d\theta_q \\
&\times f_{\downarrow}(\epsilon_1) f_{\uparrow}(\epsilon_2) (1 - f_{\downarrow}(\epsilon'_1)) (1 - f_{\uparrow}(\epsilon_1 + \epsilon_2 + \hbar\omega - \epsilon'_1)) \\
&\times \frac{m(q \cos \theta_q)^2}{4\hbar^2 q \sqrt{\epsilon_2}} \int_{-1}^1 dx \delta\left(x - \frac{-\epsilon_1 - \hbar\omega + \epsilon'_1 + \frac{\hbar^2 q^2}{2m}}{\hbar^2 q \sqrt{\epsilon_2}/m}\right) \\
&= C_{\Gamma} \left[\frac{(2m)^{3/2}}{2\hbar^3} \right]^3 \int \frac{C_q \sqrt{\epsilon_1 \epsilon_2 \epsilon'_1}}{(2\pi)^6} d\epsilon_1 d\epsilon_2 d\epsilon'_1 \\
&\times f_{\downarrow}(\epsilon_1) f_{\uparrow}(\epsilon_2) (1 - f_{\downarrow}(\epsilon'_1)) (1 - f_{\uparrow}(\epsilon_1 + \epsilon_2 + \hbar\omega - \epsilon'_1)) \\
&\times \int_{\sqrt{\epsilon'_1 - \sqrt{\epsilon_1}}}^{\sqrt{\epsilon'_1 + \sqrt{\epsilon_1}}} \frac{mq^3 dq}{6\hbar^2 \sqrt{\epsilon_2}} \int_{-1}^1 dx \delta\left(x - \frac{-\epsilon_1 - \hbar\omega + \epsilon'_1 + \frac{\hbar^2 q^2}{2m}}{\hbar^2 q \sqrt{\epsilon_2}/m}\right) \\
&= C_{\Gamma} \left[\frac{(2m)^{3/2}}{2\hbar^3} \right]^3 \int \frac{C_q \sqrt{\epsilon_1 \epsilon_2 \epsilon'_1}}{(2\pi)^6} d\epsilon_1 d\epsilon_2 d\epsilon'_1 \\
&\times f_{\downarrow}(\epsilon_1) f_{\uparrow}(\epsilon_2) (1 - f_{\downarrow}(\epsilon'_1)) (1 - f_{\uparrow}(\epsilon_1 + \epsilon_2 + \hbar\omega - \epsilon'_1)) \\
&\times \left[\int_{\sqrt{\epsilon'_1 - \sqrt{\epsilon_1}}}^{\sqrt{\epsilon'_1 + \sqrt{\epsilon_1}}} \frac{mq^3 dq}{6\hbar^2 \sqrt{\epsilon_2}} \right. \\
&\left. \theta(\sqrt{2\epsilon'_2 - \epsilon_2} + \sqrt{\epsilon_2} - q) \theta(q - (\sqrt{2\epsilon'_2 - \epsilon_2} - \sqrt{\epsilon_2})) \right].
\end{aligned} \tag{B5}$$

Note that so far the only approximation adopted is the single-sideband approximation, and that the first sideband is weak, implying $J_1(x) \approx x/2$.

When $\hbar\omega < E_{\text{F}}$, we have $\sqrt{2\epsilon'_2 - \epsilon_2} + \sqrt{\epsilon_2} \approx \sqrt{\epsilon'_1} + \sqrt{\epsilon_1} \approx 2\sqrt{\hbar^2/(2m)}k_{\text{F}}$, and $\sqrt{2\epsilon'_2 - \epsilon_2} - \sqrt{\epsilon_2} \approx \sqrt{\epsilon'_1} - \sqrt{\epsilon_1} \approx \hbar\omega/(2\sqrt{E_{\text{F}}})$. The integral over q in Eq. B5 now gives

$$\begin{aligned}
\mathcal{P}_{\text{ens}}^{\text{F}} &\approx C_{\Gamma} \left[\frac{(2m)^{3/2}}{2\hbar^3} \right]^3 \int \frac{C_q \sqrt{\epsilon_1 \epsilon_2 \epsilon'_1}}{(2\pi)^6} d\epsilon_1 d\epsilon_2 d\epsilon'_1 \\
&\times f_{\downarrow}(\epsilon_1) f_{\uparrow}(\epsilon_2) (1 - f_{\downarrow}(\epsilon'_1)) (1 - f_{\uparrow}(\epsilon_1 + \epsilon_2 + \hbar\omega - \epsilon'_1)) \\
&\times \frac{8mk_{\text{F}}^4}{3\hbar^2 \sqrt{\epsilon_2}} \left(\frac{\hbar^2}{2m} \right)^2 \\
&\approx C_{\Gamma} \left[\frac{(2m)^{3/2}}{2\hbar^3} \right]^3 E_{\text{F}}^{3/2} \frac{(\hbar\omega)^3}{8(2\pi)^6} \frac{8m}{3\hbar^2}.
\end{aligned} \tag{B6}$$

Here we adopt the approximation

$$\begin{aligned}
&\int C_q \sqrt{\epsilon_1 \epsilon_2 \epsilon'_1} d\epsilon_1 d\epsilon_2 d\epsilon'_1 \frac{1}{\sqrt{\epsilon_2}} \\
&\times f_{\downarrow}(\epsilon_1) f_{\uparrow}(\epsilon_2) (1 - f_{\downarrow}(\epsilon'_1)) (1 - f_{\uparrow}(\epsilon_1 + \epsilon_2 + \hbar\omega - \epsilon'_1)) \\
&\approx E_{\text{F}}^{-1/2} \frac{(\hbar\omega)^3}{8}.
\end{aligned} \tag{B7}$$

With the definition of the Fermi energy $(2mE_{\text{F}})^{3/2} = 3n_{3\text{D}}\hbar^3\pi^2$, we eventually obtain

$$\mathcal{P}_{\text{ens}}^{\text{F}} \approx \frac{\pi}{\sqrt{2}} N n_{3\text{D}} \sigma \left(\frac{\hbar\omega}{E_{\text{F}}} \right)^2 \sqrt{\frac{E_{\text{F}}}{m}} E_0, \tag{B8}$$

which shows explicitly the Fermi suppression factor $(\hbar\omega/E_{\text{F}})^2$.

The calculations above can be extended to the regime of small $\hbar\omega$ where multi-quanta transfer processes are relevant.

2. Finite Temperature Fermi Gases

In this section we present the calculation for the Pauli blocking factor $(T/T_{\text{F}})^2$ when $T/T_{\text{F}} \ll 1$. We further assume that $\hbar\omega \ll k_{\text{b}}T$. The non-zero temperature case is different from the zero temperature Fermi gas mainly in two aspects: first, as discussed briefly in the main text, the active Fermi shell formed by the accessible states has a thickness of $k_{\text{b}}T$ instead of $\hbar\omega$. Second, energy quanta *emission* processes are now allowed. In the lowest order approximation, the heating rate can be calculated with only $n \pm 1$ processes and leads to

$$\begin{aligned}
&\int C_q \sqrt{\epsilon_1 \epsilon_2 \epsilon'_1} d\epsilon_1 d\epsilon_2 d\epsilon'_1 \frac{1}{\sqrt{\epsilon_2}} \\
&\times \left[f_{\downarrow}(\epsilon_1) f_{\uparrow}(\epsilon_2) (1 - f_{\downarrow}(\epsilon'_1)) (1 - f_{\uparrow}(\epsilon_1 + \epsilon_2 + \hbar\omega - \epsilon'_1)) \right. \\
&\quad \left. - f_{\downarrow}(\epsilon_1) f_{\uparrow}(\epsilon_2) (1 - f_{\downarrow}(\epsilon'_1)) (1 - f_{\uparrow}(\epsilon_1 + \epsilon_2 - \hbar\omega - \epsilon'_1)) \right] \\
&= \int C_q \sqrt{\epsilon_1 \epsilon_2 \epsilon'_1} d\epsilon_1 d\epsilon_2 d\epsilon'_1 \frac{1}{\sqrt{\epsilon_2}} \\
&\times f_{\downarrow}(\epsilon_1) f_{\uparrow}(\epsilon_2) (1 - f_{\downarrow}(\epsilon'_1)) \left(-\frac{\partial f(\epsilon)}{\partial \epsilon} \hbar\omega \right) \Big|_{\epsilon=\epsilon_1+\epsilon_2-\epsilon'_1} \\
&\sim E_{\text{F}}^{-1/2} (k_{\text{b}}T)^2 \hbar\omega.
\end{aligned} \tag{B9}$$

Together with Eq. (B6), the Fermi suppression factor is readily recognized to be $(k_{\text{b}}T/E_{\text{F}})^2$.

-
- [1] S. Rahav, I. Gilary, and S. Fishman, *Phys. Rev. A* **68**, 013820 (2003).
- [2] N. Goldman and J. Dalibard, *Phys. Rev. X* **4**, 031027 (2014).
- [3] P. Hauke, O. Tieleman, A. Celi, C. Ölschläger, J. Simonet, J. Struck, M. Weinberg, P. Windpassinger, K. Sengstock, M. Lewenstein, and A. Eckardt, *Phys. Rev. Lett.* **109**, 145301 (2012).
- [4] J. Struck, J. Simonet, and K. Sengstock, *Phys. Rev. A* **90**, 031601 (2014).
- [5] C. E. Creffield, G. Pieplow, F. Sols, and N. Goldman, *New Journal of Physics* **18**, 093013 (2016).
- [6] M. Bukov, M. Kolodrubetz, and A. Polkovnikov, *Phys. Rev. Lett.* **116**, 125301 (2016).
- [7] B. M. Anderson, I. B. Spielman, and G. Juzeliūnas, *Phys. Rev. Lett.* **111**, 125301 (2013).
- [8] Z.-F. Xu, L. You, and M. Ueda, *Phys. Rev. A* **87**, 063634 (2013).
- [9] K. Jiménez-García, L. J. LeBlanc, R. A. Williams, M. C. Beeler, C. Qu, M. Gong, C. Zhang, and I. B. Spielman, *Phys. Rev. Lett.* **114**, 125301 (2015).
- [10] J. Yu, Z.-F. Xu, R. Lü, and L. You, *Phys. Rev. Lett.* **116**, 143003 (2016).
- [11] S. K. Baur, M. H. Schleier-Smith, and N. R. Cooper, *Phys. Rev. A* **89**, 051605 (2014).
- [12] J. Cayssol, B. Dra, F. Simon, and R. Moessner, *physica status solidi (RRL) Rapid Research Letters* **7**, 101 (2013).
- [13] N. H. Lindner, D. L. Bergman, G. Refael, and V. Galitski, *Phys. Rev. B* **87**, 235131 (2013).
- [14] M. Aidelsburger, M. Atala, M. Lohse, J. T. Barreiro, B. Paredes, and I. Bloch, *Phys. Rev. Lett.* **111**, 185301 (2013).
- [15] H. Miyake, G. A. Siviloglou, C. J. Kennedy, W. C. Burton, and W. Ketterle, *Phys. Rev. Lett.* **111**, 185302 (2013).
- [16] C. J. Kennedy, W. C. Burton, W. C. Chung, and W. Ketterle, *Nature Physics* **11**, 859 EP (2015).
- [17] M. Aidelsburger, M. Lohse, C. Schweizer, M. Atala, J. T. Barreiro, S. Nascimbène, N. R. Cooper, I. Bloch, and N. Goldman, *Nature Physics* **11**, 162 EP (2014).
- [18] G. Jotzu, M. Messer, R. Desbuquois, M. Lebrat, T. Uehlinger, D. Greif, and T. Esslinger, *Nature* **515**, 237 EP (2014).
- [19] B. Shteynas, J. Lee, F. C. Top, J.-R. Li, A. O. Jamison, G. Juzelin, and W. Ketterle, “How to dress radio-frequency photons with tunable momentum,” (2018).
- [20] J. Zhang, P. W. Hess, A. Kyprianidis, P. Becker, A. Lee, J. Smith, G. Pagano, I. D. Potirniche, A. C. Potter, A. Vishwanath, N. Y. Yao, and C. Monroe, *Nature* **543**, 217 EP (2017).
- [21] S. Choi, J. Choi, R. Landig, G. Kucsko, H. Zhou, J. Isoya, F. Jelezko, S. Onoda, H. Sumiya, V. Khemani, C. von Keyserlingk, N. Y. Yao, E. Demler, and M. D. Lukin, *Nature* **543**, 221 EP (2017).
- [22] S. A. Weidinger and M. Knap, *Scientific Reports* **7**, 45382 EP (2017).
- [23] A. Lazarides, A. Das, and R. Moessner, *Phys. Rev. E* **90**, 012110 (2014).
- [24] L. D’Alessio and M. Rigol, *Phys. Rev. X* **4**, 041048 (2014).
- [25] S. Choudhury and E. J. Mueller, *Phys. Rev. A* **90**, 013621 (2014).
- [26] T. Bilitewski and N. R. Cooper, *Phys. Rev. A* **91**, 033601 (2015).
- [27] S. Choudhury and E. J. Mueller, *Phys. Rev. A* **92**, 063639 (2015).
- [28] M. Genske and A. Rosch, *Phys. Rev. A* **92**, 062108 (2015).
- [29] M. Weinberg, C. Ölschläger, C. Sträter, S. Prella, A. Eckardt, K. Sengstock, and J. Simonet, *Phys. Rev. A* **92**, 043621 (2015).
- [30] M. Reitter, J. Näger, K. Wintersperger, C. Sträter, I. Bloch, A. Eckardt, and U. Schneider, *Phys. Rev. Lett.* **119**, 200402 (2017).
- [31] A. Eckardt and E. Anisimovas, *New Journal of Physics* **17**, 093039 (2015).
- [32] F. Casas, J. A. Oteo, and J. Ros, *Journal of Physics A: Mathematical and General* **34**, 3379 (2001).
- [33] V. Novičenko, E. Anisimovas, and G. Juzeliūnas, *Phys. Rev. A* **95**, 023615 (2017).
- [34] C. Raab, J. Eschner, J. Bolle, H. Oberst, F. Schmidt-Kaler, and R. Blatt, *Phys. Rev. Lett.* **85**, 538 (2000).
- [35] B. DeMarco, S. B. Papp, and D. S. Jin, *Phys. Rev. Lett.* **86**, 5409 (2001).
- [36] G. Ferrari, *Phys. Rev. A* **59**, R4125 (1999).
- [37] M. J. Holland, B. DeMarco, and D. S. Jin, *Phys. Rev. A* **61**, 053610 (2000).
- [38] D. S. Petrov, M. Holzmann, and G. V. Shlyapnikov, *Phys. Rev. Lett.* **84**, 2551 (2000).
- [39] R. G. DeVoe, *Phys. Rev. Lett.* **102**, 063001 (2009).
- [40] K. Chen, S. T. Sullivan, and E. R. Hudson, *Phys. Rev. Lett.* **112**, 143009 (2014).
- [41] C. Zipkes, S. Palzer, L. Ratschbacher, C. Sias, and M. Köhl, *Phys. Rev. Lett.* **105**, 133201 (2010).
- [42] S. Haze, M. Sasakawa, R. Saito, R. Nakai, and T. Mukaiyama, *Phys. Rev. Lett.* **120**, 043401 (2018).
- [43] W. Petrich, M. H. Anderson, J. R. Ensher, and E. A. Cornell, *Phys. Rev. Lett.* **74**, 3352 (1995).
- [44] D. J. Wineland, C. Monroe, W. M. Itano, D. Leibfried, B. E. King, and D. M. Meekhof, *Journal of research of the National Institute of Standards and Technology* **103**, 259 (1998).

Bibliography

- [1] R.P. Feynman. Simulating physics with computers. *Int J Theor Phys*, volume = 21, issue = 6-7, pages = 467–488, year = 1982, month = June, publisher = Springer, doi = <https://doi.org/10.1007/BF02650179>,.
- [2] J. Struck, C. Ölschläger, R. Le Targat, P. Soltan-Panahi, A. Eckardt, M. Lewenstein, P. Windpassinger, and K. Sengstock. Quantum simulation of frustrated classical magnetism in triangular optical lattices. *Science*, 333(6045):996–999, 2011.
- [3] Gregor Jotzu, Michael Messer, Rémi Desbuquois, Martin Lebrat, Thomas Uehlinger, Daniel Greif, and Tilman Esslinger. Experimental realization of the topological haldane model with ultracold fermions. *Nature*, 515:237 EP –, 11 2014.
- [4] Markus Greiner, Olaf Mandel, Tilman Esslinger, Theodor W. Hänsch, and Immanuel Bloch. Quantum phase transition from a superfluid to a mott insulator in a gas of ultracold atoms. *Nature*, 415(6867):39–44, 2002.
- [5] Maciej Lewenstein, Anna Sanpera, Veronica Ahufinger, Bogdan Damski, Aditi Sen(De), and Ujjwal Sen. Ultracold atomic gases in optical lattices: mimicking condensed matter physics and beyond. *Advances in Physics*, 56(2):243–379, 2007.
- [6] W. Ketterle and M. W. Zwierlein. Making, probing and understanding ultracold Fermi gases. *Nuovo Cimento Rivista Serie*, 31:247–422, May 2008.
- [7] Maxwell F. Parsons, Florian Huber, Anton Mazurenko, Christie S. Chiu, Widagdo Setiawan, Katherine Wooley-Brown, Sebastian Blatt, and Markus Greiner. Site-resolved imaging of fermionic ${}^6\text{Li}$ in an optical lattice. *Phys. Rev. Lett.*, 114:213002, May 2015.
- [8] Lawrence W. Cheuk, Matthew A. Nichols, Katherine R. Lawrence, Melih Okan, Hao Zhang, and Martin W. Zwierlein. Observation of 2d fermionic mott insulators of ${}^{40}\text{K}$ with single-site resolution. *Phys. Rev. Lett.*, 116:235301, Jun 2016.
- [9] Rajibul Islam, Ruichao Ma, Philipp M. Preiss, M. Eric Tai, Alexander Lukin, Matthew Rispoli, and Markus Greiner. Measuring entanglement entropy in a quantum many-body system. *Nature*, 528:77 EP –, 12 2015.

- [10] Colin J. Kennedy, William Cody Burton, Woo Chang Chung, and Wolfgang Ketterle. Observation of bose–einstein condensation in a strong synthetic magnetic field. *Nature Physics*, 11:859 EP –, 08 2015.
- [11] M. Aidelsburger, M. Atala, S. Nascimbène, S. Trotzky, Y.-A. Chen, and I. Bloch. Experimental realization of strong effective magnetic fields in an optical lattice. *Phys. Rev. Lett.*, 107:255301, Dec 2011.
- [12] Aviv Keshet. *A Next-Generation Apparatus for Lithium Optical Lattice Experiments*. PhD dissertation, MIT, 2012. This is a full PHDTHESIS entry.
- [13] Edward Su. *Fluctuations and State Preparation in Quantum Degenerate Gases of Soidum and Lithium*. PhD dissertation, MIT, 2014. This is a full PHDTHESIS entry.
- [14] Wujie Huang. *Spin-Orbit Coupling in Optical Superlattice*. PhD dissertation, MIT, 2015. This is a full PHDTHESIS entry.
- [15] K. B. Davis, M. O. Mewes, M. R. Andrews, N. J. van Druten, D. S. Durfee, D. M. Kurn, and W. Ketterle. Bose-einstein condensation in a gas of sodium atoms. *Phys. Rev. Lett.*, 75:3969–3973, Nov 1995.
- [16] Victor Galitski and Ian B. Spielman. Spin–orbit coupling in quantum gases. *Nature*, 494:49 EP –, 02 2013.
- [17] Vinod Kumar Joshi. Spintronics: A contemporary review of emerging electronics devices. *Engineering Science and Technology, an International Journal*, 19(3):1503 – 1513, 2016.
- [18] M. Z. Hasan and C. L. Kane. Colloquium: Topological insulators. *Rev. Mod. Phys.*, 82:3045–3067, Nov 2010.
- [19] Zhan Wu, Long Zhang, Wei Sun, Xiao-Tian Xu, Bao-Zong Wang, Si-Cong Ji, Youjin Deng, Shuai Chen, Xiong-Jun Liu, and Jian-Wei Pan. Realization of two-dimensional spin-orbit coupling for bose-einstein condensates. *Science*, 354(6308):83–88, 2016.
- [20] K. Osterloh, M. Baig, L. Santos, P. Zoller, and M. Lewenstein. Cold atoms in non-abelian gauge potentials: From the hofstadter "moth" to lattice gauge theory. *Phys. Rev. Lett.*, 95:010403, Jun 2005.
- [21] J. Ruseckas, G. Juzeliūnas, P. Öhberg, and M. Fleischhauer. Non-abelian gauge potentials for ultracold atoms with degenerate dark states. *Phys. Rev. Lett.*, 95:010404, Jun 2005.
- [22] Xiong-Jun Liu, Mario F. Borunda, Xin Liu, and Jairo Sinova. Effect of induced spin-orbit coupling for atoms via laser fields. *Phys. Rev. Lett.*, 102:046402, Jan 2009.

- [23] N.R. Cooper. Rapidly rotating atomic gases. *Advances in Physics*, 57(6):539–616, 2008.
- [24] Jean Dalibard, Fabrice Gerbier, Gediminas Juzeliūnas, and Patrik Öhberg. Colloquium: Artificial gauge potentials for neutral atoms. *Rev. Mod. Phys.*, 83:1523–1543, Nov 2011.
- [25] Frank Wilczek and A. Zee. Appearance of gauge structure in simple dynamical systems. *Phys. Rev. Lett.*, 52:2111–2114, Jun 1984.
- [26] Xiong-Jun Liu, Mario F. Borunda, Xin Liu, and Jairo Sinova. Effect of induced spin-orbit coupling for atoms via laser fields. *Phys. Rev. Lett.*, 102:046402, Jan 2009.
- [27] Y. J. Lin, K. Jiménez-García, and I. B. Spielman. Spin-orbit-coupled bose-einstein condensates. *Nature*, 471:83 EP –, 03 2011.
- [28] J. Ruseckas, G. Juzeliūnas, P. Öhberg, and M. Fleischhauer. Non-abelian gauge potentials for ultracold atoms with degenerate dark states. *Phys. Rev. Lett.*, 95:010404, Jun 2005.
- [29] Christian Flindt, Anders S. Sørensen, and Karsten Flensberg. Spin-orbit mediated control of spin qubits. *Phys. Rev. Lett.*, 97:240501, Dec 2006.
- [30] Hirokazu Miyake, Georgios A. Siviloglou, Colin J. Kennedy, William Cody Burton, and Wolfgang Ketterle. Realizing the harper hamiltonian with laser-assisted tunneling in optical lattices. *Phys. Rev. Lett.*, 111:185302, Oct 2013.
- [31] M. Aidelsburger, M. Atala, M. Lohse, J. T. Barreiro, B. Paredes, and I. Bloch. Realization of the hofstadter hamiltonian with ultracold atoms in optical lattices. *Phys. Rev. Lett.*, 111:185301, Oct 2013.
- [32] Long Zhang and Xiong-Jun Liu. Spin-orbit coupling and topological phases for ultracold atoms. 2018.
- [33] Nathaniel Q. Burdick, Yijun Tang, and Benjamin L. Lev. Long-lived spin-orbit-coupled degenerate dipolar fermi gas. *Phys. Rev. X*, 6:031022, Aug 2016.
- [34] Junru Li, Wujie Huang, Boris Shteynas, Sean Burchesky, Furkan Çağrı Top, Edward Su, Jeongwon Lee, Alan O. Jamison, and Wolfgang Ketterle. Spin-orbit coupling and spin textures in optical superlattices. *Phys. Rev. Lett.*, 117:185301, Oct 2016.
- [35] Jun-Ru Li, Jeongwon Lee, Wujie Huang, Sean Burchesky, Boris Shteynas, Furkan Çağrı Top, Alan O. Jamison, and Wolfgang Ketterle. A stripe phase with supersolid properties in spin-orbit-coupled bose-einstein condensates. *Nature*, 543:91 EP –, 03 2017.

- [36] Tin-Lun Ho and Shizhong Zhang. Bose-einstein condensates with spin-orbit interaction. *Phys. Rev. Lett.*, 107:150403, Oct 2011.
- [37] Chunji Wang, Chao Gao, Chao-Ming Jian, and Hui Zhai. Spin-orbit coupled spinor bose-einstein condensates. *Phys. Rev. Lett.*, 105:160403, Oct 2010.
- [38] Yun Li, Lev P. Pitaevskii, and Sandro Stringari. Quantum tricriticality and phase transitions in spin-orbit coupled bose-einstein condensates. *Phys. Rev. Lett.*, 108:225301, May 2012.
- [39] Massimo Boninsegni and Nikolay V. Prokof'ev. Colloquium: Supersolids: What and where are they? *Rev. Mod. Phys.*, 84:759–776, May 2012.
- [40] John Beamish. Supersolid helium. *Nature*, 427(6971):204–205, 2004.
- [41] A. B. Kuklov, L. Pollet, N. V. Prokof'ev, and B. V. Svistunov. Quantum plasticity and supersolid response in helium-4. *Phys. Rev. B*, 90:184508, Nov 2014.
- [42] Julian Léonard, Andrea Morales, Philip Zupancic, Tilman Esslinger, and Tobias Donner. Supersolid formation in a quantum gas breaking a continuous translational symmetry. *Nature*, 543:87 EP –, 03 2017.
- [43]
- [44] Sergey V. Tovstonog, Sunao Kurimura, and Kenji Kitamura. High power continuous-wave green light generation by quasiphase matching in mg stoichiometric lithium tantalate. *Applied Physics Letters*, 90(5):051115, 2007.
- [45] G. D. Boyd and D. A. Kleinman. *Journal of Applied Physics*, 39.
- [46] Y. Furukawa, K. Kitamura, A. Alexandrovski, R. K. Route, M. M. Fejer, and G. Foulon. Green-induced infrared absorption in mgo doped linbo3. *Applied Physics Letters*, 78(14):1970–1972, 2001.
- [47] E.M. Lifshits L.D. Landau. *Theoretical Physics. Mechanics*, volume 1. Phys-MathLit.
- [48] Wolfgang Paul. Electromagnetic traps for charged and neutral particles. *Rev. Mod. Phys.*, 62:531–540, Jul 1990.
- [49] Ernest D. Courant, M. Stanley Livingston, and Hartland S. Snyder. The strong-focusing synchrotron—a new high energy accelerator. *Phys. Rev.*, 88:1190–1196, Dec 1952.
- [50] Jon H. Shirley. Solution of the schrödinger equation with a hamiltonian periodic in time. *Phys. Rev.*, 138:B979–B987, May 1965.
- [51] N. Goldman and J. Dalibard. Periodically driven quantum systems: Effective hamiltonians and engineered gauge fields. *Phys. Rev. X*, 4:031027, Aug 2014.

- [52] Marin Bukov, Luca D'Alessio, and Anatoli Polkovnikov. Universal high-frequency behavior of periodically driven systems: from dynamical stabilization to floquet engineering. *Advances in Physics*, 64(2):139–226, 2015.
- [53] W. R. Salzman. Quantum mechanics of systems periodic in time. *Phys. Rev. A*, 10:461–465, Aug 1974.
- [54] Saar Rahav, Ido Gilary, and Shmuel Fishman. Effective hamiltonians for periodically driven systems. *Phys. Rev. A*, 68:013820, Jul 2003.
- [55] T. P. Grozdanov and M. J. Raković. Quantum system driven by rapidly varying periodic perturbation. *Phys. Rev. A*, 38:1739–1746, Aug 1988.
- [56] Xinyu Luo, Lingna Wu, Jiyao Chen, Qing Guan, Kuiyi Gao, Zhi-Fang Xu, L. You, and Ruquan Wang. Tunable atomic spin-orbit coupling synthesized with a modulating gradient magnetic field. *Scientific Reports*, 6:18983 EP –, 01 2016.
- [57] Jun-Ru Li, Boris Shteynas, and Wolfgang Ketterle. Floquet heating in interacting atomic gases with an oscillating force. *arXiv:1906.08747*.